

**MICRO-MACRO INVESTIGATIONS ON THE MECHANICAL
BEHAVIOR AND MATERIAL FAILURE USING THE FRAMEWORK
OF EXTENDED FINITE ELEMENT METHOD (XFEM)**

by

© **Ahmed Youssri Elruby, B.Sc., M.Sc.**

A thesis submitted to the

School of Graduate Studies

in partial fulfillment of the requirements for the degree of

Doctor of Philosophy (Mechanical Engineering)

Faculty of Engineering and Applied Science

Memorial University of Newfoundland

October 2019

St. John's, Newfoundland, Canada

Abstract

The current dissertation provides developments on mechanical behavior and material failure modeling utilizing the framework of extended finite element method (XFEM). Different types of materials, i.e., brittle and ductile were numerically investigated at different length scales. Plain epoxy resin representing the brittle behavior was prepared and tested using digital image correlation (DIC) displacement measurement system on an Instron© load-frame under different types of loading. Advanced technology methods such as optical and scan electron microscopy (SEM) were used to characterize the failure mechanisms of the tested specimens. Also, computed tomography (CT) scans were used to identify the void content within the epoxy specimens. In addition, fracture surfaces were also CT scanned to further investigate epoxy's failure mechanism closely. On the other hand, relevant reported testing results in the literature regarding low and high strength steel materials were used to represent the ductile behavior. Different micromechanical methods such as unit cell (UC) and representative volume element (RVE) were employed in the framework of finite element method (FEM) or XFEM to numerically obtain mechanical behaviors and/or investigate material damage from a microscopic point of view. Several algorithms were developed to automate micromechanical modeling in Abaqus, and they were implemented using Python scripting. Also, different user-defined subroutines regarding the material behavior and damage were developed for macroscopic modeling and implemented using Fortran. A chief contribution of the current dissertation is the extended Ramberg-Osgood (ERO) relationship to account for metal porosity which was enabled by utilizing micromechanical modeling along with regression analyses.

To my beloved wife Dina

Acknowledgements

After thanking and praising Almighty "ALLAH" for his numerous blessings throughout my program of study and my entire life. I would like to express my sincere gratitude and deepest appreciation to my parents and my lovely wife for their continuous support and inspiration to accomplish this work.

I am extremely grateful to my thesis supervisor Dr. Sam Nakhla for mentoring me throughout my program. His valuable encouragement, motivation, and advice were indispensable for accomplishing this work. I would like to extend my sincere thankfulness to him for being a great supervisor, brother and a friend. I appreciate his kindness, respect, and morals in dealing with me as well as every member of our research group. Thanks a million for everything my dear kind sir.

As well, I would like to thank the highly respected supervisory committee members, the great Dr. Amgad Hussein and Dr. Lorenzo Moro, for their valuable discussions and recommendations. Special thanks to Dr. Amgad Hussein for his extreme kindness and treating me as a son. Also, I would like to thank the examination committee members for dedicating time and effort reviewing the thesis.

Also, I would like to extend my sincere gratitude to the Academic Program Assistant in the graduate studies office, Ms. Colleen Mahoney for her continuous support during my program of study. Also, the help of Ms. Tina Dwyer is much appreciated.

I am gratefully acknowledging the financial support provided by the President's Doctoral Student Investment Fund (PDSIF) at Memorial University of Newfoundland; Natural Sciences and Engineering Research Council of Canada (NSERC), Discovery Grant Program [NSERC DG # 210415].

A handwritten signature in black ink, appearing to read "A. E. Ruby", with a horizontal line extending to the right from the end of the signature.

Table of Contents

Abstract	ii
Acknowledgements	iv
Table of Contents	v
List of Tables	ix
List of Figures	xi
List of Nomenclature or Abbreviations	xvi
Co-Authorship Statement.....	xviii
1 Introduction.....	22
1.1 Background and Research Motivation	22
1.2 Research Objectives and Significance	26
1.3 Thesis Outline	27
1.4 Reference.....	29
2 Fracture Behavior of Heavily Cross-linked Epoxy under Uniaxial Tension and Three-point Bending Loads; Testing, Fractography and Numerical Modeling	33
2.1 Abstract	33
2.2 Introduction	33
2.3 Material and Mechanical Testing.....	38
2.3.1 Material Preparation and Test Setup.....	38
2.3.2 Computed Tomography Imaging Procedure.....	41
2.4 Results and Discussion.....	43
2.4.1 Uniaxial tension test results	43
2.4.2 Three-point bending test results	46
2.5 Fractography.....	49
2.5.1 Optical Microscopy.....	49
2.5.2 Scan Electron Microscopy	53
2.5.3 Computed Tomography Imaging.....	62
2.6 Numerical Modeling	66
2.7 Conclusions	71
2.8 References	73

3	Actual Microstructural Voids Generation in Finite Element Analysis utilizing Computed Tomography Scan of Heavily Cross-linked Epoxy.....	77
3.1	Abstract	77
3.2	Introduction	77
3.3	Multiscale Modeling Employing Microstructural Voids	82
3.3.1	Computed Tomography (CT) Scan.....	84
3.3.2	Actual microstructural model generation.....	86
3.3.3	Specimen model employing micro-voids	88
3.3.4	Material model and damage.....	92
3.4	Results and Discussion.....	94
3.5	Conclusions	97
3.6	References	99
4	Strain Energy Density Based Damage Initiation in Heavily Cross-linked Epoxy Using XFEM	102
4.1	Abstract	102
4.2	Introduction	102
4.3	Theoretical background.....	106
4.4	Proposed SED Based Damage Initiation Criterion	111
4.5	Finite Element Modeling.....	116
4.6	Material and Mechanical Testing.....	118
4.7	Results and Comparisons	120
4.7.1	Material Characterization.....	120
4.7.2	Uniaxial loading.....	122
4.7.3	Three-point bending loading.....	128
4.8	Conclusions	134
4.9	References	136
5	Standard Mechanics Approach to Predict Effective Mechanical Behavior of Porous Sintered Steel Using Micromechanical RVE-based Finite Element Modeling	140
5.1	Abstract	140
5.2	Introduction	140

5.3	Theoretical Background	144
5.3.1	Standard Mechanics Approach	145
5.4	Micromechanical Finite Element Modeling.....	146
5.5	Results and Discussion.....	151
5.5.1	Effective stress-strain results	151
5.5.2	Microstructural local fields	156
5.6	Conclusions	160
5.7	References	161
6	Extending the Ramberg-Osgood relationship to Account for Metal Porosity.....	167
6.1	Abstract	167
6.2	Introduction	167
6.3	Theoretical Background	172
6.4	Micromechanical investigations for model development	177
6.5	Extended Ramberg-Osgood relationship	188
6.6	Conclusions	195
6.7	References	196
7	Two-stage finite element modeling procedure to predict elastoplastic behavior and damage of porous metals	201
7.1	Abstract	201
7.2	Introduction	201
7.3	Material model and methods	206
7.3.1	Proposed modeling procedure overview.....	206
7.3.2	Material model	209
7.3.3	Representative volume element (RVE) method.....	211
7.3.4	Macromechanical modeling and failure.....	216
7.4	Finite Element Modeling.....	221
7.4.1	Micromechanical RVE models	221
7.4.2	Macromechanical modeling and failure.....	226
7.5	Results and Discussion.....	228
7.5.1	Micromechanical RVE results	228

7.5.2	Macromechanical modeling results	232
7.6	Conclusions	239
7.7	References	241
8	Automating XFEM Modeling Process for Optimal Failure Predictions	249
8.1	Abstract	249
8.2	Introduction	250
8.3	Research Significance	253
8.4	XFEM Fundamentals and ABAQUS Implementation	254
8.4.1	Mathematical Formulation	254
8.4.2	Enrichment Zone Sizing	257
8.4.3	XFEM in ABAQUS	259
8.5	The Proposed Approach	262
8.6	Numerical Modeling	268
8.7	Specimens Preparation and Testing	269
8.8	Results and Discussion	272
8.9	Algorithm Validation with Test Data from Literature	274
8.10	Conclusions	280
8.11	References	281
9	Conclusions and Future Work	285

List of Tables

Table 2.1. LAMPOXY61 physical properties at room temperature, 25oC.	38
Table 2.2. Failure limits from uniaxial tension testing.	45
Table 2.3. Failure limits from Three-point load testing.	49
Table 3.1. Geometric features of physical voids data file resulting from CT scan post-processing.	88
Table 3.2. Epoxy resin material model parameters.	94
Table 4.1 Commonly used damage initiation mechanisms in Abaqus.	110
Table 4.2. Polynt LAMPOXY61 physical properties at 25 °C	118
Table 4.3. Failure limits for uniaxial tensile specimens	123
Table 4.4. FE predictions (uniaxial): Failure loads, displacements and percentage error.	125
Table 4.5. Failure limits for three-point loading specimens.	130
Table 4.6. FE predictions (three-point loading): Failure loads, deflections and percentage error.	132
Table 5.1 Prediction results and percentage errors compared to testing results.	155
Table 6.1 Micromechanical unit cell models material parameters.	179
Table 6.2 Different levels of porosity factor and corresponding pore radii.	185
Table 6.3 Effective material properties at different levels of porosity factor.	186
Table 6.4 Material parameters evaluated from extended R-O results at reported levels of porosity.	191
Table 7.1. Material properties of the non-porous metals.	211
Table 7.2. User-defined material (UMAT) subroutine properties.	217
Table 7.3. Low strength steel mechanical properties: predicted vs testing.	237
Table 7.4. High strength steel mechanical properties: predicted vs testing.	239
Table 8.1: Mix design for tested specimens.	270
Table 8.2: Mechanical properties from testing the six concrete specimens.	271
Table 8.3: Failure load: Testing, predictions and relative error.	272
Table 8.5: Computational effort comparison: conventional XFEM vs. proposed approach.	273
Table 8.6: L-shaped specimen mechanical properties as reported in (Unger & Eckardt, 2011).	274
Table 8.7: Proposed Algorithm versus experimental data from testing.	276
Table 8.8. Computational effort comparison (L-Shape): conventional XFEM vs. proposed approach.	277
Table 8.9: T-section specimen mechanical properties as reported in (AbdelAleem & Hassan, 2017).	278

Table 8.10. Computational effort comparison (T-section): conventional XFEM vs. proposed approach.279

List of Figures

Figure 2.1 Specimen geometry: a) uniaxial tensile dog-bone and b) three-point loading prism.	39
Figure 2.2 Load frame setup showing videoextensometer and dog-bone specimen marking.	40
Figure 2.3 Three-point load test setup showing prismatic specimen marking.....	41
Figure 2.4 Dog-bone specimen at different time frames showing stress whitening caused by inelastic deformation.....	43
Figure 2.5 Stress-strain curves for uniaxial load testing.	44
Figure 2.6 Local axial load-displacement measurements from DIC.	45
Figure 2.7 Monochromic scan of dog-bone specimens after failure.....	46
Figure 2.8 Load-deflection curves from three-point loading tests.....	47
Figure 2.9 Monochromic scan of prismatic specimens after failure.....	48
Figure 2.10 Optical microscopic images of dog-bone specimens failure surfaces.	51
Figure 2.11 Optical microscopic images of prismatic specimens' failure surfaces.....	52
Figure 2.12 Failure surface of specimen T6: a) wide view, b) zoom on area of interest, c) zoom on area of interest, and d) zoom on area of interest.	54
Figure 2.13 Failure Surface of T6: a) microcrack dimensions, b) areas of interest, c) zoom on area of interest, and d) zoom on area of interest.	56
Figure 2.14 Failure Surface of B3: a) wide view, and b) zoom on area of interest.	57
Figure 2.15 Failure Surface of B3: a) upper right-side, and b) lower right-side.	58
Figure 2.16 Failure Surface of B3, right-hand side, compressive-side.....	59
Figure 2.17 Failure Surface of B4: a) wide view, b) zoom on area of interest, c) increased zoom on area of interest, and d) further increased zoom on area of interest.	60
Figure 2.18 Failure Surface of B4 right-side: a) compressive-side, and b) tensile-side.	61
Figure 2.19 Three-dimensional CT scan of specimen T6a.....	63
Figure 2.20 Specimen T6a Planes of interest, left to right: a) largest pore volume, b) plane slightly beneath failure surface, and c) failure surface.	64
Figure 2.21 Three-dimensional CT scan of specimen T6b.....	65
Figure 2.22 Specimen T6b Planes of interest, left to right: a) largest pore volume, b) plane slightly beneath failure surface, and c) failure surface.	66
Figure 2.23 Procedures for generating actual microstructural UC model: a) OM image, b) Isolated image, c) Drawing exchange format image, and d) Actual UC model.	68
Figure 2.24 Von-Mises contour plot results of actual microstructure UC model: a) UC model, and b) Zoomed in view showing micro cracks.	69
Figure 2.25 Residual plastic strains compared to failed specimens' monochromic scans.	70
Figure 2.26 Load-displacement curves: Testing vs. numerical.	71
Figure 3.1 Finite element model involving microstructural voids procedure.....	83
Figure 3.2 Reconstructed Sample, a) without pores identified, b) with pores identified...	85

Figure 3.3 Top-view of failure surface showing local plasticity and crazes of cracking. .	86
Figure 3.4 Final microstructural slab showing voids at their exact locations.....	87
Figure 3.5 (a) Micromechanical slab finite element mesh (b) Zoomed in view.....	89
Figure 3.6 Final constructed part (b) Final convergent mesh.	90
Figure 3.7 Schematic diagram showing damaged and undamaged material behavior of epoxy.....	91
Figure 3.8 von Mises stress contour plot: (a) complete specimen (b) Cut-out at micro-voids zoomed in view (c) top view of micro-slice at different load increments.	95
Figure 3.9 Equivalent plastic strain contour plot: (a) complete specimen (b) top view of micro-slice at different load increments.....	96
Figure 3.10 The vicinity of a micro-void showing element damage status at different load increments.	97
Figure 4.1 Three-dimensional linear elastic cracked body problem.....	106
Figure 4.2 Traction-separation law: Damage initiation and evolution.	109
Figure 4.3 Tension test and three-point bending test schematic diagrams	117
Figure 4.4 (a) Dog-bone specimen profile. (b) Prism specimen profile.	119
Figure 4.5 (a) Uniaxial test setup. (b) Three-point bending setup.	120
Figure 4.6 Discoloration caused by plasticity at different time frames for uniaxial testing	121
Figure 4.7 Load vs. relative displacement from video extensometer (uniaxial tension) .	123
Figure 4.8. Load vs. relative displacement FE predictions compared to testing results..	124
Figure 4.9 Failure surfaces profiles (a, b, and c) built-in mechanisms (d) the proposed SED mechanism.	126
Figure 4.10 Plastic strains contour plot using proposed SED damage compared to discoloration from testing.	127
Figure 4.11 Specimen T1: Failure surface microscopic image.....	128
Figure 4.12 Load vs. relative displacement from video extensometer (three-point bending)	129
Figure 4.13 Load vs. deflection FE predictions compared to testing results.....	131
Figure 4.14 Von Mises contour plot and initiated crack location using proposed SED damage mechanism.....	132
Figure 4.15 Plastic strains: (a) proposed SED results (b) Specimen B5 monochromic image showing whitening.....	133
Figure 4.16 Failure surface microscopic image: (a) specimen B3 (b) specimen B4.	134
Figure 5.1 (a) Infinitesimal element with micro-pores (b) RVE mesh with single spherical void (c) RVE mesh with a center hole.....	148
Figure 5.2 Center hole model: (a) partitioned RVE (b) convergent RVE mesh.....	149
Figure 5.3 RVE models partitioning: (a) center hole (b) four holes (c) sixteen holes (d) sixty-four holes.	150

Figure 5.4 RVE models convergent mesh: (a) center hole (b) four holes (c) sixteen holes (d) sixty-four holes.....	150
Figure 5.5 Predicted effective stress-strain curves for 10% porosity: CPE4R vs. CPS4R elements.	152
Figure 5.6 Predicted vs. testing (Chawla & Deng, 2003) stress-strain curves for 16 holes RVE.....	154
Figure 5.7 Predicted stress-strain curves for 16 holes RVE with different hole distributions.	156
Figure 5.8 Von-Mises contour plots for RVEs with different holes number.....	157
Figure 5.9 Von-Mises contour plots for 16 holes RVE with different hole distributions.	158
Figure 5.10 Total energy dissipated by plastic deformation in uniformly distributed holes RVEs.	159
Figure 5.11 Total energy dissipated by plastic deformation in randomly distributed holes RVEs.	159
Figure 6.1 Non-dimensional stress vs. non-dimensional strain showing the effect of increasing the hardening exponent n	177
Figure 6.2 Schematic diagram showing finite element modeling at different scales.	178
Figure 6.3 Unit cell geometry showing initial configuration (uniform distribution) of pore locations.	179
Figure 6.4 Pore shape/distribution effect on mechanical behavior.	181
Figure 6.5 Low strength steel stress-strain curves: Micromechanical FE results vs testing (Chawla & Deng, 2005).....	183
Figure 6.6 High strength steel stress-strain curves: Micromechanical FE results vs testing (Stephens et al., 1998).....	183
Figure 6.7 Low strength steel predicted stress-strain curves at 10 porosity levels.....	185
Figure 6.8 Effect of porosity on modulus of elasticity and yield strength.....	187
Figure 6.9 Effect of total porosity on stress-strain behavior using (Eq.6.14).....	189
Figure 6.10 Predicted effective behavior using (Eq.6.14) for low strength steel at reported levels of porosity.	190
Figure 6.11 Predicted effective behavior using (Eq.6.14) for high strength steel at reported levels of porosity.....	191
Figure 6.12 Specimen geometry and three-dimensional finite element models (not to scale).	192
Figure 6.13 Low strength steel stress-strain curves: Macro numerical results vs testing (Chawla & Deng, 2005).....	194
Figure 6.14 High strength steel stress-strain curves: Macro numerical results vs testing (Stephens et al., 1998).....	194
Figure 7.1 Flowchart showing the scope of work at different scales (micro/macro).....	208
Figure 7.2 Material properties evaluation from effective stress-strain curves.....	215

Figure 7.3 Schematic diagram showing damaged and undamaged material behaviors for metals.	219
Figure 7.4 Single ellipsoidal RVE model cutaway and void geometry.	222
Figure 7.5 Ellipsoidal void shape and geometric parameters.	223
Figure 7.6 Ellipsoidal shapes at different aspect ratios: (a) $a=1.0$, (b) $a=1.5$, (c) $a=2.0$, (d) $a=2.5$	224
Figure 7.7 (a) Automatically partitioned RVE model showing edge seeding, (b) resulting high quality structured mesh.	225
Figure 7.8 RVE model showing rigid node faces highlighted in blue and red.	226
Figure 7.9 Finite element models geometry and loading conditions.	227
Figure 7.10 RVE effective stress-strain behaviors for 4.5% porosity low strength steel at different aspect ratios.	229
Figure 7.11 RVE effective elastic-plastic behavior vs low strength steel testing (Chawla & Deng, 2005).	230
Figure 7.12 RVE effective elastic-plastic behavior vs strength steel testing (Stephens et al., 1998b).	231
Figure 7.13 Elastic SED contour plot at different load increments	233
Figure 7.14 Total plastic dissipation of SED contour plots	234
Figure 7.15 SED contour plots at different load increments	235
Figure 7.16 UMDMG results showing damage initiation and evolution at different increments.	236
Figure 7.17 Stress-strain results of low strength steel at different volumetric porosity: UMDMG vs Testing (Chawla & Deng, 2005).	237
Figure 7.18 Stress-strain results of high strength steel at different volumetric porosity: UMDMG vs Testing (Stephens et al., 1998b).	239
Figure 8.1 (a) 2-D finite element mesh of a cracked body. (b) 2-D linear elastic boundary value problem with a crack	255
Figure 8.2 Crack-tip representation showing the outward normal and the tangent.	256
Figure 8.3 The Koyna dam two-dimensional profile reproduced from (<i>Abaqus V6.14–Documentation, Dassault Systèmes Simulia Corporation, 2013</i>).	260
Figure 8.4: Koyna dam 2-D problem. (a) Initially embedded crack. (b) User-defined critical region for XFEM enrichment.	261
Figure 8.5: The proposed algorithm flowchart	263
Figure 8.6: Mesh convergence (normalized stress invariant vs. mesh size)	264
Figure 8.7: Third Invariant stress field from FE simulations.	265
Figure 8.8: 2-D FE model of the beam showing critical zone identification based on a perfect case scenario	266
Figure 8.9: Beam FE model showing critical zone identification based on imperfections	267

Figure 8.10: FE refined mesh based on the automatically identified critical region	267
Figure 8.11: FE mesh showing the enriched nodes of the automatically determined critical region	267
Figure 8.12: A two-dimensional model of the beam under four-point bending	268
Figure: 8.13: (a) Specimen geometry and loading conditions. (b) Contour plot of third stress invariant showing potential region for crack onset.	275
Figure 8.14: (a) Optimized mesh and enrichment zone. (b) Predicted crack onset location using the proposed algorithm.....	276
Figure 8.15: (a) Specimen geometry and loading conditions. (b) Contour plot of third stress invariant showing potential region for crack onset.	278
Figure 8.16: (a) Optimized mesh and enrichment zone. (b) Predicted crack onset location using the proposed algorithm.....	279

List of Nomenclature or Abbreviations

3D	Three-Dimensional
AM	Additive Manufacturing
ASTM	American Standard for Testing Materials
C3D10	10-noded tetrahedral element
C3D8R	8-noded brick element with reduced integration
CAD	Computer Aided Design
CPE4R	4-noded plane strain element with reduced integration
CPS3	3-noded plane stress triangular element
CPS4R	4-noded plane stress element with reduced integration
CT	Computed Tomography
DIC	Digital Image Correlation
DXF	Drawing Exchange Format
ERO	Extended Ramberg-Osgood
FE	Finite Element
FEA	Finite Element Analysis
FEM	Finite Element Method
FRP	Fiber Reinforced Polymer
GB	Giga byte
GHz	Giga Hertz
GPa	Giga Pascal
GTN	Gurson-Tvergaard-Needleman
LS	Laser Sintering
MAXE	Maximum Nominal Strain
MAXPE	Maximum Principal Strain
MAXPS	Maximum Principal Stress
MAXS	Maximum Nominal Stress
MPa	Mega Pascal
NDE	Non-destructive Engineering

OM	Optical Microscopy
P/M	Powder Metal
PBC	Periodic Boundary Condition
PM	Powder Metallurgy
PU	Partition of Unity
QUADE	Quadratic Nominal Strain
QUADS	Quadratic Nominal Stress
RAM	Random Access Memory
R-O	Ramberg-Osgood
RVE	Representative Volume Element
SED	Strain Energy Density
SEM	Scan Electron Microscopy
SLS	Selective Laser Sintering
SPRIND	Utility Subroutine
UC	Unit Cell
UD	Unidirectional
UDMG	User-defined Damage subroutine
UDMGINI	User-defined Damage Initiation subroutine
UHARD	User-defined Hardening subroutine
UMAT	User-defined Material subroutine
UMDMG	Combined User-defined Material and Damage subroutine
VG	Volume Graphics
VM	Von Mises
XFEM	eXtended Finite Element Method

Co-Authorship Statement

I, Ahmed Youssri Elruby, hold a principle author status for all the manuscript chapters (Chapter 2 - 8) in this dissertation. Chapter 2 and 3 were co-authored by my co-researcher Mr. Stephen Handrigan and my supervisor Dr. Sam Nakhla. Chapters 4 – 7 were co-authored by my supervisor Dr. Sam Nakhla. Chapter 8 was co-authored by my supervisor Dr. Sam Nakhla and by the supervisory committee member Dr. Amgad Hussein. Co-authors contributions have facilitated the development of this work. Therefore, each co-author contribution is illustrated as per the Contributor Roles Taxonomy (CRT) below;

- Paper 1 in Chapter 2: A. Y. Elruby, Stephen Handrigan, and Sam Nakhla, “Fracture Behavior of Heavily Cross-linked Epoxy under Uniaxial Tension and Three-point Bending Loads; Testing, Fractography and Numerical Modeling” submitted to Polymer Testing Journal, May 2019.

Credit Author statement

Ahmed Elruby and Sam Nakhla: Conceptualization, Methodology, Specimen preparation and testing. **Stephen Handrigan:** Data Curation, Formal analysis and Investigation for CT scans and SEM analysis and post-processing, Software support (implementation of supporting code for CT analysis), **Ahmed Elruby:** Data Curation, Formal analysis and Investigation for experiments, Software (designing computer programs, code implementation, running simulations, numerical results), Validation of experimental results through finite element simulations in Abaqus. **Ahmed Elruby and Stephen Handrigan:** Writing – Original draft, Preparation and creation of artwork. **Sam Nakhla:** Writing – Reviewing and Editing, Supervision (oversight, leadership, planning and execution of research tasks), Project administration, Acquisition of the financial support for the project leading to this publication.

- Paper 2 in Chapter 3: A. Y. Elruby, Stephen Handrigan, and Sam Nakhla, “Actual Microstructural Voids Generation in Finite Element Analysis utilizing Computed

Tomography Scan of Heavily Cross-linked Epoxy” submitted to Advances in Engineering Software Journal, April 2019.

Credit Author statement

Ahmed Elruby and Sam Nakhla: Conceptualization, Methodology, Specimen preparation and testing of Epoxy specimens. **Stephen Handrigan:** Data Curation, Formal analysis and Investigation for CT scan and SEM analysis and post-processing, Software support (implementation of supporting code for CT analysis), **Ahmed Elruby:** Data Curation, Formal analysis and Investigation for epoxy testing, Software (designing computer programs, code implementation, running simulations, numerical results), Validation of experimental results through finite element simulation in Abaqus. **Ahmed Elruby and Stephen Handrigan:** Writing – Original draft, Preparation and creation of artwork. **Sam Nakhla:** Writing – Reviewing and Editing, Supervision (oversight, leadership, planning and execution of research tasks), Project administration, Acquisition of the financial support for the project leading to this publication.

- Paper 3 in Chapter 4: A. Y. Elruby, and Sam Nakhla, “Strain Energy Density Based Damage Initiation in Heavily Cross-linked Epoxy Using XFEM.” Theoretical and Applied Fracture Mechanics 103 (2019): 102254.

URL: <https://doi.org/10.1016/j.tafmec.2019.102254>

Credit Author statement

Ahmed Elruby and Sam Nakhla: Conceptualization, Methodology, Specimen preparation and testing of Epoxy specimens. **Ahmed Elruby:** Data Curation, Formal analysis and Investigation for epoxy testing, Software (designing computer programs, code implementation, running simulations, numerical results), Validation of experimental results through finite element simulation in Abaqus, Writing – Original draft, Preparation and creation of artwork. **Sam Nakhla:** Writing – Reviewing and Editing, Supervision (oversight, leadership, planning and execution of research tasks), Project administration, Acquisition of the financial support for the project leading to this publication.

- Paper 4 in Chapter 5: A. Y. Elruby, and Sam Nakhla, “Standard Mechanics Approach to Predict Effective Mechanical Behavior of Porous Sintered Steel Using

Micromechanical RVE-based Finite Element Modeling” under review in Material Science and Engineering A journal, December 2018.

Credit Author statement

Ahmed Elruby and Sam Nakhla: Conceptualization, Methodology. **Ahmed Elruby:** Data Curation, Formal analysis and Investigation, Software (designing computer programs, code implementation, running simulations, numerical results), Validation of finite element simulation in Abaqus, Writing – Original draft, Preparation and creation of artwork. **Sam Nakhla:** Writing – Reviewing and Editing, Supervision (oversight, leadership, planning and execution of research tasks), Project administration, Acquisition of the financial support for the project leading to this publication.

- Paper 5 in Chapter 6: A. Y. Elruby, and Sam Nakhla, “Extending the Ramberg-Osgood relationship to Account for Metal Porosity.” Metallurgical and Materials Transactions A, 50.7 (2019): 3121-3131.

URL: <https://doi.org/10.1007/s11661-019-05236-7>

Credit Author statement

Ahmed Elruby and Sam Nakhla: Conceptualization, Methodology. **Ahmed Elruby:** Data Curation, Formal analysis and Investigation, Software (designing computer programs, code implementation, running simulations, numerical results), Validation of finite element simulation in Abaqus, Writing – Original draft, Preparation and creation of artwork. **Sam Nakhla:** Writing – Reviewing and Editing, Supervision (oversight, leadership, planning and execution of research tasks), Project administration, Acquisition of the financial support for the project leading to this publication.

- Paper 6 in Chapter 7: A. Y. Elruby, and Sam Nakhla, “Elastoplastic Behavior and Failure of Porous Metals” submitted to journal of Mechanics and Physics of Solids, May 2019.

Credit Author statement

Ahmed Elruby and Sam Nakhla: Conceptualization, Methodology. **Ahmed Elruby:** Data Curation, Formal analysis and Investigation, Software (designing computer programs, code implementation, running simulations, numerical results), Validation of finite element simulation in Abaqus, Writing – Original draft, Preparation and creation of artwork. **Sam Nakhla:** Writing – Reviewing and Editing, Supervision (oversight, leadership, planning and execution of research tasks), Project administration, Acquisition of the financial support for the project leading to this publication.

- Paper 7 in Chapter 8: A. Y. Elruby, Sam Nakhla, and A. Hussein, “Automating XFEM Modeling Process for Optimal Failure Predictions” published in Mathematical Problems in Engineering journal, August 2018.

URL: <https://doi.org/10.1155/2018/1654751>

Credit Author statement

Ahmed Elruby and Sam Nakhla: Conceptualization, Methodology. **Ahmed Elruby:** Data Curation, Formal analysis and Investigation, Software (designing computer programs, code implementation, running simulations, numerical results), Validation of finite element simulation in Abaqus, Writing – Original draft, Preparation and creation of artwork. **Amgad Hussein:** Specimen preparation and testing of concrete, **Sam Nakhla:** Writing – Reviewing and Editing, Supervision (oversight, leadership, planning and execution of research tasks), Project administration, Acquisition of the financial support for the project leading to this publication.



July 2019

Ahmed Youssri Elruby

Date

1 Introduction

1.1 Background and Research Motivation

In many engineering applications such as aerospace, marine and automotive industries different classes of materials are being used. Among these are organic materials such as polymers, inorganic materials such as metallic alloys and a wide variety of fiber reinforced polymers (FRPs) which lie under the main category of composite materials. Mechanical behavior is the key role of understanding how a material deforms under applied loads. Different failure mechanisms are associated with each material type. Generally, material failure can be classified mainly into two main categories; brittle failure signified by low strain-to-failure capacity and ductile failure where significant inelastic deformation occurs ahead of final failure. In fact, material failure would be a combination of both brittle and ductile behavior where one behavior is dominating the damage mechanism while the other is minorly existing. To justify this claim, consider the fractured surface of a typical ductile metallic specimen under uniaxial tension, which is commonly a cup and cone shaped after separation. It is well-known that the cup and cone shape results from both shear and normal stresses where if the failure mechanism was purely ductile the failure surfaces should have been at 45° . Also, for most of brittle materials such as concrete, epoxy and even glass a minor plastic deformation would occur ahead of final failure. Usually failure criteria and damage models are developed to serve for either ductile or brittle mechanisms. In other words, a generic damage model that is applicable for both types is hard to develop.

Precise modeling and simulation of mechanical behaviors is an asset for early design stages enabling an insight into the structure performance. Perhaps the most referenced type of

analysis regarding structural behavior is the finite element analysis (FEA). The main advantage of utilizing FEA in structural analysis is dealing with sophisticated problems involving complex geometries and boundary conditions where a closed form solution may not exist. Several commercially available finite element codes (e.g., Abaqus and LS-Dyna) are generally used in both industry and academia. Also, inhouse finite element (FE) codes can be developed for a specific problem by optimizing the code for it. FE modeling accuracy is dependent on several aspects such as boundary conditions, material definition and meshing. The proper definition of each aspect requires a grasp understanding of physical features regarding the studied problem as well as the proper way of representing these features in a numerical model. Usually, a FE user would spend relatively long time until reaching a suitable efficient model. Also, required computational runtime may vary from minutes to several weeks depending on the problem size and available processing resources. In addition, post-processing the numerical results usually requires substantial user effort and time. Therefore, it can be concluded that FE model accuracy is mainly tied to user-experiences/skills. Enhancing available tools or modeling techniques would act as a significant contribution to the pool of knowledge for both engineers as well as researchers.

Studying fracture mechanics using the conventional FE method possess the need of embedding a crack into the FE mesh *a priori*. Besides, remeshing is required to enable the crack front to conform to the mesh boundaries. Embedding a crack in the analysis will bias the numerical results. Also, the remeshing requirement is computationally inefficient and imposed runtime requirements would be massive. Another approach which is currently implemented in finite element codes is the element deletion method where a certain

criterion is set to define a material point failure. Once the criterion is encountered the stiffness of the associated element is enforced to zero. While this approach alleviates the remeshing requirement, it would require relatively large number of elements to meet acceptable results accuracy. Moreover, cracks are not introduced to the failed elements nor the elements are removed from mesh. In other words, fracture surfaces are not predicted. The extended finite element method was originally proposed by (T. Belytschko & Black, 1999) providing a method for solving crack propagation problem with minimal remeshing. The method was later advanced to account for crack propagation without remeshing (Moës, Dolbow, & Belytschko, 1999). The method relies on special nodal enrichment applying the partition of unity (PU) theorem (Melenk & Babuška, 1996) to the conventional FE method. These nodal enrichments enable accounting for cracks within an enriched element without the need for remeshing. Notably the method can be applied for different class of problem other than structural problems. In other words, the method can be applied to any differential equation representing a physical problem that can be numerically solved using the FE discretization (Ted Belytschko, Gracie, & Ventura, 2009b). The method has been utilized to study different class of problems with the focus on fracture mechanics problems. The method is available in commercial FE codes such as Abaqus since 2009. In a relatively recent study by Duarte et al. (Duarte, Díaz Sáez, & Silvestre, 2017) comparing the numerical implementation of Hashin's criterion to that of XFEM in Abaqus applied to predict of FRPs, they showed that XFEM has the advantage of predicting crack onset, evolution and final fracture surface. However, the predicted failure loads using built-in damage initiation mechanisms in Abaqus (i.e., stress/strain-based) were over estimated.

Therefore, they concluded that further investigation into damage initiation mechanisms is required. In fact, numerically obtained results using XFEM are dominated by the chosen damage model.

As mentioned earlier, the perfect case scenario of seamless brittle or ductile behavior is almost inexistent for many practical applications. Therefore, it is necessary to account for both contributions on material's failure. The current research aimed to enhance the accuracy of numerical predictions utilizing the general framework of both conventional finite element method (FEM) and XFEM. Also, minimizing computational effort besides attempting to alleviate or minimize user-dependency was targeted. In addition, developing a damage model within the framework of XFEM accounting for both brittle and ductile behaviors contributions in an attempt of proposing a relatively generic damage criterion that can be applied to brittle as well as ductile materials. Regarding mechanical testing program, plain epoxy resin and some of concrete specimens were prepared and tested at Memorial university's laboratories. Testing results regarding different types of steels were obtained from the literature. Different modeling approaches were employed in the conducted research. Diverse micromechanical methods such as UC and RVE were combined in FEA. Also, an example on multiscale modeling utilizing physical representation of microscopic features (i.e., micro-voids) is provided. In addition, a two-stage FE procedure employing micromechanical RVEs to numerically predict macroscopic material properties for macroscale modeling was proposed. A miniature Python scripting library was developed for generating different class of micromechanical models in FEA.

Also, a couple of macroscopic user-defined material subroutines were developed and implemented in Fortran.

1.2 Research Objectives and Significance

A chief objective of the current research was to investigate the mechanical behavior of plain epoxy resin being the most commonly used resin material in the majority of FRPs. Also, epoxy resins are widely used as a layup adhesive in composite laminates. Moreover, two typical failure modes of composite materials are dominated by the resin material, namely, matrix cracking and delamination (Jones, 1999; P.K. Mallick, 2007). Most of research articles in literature focus on the composite behavior not the individual constituents (Dong, 2016; Pawar & Ganguli, 2006; Frans P. Van Der Meer, 2016). Besides, few studies were found in literature investigating plain epoxy resin (L. E. Asp, Berglund, & Talreja, 1996; Fiedler, Hojo, Ochiai, Schulte, & Ando, 2001; Jordan, Foley, & Siviour, 2008; Kinloch & Williams, 1980). As a result, the plain epoxy resin is thoroughly investigated in the current research with the objective of better understanding its failure mechanism. Also, manufacturing imperfections in composite materials such as voids are known for their detrimental effect on mechanical behavior (Di Landro et al., 2017; Huang & Talreja, 2005; Kim & Kim, 2005; W. V. Liebig, Leopold, & Schulte, 2013; Wilfried V. Liebig, Viets, Schulte, & Fiedler, 2015; Nikishkov, Airoidi, & Makeev, 2013; Zhu, Wu, Li, Zhang, & Chen, 2011). All the above triggered and motivated the conducted studies regarding epoxy resin testing, fractographic analyses and numerical modeling at different length scales.

On the other hand, edge technologies such as 3D printing are currently being utilized to produce final metallic parts in various engineering applications (Frazier, 2014; Gao et al., 2015; Herzog, Seyda, Wycisk, & Emmelmann, 2016). Among these technologies is the selective laser sintering (SLS) technique which is commonly used for steel parts production (Aboulkhair, Everitt, Ashcroft, & Tuck, 2014; Zaharin et al., 2018). The manufacturing process involves significant thermal cycles owed to the subsequent melting or fusion and solidification of the powder metal during the printing successive layers (Puydt et al., 2014; Vilaro, Colin, & Bartout, 2011). These cycles results in micro-porosity which has proven to deteriorate the material behavior in both linear and plastic regimes (R. A. Hardin & Beckermann, 2013). To the author best of knowledge, a complete material model accounting for effective behavior of porous metals regarding elastic and plastic behaviors is inexistent. Therefore, a second chief objective of the conducted work was focused on the complete mechanical behavior (i.e., elastoplastic) of porous metals in the low porosity range, i.e. less than 10%.

Finally, developing a generic algorithm attempting to automate XFEM modeling procedure was targeted to minimize computational efforts and user-dependency while maintaining optimal predictions accuracy.

1.3 Thesis Outline

This dissertation consists of nine chapters described as follows:

Chapter 1 demonstrates the background, motivation, objectives, significance, and scope of research conducted in the current thesis.

Chapter 2 presents a comprehensive study on failure characterization of plain epoxy resin under different types of loading using edge technologies in testing (i.e., digital image correlation). Fractographic analyses using optical microscopy (OM), computed tomography (CT) and scan electron microscopy (SEM) were conducted to enable precise investigation of failure mechanisms. Also, numerical modeling is provided.

Chapter 3 illustrates the developed algorithm for generating micromechanical finite element models representing physical microstructural features (i.e., micro-voids) within a specimen sized model. The micromechanical voids were generated based on actual computed tomography scans of tested Epoxy.

Chapter 4 proposes a material damage model based on strain energy density for brittle materials (e.g. plain epoxy) accounting for elastoplastic behavior of epoxy within the framework of extended finite element od (XFEM). The damage model was implemented in a user-defined damage subroutine in mainstream finite element software Abaqus.

Chapter 5 investigates the validity of applying the unit cell (UC) method to enable predicting elastic-plastic behavior of porous metals using micromechanical FEA. Also, validation against reported testing results from the literature is provided.

Chapter 6 presents the developed extended Ramberg-Osgood (ERO) relationship accounting for metal porosity. In this work, numerical micromechanical models were used in conjunction with regression analyses to enable extending the original R-O relationship. Notably, the ERO relationship is one of the major contributions of this dissertation.

Chapter 7 provides a two-stage finite element procedure for elastoplastic behavior and damage of porous metals. A user-defined material damage subroutine was developed and implemented to predict final failure of porous metals within the framework of XFEM utilizing numerically obtained elastic-plastic behavior from micromechanical representative volume elements (RVEs). Also, a porosity dependent relationship to evaluate the critical value of strain energy density (SED) of porous metals was provided and validated against testing results from the literature.

Chapter 8 demonstrate the developed algorithm for automating XFEM modeling procedure for accurate structural failure predictions. In which, a generic algorithm was developed in Python to automate the modeling process including mesh convergence in Abaqus with the objective of automatic identification of potential failure region(s). validation against full-scale testing results from own and reported testing results is provided.

Chapter 9 presents the summary and recommendations from the completed research

1.4 Reference

- Aboulkhair, N. T., Everitt, N. M., Ashcroft, I., & Tuck, C. (2014). Reducing porosity in AlSi10Mg parts processed by selective laser melting. *Additive Manufacturing*, 1, 77–86. <https://doi.org/10.1016/j.addma.2014.08.001>
- Asp, L. E., Berglund, L. A., & Talreja, R. (1996). A criterion for crack initiation in glassy polymers subjected to a composite-like stress state. *Composites Science and Technology*, 56(11), 1291–1301. [https://doi.org/10.1016/S0266-3538\(96\)00090-5](https://doi.org/10.1016/S0266-3538(96)00090-5)
- Belytschko, T., & Black, T. (1999). Elastic crack growth in finite elements with minimal remeshing. *International Journal for Numerical Methods in Engineering*, 45(5), 601–620. [https://doi.org/10.1002/\(SICI\)1097-0207\(19990620\)45:5<601::AID-NME598>3.0.CO;2-S](https://doi.org/10.1002/(SICI)1097-0207(19990620)45:5<601::AID-NME598>3.0.CO;2-S)

- Belytschko, Ted, Gracie, R., & Ventura, G. (2009). A Review of Extended / Generalized Finite Element Methods for Material Modelling. *Modelling and Simulation in Materials Science and Engineering*, 17.4, 0430(4). <https://doi.org/10.1088/0965-0393/17/4/043001>
- Di Landro, L., Montalto, A., Bettini, P., Guerra, S., Montagnoli, F., & Rigamonti, M. (2017). Detection of voids in carbon/epoxy laminates and their influence on mechanical properties. *Polymers and Polymer Composites*.
- Dong, C. (2016). Effects of Process-Induced Voids on the Properties of Fibre Reinforced Composites. *Journal of Materials Science and Technology*, 32(7), 597–604. <https://doi.org/10.1016/j.jmst.2016.04.011>
- Duarte, A. P. C., Díaz Sáez, A., & Silvestre, N. (2017). Comparative study between XFEM and Hashin damage criterion applied to failure of composites. *Thin-Walled Structures*, 115(October 2016), 277–288. <https://doi.org/10.1016/j.tws.2017.02.020>
- Fiedler, B., Hojo, M., Ochiai, S., Schulte, K., & Ando, M. (2001). Failure behavior of an epoxy matrix under different kinds of static loading. *Composites Science and Technology*, 61(11), 1615–1624. [https://doi.org/10.1016/S0266-3538\(01\)00057-4](https://doi.org/10.1016/S0266-3538(01)00057-4)
- Frazier, W. E. (2014). Metal additive manufacturing: A review. *Journal of Materials Engineering and Performance*, 23(6), 1917–1928. <https://doi.org/10.1007/s11665-014-0958-z>
- Gao, W., Zhang, Y., Ramanujan, D., Ramani, K., Chen, Y., Williams, C. B., ... Zavattieri, P. D. (2015). The status, challenges, and future of additive manufacturing in engineering. *CAD Computer Aided Design*, 69, 65–89. <https://doi.org/10.1016/j.cad.2015.04.001>
- Hardin, R. A., & Beckermann, C. (2013). Effect of porosity on deformation, damage, and fracture of cast steel. *Metallurgical and Materials Transactions A: Physical Metallurgy and Materials Science*, 44(12), 5316–5332. <https://doi.org/10.1007/s11661-013-1669-z>
- Herzog, D., Seyda, V., Wycisk, E., & Emmelmann, C. (2016). Additive manufacturing of metals. *Acta Materialia*, 117, 371–392. <https://doi.org/10.1016/j.actamat.2016.07.019>
- Huang, H., & Talreja, R. (2005). Effects of void geometry on elastic properties of unidirectional fiber reinforced composites. *Composites Science and Technology*, 65(13), 1964–1981. <https://doi.org/10.1016/j.compscitech.2005.02.019>
- Jones, R. M. (1999). Mechanics of composite materials. *Mechanics of Composite Materials*, p. 519. <https://doi.org/10.1007/BF00611782>
- Jordan, J. L., Foley, J. R., & Siviour, C. R. (2008). Mechanical properties of Epon 826/DEA epoxy. *Mechanics of Time-Dependent Materials*, 12(3), 249–272. <https://doi.org/10.1007/s11043-008-9061-x>
- Kim, N. H., & Kim, H. S. (2005). Micro-void toughening of thermosets and its

- mechanism. *Journal of Applied Polymer Science*, 98(3), 1290–1295.
<https://doi.org/10.1002/app.22262>
- Kinloch, A. J., & Williams, J. G. (1980). Crack blunting mechanisms in polymers. *Journal of Materials Science*, 15(4), 987–996. <https://doi.org/10.1007/BF00552112>
- Liebig, W. V., Leopold, C., & Schulte, K. (2013). Photoelastic study of stresses in the vicinity of a unique void in a fibre-reinforced model composite under compression. *Composites Science and Technology*, 84, 72–77.
<https://doi.org/10.1016/j.compscitech.2013.04.011>
- Liebig, Wilfried V., Viets, C., Schulte, K., & Fiedler, B. (2015). Influence of voids on the compressive failure behaviour of fibereinforced composites. *Composites Science and Technology*, 117, 225–233. <https://doi.org/10.1016/j.compscitech.2015.06.020>
- Melenk, J. M., & Babuška, I. (1996). The partition of unity finite element method: Basic theory and applications. *Computer Methods in Applied Mechanics and Engineering*, 139(1–4), 289–314. [https://doi.org/10.1016/S0045-7825\(96\)01087-0](https://doi.org/10.1016/S0045-7825(96)01087-0)
- Moës, N., Dolbow, J., & Belytschko, T. (1999). A finite element method for crack growth without remeshing. *International Journal for Numerical Methods in Engineering*, 46(1), 131–150. [https://doi.org/10.1002/\(SICI\)1097-0207\(19990910\)46:1<131::AID-NME726>3.0.CO;2-J](https://doi.org/10.1002/(SICI)1097-0207(19990910)46:1<131::AID-NME726>3.0.CO;2-J)
- Nikishkov, Y., Airoidi, L., & Makeev, A. (2013). Measurement of voids in composites by X-ray Computed Tomography. *Composites Science and Technology*, 89, 89–97.
<https://doi.org/10.1016/j.compscitech.2013.09.019>
- P.K. Mallick. (2007). Fiber-Reinforced Composites: Materials, Manufacturing, and Design. In *CRC Press*.
- Pawar, P. M., & Ganguli, R. (2006). Modeling progressive damage accumulation in thin walled composite beams for rotor blade applications. *Composites Science and Technology*, 66(13), 2337–2349. <https://doi.org/10.1016/j.compscitech.2005.11.033>
- Puydt, Q., Flouriot, S., Ringeval, S., De Geuser, F., Estevez, R., Parry, G., & Deschamps, A. (2014). Relationship Between Microstructure, Strength, and Fracture in an Al-Zn-Mg Electron Beam Weld: Part II: Mechanical Characterization and Modeling. *Metallurgical and Materials Transactions A*, 45(13), 6141–6152.
<https://doi.org/10.1007/s11661-014-2567-8>
- Van Der Meer, F. P. (2016). Micromechanical validation of a mesomodel for plasticity in composites. *European Journal of Mechanics, A/Solids*, 60.
<https://doi.org/10.1016/j.euromechsol.2016.06.008>
- Vilaro, T., Colin, C., & Bartout, J. D. (2011). As-fabricated and heat-treated microstructures of the Ti-6Al-4V alloy processed by selective laser melting. *Metallurgical and Materials Transactions A: Physical Metallurgy and Materials Science*, 42(10), 3190–3199. <https://doi.org/10.1007/s11661-011-0731-y>
- Zaharin, H., Abdul Rani, A., Azam, F., Ginta, T., Sallih, N., Ahmad, A., ... Zulkifli, T. Z.

- A. (2018). Effect of Unit Cell Type and Pore Size on Porosity and Mechanical Behavior of Additively Manufactured Ti6Al4V Scaffolds. *Materials*, 11(12), 2402. <https://doi.org/10.3390/ma11122402>
- Zhu, H., Wu, B., Li, D., Zhang, D., & Chen, Y. (2011). Influence of Voids on the Tensile Performance of Carbon/epoxy Fabric Laminates. *Journal of Materials Science and Technology*, 27(1), 69–73. [https://doi.org/10.1016/S1005-0302\(11\)60028-5](https://doi.org/10.1016/S1005-0302(11)60028-5)

2 Fracture Behavior of Heavily Cross-linked Epoxy under Uniaxial Tension and Three-point Bending Loads; Testing, Fractography and Numerical Modeling

2.1 Abstract

In this article, heavily cross-linked epoxy was characterized under different types of loading with an insight into its failure behavior. The scope of work involves detailed testing procedures utilizing high precision digital image correlation (DIC) system for all strain measurements. Yield identification method is proposed utilizing the stress-whitening phenomenon. Fractographic analysis using optical and scan electron microscopes were also provided. In addition, computed tomography (CT) scan were employed to characterize existing manufacturing imperfections such as voids. Numerical modeling using XFEM utilizing the actual microstructure is conducted. Also, specimen sized modeling for failure predictions is provided. Testing results and fractographic analyses showed that failure initiation is caused by micro-cavitation and possibly leading to fracture. The final failure was dominated by an unstable fracture behavior under different types of loading. Global plastic deformation was observed in the case of uniaxial tension while local plasticity was observed in three-point bending specimens. It can be concluded that epoxies failure under combined state of stresses is complex and simple stress/strain-based failure criteria are not well-suited for failure predictions.

2.2 Introduction

Fiber reinforced polymers (FRP) are widely used in many engineering fields such as automotive, marine and aerospace industries. FRP are mainly preferred for their enhanced physical and mechanical properties such as thermal stability and strength-to-weight ratio.

Heavily cross-linked thermoset polymers are usually used as matrix materials for FRP. Most of FRP composites are manufactured using epoxy as the resin material (P.K. Mallick, 2007). Also, epoxies are widely used in lamination process as an adhesive material. Epoxy resins have excellent resistance to chemicals and harsh environmental conditions. In addition, cured epoxies have the advantage of low-shrinkage over other resin materials (Uygunoglu, Gunes, & Brostov, 2015). However, cured epoxy resins exhibit low strain-to-failure capacity owed to brittleness resulting from polymerization process (Zhenqing Wang, Liu, Liang, & Zhou, 2013). Brittleness of cured epoxies dominates the overall strain-to-failure capacity of FRP (Pulungan, Lubineau, Yudhanto, Yaldiz, & Schijve, 2017). Moreover, manufacturing defects in FRP laminated composites such as voids, resin rich regions and fiber misalignment have a detrimental influence on composite mechanical properties (Kalantari, Dong, & Davies, 2017; Y. Li, Stier, Bednarczyk, Simon, & Reese, 2016; Zhen Wang et al., 2016). While several manufacturing methods are being utilized to minimize void content during fabrication procedures such as autoclaving and vacuum bagging, however voids cannot be entirely avoided. Manufacturing defects such as inclusions/voids have a dominant effect on matrix failure (Hagstrand, Bonjour, & Månson, 2005; Kalantari et al., 2017; W. V. Liebig et al., 2013; Wilfried V. Liebig et al., 2015).

The anisotropic behavior of heterogeneous materials such as polymeric composites is complex in terms of failure modes (F. P. Van Der Meer, Sluys, Hallett, & Wisnom, 2012). Mainly there are four damage modes controlling fracture process of FRP. Two of which are dominated by resin materials, namely matrix cracking and ply delamination (Bieniaś, Dębski, Surowska, & Sadowski, 2012; Lachaud, Espinosa, Michel, Rahme, & Piquet,

2015; Pawar & Ganguli, 2006; Pollayi & Yu, 2014). The total void content is considered as a property reducing agent and stresses have the tendency to build up in their vicinities (Wilfried V. Liebig et al., 2015). In addition, resin materials in FRP are subject to a complex state of stresses (Esna Ashari & Mohammadi, 2012; Fard, 2011; Talreja, 2014) which highlights the need of developing effective methods for characterization and modeling. As a result, several theories have been proposed for failure analysis of composite materials in the literature (Camanho, Arteiro, Melro, Catalanotti, & Vogler, 2015; Christensen, 2001; Daniel, Daniel, & Fenner, 2018; Hinton.M.J, Kaddour.A.S, & Soden.P.D, 2002; Isaac & Ori, 2013; E. M. Wu & Tsai, 1971). Most of failure theories are based on linear elasticity treating each composite constituent (i.e. matrix or fiber) with a stress or strain based failure limits (Daniel et al., 2018). For example, the Hashin-Rotem failure criterion which is a macroscale failure criterion for unidirectional (UD) composites relying on two failure modes, matrix cracking and fiber breakage (Hashin & Rotem, 1973). Noteworthy to mention that Hashin's damage criteria represent the foundation for many available stress based theories, where individual failure limits for both fiber and matrix are used to define the failure envelope (Dávila, Camanho, & Rose, 2005). More advanced failure theories such as the Tsai-Hill and the Tsai-Wu (Isaac & Ori, 2013; E. M. Wu & Tsai, 1971) utilize a criterion where all stress components are involved in a polynomial form (Daniel, 2015). These failure theories prediction have significant differences even when dealing with a UD lamina as elaborated by Talreja in (Talreja, 2014) and Daniel in (Daniel, 2015). Asp et al. (L. E. Asp et al., 1996) proposed a strain energy based failure criterion for damage initiation

in glassy polymers to account for composite-like stresses on epoxy failure. Their criterion proved very good agreement with testing results.

Computed Tomography (CT) scanning is a valuable tool for the use of non-destructive engineering (NDE) methods to investigate damage in composites, such as cracks (Baumann, Kennedy, & Herbert, 1984; Verges, Schilling, Herrington, Tatiparthi, & Karedla, 2005), fracture (Aroush et al., 2005), fibre breakage (Wright, Fu, Sinclair, & Spearing, 2008), and voids (Lambert, Chambers, Sinclair, & Spearing, 2012; Nikishkov et al., 2013). Baumann et al. were one of the first groups to evaluate the effectiveness of a medical CT scanner for the use in NDE of composite materials (Baumann et al., 1984). Baumann et al. were able to resolve resolutions on the order of 500 μ m and recommended future researchers to utilize dye or other fluids to visually improve distinguishing features of cracks (Baumann et al., 1984). Building upon the foundation set by Baumann et al., Schilling et al. were able to characterize microcracking in fiber-reinforced polymer laminates and determined the maximum sample size (1.5mm) to obtain a 0.5 to 1 μ m resolution at the crack tip without the use of dye (Verges et al., 2005). It was concluded in [2] that the use of dye to contrast the sample allowed for the investigation of larger samples. In 2006, Aroush et al. utilized 2 μ m in-situ CT scanning to study in-situ fracture (Aroush et al., 2005). At the same time, Baruchel et al. demonstrated that CT scanners were capable of obtaining resolutions on the 0.3 μ m scale (Baruchel et al., 2006). More recently, Lambert et al. demonstrated the first 3D void analysis within composite materials at a resolution of 8 μ m, obtaining size, distribution, and shape of approximately 10,000 voids (Lambert et al., 2012). Lastly, the work of Nikishokov et al. successfully demonstrated measuring voids in

epoxy composites using CT scanning with resolutions of 5.6 to 29.4 μ m (Nikishkov et al., 2013).

To this end, matrix materials have a dominant role in composite materials failure. While several failure theories exist, most of them assumed linear isotropy and the homogeneity of matrix materials. In addition, manufacturing imperfections such as inclusions/voids have a significant effect on resin materials failure. Following simple logic, resin material is considered as the weakest link in a FRP which was shown to initiate damage in several cases and possibly lead to final failure. This highlighted the need for a thorough investigation on plain epoxy failure behavior. The main objective is to identify the failure mechanisms of neat epoxy under different types of loading with an insight into fractured surfaces. In the current work, plain epoxy resin was prepared and tested under different types of loading. Testing measurements were obtained using a high precision digital image correlation system (DIC). A fractographic analysis using optical and scan electron microscopies (SEM) were conducted. In addition, computed tomography imaging was used to quantify manufacturing defects and further investigate fracture surfaces. Building upon the work of Lambert et al. (Lambert et al., 2012) and Nikishokov et al. (Nikishkov et al., 2013), the current study utilizes CT scanning to measure voids within a pure epoxy sample. The void size and total porosity within the samples were compared to results obtained through Optical Microscopy and Scanning Electron Microscopy (SEM). The utilization of CT imaging allowed for through-thickness investigation of void size, distribution, and total void volume. Numerical modeling analyses at micro and macro scales utilizing the framework of XFEM in Abaqus are provided.

2.3 Material and Mechanical Testing

2.3.1 Material Preparation and Test Setup

LAMPOXY61 Plain epoxy resin slab was prepared and cured for the current investigation by Polynt Composites Canada, Inc. the resin and the hardener were mixed by a weight ration 6:1 and allowed to cure in a metallic mold without vacuum application. This type of resin is commonly used in fiber reinforced composites layup lamination. **Table 2.1** shows the resin as well as the hardener physical properties as provided by manufacturer. Mixture constituents have a shelf life of 90 days, a pot life of approximately 20 mins and the tack-free time is 5 hours.

Table 2.1. LAMPOXY61 physical properties at room temperature, 25oC.

Lamination Epoxy properties	Resin material EPO-LAMPOXY 61	Hardener material EPO-LAMCAT 61
Viscosity (mPs)	1200-1400	25-50
Density (g/ml)	1.09-1.12	0.96-0.98
Weight (%)	85.72	14.28

To minimize surface flaws from both sides, the plain resin slab was milled down to a thickness of 9mm. To avoid biasing testing results, all specimens were prepared from the same plain resin slab. Six dog-bone tensile specimens were machined from the slab according to ASTM D638-14 recommendations. In addition to, a set of six prismatic specimens prepared as per ASTM D790-17 recommendations. Schematic diagrams showing specimens dimensions are shown in **Figure 2.1a** and **Figure 2.1b**, respectively.

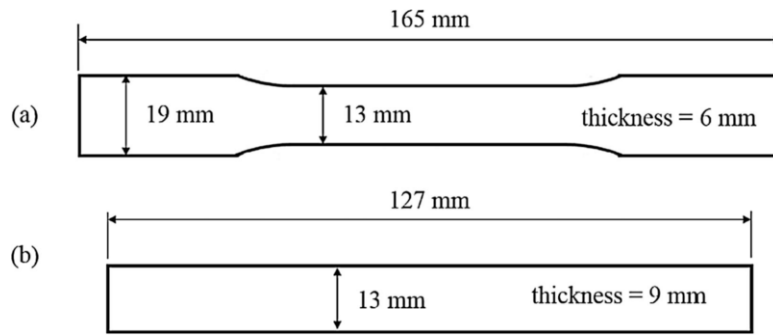


Figure 2.1 Specimen geometry: a) uniaxial tensile dog-bone and b) three-point loading prism.

Both uniaxial tension and three-point loading tests were carried in an Instron E10000 load frame utilizing high precision non-contacting strain measurement with a $0.5 \text{ microns} \pm 1.0 \%$ resolution. The load frame showing the dog-bone specimen setup along with the video extensometer are shown in **Figure 2.2**. Dog-bone specimens were fixed from both ends using deeply scored grip surfaces to avoid slippage. Specimens were fixed from their lower ends while a displacement load was applied to their upper end at a rate of 1 mm/min which is the minimum required by the testing standard. As can be seen from the zoomed view of dog-bone specimen, two longitudinal and lateral marks were used for local axial and lateral strain measurements, respectively. The specimens were cautiously marked within the specified standard gauge lengths for both strain measurements, axial and lateral.

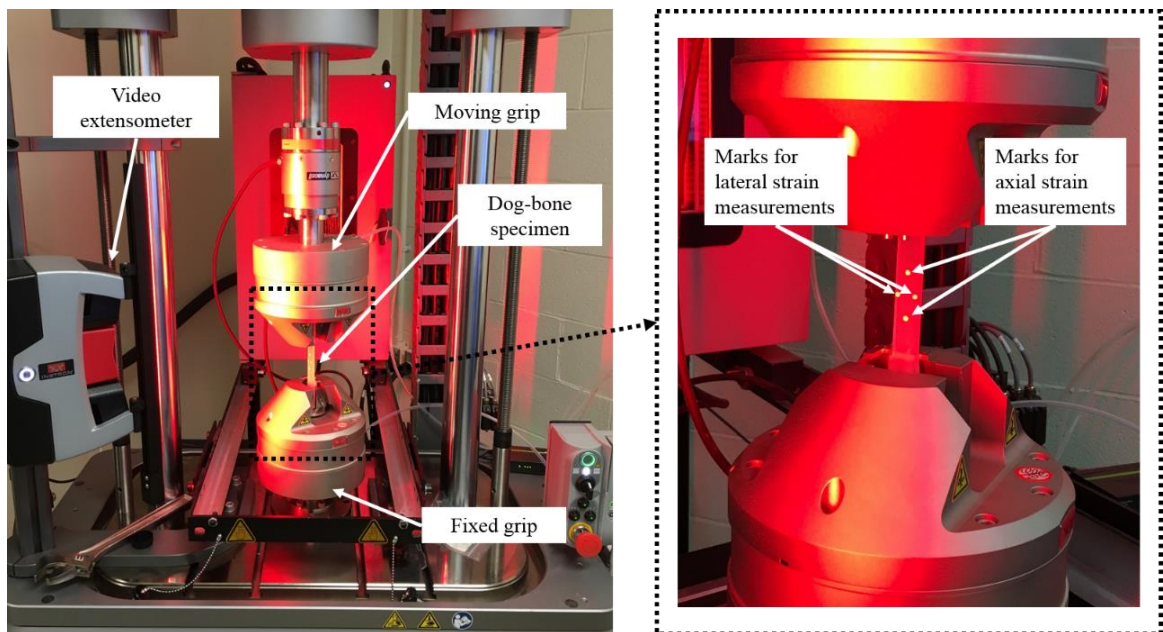


Figure 2.2 Load frame setup showing videoextensometer and dog-bone specimen marking.

Figure 2.3 shows three-point bending test setup, the lower rollers were fixed while the upper roller was used for load application at a rate of 1mm/min. Standard rollers coated with a thin film of lubricant were used to minimize frictional effect on testing results. Mid-span deflection was measured using a single mark on prismatic specimen correlated to a fixed reference mark as shown in **Figure 2.3**.

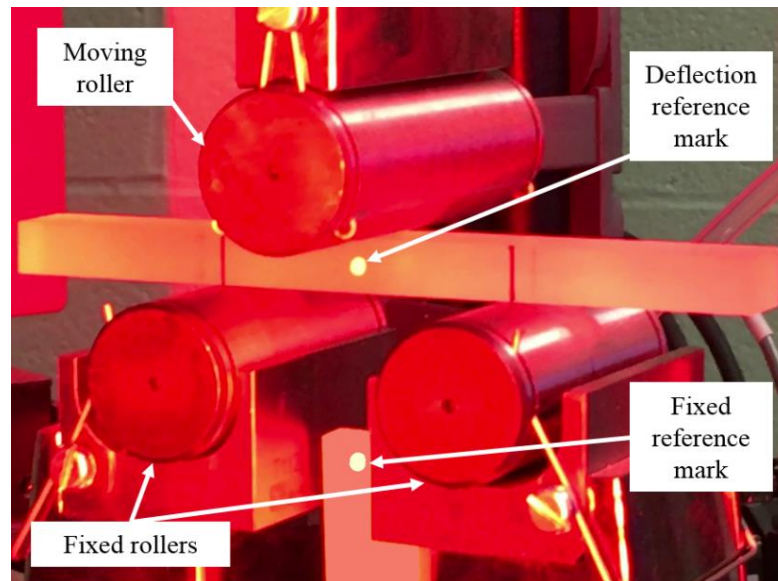


Figure 2.3 Three-point load test setup showing prismatic specimen marking.

Heavily cross-linked epoxy systems are known for their low strain to failure capacities. Identifying the onset of yielding for such material is quite problematic. A novel approach for accurate determination of yield onset is proposed in the current work for this matter. Uniaxial testing procedures were synchronically video recorded with strain measurements. Monochromic image analysis was used for efficient identification of yielding, details on this matter are discussed in the following section. Stress-strain behavior of the material was used to report testing results. Also, failure stresses and strains were used to characterize the fracture behavior of plain resin material. On the other hand, load-deflection curves were used to reporting three-point bending test results.

2.3.2 Computed Tomography Imaging Procedure

To establish repeatability of the scans, the scanner was calibrated to ensure no more than 0.5% error. All samples were scanned following a similar procedure, except where failure surfaces were inspected. No filter material was used pre- or post-scanning. The samples

were scanned with a Reflection Rotation 225 target head and tungsten target material utilizing the Nikon XT H225 ST system. Inspect X software from Nikon was utilized in the scanning procedure. A total of 3141 projections were collected with two-frame averaging. After scanning was complete, verification of the results was performed to ensure consistency. The center of rotation was validated and showed a less than one-pixel error. A slightly modified scanning procedure was followed for the samples which required observation of the failure surfaces. These samples were scanned in a tilted position to avoid beam hardening artifacts which usually appear on the top and bottom surfaces.

Next, reconstruction of the samples was performed in CT Pro 3D with noise reduction, scattering reduction, and beam hardening corrections applied. Analysis of the reconstructed samples was performed in Volume Graphics VGStudio MAX 3.0 software. Utilizing VGStudio MAX 3.0, surfaces were determined using the advanced surface determination tool. The spatial resolution (voxel size) of this method was between 9.3 and 11.12 μm .

After the samples were reconstructed, the determination of voids was performed using the Otsu (Otsu, 1979) global thresholding method within VGStudio MAX 3.0 software. The Otsu (Otsu, 1979) global thresholding method has been shown to be applicable and accurate to identify and measure voids. The method derives a threshold based on the gray level histogram to avoid qualitative analysis of thresholds. Using a single thresholding value, this method is capable of segmenting voids from the parent material. Within the software, two thresholding values were defined for two separate materials – air and bulk epoxy. Throughout the samples, areas of interest were analyzed if the grey value was below the threshold for air and was fully enclosed within that of bulk material. These areas of interest

were then further investigated as potential voids such that the fully enclosed area must be at least 24 voxels in size to be classified as a void.

2.4 Results and Discussion

2.4.1 Uniaxial tension test results

The onset of plastic deformation was efficiently identified using synchronized video record along with DIC strain measurements. Monochromatic images from synchronized record were used to observe stress-whitening caused by plastic deformation. Plain epoxy resin has an opaque transparent glass-like color which turns into an observable white color upon inelastic deformation. **Figure 2.4** shows monochromatic images from the synchronized record of a dog-bone specimen from testing. As can be observed, plastic deformation started at time frame 145s, time frame value was used to efficiently determine the onset of yielding and correspondingly yield stress. Inelastic deformation originated from mid-span and slightly biased towards the moving grip. Plastic deformation continued to build up throughout the specimen narrow section which can be observed by inspecting the first- and last-time frames.

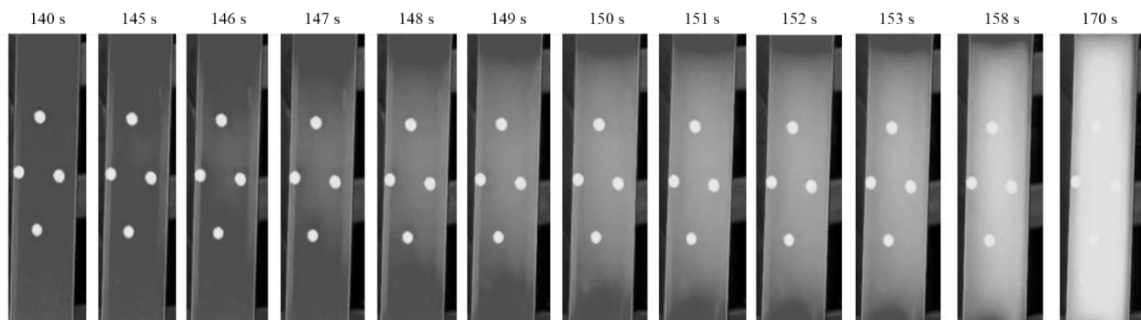


Figure 2.4 Dog-bone specimen at different time frames showing stress whitening caused by inelastic deformation.

Six dog-bone plain resin specimens were tested under uniaxial loading until failure. The stress-strain results are shown in **Figure 2.5**. Mechanical behaviors of all specimens are almost identical in the linear regime. Almost all specimens hold a linear behavior up to 90% of the loading capacity followed by unstable brittle failure. Noteworthy to mention that none of the specimens showed a necking type failure behavior.

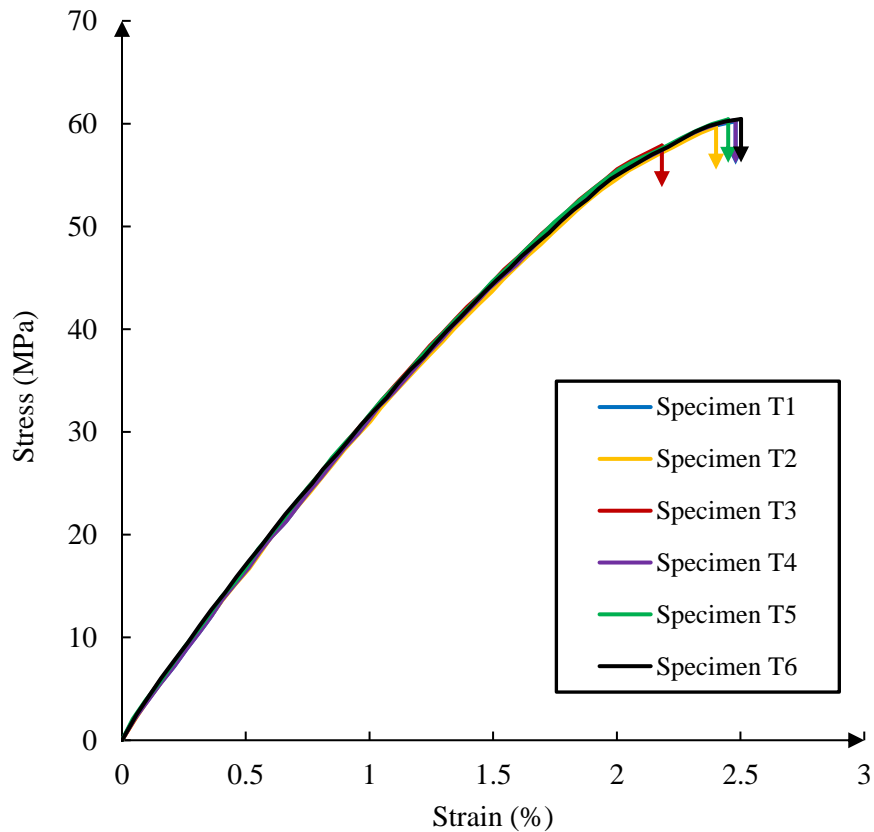


Figure 2.5 Stress-strain curves for uniaxial load testing.

Slight variations in both stress and strain failure limits were observed. **Table 2.2** documents failure limits of each specimen and the fracture energy from testing results. The mean values of elastic constants, namely modulus of elasticity and Poisson's ratio were 3.328 GPa and 0.361, respectively.

Table 2.2. Failure limits from uniaxial tension testing.

specimen number	failure stress (MPa)	failure strain (%)	fracture energy (N/m)
T1	53.82	2.187	1.885
T2	59.70	2.401	2.039
T3	60.22	2.481	2.108
T4	60.35	2.482	2.018
T5	60.46	2.502	2.114
T6	60.42	2.452	2.101

The DIC local measurements of regarding load-displacement results are shown in **Figure 2.6**. Local measurements showed similar plateau to that of global ones. Specimen T5 showed the maximum local displacement and load at failure as 687 μm and 4734N, respectively. The lowest values were recorded by specimen T1 as 551 μm and 4546N.

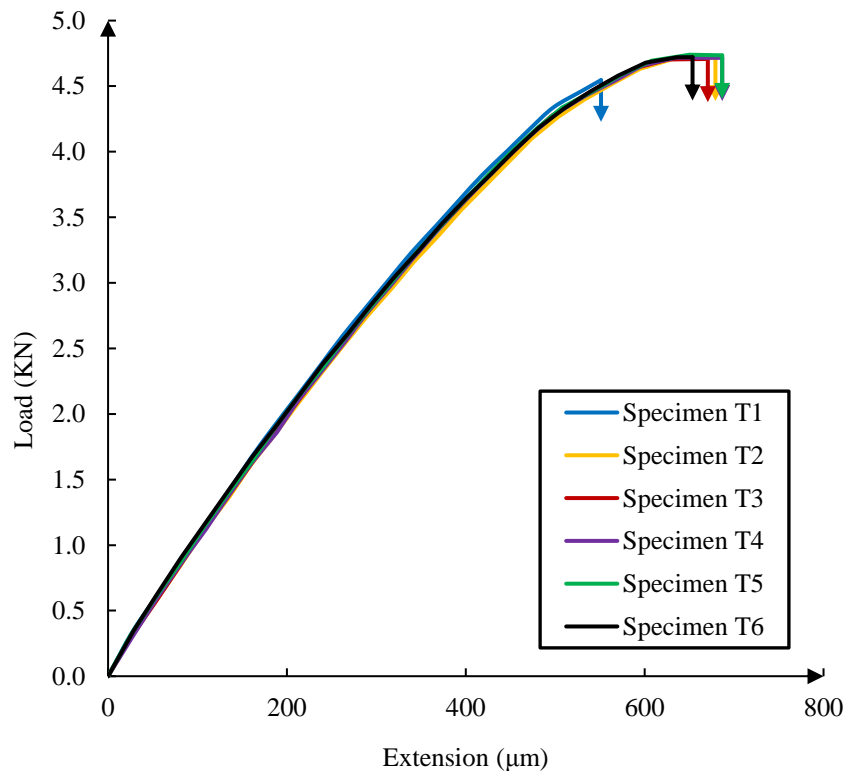


Figure 2.6 Local axial load-displacement measurements from DIC.

Fractured specimens from uniaxial tension testing were scanned and monochromatic images are presented in **Figure 2.7**. All specimens showed a fractured surface normal to load application direction implying that brittle type of failure dominated the fracture mechanism. Even though plastic deformation was minimal, stress-whitening caused by plastic deformation can be observed in all specimens. The lowest intensity of whitening was shown by specimen T1. Further, details on the failure mechanisms are provided in the following section.

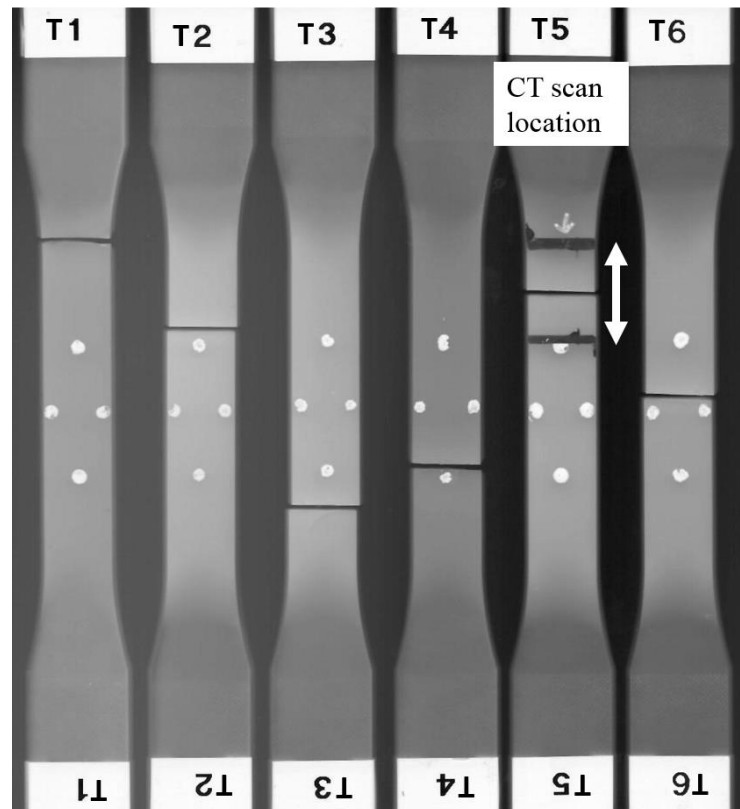


Figure 2.7 Monochromatic scan of dog-bone specimens after failure.

2.4.2 Three-point bending test results

Six prismatic specimens were prepared for testing under three-point loading. The load versus net deflection results obtained using DIC are presented in **Figure 2.8**. The arrows

on the figure shows the failure limits in terms of loads and displacements. Testing results from different specimens are almost coinciding with very similar behavior in the linear region.

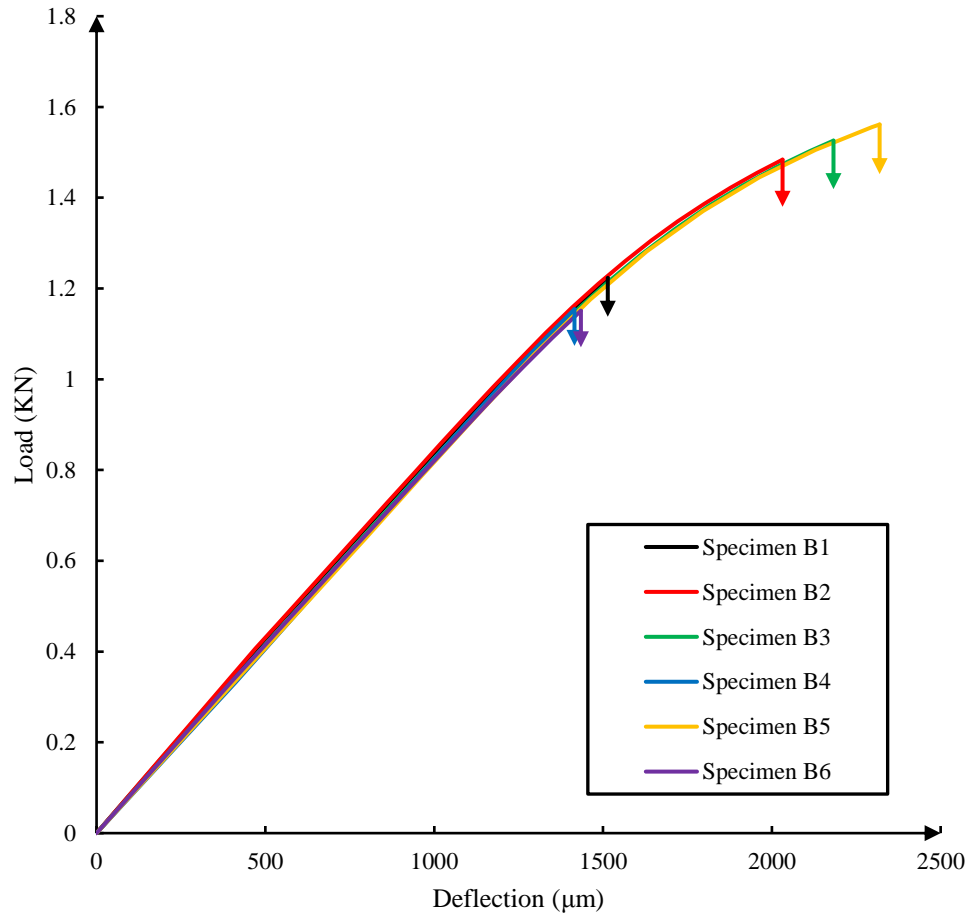


Figure 2.8 Load-deflection curves from three-point loading tests.

Three specimens showed a linear behavior almost until final brittle failure, namely specimens B1, B4 and B6. On the other hand, specimens B2, B3 and B5 exhibited significant plastic deformation ahead of final unstable fracture. A stress element in a prism under three-point loading will experience both maximum bending and shear stresses at mid-span. Fractured prisms monochromic scan is shown in **Figure 2.9**. As can be noticed, local

inelastic deformation appears in the lower mid-segment of specimens B2, B3 and B5. Load-deflection results signifies the significant plastic deformation. On the other hand, the rest of the specimens had minimal plastic deformation ahead of final failure. Detailed failure and fractographic analysis are provided in the following section.

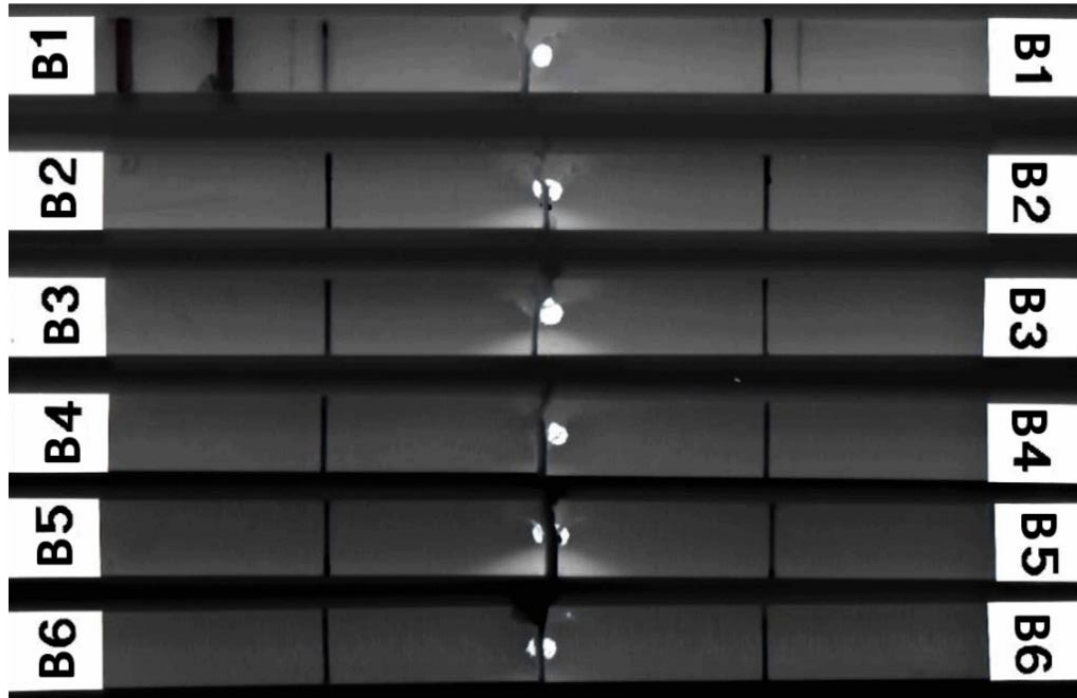


Figure 2.9 Monochromatic scan of prismatic specimens after failure.

A quantitative comparison of obtained failure loads and deflections is provided in **Table 2.3**. Specimen B6 recorded the lowest failure load with a value of 1070N while specimen B4 recorded the lowest failure deflection with a value of 1416 μ m. Both specimens showed almost identical behavior and their final failure was dominated by brittleness. Specimen B1 had slightly higher failure limits while the brittle behavior still dominated the final fracture. On the other hand, specimens B2, B3 and B5 had significantly deformed in an inelastic

manner resulting in higher failure limits. Maximum values were recorded by specimen B5 at failure limits of 1452N and 2319 μ m for load and deflection, respectively.

Table 2.3. Failure limits from Three-point load testing.

specimen number	failure load (N)	failure deflection (μ m)
B1	1138	1514
B2	1380	2032
B3	1419	2183
B4	1074	1416
B5	1452	2319
B6	1070	1435

2.5 Fractography

As it was stated prior, the presence of voids have a dominant effect of the failure of a material (Hagstrand et al., 2005; Kalantari et al., 2017; W. V. Liebig et al., 2013; Wilfried V. Liebig et al., 2015). To understand this effect, a fractographic analysis was performed to view failure initiation in the presence of voids. First, optical microscopic images for fractured surfaces are provided. Second a closer investigation using scanning electron microscope (SEM) was conducted. Lastly, a computed tomography (CT) scan was completed, showing the void content in cured neat epoxy and an investigation on the fractured surface after failure.

2.5.1 Optical Microscopy

As an initial investigation step, the failed surfaces from both uniaxial and three-point bending specimens were explored using optical microscopy. First, fractured surfaces from dog-bone specimens are shown in **Figure 2.10**. As can be seen, the failure mechanism in tension was consistent in all tested specimens. A glass-like behavior regarding fractured

surfaces was observed originating from a micro-cavitation and scattering towards edges. The failure onset in each specimen is highlighted using red arrows on each surface. Confirming with literature findings, failure initiation was attributed to micro-cavitation with local inelastic deformation in its vicinity. Also, macro cracks crazing was observed to originate from larger size voids shattering towards the edges of each specimen. Brittle failure in all dog-bone specimens dominated the failure mechanism. Examining fractured surfaces from prismatic specimens (**Figure 2.11**), i.e. three-point bending tests, some showed local plastic deformation ahead of final unstable failure. These specimens (B2, B3 and B5) are same ones recording higher failure limits as can be observed from **Figure 2.11**.

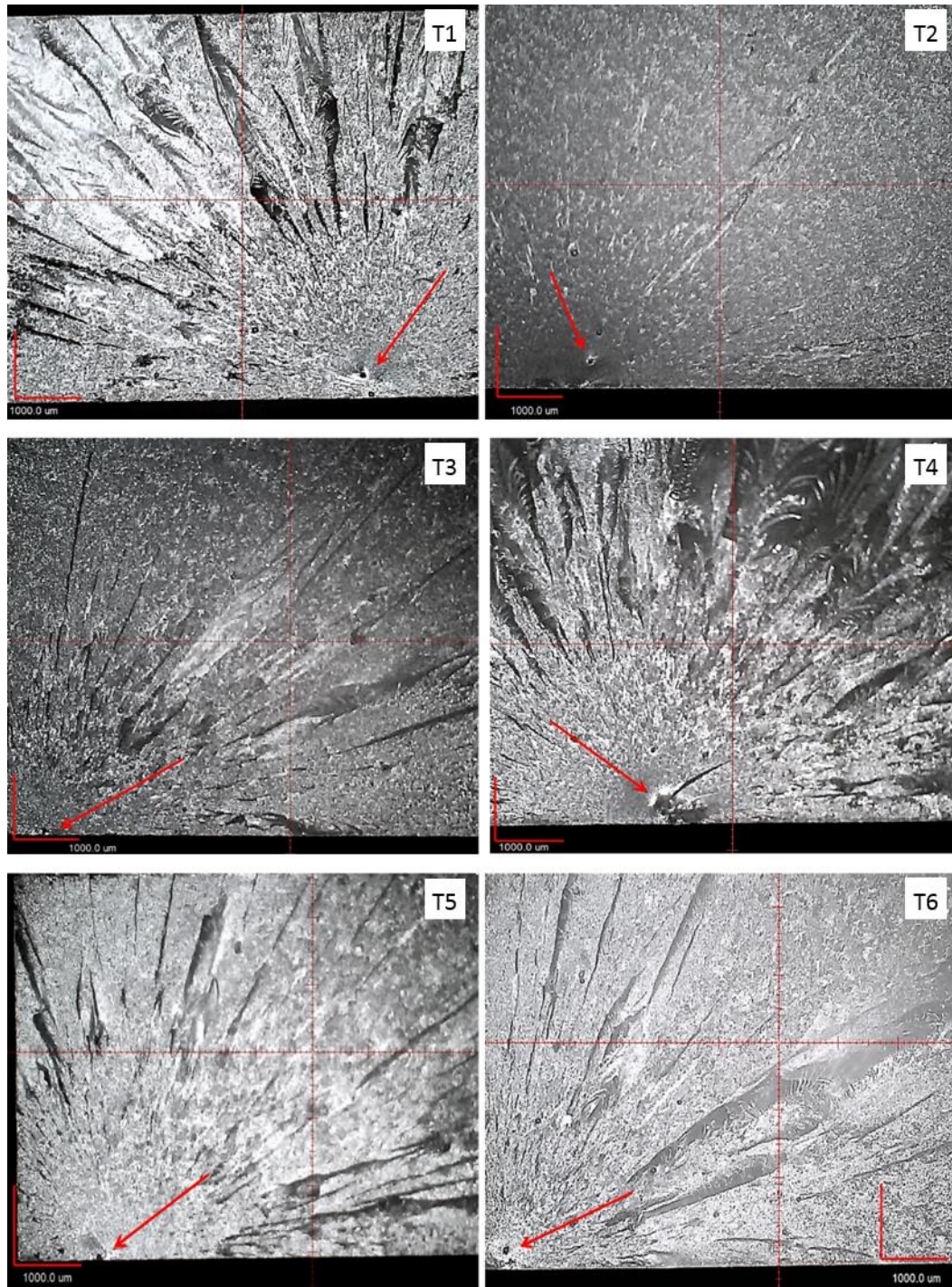


Figure 2.10 Optical microscopic images of dog-bone specimens failures surfaces.

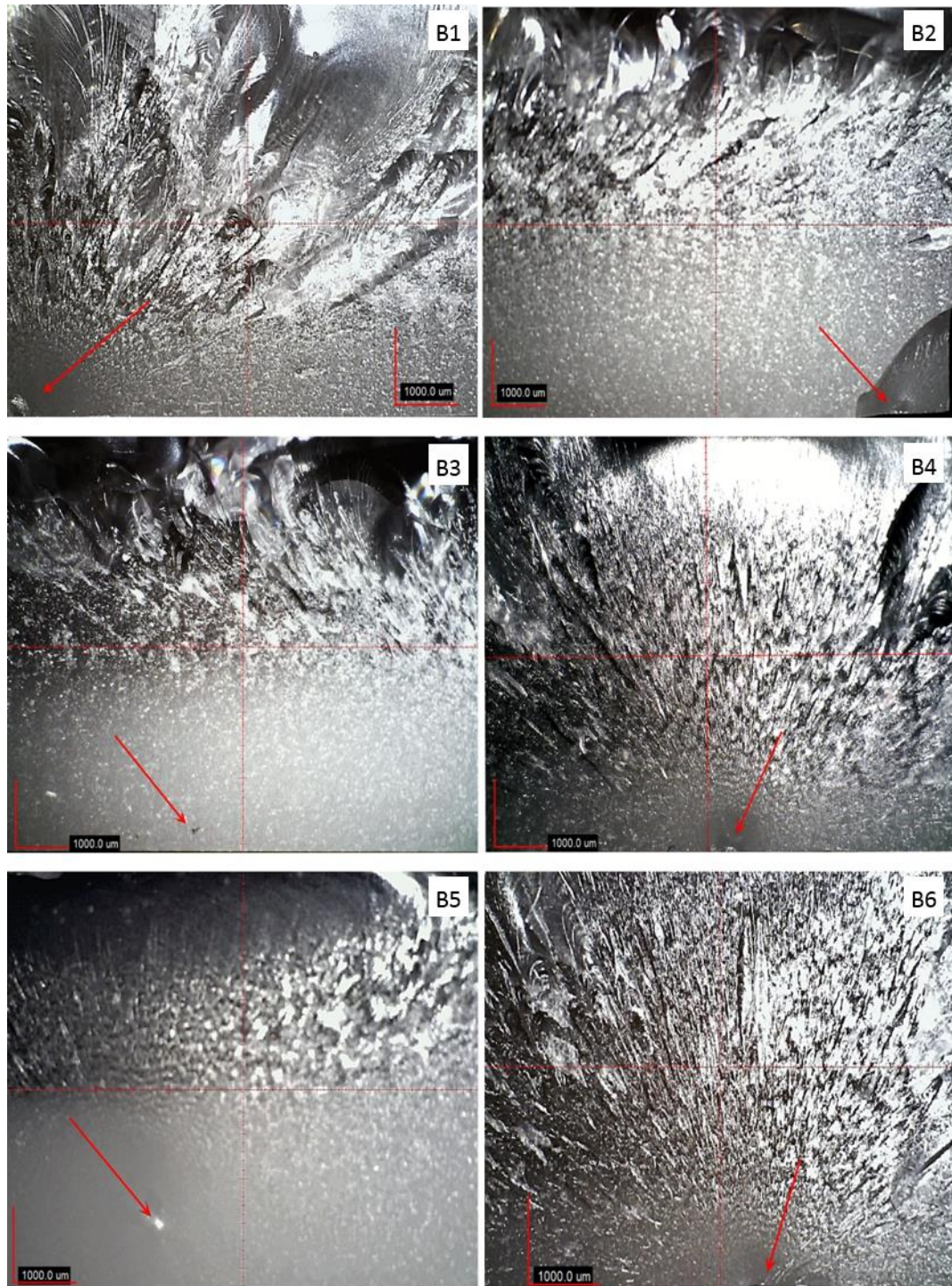


Figure 2.11 Optical microscopic images of prismatic specimens' failure surfaces.

2.5.2 Scan Electron Microscopy

The samples were observed using a field emission gun FEI MLA 650FEG Scanning Electron Microscope (SEM). The samples were carbon coated to reduce surface charging. One tension and two three-point bending samples were tested; samples T6, B3, and B4. Since all tension samples underwent similar amounts of plastic deformation only a single specimen was analyzed (**Figure 2.6**). Conversely, for bending, differing amounts of plastic deformation were observed (**Figure 2.8**) – B3 underwent significant plastic deformation whereas B4 underwent minimal plastic deformation. As such, both B3 and B4 samples were studied to investigate differences in failure surfaces. It was observed that void sizes obtained through SEM were similar to those obtained from optical microscopy. Utilizing the higher magnification capabilities of SEM, a more invasive investigation into the failure was performed, identifying key features on the failure surfaces such as cracks extending from voids.

2.5.2.1 Specimen T6

A failure surface for T6 was observed using the secondary electron detector in the SEM (**Figure 2.12a-d**). The propagation of failure within the sample was from lower right towards upper left. Observing **Figure 2.12b**, it is evident that many voids were within the microstructure of T6. Upon further inspection of T6 in **Figure 2.12c**, it is evident that the specimen underwent initial slow-ductile failure due to the smooth, featureless surface around initial failure. Further investigation, shown in **Figure 2.12d**, shows a void with diameter of 47.4 μm present at the initiation of crack propagation. This void was the internal defect at which failure initiated. The initial crack which propagated from this void was

approximately $4.8\mu\text{m}$ across and was the only crack which propagated throughout the initial slow-ductile failure region. Following the propagation of this initial crack, a transition of the surface was observed (**Figure 2.12c**). The smooth, featureless surface around the void and initial crack was followed by flat, elongated cracks and surface tears, indicating brittle failure. The surface transitions once again from flat topography to highly pronounced cracks and surface tears, indicating rapid tearing of the surface (**Figure 2.12a-b**) during final failure.

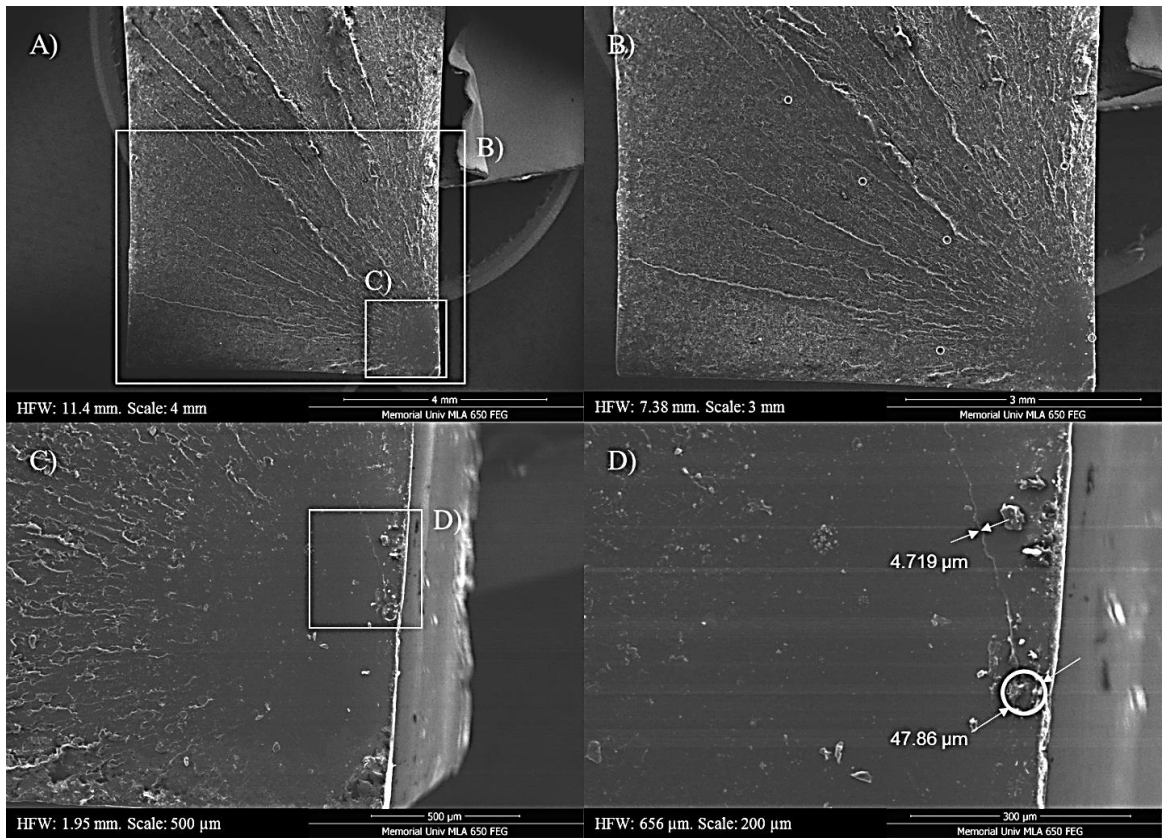


Figure 2.12 Failure surface of specimen T6: a) wide view, b) zoom on area of interest, c) zoom on area of interest, and d) zoom on area of interest.

Upon closer inspection of sample T6, it was observed that due to its neat epoxy nature, the microcracks propagated deep into the matrix with obvious surface features. In **Figure**

2.13a, the transition from brittle failure to rapid tearing was observed. The lower right portion of **Figure 2.13a** possesses flat, elongated cracks which transition to highly pronounced cracks and surface tears moving from lower right towards the upper left. These surface features are consistent with brittle failure transitioning into rapid tearing failure. The large cracks present in **Figure 2.13a** were on the order of 139-152 μ m wide, with large surface deformities, once again indicating tearing occurred. **Figure 2.13b** shows the areas of interest from **Figure 2.13a** that are investigated in **Figure 2.13c** and **Figure 2.13d**.

Figure 2.13c provides an enhanced view of one of the large surface deformities indicative of rapid tearing. The onset of this rapid tearing can be observed in **Figure 2.13d** with a large ridge stretching from the lower middle to the upper left. In addition, it is clearly indicated by the direction of parabolic surface striations that failure occurred from lower right to upper left of the image, consistent with the previous observations. The short distance between successive striations indicates fast-brittle failure, which was expected since region (**d**) was within the brittle failure region previously indicated. Moving from region (**d**) towards the upper left to region (**c**), it is evident that the brittle failure observed in region (**d**) transitions to rapid tearing in region (**c**) and beyond.

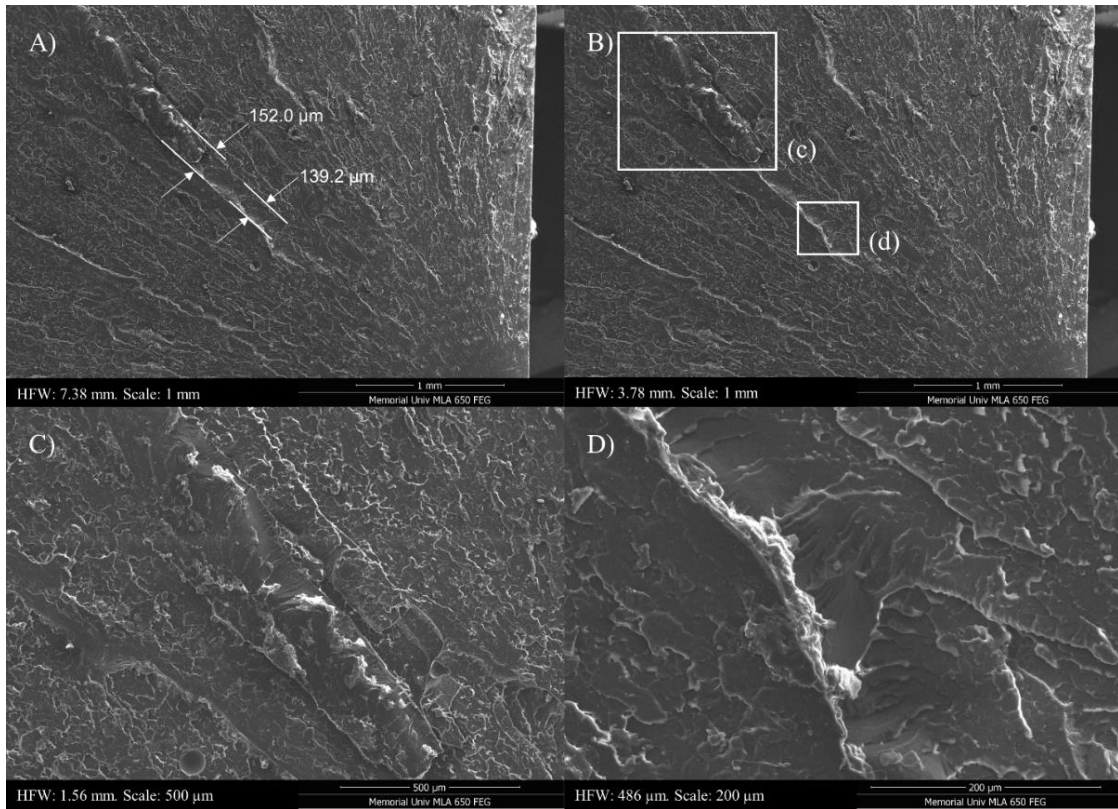


Figure 2.13 Failure Surface of T6: a) microcrack dimensions, b) areas of interest, c) zoom on area of interest, and d) zoom on area of interest.

2.5.2.2 Specimen B3

The failure surface of sample B3 is provided in **Figure 2.14**. As observed in sample T6, sample B3 exhibits a smooth surface near failure initiation, indicative of initially slow-ductile failure. It is observed in **Figure 2.14a** that failure originated in the top right and propagated to the bottom left. It is not as obvious in this sample if failure occurred at a pore as this topography may have been lost as the sample broke into separate pieces. At the top of the image, the sample was in tension while the bottom was in compression. Failure initiated on the tensile side and propagated through to the compressive side, hence the transition from slow-ductile, to brittle, to rapid final tearing observed when moving from the tensile side to compressive side.

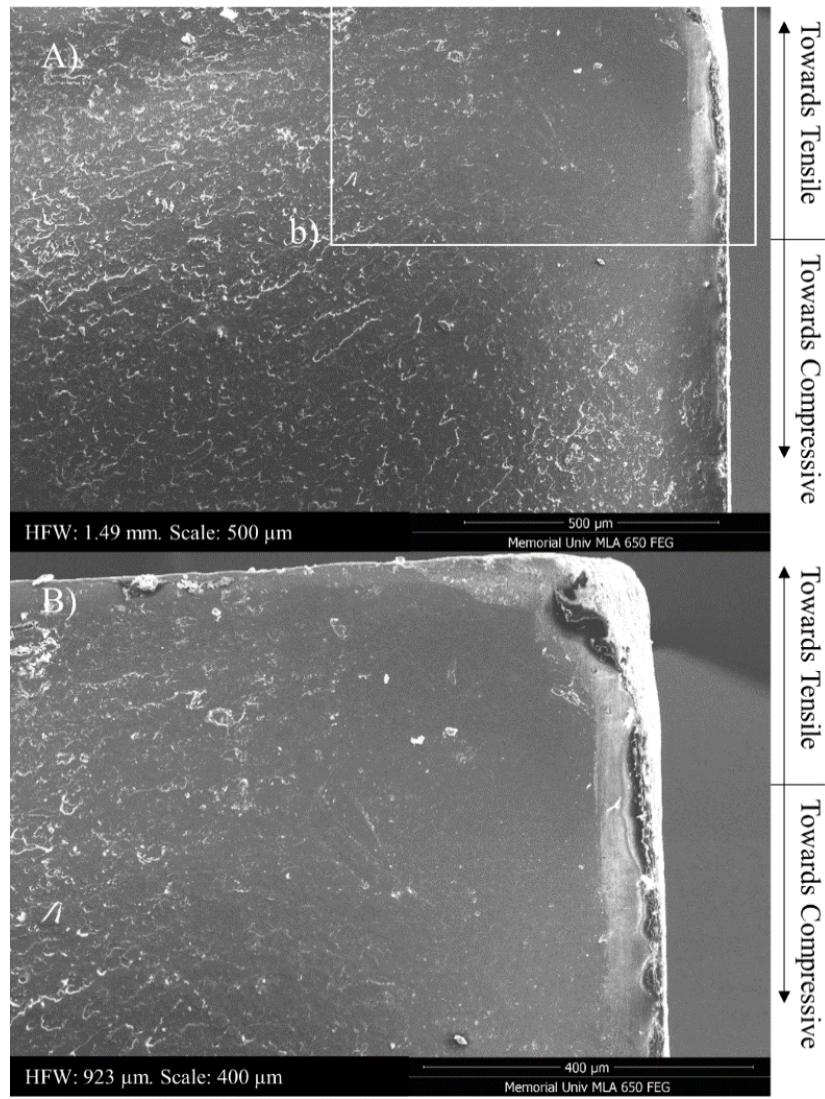


Figure 2.14 Failure Surface of B3: a) wide view, and b) zoom on area of interest.

Moving down the right side of the sample, a change in surface topography was noticed (**Figure 2.15**). The specimen's surface topography changed from smooth and relatively featureless to flat elongated cracks and tears, indicating a transition to brittle failure, as observed in **Figure 2.15a**. Moving further down the specimen surface, the transition of flat elongated cracks into prominent cracks and ridges, thus indicating the onset of rapid tearing of the surface (**Figure 2.15b**).

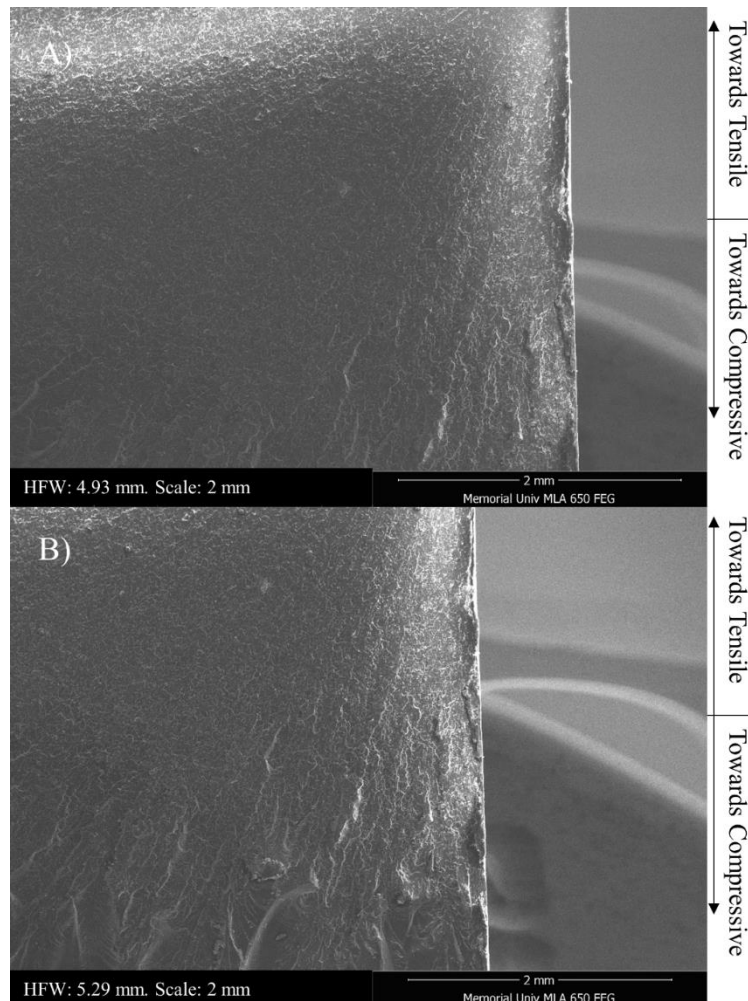


Figure 2.15 Failure Surface of B3: a) upper right-side, and b) lower right-side.

When moving further down the right side towards the bottom of the specimen and into the compressive-side of the sample, the surface topography changed once again with large cavitation, cracks, grooves, and surface defects, as shown in **Figure 2.16**. When moving from top to bottom in **Figure 2.16**, the transition from brittle failure to rapid tearing is observed. At the top of the image, the end of brittle failure was observed with flat, elongated cracks and surface topography transitioning into large prominent cracks indicating the onset of rapid tearing failure. At the bottom of **Figure 2.16**, a large groove is present, indicating the location of final tearing and separation of the sample.

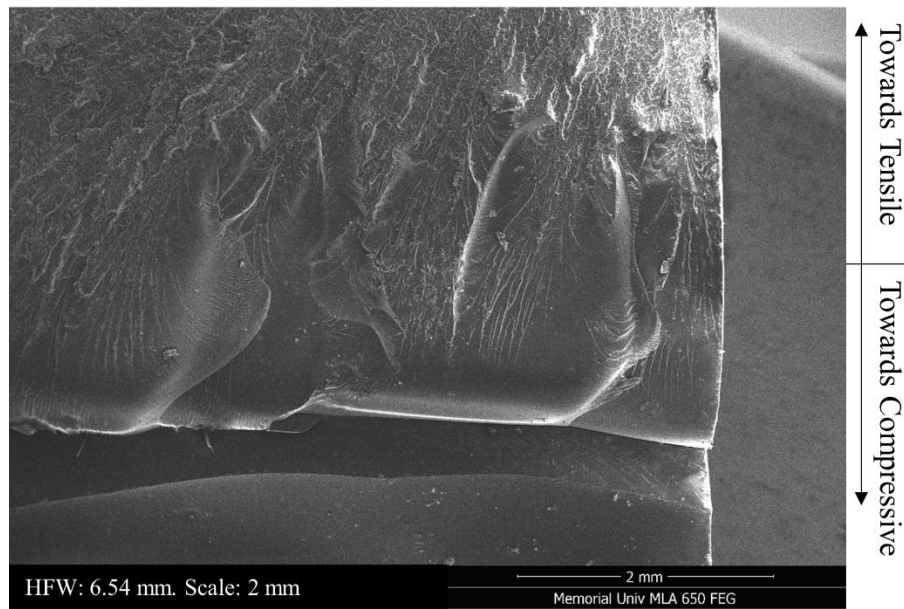


Figure 2.16 Failure Surface of B3, right-hand side, compressive-side.

2.5.2.3 Specimen B4

The failure surface of sample B4 is provided in **Figure 2.17**. As observed in the previous samples, sample B4 exhibits a smooth surface near failure initiation, indicative of initially slow-ductile failure. It is observed in **Figure 2.17a-b** that failure originated in the bottom middle, initiating at an internal defect, and propagated upwards. Like Sample B3, failure initiated on the tensile side and propagated through to the compressive side. Focusing more closely around the area of initial failure, multiple cracks were observed, as shown in **Figure 2.17c**. It was observed that while several cracks began to propagate, only one propagated until the onset of brittle failure – the crack propagating upwards. The other cracks appear to cease propagation within this slow-ductile region as shown in **Figure 2.17c** and **Figure 2.17d**, respectively.

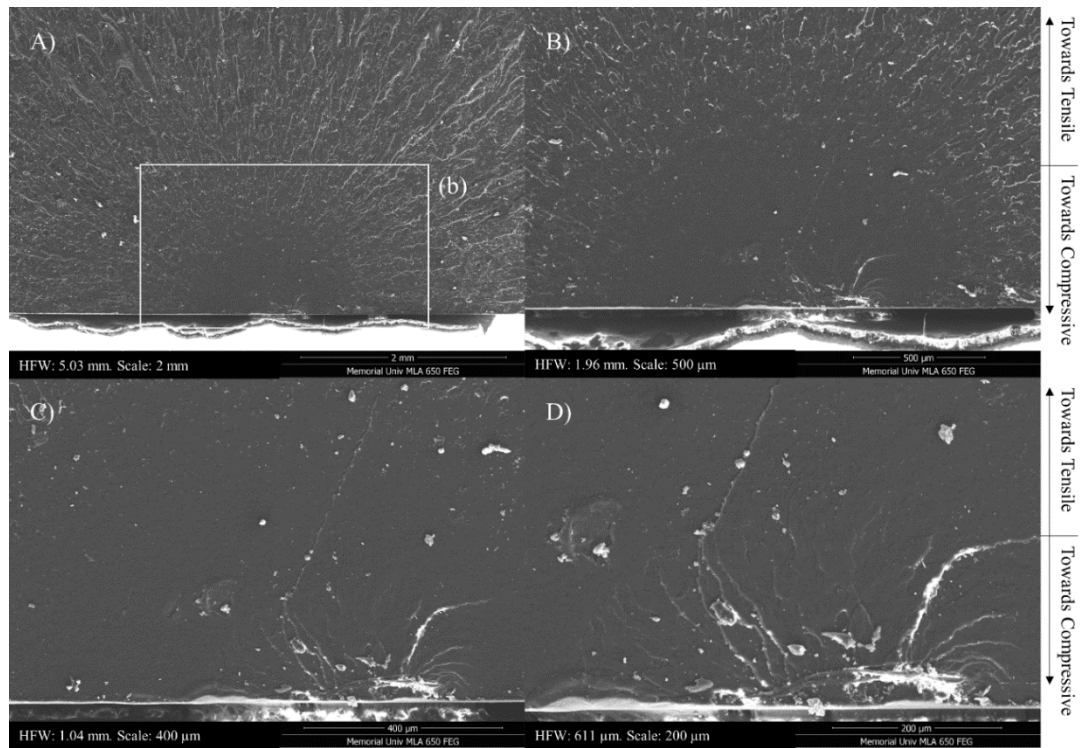


Figure 2.17 Failure Surface of B4: a) wide view, b) zoom on area of interest, c) increased zoom on area of interest, and d) further increased zoom on area of interest.

When observing a composite image of the right-hand side of the specimen from tensile side to compressive side (**Figure 2.18**), similar surface features were observed as were present in sample B3. The surface around initial failure was smooth and featureless, transitioning into flat, elongated cracks, further transitioning into large surface cracks, cavitation, and grooves. Indicating a transition from initial slow-ductile failure, to brittle failure through to rapid tearing failure during final separation.

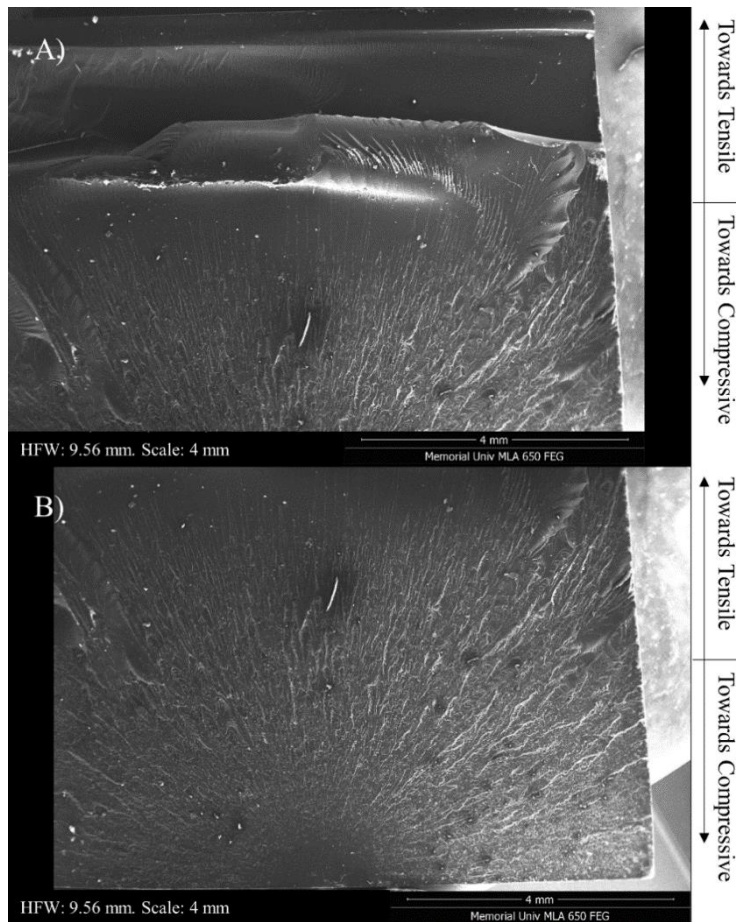


Figure 2.18 Failure Surface of B4 right-side: a) compressive-side, and b) tensile-side.

No distinct differences were observed in the failure surfaces between B3 and B4, except in the area of initial failure. Sample B3 possessed a single internal pore from which a single crack propagated, leading to failure. Conversely, sample B4 does not appear to originate from an internal pore and originates from micro cavities, or defects, on the surface. In addition, the numerous cracks within the initial failure region of sample B4 were indicative of higher stress concentrations near the region of initial failure. As such, the difference in the degree of yielding observed in samples B3 and B4 was due to the presence of a surface defect which caused stress concentrations near the region of initial failure, resulting in sample B4 failing sooner than sample B3.

2.5.3 Computed Tomography Imaging

Next, failure surfaces were analyzed using CT imaging to quantify the void size, volume, and distribution through the sample. Due to the resolution of the scans, voids greater than 40 μm in diameter are confidently observed as this implies two or more voxels across for each void. For consistency, the same set of parameters were used for scanning and analysis. The imaging allowed for determination of internal voids and defects present in the neat epoxy samples. It was determined that void sizes obtained from CT imaging were similar to those observed through optical microscopy and SEM, providing further confidence in the application of CT imaging to study voids within neat epoxy.

Prior to studying the failure surfaces, a portion of the neat epoxy slab was studied to determine the void volume, as well as the smallest and largest voids from the bulk epoxy. The void volume observed in the sample of neat epoxy was 0.467 mm³, with the smallest and largest single void volumes of 0.000006 mm³ and 0.00097 mm³, respectively. The diameters of the voids ranged from 20 μm to 190 μm

2.5.3.1 Specimen T6a

The first failure piece of sample T6 (T6a) was determined to have a pore volume of 0.303 mm³, with the smallest and largest single pore volumes of 0.00001 mm³ and 0.000482 mm³, respectively. The diameters of the pores ranged from 40 μm to 130 μm . Like the bulk neat epoxy, the pore diameters were consistent with results found in optical microscopy and SEM. A 3D transparent scan is shown in **Figure 2.19**.

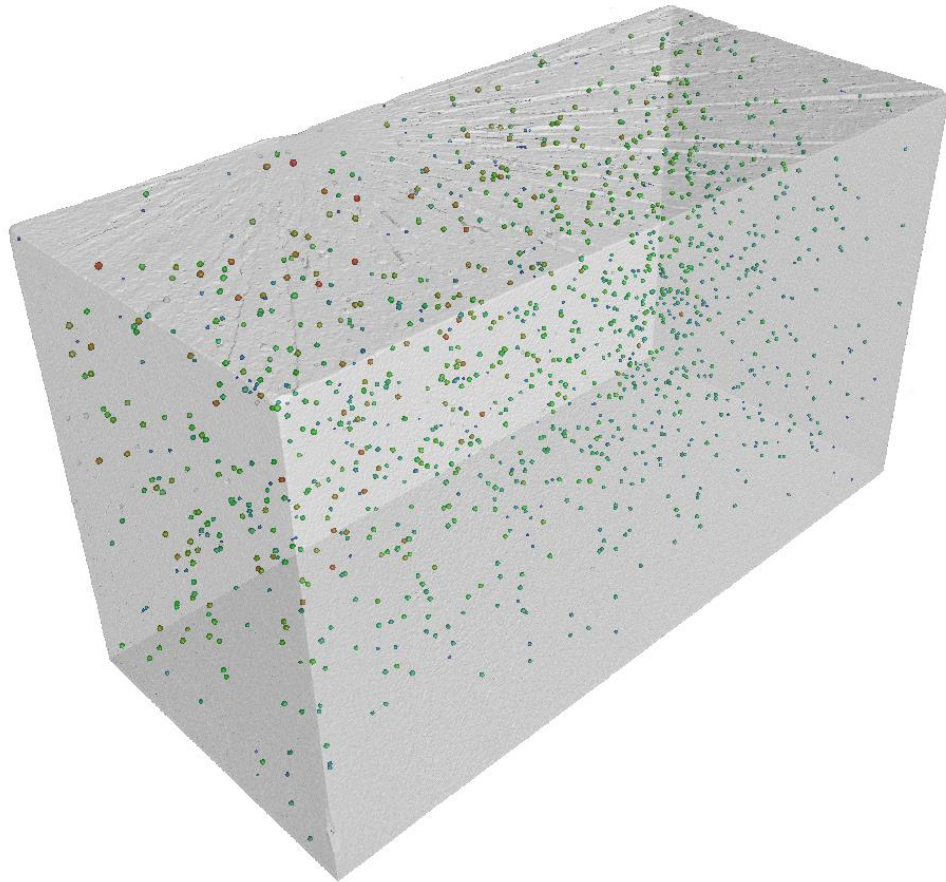


Figure 2.19 Three-dimensional CT scan of specimen T6a

Upon closer inspection of the pores within the sample, three slices were observed – one located at the plane of largest pore volume, one located just beneath the failure surface, and one located at the failure surface. **Figure 2.20a** shows the plane of largest pore volume for T6a. This plane had a pore volume of 0.001661 mm³. **Figure 2.20b** shows the plane just below the failure surface. Closely observing this plane, there were two pores on the left-hand side at the edge of the sample, highlighted in red circles. This sample failed at a plane just slightly above the lower highlighted region, initiating at an edge pore as shown in **Figure 2.20c**. The long stretches of black in **Figure 2.20c** were artifacts of the CT imaging and a result of contrast with the material surfaces at various topographies.

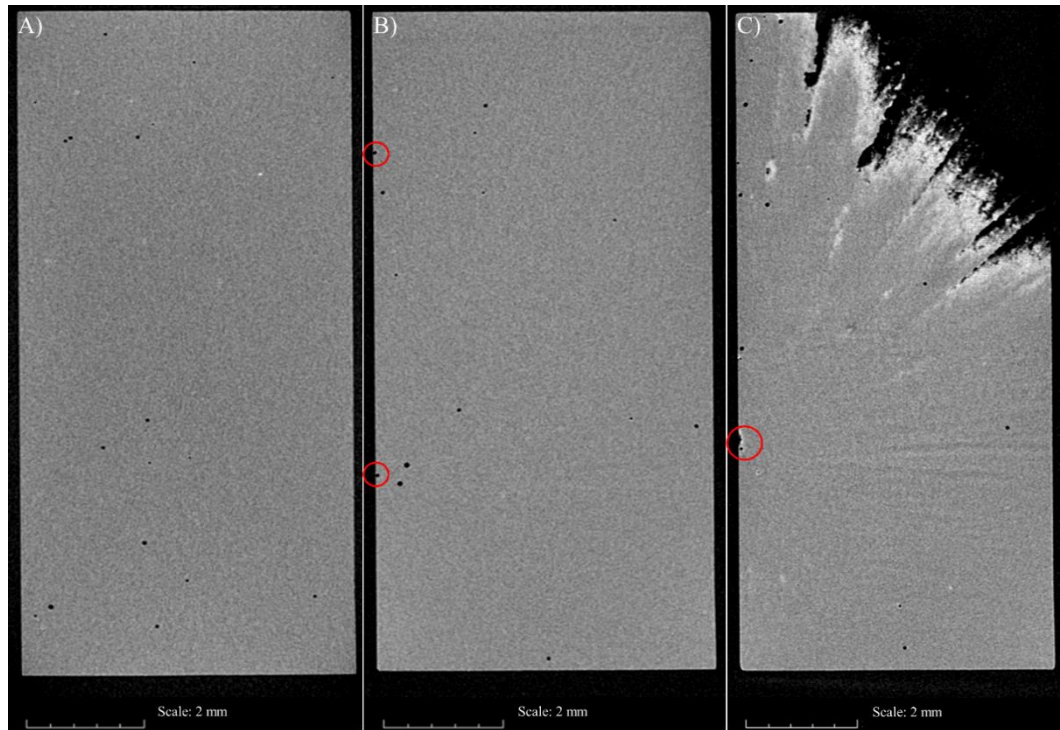


Figure 2.20 Specimen T6a Planes of interest, left to right: a) largest pore volume, b) plane slightly beneath failure surface, and c) failure surface.

2.5.3.2 Specimen T6b

Next, the other failure surface, T6b, was scanned. T6b was determined to have a pore volume of 0.257 mm³, with the smallest and largest single pore volume of 0.000011 mm³ and 0.000476 mm³, respectively. The diameters of the pores ranged from 40µm to 150µm. Pore sizes were approximately the same size as the other sample, T6a. Once again, the pore diameters were consistent with results found in optical microscopy and SEM. A 3D transparent scan is shown in **Figure 2.21**.

Like T6a, three slices were observed for closer inspection **Figure 2.22a** shows the plane of largest pore volume for T6b. This plane had a pore volume of 0.000949 mm³. **Figure 2.22b** shows the plane just beneath the failure surface. Closely observing this plane, there is a single pore on the left-hand side, which is at the edge of the sample, highlighted in a red

circle. When moving up through the sample to the failure surface, **Figure 2.22c**, it is obvious that failure initiated at an edge pore, highlighted with red circle, similar to the one in **Figure 2.22b**.

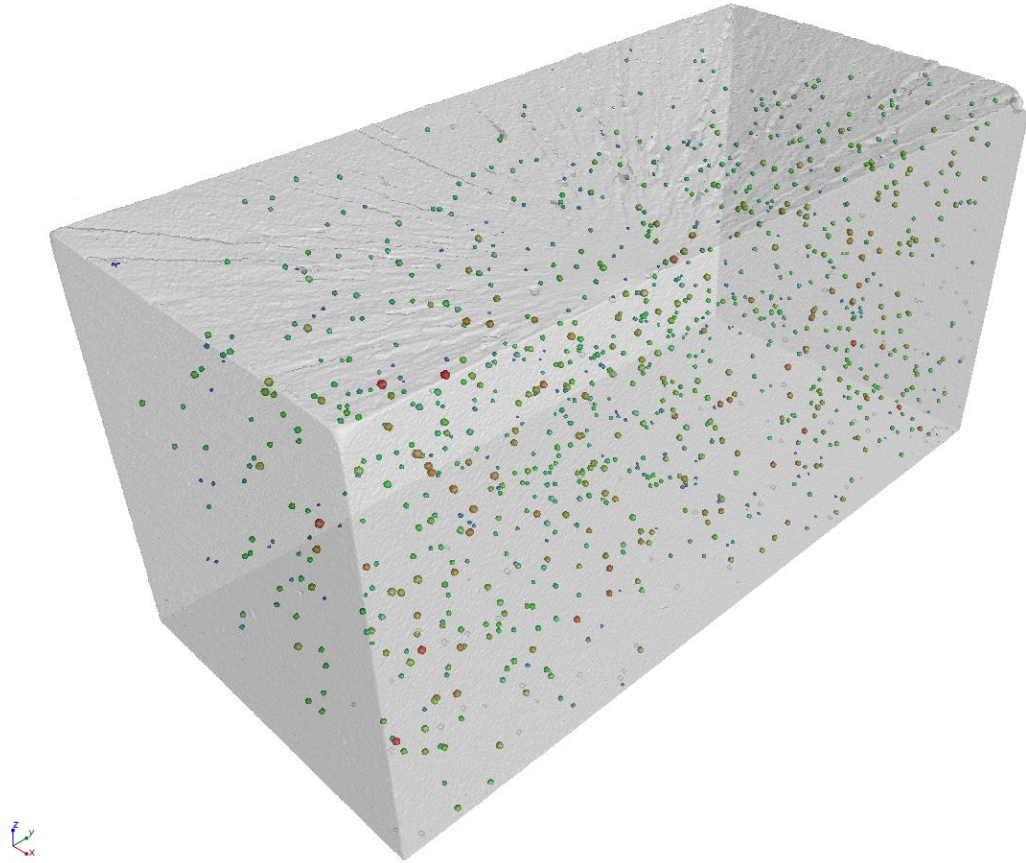


Figure 2.21 Three-dimensional CT scan of specimen T6b.

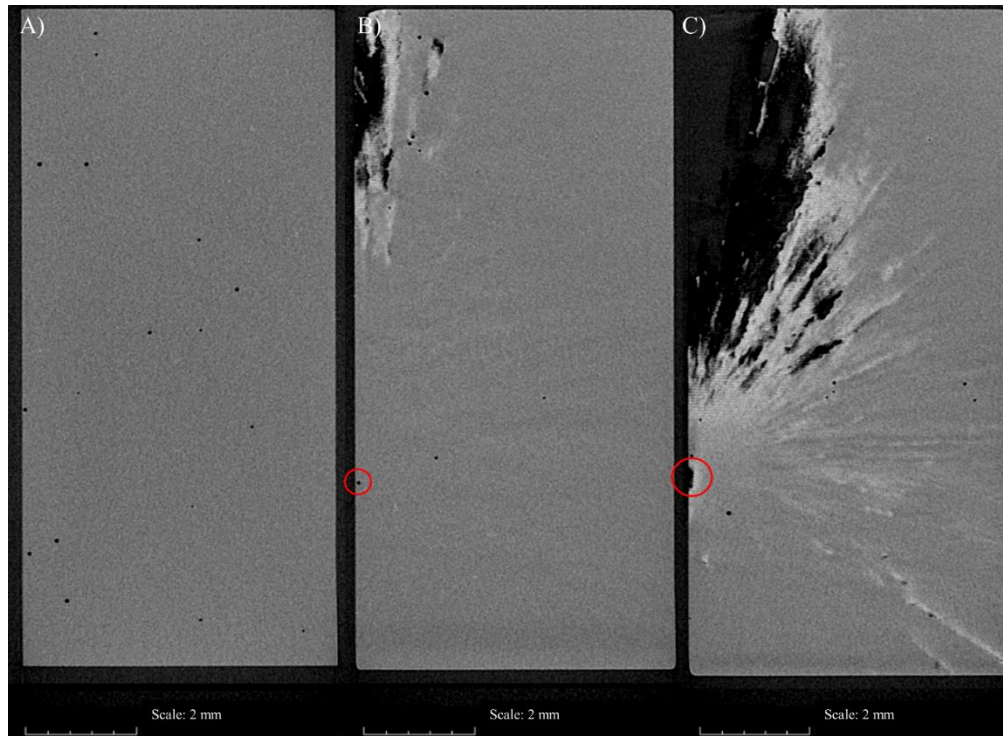


Figure 2.22 Specimen T6b Planes of interest, left to right: a) largest pore volume, b) plane slightly beneath failure surface, and c) failure surface.

The advantage of CT scanning over conventional optical microscopy and SEM analyses is the ability to obtain through-thickness distribution and sizes of voids. This data is incredibly useful for further investigation through numerical analysis.

2.6 Numerical Modeling

A micromechanical investigation for tested epoxy is provided using the framework of extended finite element method (XFEM). The unit cell (UC) method was employed in finite element analysis to predict the mechanical behavior from the actual microstructure. Necessary set of continuity boundary conditions were applied to enable predicting continuum mechanical behavior. This procedure was necessary, and it is slightly different than homogenization techniques. This approach have the advantage of obtaining mechanical behavior in elastic-plastic regimes rather than discrete stiffness properties.

Also, preliminary fracture analysis was conducted on the actual microstructural UC. Finally, macroscale modeling of conducted testing is also provided to predict macroscopic failure.

The procedures for generating the UC model are presented in **Figure 2.23**. The microscopic image shown in **Figure 2.23a** was utilized to isolate an image representing micro voids to be used in the analysis. **Figure 2.23b** shows a monochromic image used to isolate the actual structural voids with a unit size of $1000\mu\text{m}$. Image format was then converted to a drawing exchange format (DXF) as shown in **Figure 2.23c** to enable importing actual microstructure into Abaqus interface. Finally, the actual microstructural UC model was generated as shown in **Figure 2.23d**. The convergent mesh had approximately 62000 triangular elements, namely CPS3 which is a three-noded plane stress element. A solid homogeneous section was used to apply the material definition to all UC models. The material behavior was defined using deformation plasticity theory utilizing the modulus of elasticity and Poisson's ratio for linear behavior while the yield stress together with the hardening exponent defines the plastic flow.

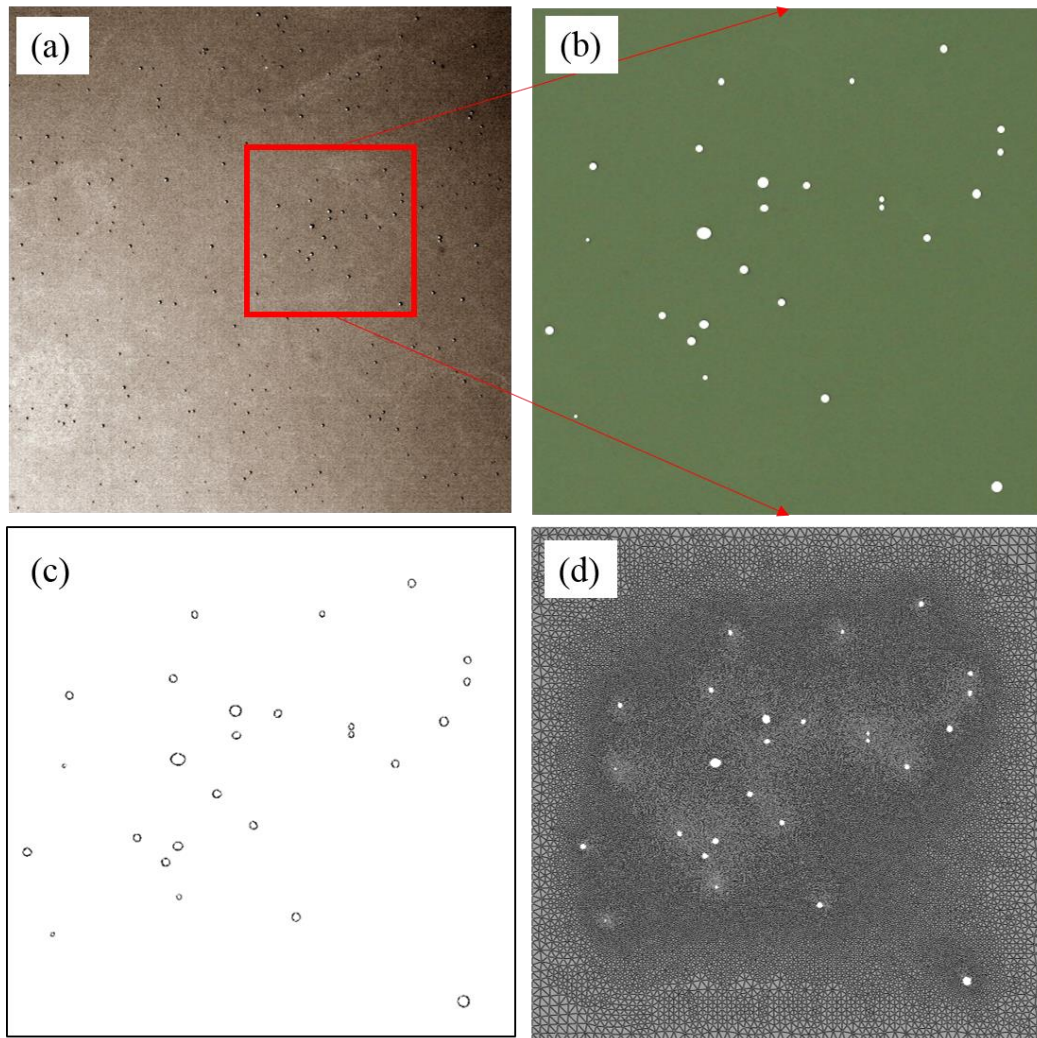


Figure 2.23 Procedures for generating actual microstructural UC model: a) OM image, b) Isolated image, c) Drawing exchange format image, and d) Actual UC model.

Micromechanical UC presenting actual voids distribution was utilized within the framework of XFEM to investigate failure initiation. Damage process is initialized depending on maximum principal stress while the evolution was enabled on energy basis. Traction separation law details are illustrated in Abaqus documentation (*Abaqus V6.14–Documentation, Dassault Systèmes Simulia Corporation, 2013*). **Figure 2.24a** presents the

contour plot of von-Mises stress for the actual microstructure UC model while a zoomed in view showing the micro cracks is provided in **Figure 2.24b**. The micro-cracks initiated at the largest hole/void signifying that failure onset at a micro-scale will possibly be in the vicinity of the larger voids. In fact, this observation was documented in conducted testing observations. Stress concentrations in the vicinity of holes triggered the onset of damage in microstructural UCs. There is a possibility that micro-cracks cause coalescence and activate damage at the macroscopic scale.

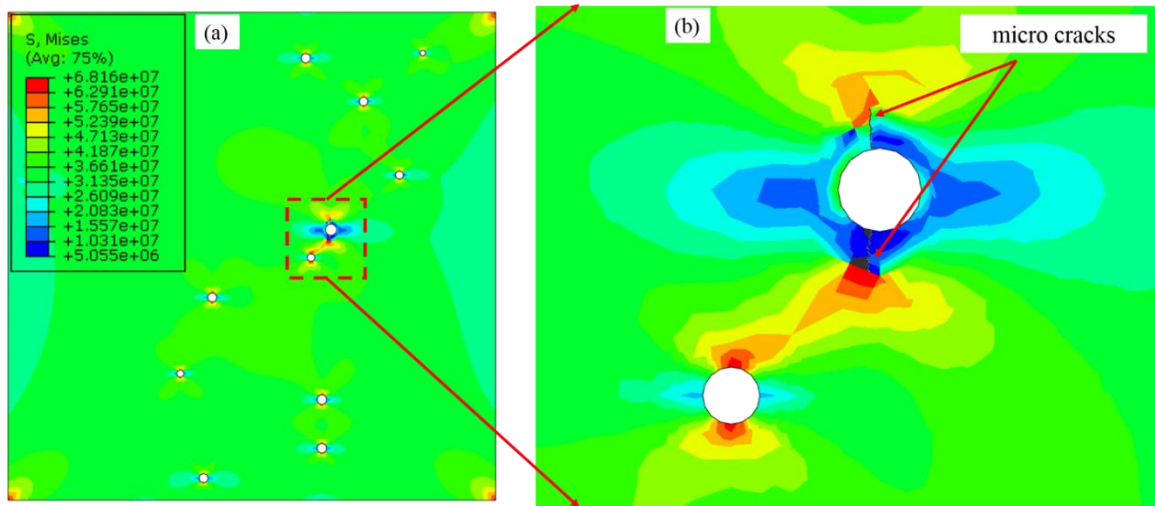


Figure 2.24 Von-Mises contour plot results of actual microstructure UC model: a) UC model, and b) Zoomed in view showing micro cracks.

Specimen sized three- dimensional models were constructed following the specimens' geometries outlined in **Figure 2.1**. The convergent meshes for the dog-bone and prismatic specimens had approximate sizes of 45000 and 30000 brick (C3D8R) elements, respectively. The standard testing procedures regarding loading conditions were utilized to define each model boundary and loading conditions. Both models were loaded until final failure using the framework of XFEM in Abaqus. The residual plasticity contour plots are compared to monochromic scans of actual failed specimens as presented in **Figure 2.25**.

The dog-bone and the prismatic specimens comparisons are shown by **Figure 2.25a** and **Figure 2.25b**, respectively. As can be observed, stress-whitening phenomena in the actual specimens are in excellent agreement with residual plastic strains contour plots. Also, predicted failure surfaces locations and shapes were very close to actual ones. Even though the final failure is dominated by brittleness, the plastic deformations were obvious. The precise results from numerical analyses can be attributed to precise identification of yielding stresses explained in **Section 2.4.1**.

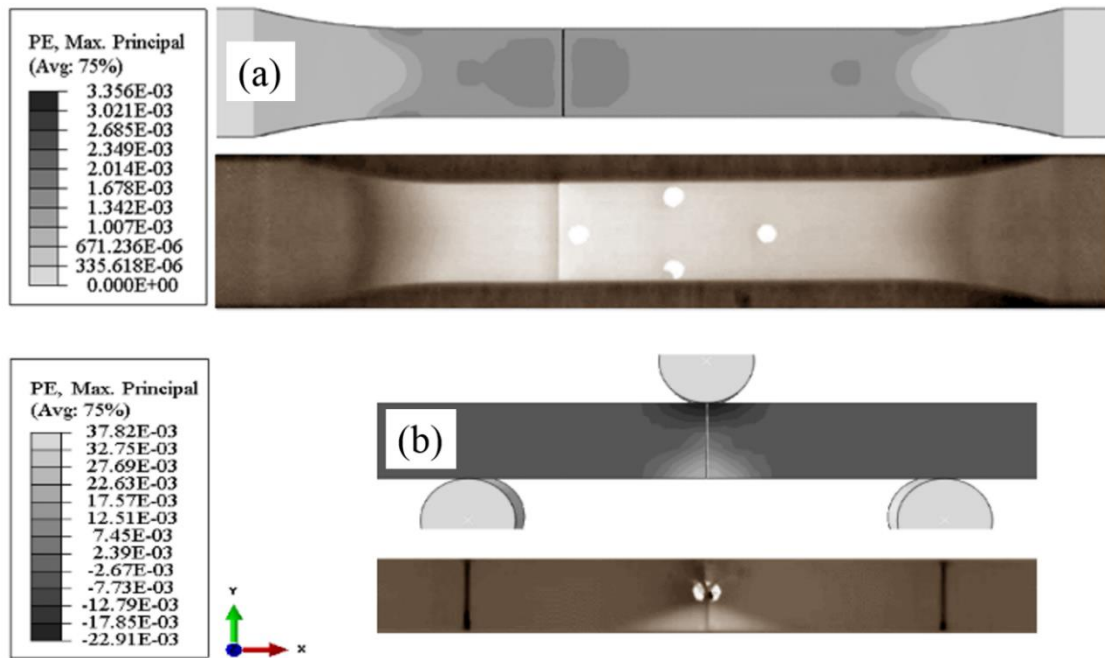


Figure 2.25 Residual plastic strains compared to failed specimens' monochromic scans.

The average curve of load-displacement testing results was used to validate the specimen sized model results as shown in **Figure 2.26**. Comparing both behaviors, it can be observed that numerical results are in excellent agreement with the average testing results. Both linear and non-linear behaviors were precisely predicted. Regarding failure limits, the numerical results showed a lower bound signifying conservative type of predictions.

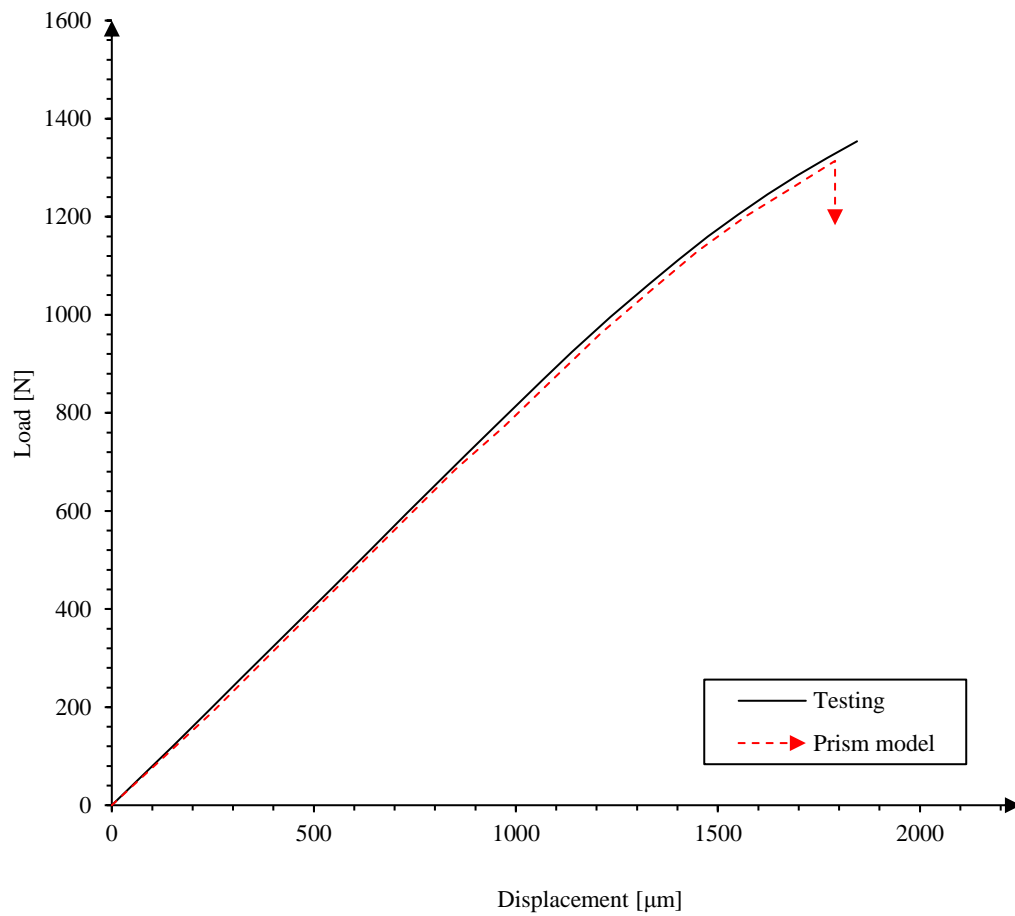


Figure 2.26 Load-displacement curves: Testing vs. numerical.

2.7 Conclusions

In this work, a thorough investigation on plain epoxy failure under different types of loading was conducted. Neat epoxy resin was tested under uniaxial tension and three-point bending loads. Accurate strain measurements were enabled using a high precision non-contact digital image correlation (DIC) system. Fractographic analyses using optical microscopy, scan electron microscopy (SEM) and computer tomography (CT) scan were also presented. Also, numerical modeling analyses utilizing the framework of XFEM at

micro and macro scales were provided. From the conducted research the following conclusions can be withdrawn;

- Heavily cross-linked epoxy resins were characterized by undergoing brittle final failure in the case of uniaxial loading. However, minimal plastic deformation was observed.
- Under three-point loading the failure behavior is a complex type of failure dominated by unstable final failure.
- The proposed method of stress-whitening yield identification enabled reliable and efficient numerical modeling at micro and macro scales. In which, the yield stress was experimentally identified using minimal testing effort and therefore, accurate mechanical behavior was defined in the material model for computational analyses.
- Microscopic analyses using three different methods characterized micro voids radii ranging from 40-150 μm with almost perfect spherical shapes.
- The current work demonstrated the effectiveness of CT scanning to obtain through-thickness pore size and total porosity. The results were compared to results obtained through Optical Microscopy (approximate void sizes and total porosity) and SEM (approximate void sizes).
- Fractographic analysis revealed that micro-cavitation was leading to damage initiation and possible final failure in glassy polymers under different types of loading. Same can be concluded from micromechanical modeling results.

- Complex failure mechanisms were observed in specimens under three-point loading. While the failure initiated in a vicinity of micro-cavitation, there exist a transition region signifying going from ductile to brittle behavior.

2.8 References

- Abaqus V6.14– Documentation, Dassault Systèmes Simulia Corporation, Providence, Rhode Island (2013).
- Aroush, D. R.-B., Maire, E., Gauthier, C., Youssef, S., Cloetens, P., & Wagner, H. D. (2005). A study of fracture of unidirectional composites using in situ high-resolution synchrotron X-ray microtomography. *Composites Science and Technology*, 66(10), 1348–1353. <https://doi.org/10.1016/j.compscitech.2005.09.010>
- Asp, L. E., Berglund, L. A., & Talreja, R. (1996). A criterion for crack initiation in glassy polymers subjected to a composite-like stress state. *Composites Science and Technology*, 56(11), 1291–1301. [https://doi.org/10.1016/S0266-3538\(96\)00090-5](https://doi.org/10.1016/S0266-3538(96)00090-5)
- Baruchel, J., Buffiere, J. Y., Cloetens, P., Di Michiel, M., Ferrie, E., Ludwig, W., ... Salvo, L. (2006). Advances in synchrotron radiation microtomography. *Scripta Materialia*, 55(1 SPEC. ISS.), 41–46. <https://doi.org/10.1016/j.scriptamat.2006.02.012>
- Bauer, R. S., Stewart, S. L., & Stenzenberger, H. D. (2000). COMPOSITE MATERIALS , THERMOSET POLYMER-MATRIX. In In Kirk-Othmer Encyclopedia of Chemical Technology, (Ed.). <https://doi.org/10.1002/0471238961.2008051802012105.a01>
- Baumann, K. J., Kennedy, W. H., & Herbert, D. L. (1984). Computed Tomography X-Ray Scanning NDE of Graphite/Epoxy Coupons. *Journal of Composite Materials*, 18(6), 536–544. <https://doi.org/10.1177/002199838401800603>
- Bieniaś, J., Dębski, H., Surowska, B., & Sadowski, T. (2012). Analysis of microstructure damage in carbon/epoxy composites using FEM. *Computational Materials Science*, 64, 168–172. <https://doi.org/10.1016/j.commatsci.2012.03.033>
- Camanho, P. P., Arteiro, A., Melro, A. R., Catalanotti, G., & Vogler, M. (2015). Three-dimensional invariant-based failure criteria for fibre-reinforced composites. *International Journal of Solids and Structures*, 55, 92–107. <https://doi.org/http://dx.doi.org/10.1016/j.ijsolstr.2014.03.038>
- Christensen, R. M. (2001). a Survey of and Evaluation Methodology for Fiber Composite Material Failure Theories. *Seven*, 25–40.
- Daniel, I. M. (2015). Constitutive behavior and failure criteria for composites under static and dynamic loading. *Meccanica*, 50(2), 429–442. <https://doi.org/10.1007/s11012-013-9829-1>

- Daniel, I. M., Daniel, S. M., & Fenner, J. S. (2018). A new yield and failure theory for composite materials under static and dynamic loading. *International Journal of Solids and Structures*, 148–149, 79–93. <https://doi.org/10.1016/j.ijsolstr.2017.08.036>
- Dávila, C. G., Camanho, P. P., & Rose, C. A. (2005). Failure criteria for FRP laminates. *Journal of Composite Materials*, 39(4), 323–345. <https://doi.org/10.1177/0021998305046452>
- Esna Ashari, S., & Mohammadi, S. (2012). Fracture analysis of FRP-reinforced beams by orthotropic XFEM. *Journal of Composite Materials*, 46(11), 1367–1389. <https://doi.org/10.1177/0021998311418702>
- Fard, M. Y. (2011). Nonlinear inelastic mechanical behavior of epoxy resin polymeric materials. ARIZONA STATE UNIVERSITY.
- Hagstrand, P. O., Bonjour, F., & Månson, J. A. E. (2005). The influence of void content on the structural flexural performance of unidirectional glass fibre reinforced polypropylene composites. *Composites Part A: Applied Science and Manufacturing*, 36(5), 705–714. <https://doi.org/10.1016/j.compositesa.2004.03.007>
- Hashin, Z., & Rotem, A. (1973). A Fatigue Failure Criterion for Fiber Reinforced Materials. *Journal of Composite Materials*, 7(4), 448–464. <https://doi.org/10.1177/002199837300700404>
- Hinton.M.J, Kaddour.A.S, & Soden.P.D. (2002). A comparison of the predictive capabilities of current failure theories for composite laminates, judged against experimental evidence. In *Composites Science and Technology* (Vol. 62). [https://doi.org/10.1016/S0266-3538\(02\)00125-2](https://doi.org/10.1016/S0266-3538(02)00125-2)
- Isaac, M. D., & Ori, I. (2013). *Engineering Mechanics of composite materials*. Oxford University Press, 2, 1–403. <https://doi.org/5fad72a8bc5942d089cc71406c6287da>
- Kalantari, M., Dong, C., & Davies, I. J. (2017). Effect of matrix voids, fibre misalignment and thickness variation on multi-objective robust optimization of carbon/glass fibre-reinforced hybrid composites under flexural loading. *Composites Part B: Engineering*, 123, 136–147. <https://doi.org/10.1016/j.compositesb.2017.05.022>
- Lachaud, F., Espinosa, C., Michel, L., Rahme, P., & Piquet, R. (2015). Modelling Strategies for Simulating Delamination and Matrix Cracking in Composite Laminates. *Applied Composite Materials*, 22(4), 377–403. <https://doi.org/10.1007/s10443-014-9413-4>
- Lambert, J., Chambers, A. R., Sinclair, I., & Spearing, S. M. (2012). 3D damage characterisation and the role of voids in the fatigue of wind turbine blade materials. *Composites Science and Technology*, 72(2), 337–343. <https://doi.org/10.1016/j.compscitech.2011.11.023>
- Li, Y., Stier, B., Bednarczyk, B., Simon, J. W., & Reese, S. (2016). The effect of fiber misalignment on the homogenized properties of unidirectional fiber reinforced composites. *Mechanics of Materials*, 92, 261–274.

- <https://doi.org/10.1016/j.mechmat.2015.10.002>
- Liebig, W. V., Leopold, C., & Schulte, K. (2013). Photoelastic study of stresses in the vicinity of a unique void in a fibre-reinforced model composite under compression. *Composites Science and Technology*, 84, 72–77.
<https://doi.org/10.1016/j.compscitech.2013.04.011>
- Liebig, Wilfried V., Viets, C., Schulte, K., & Fiedler, B. (2015). Influence of voids on the compressive failure behaviour of fibereinforced composites. *Composites Science and Technology*, 117, 225–233. <https://doi.org/10.1016/j.compscitech.2015.06.020>
- Nikishkov, Y., Airolidi, L., & Makeev, A. (2013). Measurement of voids in composites by X-ray Computed Tomography. *Composites Science and Technology*, 89, 89–97.
<https://doi.org/10.1016/j.compscitech.2013.09.019>
- Otsu, N. (1979). A Threshold Selection Method from Gray-Level Histograms. *IEEE Transactions on Systems, Man, and Cybernetics*, C(1), 62–66.
<https://doi.org/10.1109/TSMC.1979.4310076>
- P.K. Mallick. (2007). *Fiber-Reinforced Composites: Materials, Manufacturing, and Design*. In CRC Press.
- Pawar, P. M., & Ganguli, R. (2006). Modeling progressive damage accumulation in thin walled composite beams for rotor blade applications. *Composites Science and Technology*, 66(13), 2337–2349. <https://doi.org/10.1016/j.compscitech.2005.11.033>
- Pollayi, H., & Yu, W. (2014). Modeling matrix cracking in composite rotor blades within VABS framework. *Composite Structures*, 110(1), 62–76.
<https://doi.org/10.1016/j.compstruct.2013.11.012>
- Pulungan, D., Lubineau, G., Yudhanto, A., Yaldiz, R., & Schijve, W. (2017). Identifying design parameters controlling damage behaviors of continuous fiber-reinforced thermoplastic composites using micromechanics as a virtual testing tool. *International Journal of Solids and Structures*, 117.
<https://doi.org/10.1016/j.ijsolstr.2017.03.026>
- Talreja, R. (2014). Assessment of the fundamentals of failure theories for composite materials. *Composites Science and Technology*, 105, 190–201.
<https://doi.org/10.1016/j.compscitech.2014.10.014>
- Uygunoglu, T. K. U., Gunes, I. K. U., & Brostov, W. of N. T. (2015). physical and Mechanical properties of polymer comppsite with high content. *Materials Research*, 18(6), 1188–1196. <https://doi.org/10.1590/1516-1439.009815>
- Van Der Meer, F. P., Sluys, L. J., Hallett, S. R., & Wisnom, M. R. (2012). Computational modeling of complex failure mechanisms in laminates. *Journal of Composite Materials*, 46(5), 603–623. <https://doi.org/10.1177/0021998311410473>
- Verges, M. A., Schilling, P. J., Herrington, P. D., Tatiparthi, A. K., & Karedla, B. R. (2005). X-ray computed microtomography of internal damage in fiber reinforced polymer matrix composites. *Composites Science and Technology*, 65(14), 2071–

2078. <https://doi.org/10.1016/j.compscitech.2005.05.014>
- Wang, Zhen, Yu, T., Bui, T. Q., Trinh, N. A., Luong, N. T. H., Duc, N. D., & Doan, D. H. (2016). Numerical modeling of 3-D inclusions and voids by a novel adaptive XFEM. *Advances in Engineering Software*, 102, 105–122.
<https://doi.org/10.1016/j.advengsoft.2016.09.007>
- Wang, Zhenqing, Liu, F., Liang, W., & Zhou, L. (2013). Study on tensile properties of nanoreinforced epoxy polymer: Macroscopic experiments and nanoscale FEM simulation prediction. *Advances in Materials Science and Engineering*, 2013.
<https://doi.org/10.1155/2013/392450>
- Wright, P., Fu, X., Sinclair, I., & Spearing, S. M. (2008). Ultra high resolution computed tomography of damage in notched carbon fiber-epoxy composites. *Journal of Composite Materials*, 42(19), 1993–2002.
<https://doi.org/10.1177/0021998308092211>
- Wu, E. M., & Tsai, S. W. (1971). A General Theory of Strength for Anisotropic Materials. *Journal of Composite Materials*, 5(1), 58–80.
<https://doi.org/10.1177/002199837100500106>

3 Actual Microstructural Voids Generation in Finite Element Analysis utilizing Computed Tomography Scan of Heavily Cross-linked Epoxy

3.1 Abstract

In the present work, computed tomography (CT) was used to characterize the microstructural voids content in a plain epoxy resin like the one used in aerospace applications. A Python script was developed and implemented within the mainstream finite element (FE) software Abaqus to generate actual microstructural FE model employing computed tomography (CT) scan of heavily cross-linked epoxy. Developed script enabled modeling sophisticated microstructural features such as micro-voids based on their actual size/location. Specimen sized model utilizing finite microstructural region was used to investigate the material behavior and damage initiation at microscales utilizing the framework of extended finite element method (XFEM). The proposed algorithm is capable of generating a micromechanical model in less than one-minute runtime. Prediction results proved excellent agreement compared to experimental data from the current investigation besides the literature findings.

3.2 Introduction

Composite materials are widely used in numerous engineering applications such as aerospace, automotive and biomedical (Arumugam, Saravanakumar, & Santulli, 2018; Koerber et al., 2018). Composites are usually preferred over metallic materials for their enhanced mechanical properties at relatively lower densities (Z. C. Su, Tay, Ridha, & Chen, 2015). However, Composite materials are known for multiple failure modes that are driven by their constituents' behaviors. Two out of four typical failure modes of composites are

dominated by the resin material, namely matrix cracking and separation of plies or delamination (Chevalier, Morelle, Camanho, Lani, & Pardoen, 2018; Yang et al., 2017). Also, composite failure is strongly associated with manufacturing defects such as resin rich regions and voids (Di Landro et al., 2017; Giddings, Bowen, Salo, Kim, & Ive, 2010; W. V. Liebig et al., 2013; Spaggiari & O'Dowd, 2012a) which are intensely tied to the used resin materials. Epoxy polymers represent the majority of matrix and adhesive materials in composite manufacturing (P.K. Mallick, 2007). Heavy cross-linkage occurs during the polymerization process resulting in a tridimensional network or structure (Uygunoglu et al., 2015). The polymerization process results in a thermally stable polymer with excellent resistance to harsh environmental conditions (Jones, 1999). However, the resulting resin material is usually of a brittle behavior (Isaac & Ori, 2013) owed to the pressure and thermal cycles during the curing process (Daniel, Luo, Schubel, & Werner, 2009). The curing process usually results in undesired void content which is known for deteriorating the mechanical behavior (Huang & Talreja, 2005). Some advanced manufacturing techniques are being utilized to reduce the void content such as autoclaving vacuum bagging (Di Landro et al., 2017; Park, Choi, & Choi, 2010) yet; they are unavoidable.

Computed tomography (CT) is a useful tool to investigate the internal defects of composite materials. CT scanning allows for the non-destructive analysis of materials, particularly for meeting manufacturing standards. The work of Schell et al. (Schell, Renggli, van Lenthe, Müller, & Ermanni, 2006) demonstrated that micro-CT scans enable engineers to investigate the distribution/size of void defects within glass fiber reinforced polymers. Also, the work of Sharma et al. (R. Sharma, Deshpande, Bhagat, Mahajan, & Mittal, 2013)

provided in-depth investigation of cracks and voids in carbon-carbon composites. They are investigating various voids such as micro and large voids, as well as cracks with interfacial, matrix, and intra-bundle cracks. More recently several works have extended the usefulness of CT scanning to obtain internal defects to be further studied in finite element analysis. The work of Shigang et al. (Shigang, Rujie, & Yongmao, 2015) investigated the thermal conductivity of woven carbon-carbon composites under the presence of voids. Shigang et al. (Shigang, Rujie, et al., 2015) utilize CT scanning to obtain the void volume fractions for both the fibers and matrix to then study with finite elements (FE). A representative volume element (RVE) is created, and the voids are imported into the model following a Monte Carlo approach where randomly selected elements are turned into voids (assigned properties of air) until the void volume fraction is obtained in both fiber and matrix. Shigang et al. (Shigang, Rujie, et al., 2015) finite element results showed good agreement when compared to compare both theoretical and experimental ones. Unfortunately, Shigang et al. (Shigang, Rujie, et al., 2015) do not study the effect of voids. Instead CT scanning is used only as a tool to obtain a more thorough model. In a similar work, Shigang et al. (Shigang, Xiaolei, Yiqi, Yongmao, & Daining, 2014) investigate the performance of carbon-carbon composites undergoing three-point bending with the presence of voids. Shigang et al. (Shigang et al., 2014) utilize CT scanning to obtain the void volume fraction in the fibers, matrix, and fiber-matrix interface. The void volume fraction is obtained by calculating the two-dimensional area of the voids and converting to three-dimensional volume by dividing by the total surface area. These void volume fractions are then utilized in finite elements through the implementation of a Monte Carlo approach to randomly select elements and

reduce the stiffness of said elements by a factor of $10e-6$. Shigang et al. (Shigang et al., 2014) compare their experimental results to two finite element models – one without the voids and one with the voids. The presence of voids within the composite has reduced the strength of the material, with an apparent reduction in the load-deflection curve. Lastly, the work of Shigang et al. (Shigang, Daining, Rujie, & Yongmao, 2015) studied the effect of voids on the performance of carbon-carbon composites undergoing uniaxial tension. Shigang et al. (Shigang, Daining, et al., 2015) extend their previous work (Shigang et al., 2014) by studying the same model now undergoing uniaxial tension. Once again, a Monte Carlo approach was utilized to randomly select elements and reduce their stiffness by a factor of $10e-6$. Comparing experimental results to two finite element models, one without the voids and one with the voids, Shigang et al. [5] demonstrated the importance of including internal defects for enhanced analysis of composite materials. The uniaxial tension results (Shigang et al. (Shigang, Daining, et al., 2015)) demonstrate the significant variance in the prediction of ultimate stress with and without the presence of voids. The inclusion of voids allowed for more accurate predictions of the mechanical performance, closely resembling the experimental results. Shigang et al. (Shigang, Daining, et al., 2015) also investigate the effect of void location on the mechanical performance of the composite; focusing the voids entirely in the fibers, entirely in the matrix, and entirely in the fiber-matrix interface. Shigang et al. (Shigang, Daining, et al., 2015) demonstrated that the location of voids clearly influenced the mechanical performance. When the voids were concentrated entirely within the fibers, the most significant effect to reduce the mechanical performance was observed. When the voids were concentrated within either the matrix or

the interfaces, the effect was not as significant when compared to the no void scenario. Lastly, Shigang et al. (Shigang, Daining, et al., 2015) investigate the effect of various void volume fractions concentrated entirely in the fibers since this had the most substantial impact on mechanical performance. Shigang et al. (Shigang, Daining, et al., 2015) clearly demonstrated that as void volume fraction increases within the fibers, the mechanical performance is drastically reduced. A reduction of approximately 7% in the tensile strength was observed for a void volume fraction of 0.25% when compared to the same model with no voids – a significant reduction for an insignificant void volume.

While the work of Shigang et al. (Shigang, Daining, et al., 2015; Shigang et al., 2014) have demonstrated the importance of CT scanning to obtain internal defects for enhanced understanding of mechanical performance, there are some critical means of improving the analysis. First, the conversion of two-dimensional area to three-dimensional volume is a rough approximation of the real void volume. The shape of the voids, as well as the position of the voids, throughout the composite, mean that observing just a two-dimensional slice could introduce significant errors. Second, the implementation of a Monte Carlo approach to import these voids randomly throughout the model has its disadvantages. Namely, its implementation may be restricted to advanced users. In addition to the difficulty of developing the model, the random distribution may bias prediction results. Besides, it is impossible to be representative of the experimental distribution. From the CT scans, it is possible that the voids within the composite are concentrated in critical areas and using a Monte Carlo approach could result in significant errors if the random distribution does not focus the voids within the correct location. Also, there may be large clusters of voids which

may have a more dominant effect than the same void volume fraction distributed throughout the entire matrix.

Therefore, a finite element procedure is proposed to alleviate the abovementioned challenges. A Python script is developed and implemented within the framework of commercially available FE software Abaqus, to represent physical microstructural voids features within the models. Computed tomography (CT) scan is utilized to characterize the void content in epoxy samples which were prepared and tested to investigate the effect of voids on the damage process from a microscopic point of view. Also, a strain energy density (SED) based damage subroutine was implemented to enable numerical investigation of microscopic damage process.

3.3 Multiscale Modeling Employing Microstructural Voids

The proposed finite element procedures are outlined in the flowchart presented by **Figure 3.1**. As can be seen, three main stages summarize the modeling procedures. The first stage utilizes computed tomography (CT) scan to investigate voids in plain epoxy resin at the microscale. Processing the CT scan results using Volume Graphics VGStudio MAX 3.0 software enabled identifying the actual microstructural voids physical dimensions and exact locations. A data file Employing these physical quantities is generated with each void radius and the corresponding location.

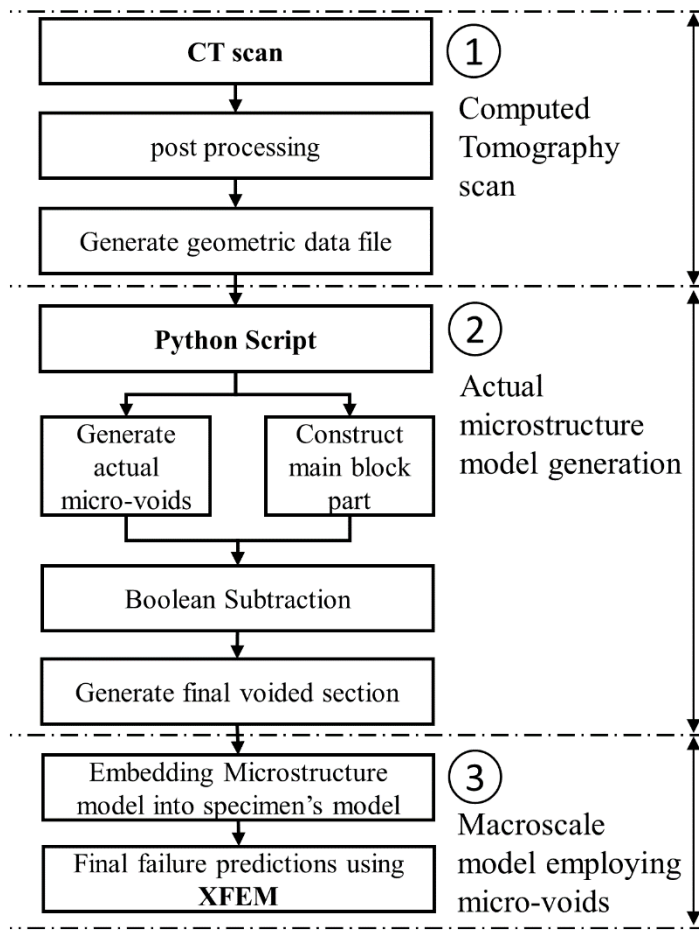


Figure 3.1 Finite element model involving microstructural voids procedure.

In the second stage, a Python script was developed and implemented in Abaqus to automate micromechanical model generation. In which, the physical scanned epoxy specimen is used to generate a slab with microstructural features (i.e., voids). Slab thickness is user-determined based on the region of interest while each void location/size is read from the geometric data file resulting from post-processing the CT scan. The geometries of created voids are subtracted from the main block part, i.e., Boolean subtraction to generate the final voided slab. Finally, in the third stage, a specimen sized model is created employing the actual representation of micromechanical voids represented by the embedded

micromechanical slab. Extended finite element method (XFEM) framework is utilized to investigate the onset of failure from a microscopic point of view. Particulars regarding each stage are thoroughly illustrated in subsections 3.3.1, 3.3.2, and 3.3.3.

3.3.1 Computed Tomography (CT) Scan

Several samples were scanned through computed tomography (CT) to characterize their micro-voids content. Samples were scanned with a Reflection Rotation 225 target head and tungsten target material utilizing the Nikon XT H225 ST system. No filters were used pre/post-scanning. Also, the samples were scanned in a tilted position to reduce the effect of beam hardening. Using Nikon's Inspect X software, 3141 projections were collected with two-frame averaging. The quality of the scanning results was investigated to ensure consistency. To verify the scanning quality, the center of rotation was examined and showed less than one-pixel deviation. After verifying the quality of the scans, the three-dimensional reconstruction was performed utilizing CT Pro 3D (**Figure 3.2a**). In the generation of the three-dimensional reconstruction, noise reduction, scattering reduction, and beam hardening corrections were applied. The reconstructed samples were then analyzed in Volume Graphics VGStudio MAX 3.0 software, allowed for the determination of surfaces using the advanced surface determination tool. The next step was to obtain the void distribution, in which the Otsu (Otsu, 1979) global thresholding method is utilized within VGStudio MAX 3.0. The Otsu (Otsu, 1979) thresholding method derives a single thresholding value such that it segments voids from the parent material. Within VGStudio MAX 3.0, one thresholding value was identified for the epoxy and another for air. Next, the threshold values were applied to the reconstruction to identify voids. Key interest areas

were defined as being areas where the threshold value of air was surrounded by the threshold value for epoxy. These areas were then required to have a fully enclosed area of at least 24 voxels to be classified as voids. The reconstructed sample with pores identified is shown in **Figure 3.2b**.

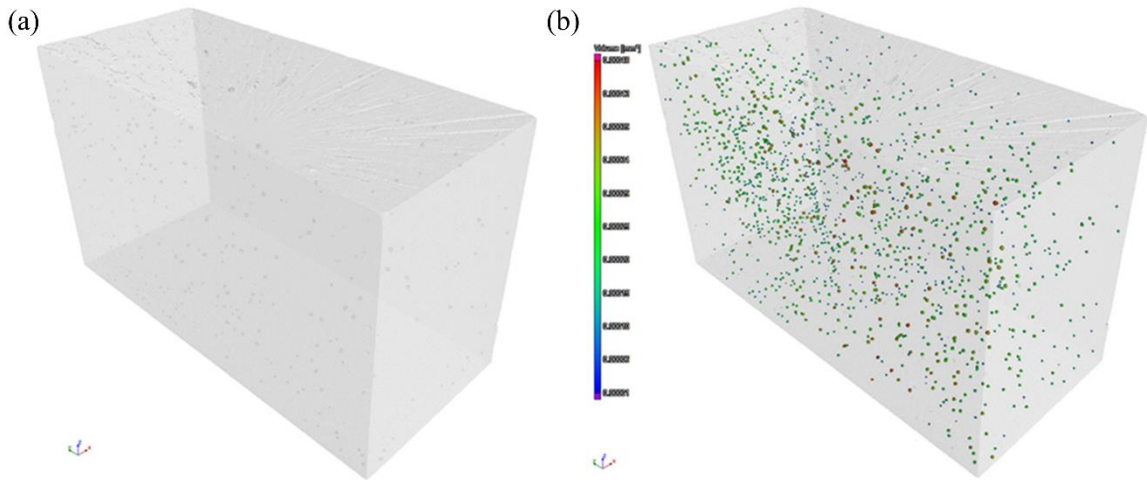


Figure 3.2 Reconstructed Sample, a) without pores identified, b) with pores identified

Of crucial importance was the failure surface as this area of the sample possessed certain qualities which ultimately led to the failure of the sample. Within the reconstructed sample, the failure surface was identified, and a volume of the sample from the failure surface down into the bulk became the region of interest. The entire reconstructed sample was approximately 6 mm x 13 mm x 8 mm with a void volume fraction of 0.051%, whereas the failure surface segment (see **Figure 3.3**) was approximately 6 mm x 13 mm x 0.7 mm with a void volume fraction of 0.044%. As can be observed, damage initiation seems to have an onset coinciding with the largest void. A local plasticity zone bounded was observed in the vicinity of that void as shown by the dashed line on **Figure 3.3**. Finally, several crazes of cracking can be observed signifying an unstable failure of the material, i.e., brittleness dominated.

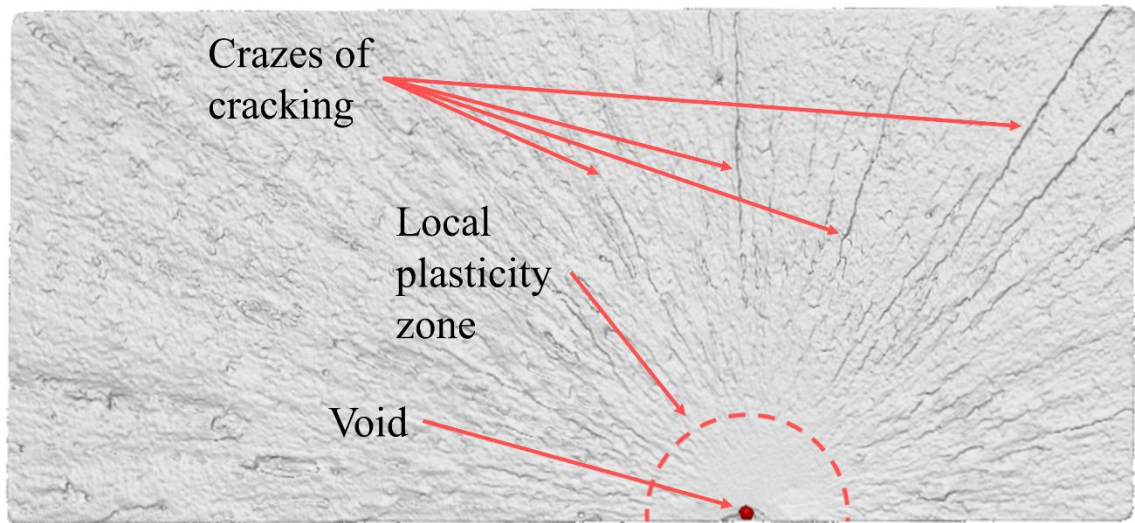


Figure 3.3 Top-view of failure surface showing local plasticity and crazes of cracking.

3.3.2 Actual microstructural model generation

A chief objective of the proposed work is to generate microstructural features (i.e., voids) within the finite element model of plain epoxy. CT technique was employed to scan the prepared epoxy resin to characterize the void content besides physical features (i.e., size/location). For illustration purpose, a schematic diagram for model generation is presented in **Figure 3.4**.

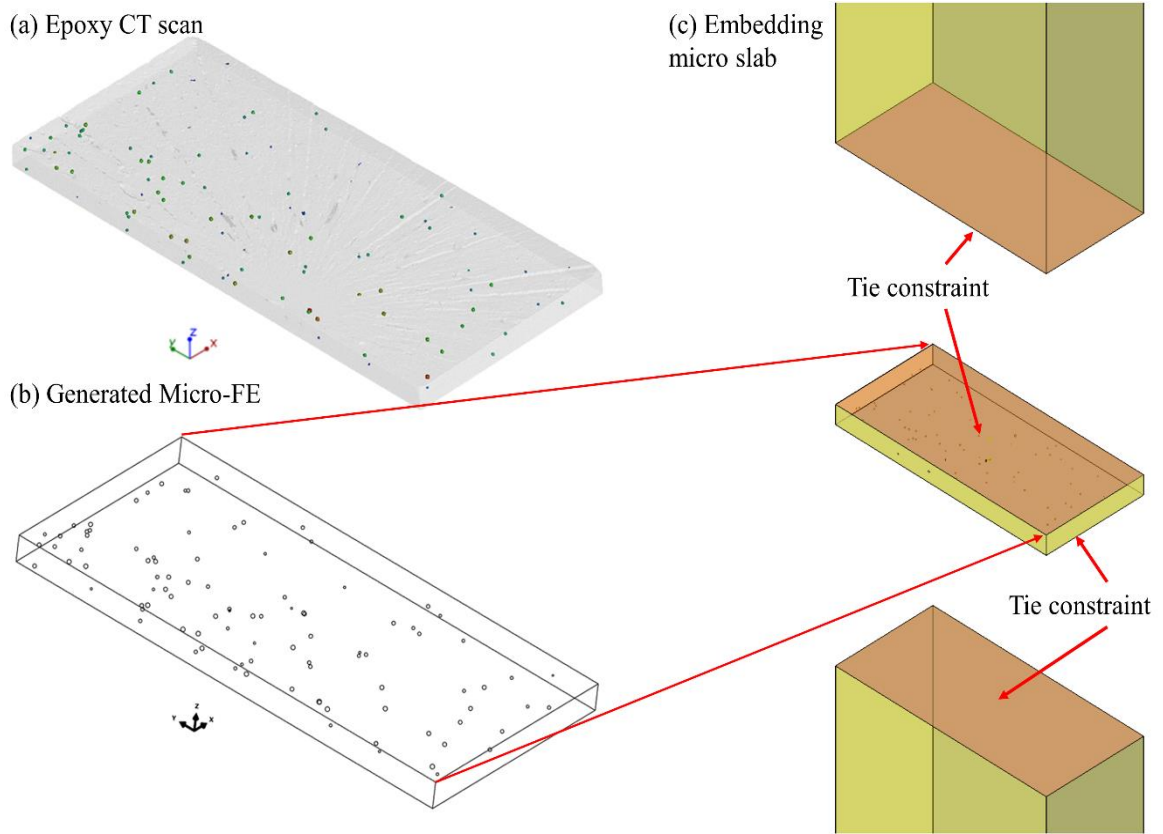


Figure 3.4 Final microstructural slab showing voids at their exact locations.

The CT scan of tested epoxy was used to generate a micromechanical slab of 700 μm thickness and identical cross-section to that of the tested specimen as shown in **Figure 3.4a**. A Python script was developed to automate micromechanical model generation from the CT scan. The algorithm starts by uploading data file entries into a repository file to be used for generating actual micro-voids within the FE model. **Table 3.1** illustrates the structure of the data file resulting from stage 1, where the first column represents an index i , specifying the current void number while the remaining columns are used for physical features. Each void is created as an independent part utilizing its current radius r_i , represented by the second column in **Table 3.1**. The total number of voids n , is determined from the size of the data file.

Table 3.1. Geometric features of physical voids data file resulting from CT scan post-processing.

Index indicating current void i	Actual void radius, r_i (μm)	x-coordinate, x_i (μm)	y-coordinate, y_i (μm)	z-coordinate, z_i (μm)
1	38.0	3970.0	7420.0	250.0
2	43.0	2550.0	9140.0	250.0
...
n	28.0	2380.0	2540.0	1000.0

After creating all voids, a block part is constructed utilizing the same scanned specimen dimensions. All associated voids are repositioned to their exact physical coordinates namely, x_i , y_i and z_i as illustrated in **Table 3.1**. The following step requires a Boolean subtraction operation on the geometry of all parts, in which the void parts are subtracted from the main block part resulting in an equivalent voided part to that of the CT scan as presented in **Figure 3.4b**. As can be observed, the proposed script enabled a precise representation of microstructural voids automatically. Notably, the running time to generate the presented micromechanical model (**Figure 3.4b**) is less than one minute. Manual generation of such model can be deemed unattainable or extensively time consuming.

3.3.3 Specimen model employing micro-voids

The final stage regarding specimen sized model employing micromechanical slab is accomplished by assembling the micromechanical FE slab into the specimen model. Incorporating the micro model into the specimen model should be precisely defined to ensure domain's piecewise continuity. Therefore, top and bottom surfaces of the micromechanical slab, highlighted in orange color (**Figure 3.4c**) are tied to opposing surfaces of the specimen. The corresponding nodes are tied together during simulations to avoid a discontinuity at these surfaces which may bias numerical results. Also, these

constraints enable meshing the macromechanical portion with significantly refined mesh while maintaining moderately coarse mesh for the rest of the specimen. The micromechanical slab final mesh is shown in **Figure 3.5a**, while a zoomed in view, is provided in **Figure 3.5b**, note that both figures were generated with translucency to enable visualizing internal voids.

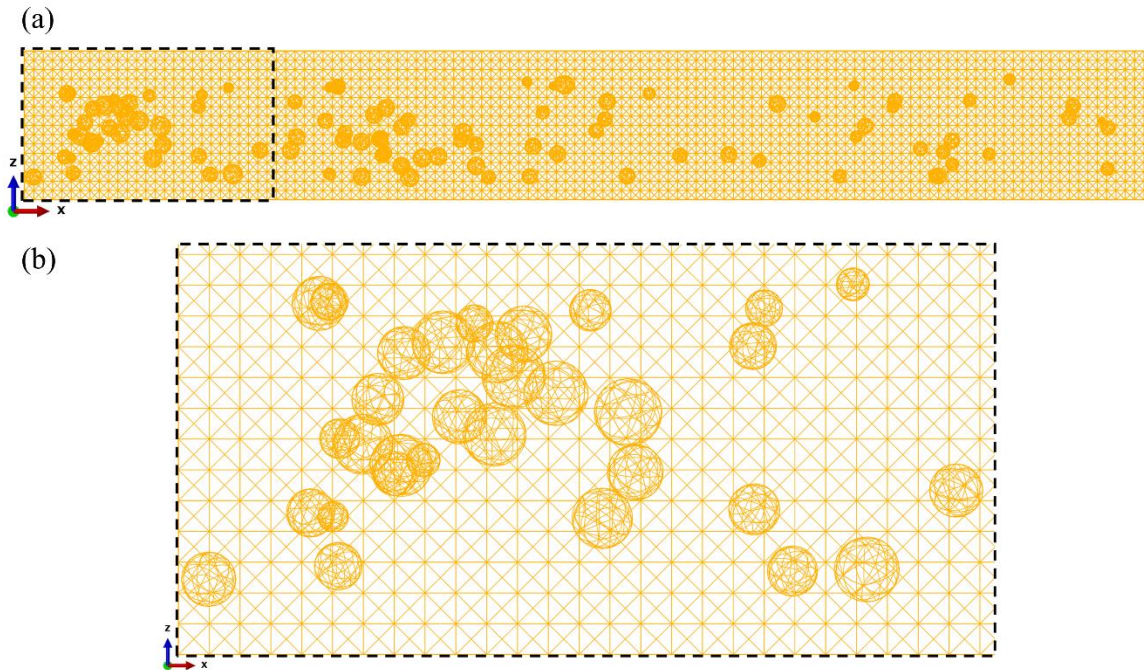


Figure 3.5 (a) Micromechanical slab finite element mesh (b) Zoomed in view.

This meshing technique resulted in a significant enhancement regarding computational efforts. Instead of maintaining a microscopic characteristic length in the mesh, the technique enabled varying the elemental lengths according to the physical features of each region. Accordingly, the resulting final part together with the final convergent mesh are shown in **Figure 3.6a** and **Figure 3.6b**, respectively. The micromechanical portion was meshed using quadratic tetrahedral elements, namely C3D10 while linear hexahedral elements, C3D8R were used to mesh the rest of the domain. The convergent mesh had an

approximate size of 47000 elements with a maximum and minimum characteristic length of hundred μm and seven μm , respectively.

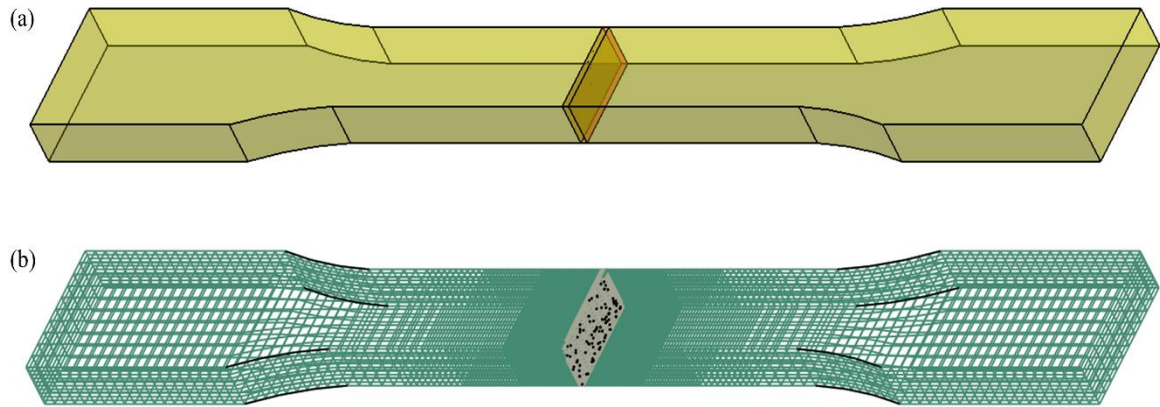


Figure 3.6 Final constructed part (b) Final convergent mesh.

As mentioned earlier, the main objective is modeling the actual microstructural voids in the tested epoxy to investigate the effect of voids on mechanical behavior and failure at microscales. The framework of the extended finite element method (XFEM) in Abaqus is employed for that purpose. XFEM in general works by nodal enrichments utilizing special shape functions to account for discontinuities within an enriched element such as cracks (Ted Belytschko, Gracie, & Ventura, 2009a). In other words, it accounts for crack onset as well as propagation without requiring the FE mesh to conform to the crack front. A damage initiation criterion is defined for crack onset besides an evolution law for propagation (Abdelaziz & Hamouine, 2008). Consider the material behavior of an enriched element as shown in **Figure 3.7**. The hypothetical stress-strain behavior of epoxy material is presented by the solid line in which no damage is defined for the material. In other words, this is typical behavior of conventional elements from a material's point of view. On the other hand, enriched elements are associated with a damage model defining the material

degradation resulting from loading the material beyond the initiation criterion. Upon increasing the load, the material will continue to degrade following the dashed lined path until failure as shown in **Figure 3.7**.

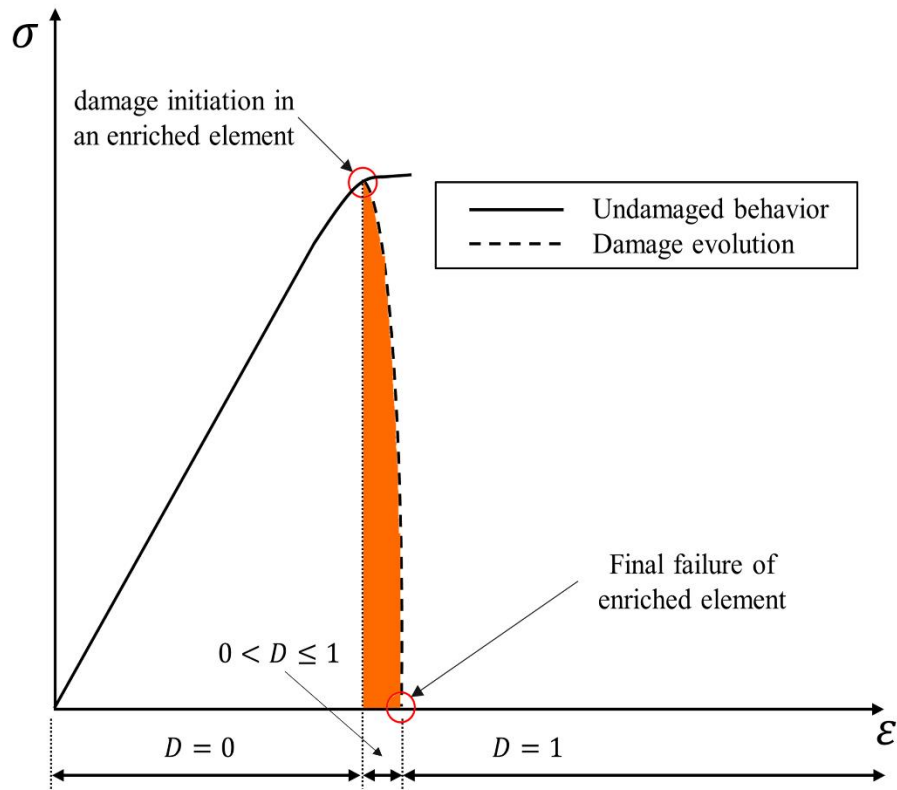


Figure 3.7 Schematic diagram showing damaged and undamaged material behavior of epoxy.

The material failure from a numerical point of view may be defined as the total loss of load-bearing capability as a result of progressive deterioration in the material stiffness. A damage factor, D is useful to express the deterioration process of an enriched element. Three regions are identified on the schematic behavior, namely undamaged, partially damaged and fully damaged. The first region has a zero damage while in the second region (highlighted in orange), the damage factor has a value between zero and unity. Finally, a unity value defines final failure at a material point and complete separation of an enriched

element. During the analysis at any step, the damage stress tensor is evaluated as $\sigma_{ij}^D = (1 - D)\sigma_{ij}$. The implemented damage initiation criteria in Abaqus are either stress or strain based. As can be concluded from the literature (L. E. Asp et al., 1996; Elnekhaily & Talreja, 2018; Huang & Talreja, 2005; Talreja, 2014) besides the current investigation findings, the failure of epoxy is dominated by voids. Therefore, critical strain energy density (SED), $W_{critical}$ was used as the crack initiation mechanism in a user-defined subroutine while the damage evolution was controlled by the fracture energy.

3.3.4 Material model and damage

The material model of epoxy material is defined utilizing the deformation plasticity theory in Abaqus which is based on the Ramberg-Osgood (RO) relationship (Ramberg & Osgood, 1943). The material model for a generalized case of stress state reads as

$$E\boldsymbol{\varepsilon}_{ij} = (1 + \nu)\sigma_{dev} - (1 - 2\nu)\sigma_{hyd}\mathbf{I} + \frac{3}{2}\alpha\left(\frac{\sigma_{mises}}{\sigma_y}\right)^{n-1}\sigma_{dev} \quad (\text{Eq.3.1})$$

where E is the young's modulus, ν is the Poisson's ratio, σ_y is yield stress while α is the yield offset and n is the hardening exponent for the non-linear term, i.e., $n \geq 1$. $\boldsymbol{\varepsilon}_{ij}$ and $\boldsymbol{\sigma}_{ij}$ define the strain and the stress tensors, respectively. \mathbf{I} is the identity matrix, σ_{dev} is the stress deviator tensor while σ_{hyd} is the equivalent hydrostatic stress and σ_{mises} defines the Mises flow stress. (Eq.3.2) to (Eq.3.4) define the stress invariants.

$$\sigma_{hyd} = -\frac{1}{3}\boldsymbol{\sigma}_{ij}:\mathbf{I} \quad (\text{Eq.3.2})$$

$$\sigma_{dev} = \boldsymbol{\sigma}_{ij} + \sigma_{hyd}\mathbf{I} \quad (\text{Eq.3.3})$$

$$\sigma_{mises} = \sqrt{\frac{3}{2}\boldsymbol{\sigma}_{dev}:\boldsymbol{\sigma}_{dev}} \quad (\text{Eq.3.4})$$

The model is assumed to be compressible in the linear region and incompressible in the non-linear one where the plastic flow is normal to Mises stress (*Abaqus V6.14–Documentation, Dassault Systèmes Simulia Corporation, 2013*). **(Eq.3.1)** is reduced to a uniaxial state of stress to identify the material parameters of the plasticity model, reading as

$$E\varepsilon = \sigma_i + \alpha\sigma_i \left(\frac{\sigma_i}{\sigma_y} \right)^{n-1} \quad \text{(Eq.3.5)}$$

where σ_i represents the stress component along the i^{th} direction. The above relationship is nonlinear at all stress values where the non-linearity becomes significant at stress values approaching/exceeding σ_y . In the current work, a user-defined damage subroutine is developed and implemented to predict the final failure of epoxy resin. In which, the damage factor, D is controlled based on critical strain energy density (SED). Assuming small deformations (i.e., less than 10%), the SED for the material model defined by **(Eq.3.5)** can be obtained as

$$W = \int_0^{\sigma_f} \sigma_{ij} d\varepsilon_{ij} = \frac{(1 + \nu)(\sigma_{mises})^2}{3E} + \frac{3(1 - 2\nu)(\sigma_{hyd})^2}{2E} + \frac{n\alpha(\sigma_{mises})^{n+1}}{E(n + 1)(\sigma_y)^{n-1}} \quad \text{(Eq.3.6)}$$

The expression enables evaluating SED for a general state of stress at enriched elements. Noteworthy to mention that SED is invariant under rotation of coordinates (Jones, 1999; Jones, 2009; Shames, 1997). Therefore, damage initiation condition in the developed subroutine reads

$$f = \frac{\langle W \rangle}{W_c} \quad \text{(Eq.3.7)}$$

where $f = 1$ signifies the onset of damage within an enriched element. The Macaulay brackets $\langle \cdot \rangle$ signifies that pure compressive state of stress does not initiate damage. $W_{critical}$ represents the critical value of SED which can be evaluated from the area under the load-displacement curve of a uniaxial tension test (Jones, 1999, 2009; Shames, 1997). SED expressed by (Eq.3.6) can be rewritten for a uniaxial state of stress after some manipulation as

$$W_c = \frac{\sigma_f^2}{E} \left(\frac{\alpha n}{n+1} + \frac{1}{2} \right) \quad (\text{Eq.3.8})$$

where σ_f is the failure stress and E is the elasticity modulus. The hardening exponent n and the yield offset α can be obtained from the stress-strain curve of uniaxial tensile test. The determined material parameters for the tested epoxy resin are documented in **Table 3.2**.

Table 3.2. Epoxy resin material model parameters.

Property	E (GPa)	ν	n	α	σ_y (MPa)	W_c (MPa)
Epoxy	3.11	0.36	9.87	0.20	58.12	0.62

3.4 Results and Discussion

In the current section, finite element simulation results are provided and discussed. For better visualization, the mesh gridlines were removed from all the following figures. A uniform continuous stress distribution can be observed from the full-size model contour plot regarding von Mises stress as shown in **Figure 3.8a**, which can be attributed to proper constraints application between different scales (see **Figure 3.4c**) as explained in subsection 3.3.3. A closer view on a cutout section showing micro-voids is presented in **Figure 3.8b** where the micro-voids can be barely observed due to their infinitesimal sizes. The top view of the cut-out at different load increments provides a better illustration of

stress distribution as depicted in **Figure 3.8c**. Stress concentrations in the vicinity of voids were observed to build up as the load increased. Also, voids with larger radii were more likely to have intense stress concentrations. This observation was consistent from the current CT investigation to actual failure surfaces from dog-bone specimens showed that cracks were originating from relatively larger voids.

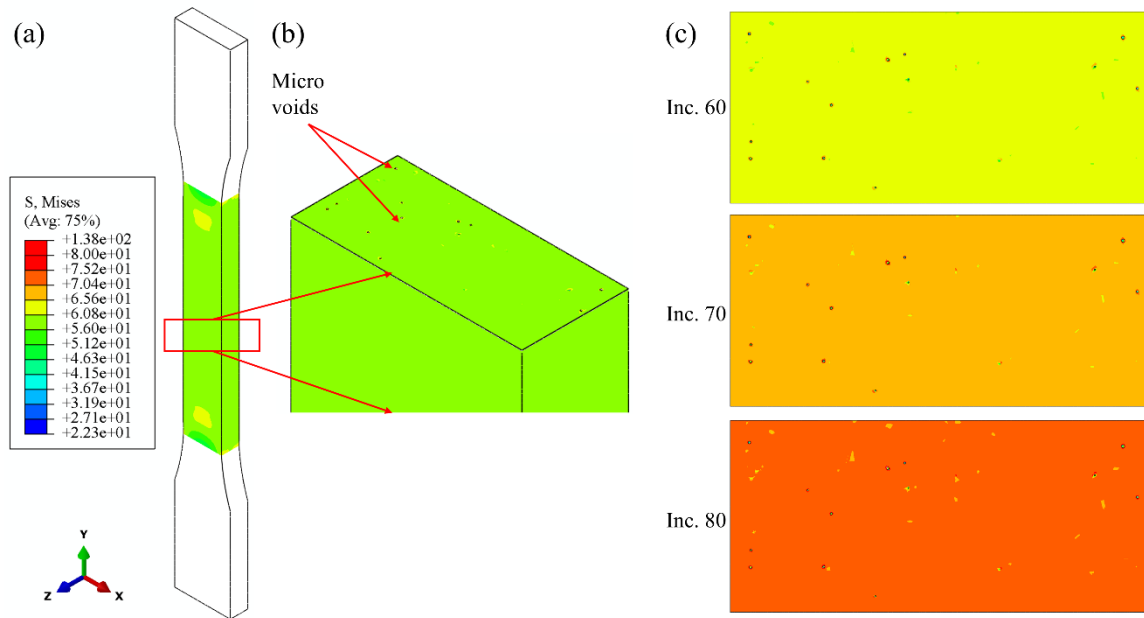


Figure 3.8 von Mises stress contour plot: (a) complete specimen (b) Cut-out at micro-voids zoomed in view (c) top view of micro-slice at different load increments.

Figure 3.9 provides the contour plot of equivalent plastic strains for the complete specimen (**Figure 3.9a**) besides the top view of another cutout section (**Figure 3.9b**) with different voids distribution. In general, the material exhibited global plastic deformation in as can be observed from the specimen's narrow section contour plot. Even though brittleness dominated the fracture behavior of plain epoxy, there exists minor plastic deformation ahead of failure (see **Figure 3.3**). Voids at microscale lengths can be significant regarding stress concentration leading to micro-cavitation and possible initiation of cracks.

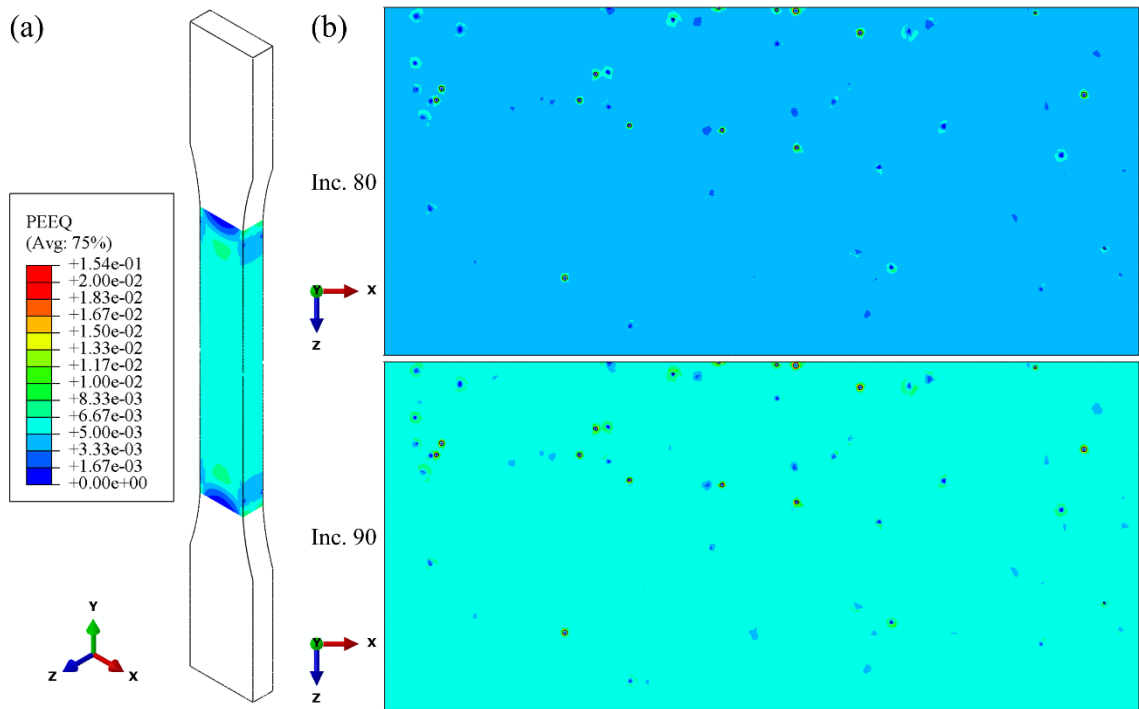


Figure 3.9 Equivalent plastic strain contour plot: (a) complete specimen (b) top view of micro-slice at different load increments.

Regarding failure and damage initiation at a microscopic scale, micro-cracks initiated in the vicinity of the largest void. The cracked surfaces were found to be normal to the load application direction which implies that brittleness dominated the failure behavior. These observations are consistent with findings from the current study as revealed by the CT scan of fractured specimens. Also, as reported in the literature (L. E. Asp et al., 1996; Bressers, 2002), micro-cavitation was found to initiate and possibly lead to larger cracks in plain epoxy resin. A cut-out section passing through the most significant void is depicted in Figure 3.10 to illustrate the microscopic damage process. As can be observed, the first damage incident occurred at load increment 93 where the color of the highlighted region signifies the intensity of damage as per the provided legend. Upon increasing the loads, more damaged elements could be observed as shown by the frames at load increments 95

and 97, respectively. Load increment 98 shows that three elements located just outside the spheroidal void had most severe damage. Damage originated from the most significant void, and the propagation at microscale shows the potential direction towards the bulk edges. This observation is also consistent with observations from testing where the cracks or crazes seemed to have an origin coinciding with the largest spheroidal void origin.

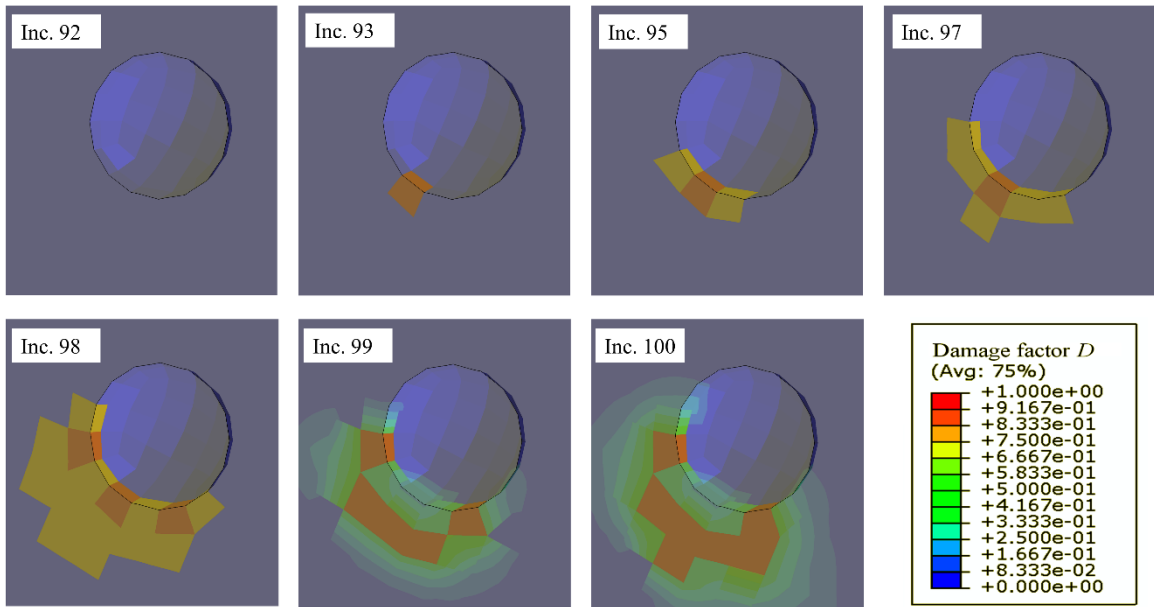


Figure 3.10 The vicinity of a micro-void showing element damage status at different load increments.

3.5 Conclusions

In the current work, the microstructure of plain epoxy resin was investigated utilizing computed tomography (CT) scan. An approximate total volumetric void content of 0.05% was identified from different samples. A Python script was developed to incorporate physical microstructures features (i.e., micro-voids) in a multiscale domain finite element model. Strain energy density (SED) damage criterion was implemented to enable

microscopic damage modeling in Abaqus. From the provided study the following can be concluded;

- The CT scan investigations enabled quantifying physical microstructural features such as voids regarding their actual size/location.
- The CT scan of the failed specimen revealed that crazes of cracking were originating from the largest void in the fractured surface.
- Developed Python script enabled incorporating real microstructural features (i.e., voids) in a multiscale finite element model automatically without user intervention.
- The automatic generation of the micromechanical model (as shown in **Figure 3.4b**) required less than one-minute runtime.
- The proposed algorithm is capable of generating the real microstructural features rather than an estimate or a representative model as in the case of Monte Carlo based simulations (Shigang, Daining, et al., 2015; Shigang, Rujie, et al., 2015; Shigang et al., 2014). Notably, this facilitates the precise model building for enhanced analyses.
- Incorporating strain energy density (SED) to control the microstructural damage process within the frame of XFEM enabled a closer investigation on the damage mechanism at a microscale.

Numerical results were consistent with observations from testing showing that microstructural voids were dominating the onset of material damage.

3.6 References

- Abaqus V6.14– Documentation, Dassault Systèmes Simulia Corporation. (2013). Providence, Rhode Island.
- Abdelaziz, Y., & Hamouine, A. (2008). A survey of the extended finite element. *Computers and Structures*, 86(11–12), 1141–1151. <https://doi.org/10.1016/j.compstruc.2007.11.001>
- Arumugam, V., Saravanakumar, K., & Santulli, C. (2018). Damage characterization of stiffened glass-epoxy laminates under tensile loading with acoustic emission monitoring. *Composites Part B: Engineering*, 147(April), 22–32. <https://doi.org/10.1016/j.compositesb.2018.04.031>
- Asp, L. E., Berglund, L. A., & Talreja, R. (1996). A criterion for crack initiation in glassy polymers subjected to a composite-like stress state. *Composites Science and Technology*, 56(11), 1291–1301. [https://doi.org/10.1016/S0266-3538\(96\)00090-5](https://doi.org/10.1016/S0266-3538(96)00090-5)
- Belytschko, T., Gracie, R., & Ventura, G. (2009). A review of extended/generalized finite element methods for material modeling. *Modelling and Simulation in Materials Science and Engineering*, 17(4). <https://doi.org/10.1088/0965-0393/17/4/043001>
- Bressers, O. F. J. T. (2002). Craze initiation in glassy polymer systems. Technische Universiteit Eindhoven.
- Chevalier, J., Morelle, X. P., Camanho, P. P., Lani, F., & Pardoën, T. (2018). On a unique fracture micromechanism for highly cross-linked epoxy resins. *Journal of the Mechanics and Physics of Solids*, 122, 502–519. <https://doi.org/10.1016/J.JMPS.2018.09.028>
- Daniel, I. M., Luo, J. J., Schubel, P. M., & Werner, B. T. (2009). Interfiber/interlaminar failure of composites under multi-axial states of stress. *Composites Science and Technology*, 69(6), 764–771. <https://doi.org/10.1016/j.compscitech.2008.04.016>
- Di Landro, L., Montalto, A., Bettini, P., Guerra, S., Montagnoli, F., & Rigamonti, M. (2017). Detection of voids in carbon/epoxy laminates and their influence on mechanical properties. *Polymers and Polymer Composites*.
- Elnekhaily, S. A., & Talreja, R. (2018). Damage initiation in unidirectional fiber composites with different degrees of nonuniform fiber distribution. *Composites Science and Technology*, 155. <https://doi.org/10.1016/j.compscitech.2017.11.017>
- Giddings, P. F., Bowen, C. R., Salo, A. I. T., Kim, H. A., & Ive, A. (2010). Bistable composite laminates: Effects of laminate composition on cured shape and response to thermal load. *Composite Structures*, 92(9), 2220–2225. <https://doi.org/10.1016/j.compstruct.2009.08.043>
- Huang, H., & Talreja, R. (2005). Effects of void geometry on elastic properties of unidirectional fiber reinforced composites. *Composites Science and Technology*, 65(13), 1964–1981. <https://doi.org/10.1016/j.compscitech.2005.02.019>

- Isaac, M. D., & Ori, I. (2013). *Engineering Mechanics of composite materials*. Oxford University Press, 2, 1–403. <https://doi.org/5fad72a8bc5942d089cc71406c6287da>
- Jones, R. M. (1999). *Mechanics of composite materials*. *Mechanics of Composite Materials*, p. 519. <https://doi.org/10.1007/BF00611782>
- Jones, R. M. (2009). *Deformation theory of plasticity*. Bull Ridge Corporation.
- Koerber, H., Kuhn, P., Ploeckl, M., Otero, F., Gerbaud, P. W., Rolfes, R., & Camanho, P. P. (2018). Experimental characterization and constitutive modeling of the non-linear stress–strain behavior of unidirectional carbon–epoxy under high strain rate loading. *Advanced Modeling and Simulation in Engineering Sciences*. <https://doi.org/10.1186/s40323-018-0111-x>
- Leung, C. K. Y., & Hou, D. (2015). Numerical Simulation of Chloride Diffusion in Reinforced Concrete Structures With Cracks. *Journal of Materials in Civil Engineering*, 27(3), 1–11. [https://doi.org/10.1061/\(ASCE\)MT.1943-5533.0001057](https://doi.org/10.1061/(ASCE)MT.1943-5533.0001057).
- Liebig, W. V., Leopold, C., & Schulte, K. (2013). Photoelastic study of stresses in the vicinity of a unique void in a fibre-reinforced model composite under compression. *Composites Science and Technology*, 84, 72–77. <https://doi.org/10.1016/j.compscitech.2013.04.011>
- Otsu, N. (1979). A Threshold Selection Method from Gray-Level Histograms. *IEEE Transactions on Systems, Man, and Cybernetics*, C(1), 62–66. <https://doi.org/10.1109/TSMC.1979.4310076>
- P.K. Mallick. (2007). *Fiber-Reinforced Composites: Materials, Manufacturing, and Design*. In CRC Press.
- Park, S. Y., Choi, W. J., & Choi, H. S. (2010). The effects of void contents on the long-term hygrothermal behaviors of glass/epoxy and GLARE laminates. *Composite Structures*, 92(1), 18–24. <https://doi.org/10.1016/j.compstruct.2009.06.006>
- Ramberg, W., & Osgood, W. R. (1943). Description of stress-strain curves by three parameters. In National Advisory Committee for Aeronautics. <https://doi.org/10.1016/j.matdes.2009.07.011>
- Schell, J. S. U., Renggli, M., van Lenthe, G. H., Müller, R., & Ermanni, P. (2006). Micro-computed tomography determination of glass fibre reinforced polymer meso-structure. *Composites Science and Technology*, 66(13), 2016–2022. <https://doi.org/10.1016/j.compscitech.2006.01.003>
- Shames, I. H. (1997). *Elastic and inelastic stress analysis*. CRC Press.
- Sharma, R., Deshpande, V. V., Bhagat, A. R., Mahajan, P., & Mittal, R. K. (2013). X-ray tomographical observations of cracks and voids in 3D carbon/carbon composites. *Carbon*, 60, 335–345. <https://doi.org/10.1016/j.carbon.2013.04.046>
- Shigang, A., Daining, F., Rujie, H., & Yongmao, P. (2015). Effect of manufacturing defects on mechanical properties and failure features of 3D orthogonal woven C/C composites. *Composites Part B: Engineering*, 71, 113–121.

- <https://doi.org/10.1016/j.compositesb.2014.11.003>
- Shigang, A., Rujie, H., & Yongmao, P. (2015). A Numerical Study on the Thermal Conductivity of 3D Woven C/C Composites at High Temperature. *Applied Composite Materials*, 22(6), 823–835. <https://doi.org/10.1007/s10443-015-9438-3>
- Shigang, A., Xiaolei, Z., Yiqi, M., Yongmao, P., & Daining, F. (2014). Finite Element Modeling of 3D Orthogonal Woven C/C Composite Based on Micro-Computed Tomography Experiment. *Applied Composite Materials*, 21(4), 603–614. <https://doi.org/10.1007/s10443-013-9353-4>
- Spaggiari, A., & O’Dowd, N. (2012). The influence of void morphology and loading conditions on deformation and failure of porous polymers: A combined finite-element and analysis of variance study. *Computational Materials Science*, 64, 41–46. <https://doi.org/10.1016/j.commatsci.2011.12.022>
- Su, Z. C., Tay, T. E., Ridha, M., & Chen, B. Y. (2015). Progressive damage modeling of open-hole composite laminates under compression. *Composite Structures*, 122, 507–517. <https://doi.org/10.1016/j.compstruct.2014.12.022>
- Talreja, R. (2014). Assessment of the fundamentals of failure theories for composite materials. *Composites Science and Technology*, 105, 190–201. <https://doi.org/10.1016/j.compscitech.2014.10.014>
- Uygunoglu, T. K. U., Gunes, I. K. U., & Brostov, W. of N. T. (2015). physical and Mechanical properties of polymer comppsite with high content. *Materials Research*, 18(6), 1188–1196. <https://doi.org/10.1590/1516-1439.009815>
- Yang, Y., Liu, X., Wang, Y. Q., Gao, H., Li, R., & Bao, Y. (2017). A progressive damage model for predicting damage evolution of laminated composites subjected to three-point bending. *Composites Science and Technology*, 151, 85–93. <https://doi.org/10.1016/j.compscitech.2017.08.009>

4 Strain Energy Density Based Damage Initiation in Heavily Cross-linked Epoxy Using XFEM

4.1 Abstract

This article proposes a damage initiation criterion based on the total strain energy density (SED) for glassy polymers such as epoxy resins. The proposed damage initiation model was developed and implemented in a user-defined subroutine in the finite element code Abaqus using extended finite element method (XFEM). Numerical results were verified with uniaxial and three-point bending tests. To accurately assess predictions, a high precision digital image correlation (DIC) system was utilized for precise strain measurements. Also, synchronized image processing was used for efficient identification of yielding whenever it occurred. Furthermore, a microscopic investigation of fractured surfaces using optical microscopy was conducted. Micro-cavitation were consistently observed in all failed specimens identifying that brittle behavior dominated the final fracture. Comparisons with built-in damage models in Abaqus concluded enhanced and conservative predictions of the currently developed and implemented model.

4.2 Introduction

Fiber-reinforced polymer (FRP) composites are widely used in aerospace, marine and automotive engineering industries (P.K. Mallick, 2007). Wide application spectrum of FRP motivated intensive investigations of their failure modes. Generally, there are four damage failure modes in FRP composites, namely matrix cracking, fiber breakage, interfacial debonding and ply delamination (P.K. Mallick, 2007). In particular, matrix cracking and ply delamination are typical modes leading to final failure of laminated composites (Lachaud et al., 2015; Pawar & Ganguli, 2006; Pollay & Yu, 2014). These typical modes

are deleteriously affected by manufacturing defects in resin materials such as voids and resin rich regions (Hagstrand et al., 2005; Jeong & Pan, 1995; Kalantari et al., 2017). Void content is considered as a property reducing agent besides acting as stress concentrators (Bressers, 2002; W. V. Liebig et al., 2013; Uygunoglu et al., 2015; Yamini & Young, 1980). Epoxy resins most commonly used for both the structural matrix and the stacking adhesive materials (Aho, Nerg, & Pyrhönen, 2007; Pawar & Ganguli, 2006; Pollayi & Yu, 2014; Zhenqing Wang et al., 2013). These resins consist of a densely cross-linked polymer that, after curing, forms three-dimensional polymeric networks of covalent bonds. The strong covalent bonds result in a thermo-mechanically stable polymer with favorable environmental resisting properties. However, cured epoxy exhibit low strain-to-failure capacity due to the brittleness of the thermosetting polymer (Pawar & Ganguli, 2006; Pollayi & Yu, 2014; Zhenqing Wang et al., 2013). This particular behavior dominates the overall strain-to-failure capacity of the FRP composite leading to the brittle type of failure. Therefore, all these considerations underlined the importance as well as posing the need for developing efficient damage prediction tools for epoxy resins.

In the meantime, recent advances in computational methods resulted in reliable techniques focused on damage initiation and propagation. The eXtended Finite Element Method (XFEM) initially proposed by Belytschko and Black (T. Belytschko & Black, 1999) based on the partition of unity theory (Melenk & Babuška, 1996) to solve crack problems eliminated the necessity to update the mesh. Therefore, XFEM became a well-established method studying fracture mechanics problems to account for crack onset as well as propagation (Abdelaziz & Hamouine, 2008; Ted Belytschko et al., 2009a; H. Li, Li, &

Yuan, 2018; J. H. Song, Wang, & Belytschko, 2008; Sukumar, Dolbow, & Moës, 2015; van Dongen, van Oostrum, & Zarouchas, 2018; Yazid, Abdelkader, & Abdelmadjid, 2009). In other words, XFEM lends itself the superiority over conventional FEM when analyzing failure and damage problems. Consequently, the method became available in the mainstream finite element analysis codes such as Abaqus (*Abaqus Documentation*, 2014) and LS-DYNA (LS-DYNA, 2013). As a result, researchers employed XFEM to study composite structures failure investigating its predictions accuracy. For example, Petrov et al. (Petrov, Gorbatikh, & Lomov, 2018) presented a parametric study for assessing the performance of XFEM applied to cross-ply composite laminates cracking. XFEM results were in a good agreement following the testing results trend reported by Yokozeki et al. (Yokozeki, Iwahori, & Ishiwata, 2007). However, the XFEM predictions overestimated the number of cracks as well as corresponding strains and stresses (Petrov et al., 2018). Also, Duarte et al. (Duarte et al., 2017) provided a comparative study between numerical outcomes of XFEM-implementation and Hashin's damage criterion implementation in Abaqus applied to the failure of composite plates. They concluded that while XFEM had the advantage of showing the crack onset, opening and propagation; numerically predicted failure loads were overestimated. They concluded that further investigation is required since stress-based criteria in XFEM implementation led to what they referred to as "stiffer post-cracked behavior" (Duarte et al., 2017). This highlights the importance of accurate damage initiation criteria. Therefore, XFEM presents the potential of an efficient framework for failure analysis of composites given an accurate failure model or criterion is implemented within to surmount over-prediction of failure conditions.

Several stress/strain-based failure models have been proposed for failure prediction in resins material (Elnekhaily & Talreja, 2018; Talreja, 2014). For instance, Asp et al. (L. E. Asp et al., 1996) investigated the crack initiation in three epoxy systems and proposed a failure criterion based on the dilatational Strain Energy Density (SED). The uniaxial testing results obtained from this study showed good agreement with the benchmark failure envelopes proposed by Bauwens (Bauwens, 1970) and Raghava et al. (Raghava, Caddell, & Yeh, 1973). On the other hand, the results of three-point bending tests yielded a contradicted level of agreement. Another study conducted by Knauss (Knauss, 2012) indicated the importance of the dilatational component of strain energy when dealing with polymers under a uniaxial state of stress. However, the matrix material in a composite is subject to a complex state of stresses (Leif E. Asp, Berglund, & Gudmundson, 1995). Hence, further investigations are required to enhance the prediction accuracy of currently existing failure criteria of resin materials.

Despite the numerical complexity in predicting failure of brittle materials such as epoxy, especially under a combined state of stress, developing improved damage models is increasingly needed as they can provide reliable tools for early design stages. In this research, an improved damage initiation criterion is proposed to predict failure in brittle materials, particularly in epoxy. The proposed damage model was derived accounting for both dilatational and distortional energy densities. Within the framework of XFEM, the total SED criterion is implemented in a user-defined damage initiation subroutine (UDMGINI) using FORTRAN. Comparisons were held between the proposed damage model and available XFEM built-in damage models in Abaqus. For validation of all

numerical predictions, neat epoxy resin specimens were prepared and tested under uniaxial and three-point bending. Accurate strain measurements were obtained for all tested specimens using a high-precision Digital Image Correlation (DIC) system. Also, plastic behavior was efficiently captured using synchronized video processing together with testing measurements from DIC. Furthermore, failure mechanisms were examined using optical microscopic imaging.

4.3 Theoretical background

The scope of the current work utilizes the framework of XFEM; hence a brief overview of the method is provided. A general three-dimensional elasticity problem as shown in **Figure 4.1** is considered. The domain Ω is bounded by the boundary Γ which composes of three sets, namely, Γ_u , Γ_t and Γ_c such that $\Gamma = \Gamma_u \cup \Gamma_t \cup \Gamma_c$. The displacements are imposed on Γ_u , while tractions are imposed on Γ_t .

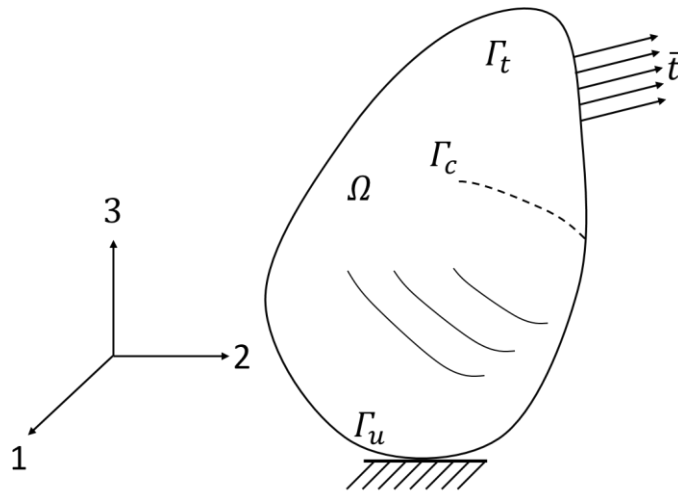


Figure 4.1 Three-dimensional linear elastic cracked body problem

The equilibrium equations and the constitutive relationships are given by (Eq.4.1) The crack surface represented by Γ_c is assumed to be traction-free.

$$\nabla \cdot \sigma = 0 \quad \sigma = \mathbf{C} : \varepsilon \quad \text{in } \Omega \quad (\text{Eq.4.1})$$

where ∇ is the gradient operator, σ is the Cauchy stress tensor, and \mathbf{C} is Hooke's tensor and ε is the strain tensor. The prescribed tractions are given by

$$\sigma \cdot \mathbf{n} = \bar{\mathbf{t}} \quad \text{on } \Gamma_t \quad (\text{Eq.4.2})$$

where \mathbf{n} is the outward unit normal vector to Γ_t . Consequently, for traction free crack surface $\sigma \cdot \mathbf{n} = 0$. Under the assumptions of small strains and displacements, the kinematic equations read

$$\varepsilon = \frac{1}{2}(\nabla \mathbf{u} + \nabla^T \mathbf{u}) \equiv \varepsilon(\mathbf{u}) \quad \text{on } \Omega \quad (\text{Eq.4.3})$$

where ε is the linearized strains and \mathbf{u} is the displacement field. (Eq.4.1) and (Eq.4.2) along with the boundary conditions represent the strong form of the governing equations. In order to transform strong formulation of the problem into a weak form which is better suited for finite element computations (Moës & Belytschko, 2002), the displacement \mathbf{u} must belong to a set of kinematically admissible displacement fields (T. Belytschko & Black, 1999; Melenk & Babuška, 1996; Pommier, Gravouil, & Combescure, 2013). The weak formulation for solving equilibrium equations is given by (Eq.4.4) which is solved using the Galerkin's method. The Galerkin's formulation is the one followed in mainstream FE software.

$$\int_{\Omega} \sigma(\mathbf{u}^h) : \varepsilon(\mathbf{v}^h) d\Omega = \int_{\Gamma_t} \bar{\mathbf{t}} \cdot (\mathbf{v}^h) d\Gamma \quad (\text{Eq.4.4})$$

The XFEM works by enriching the domain of conventional FE mesh with special shape functions to account for the strong discontinuities in the displacement field (e.g., cracked surface) as well as the crack tip singularity. The general shape functions of XFEM takes the following form

$$u^h(x) = \sum_{i \in I} u_i N_i + \sum_{j \in J} b_j N_j H(x) + \sum_{k \in K} N_k \left[\sum_{l=1}^4 c_k^l F_l(x) \right] \quad (\text{Eq.4.5})$$

where u^h is the global displacement, N_i are the shape functions and u_i are the degrees of freedom at node i . $H(x)$ is the Heaviside function or jump function to represent discontinuity across the crack surface, N_j are the shape functions related to the discontinuity at node j , while b_j are the additional degrees of freedom associated to the jump function. $F_l(x)$ are the crack-tip enrichment functions, N_k are the shape functions related to the crack-tip at node k and c_k^l are the additional degrees of freedom related to the elastic asymptotic crack-tip enrichment functions.

The implemented XFEM-based cohesive behavior in Abaqus adopts a damage mechanism that allows for crack onset as well as propagation at any material point in the domain Ω . A cracked surface Γ_c is introduced in an enriched element using the stress-strain state defined by (Eq.3.1) and (Eq.3.3). The damage process consists of two stages, namely, crack initiation and damage evolution. The crack initiation points to the cohesive response onset of degradation at an enriched element, while the damage evolution stage represents the material behavior after a crack is being initiated. In this stage, the material degradation in an enriched element is allowed using a bilinear-traction separation law as shown in **Figure**

4.2. T and δ represent the cohesive traction and the separation displacement, respectively. The material degradation is introduced to the material stiffness through a scalar damage factor D , where an undamaged material corresponds to a zero value while completely damaged material corresponds to a unity value. The damage evolution can be based on displacement at failure or fracture energy.

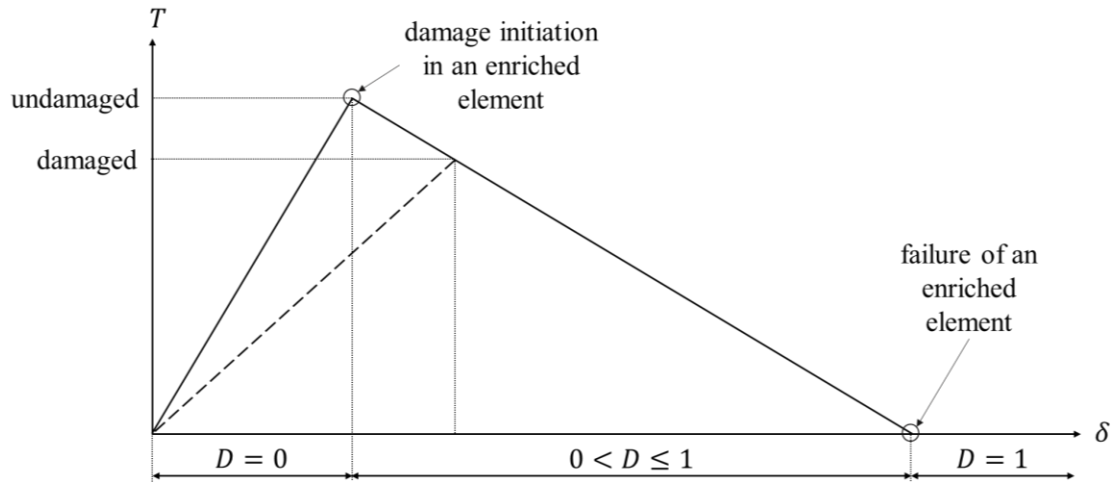


Figure 4.2 Traction-separation law: Damage initiation and evolution.

Based on literature findings (Abdelaziz & Hamouine, 2008; Fries & Belytschko, 2010; H. Li et al., 2018; Yazid et al., 2009), XFEM in its current implementation is well suited for crack propagation problems. Hence, damage evolution is not the scope of the current work. On the other hand, failure predictions were overestimated using built-in damage initiation mechanisms. Built-in damage initiation mechanisms are either stress or strain based which may capture the behavior of one aspect at the expense of the other. Therefore, the commonly used damage initiation mechanisms are briefly overviewed. Crack initiation begins when a specific failure criterion f is encountered. The damage initiation is said to begin when f is equal to unity. The failure criterion defining function is either stress or strain based. For convenience, the damage initiation mechanisms are illustrated in terms of

stresses while strains follow the same context. **Table 4.1** summarizes the three main damage initiation mechanisms and their defining equations, the standard Abaqus notation is followed.

Table 4.1 Commonly used damage initiation mechanisms in Abaqus.

Damage initiation	Symbol	Defining equation	nominal values
Maximum principal stress (MAXPS)	$\sigma_{p_{max}}$	$f = \left\{ \frac{\langle \sigma_{max} \rangle}{\sigma_{max}^o} \right\}$	σ_{max}^o
Maximum nominal stress (MAXS)	t	$f = \max \left\{ \frac{\langle t_n \rangle}{t_n^o}, \frac{t_s}{t_s^o}, \frac{t_t}{t_t^o} \right\}$	t_n^o, t_s^o, t_t^o
Quadratic nominal stress (QUADS)	t	$f = \left\{ \frac{\langle t_n \rangle}{t_n^o} \right\}^2 + \left\{ \frac{t_s}{t_s^o} \right\}^2 + \left\{ \frac{t_t}{t_t^o} \right\}^2$	t_n^o, t_s^o, t_t^o

First, the maximum principal stress (MAXPS) which requires one principal value to initiate damage, namely, principal stress nominal value σ_{max}^o . The symbol $\langle \rangle$ represents the Macaulay bracket which signifies that purely compressive state of stress does not initiate damage. The associated stress/strain values are calculated at each material point and compared to their nominal values denoted by the omicron superscript symbol. The nominal values are the ones required to be determined from material characterization and testing. Second, the maximum nominal stress (MAXS) which works by evaluating nominal traction stress vector t components. In general, three-dimensional problems, t has three components; a normal component to the crack surface and two shear components t_n and t_t . Finally, the nominal quadratic stress (QUADS) which is based on the calculation of a quadratic interaction function involving nominal stress ratios as shown in **Table 4.1**. This occurs only when the summation of the quadratic ratios in the defining function is equal to

unity. As concluded from references (Duarte et al., 2017; Petrov et al., 2018), stress/strain based damage initiation criteria lead to overestimated failure predictions. Hence, a user-defined damage initiation mechanism is proposed based on the strain energy density (SED) coupled with the built-in fracture energy damage evolution of Abaqus. The proposed SED damage mechanism details together with the implementation are explained in subsection 4.4. The detailed analysis and comparisons with testing results are presented in subsection 4.7.

4.4 Proposed SED Based Damage Initiation Criterion

Further clarification on strain energy-based failure criteria is emphasized to substantiate the proposed approach. The maximum distortional strain-energy theory which is the basis of von Mises failure criterion states that the failure by yielding under a combination of stresses occurs when the energy of distortion equals or exceeds the energy of distortion resulting from the uniaxial state of stress when the yield strength is reached (Hencky, 1924; Knauss, 2012; Ukadgaonker & Awasare, 1995; von Mises, 1913). The von Mises criterion is widely used to predict failure in ductile materials. The distortional strain energy density U_d in terms of Cauchy's stress tensor σ_{ij} and the modulus of rigidity G reads as

$$U_d = \frac{1}{4G} (\sigma_{ij}\sigma_{ij} - \frac{1}{3} [tr(\sigma_{ij})]^2) \quad \text{(Eq.4.6)}$$

On the other hand, in heavily cross-linked epoxy systems (N.B., brittle materials), they are characterized by low strain-to-failure capacity. The yielding is suppressed while brittle fracture caused by crack growth from cavitation occurs (L. E. Asp et al., 1996; Leif E. Asp et al., 1995; Elnekhaily & Talreja, 2018; Talreja, 2014). The distortional energy at a

material point for such material is minimal while the hydrostatic effect given by the dilatational energy is dominant. The hydrostatic tension could trigger the critical condition of the micro-cavitation formation (L. E. Asp et al., 1996; Elnekhaily & Talreja, 2018; Talreja, 2014). Once a cavity is introduced into the material it is more likely to initiate a crack orthogonal to maximum tensile principal stress causing brittle failure (L. E. Asp et al., 1996). Hence, a failure criterion for glassy polymers based on the dilatational energy density has been assessed as a yield failure criterion accounting for hydrostatic stress effect on deviatoric stress to yielding. **Asp et al.** (L. E. Asp et al., 1996) proposed a failure criterion **utilizing the** critical value for dilatational SED assuming the material to behave linearly elastic and the distortional energy density at a material point to be negligible, which is acceptable for brittle materials. The criterion reads as follows

$$U_h = \frac{1 - 2\nu}{6E} [tr(\sigma_{ij})]^2 = U_h^{crit} \quad (\text{Eq.4.7})$$

where U_h is the dilatational SED, σ_{ij} is the stress tensor and U_h^{crit} is the corresponding critical value at which failure occurs. Their criterion has proven to be in good agreement with testing measurements. It can be anticipated that failure can be dominated by either distortional or dilatational SED components depending on the material type. However, both strain energy components should be considered. For example, in the case of brittle materials such as heavily cross-linked epoxies; the failure would occur at low strains (less than ~2%). This type of failure is said to be brittle where the volumetric distortion is finite and is assumed to be negligible while in fact, it should be considered.

In the current work, a damage initiation mechanism is proposed and implemented in a user-defined subroutine in Abaqus based on the total SED, Sih (Sih, 1991) reading as follows

$$U_c = \left. \frac{dW}{dV} \right|_{crit} = \int_0^{\varepsilon_c} \sigma d\varepsilon \quad (\text{Eq.4.8})$$

where $\left. \frac{dW}{dV} \right|_{crit}$ represents the critical value of SED, ε is the uniaxial strain and σ is the corresponding stress. The fracture strain is denoted by ε_c . The material toughness is defined as the strain energy absorbed by a material to introduce fracture. It is also considered as a material property independent of the axes orientation which is necessary to develop a failure criterion. In this method, the failure criterion is accounting for both contributions, the distortional as well as that of the hydrostatic. Assuming linear isotropy, the total SED reads

$$\left. \frac{dW}{dV} \right|_c = U_d + U_h = \frac{1}{2} \sigma_{ij} \left(\frac{\sigma_{ij}}{2\mu} - \frac{\lambda \delta_{ij} \sigma_{kk}}{2\mu + 3\lambda} \right) \quad (\text{Eq.4.9})$$

where $\lambda = \frac{E\nu}{(1+\nu)(1-2\nu)}$ represents Lamé's first parameter, δ_{ij} is the Kronecker delta, $\mu = \frac{E}{2(1+\nu)}$ is the modulus of rigidity and σ_{kk} denotes the normal stress components. Both constants, λ and μ , can be calculated upon the determination of the elastic modulus and the Poisson's ratio. The determination of the stress components may be quite difficult for a complex state of stress. Therefore, one can deal with a uniaxial load case to determine the critical value causing failure. This is possible due to the fact that the total critical SED is defined in terms of the first and second invariants of stress tensor along with two material independent parameters (Timoshenko & J. N. Goodier, 2010). Consequently, it can be

utilized as a material property. Unlike most of the available failure criteria which requires the determination of four material constants at least. The critical value of the proposed criterion is determined using the two material constants and the failure stress under uniaxial loading. It is noteworthy of mentioning, that these constants represent the minimum number of characterizing a material.

To this end, a user-defined damage initiation subroutine (UDMGINI) is implemented in Abaqus to incorporate a damage mechanism based on total critical SED as a crack initiation criterion together with the fracture energy to control damage evolution. The standard Abaqus notation is followed throughout the current section. The UDMGINI subroutine procedure is presented in **Algorithm 4.1**. The procedure is repeated for every enriched element throughout the FE mesh. First, the material mechanical properties are defined using material properties 'call function'. Namely, the elastic modulus E , the Poisson's ratio ν , and the critical value of SED, $\left. \frac{dW}{dV} \right|_c$. Second, is the matrices initialization step, in which two arrays are defined and zeroed. The first array is the principal stresses array while the second is the direction cosines array. Afterwards, the material constants from **(Eq.4.9)**, λ and μ , are evaluated and the utility subroutine SPRIND is then used to calculate the principal stresses and their corresponding directions based on the loading conditions of the current load step. The calculated values are assigned to the designated arrays. The maximum principal stress is then identified using a while-loop. The next step is the evaluation of the current value of total SED based on the stresses corresponding to the current load step. The condition for damage initiation is checked by comparing the total SED to the critical value set for crack initiation. Finally, a while-loop is used to assign the crack direction to be

normal to the maximum principal stress reached which is consistent with the testing results as will be shown later.

Algorithm 4.1 Damage Initiation Subroutine (UDMGINI)

Input: E, ν, U_c

Initialize: Initialize matrices → Set matrices dimensions

1: PS(3) → PS: Principal Stress, an: direction
 an(3,3) cosines
 PS(1) = ZERO

2: PS(2) = ZERO → Zeroing Principal stress vector
 PS(3) = ZERO

3: Evaluate: $\lambda = \frac{E\nu}{(1+\nu)(1-2\nu)}$ → Material Constants
 $\mu = \frac{E}{2(1+\nu)}$

4: Call SPRIND → Calculate principal values and directions

5: Assign calculated principal values to Sig1, Sig2, Sig3 variables

6: **while** K1 = 3, ndi → Check max value

7: **if** PS(K1) > Sig1

8: Sig1 = PS(K1)

9: Kmax = K1

10: **endif**

11: **end while**

12: Sig_max = Sig1 → Assign current max. principal stress

13: Compute: U_c → Using (Eq.4.9)

14: **if** ($U_c/Props(1)$) > 1 → Check if the failure criterion is met

15: **while** K1 = 1, ndi

16: Fnormal(K1,1) = an(Kmax, K1) → Assign crack direction

17: **end while**

18: **return**

19: **end**

For validation, two three-dimensional FE models were used to assessing the proposed damage initiation criterion. The two models are simulating uniaxial and three-point bending tests, respectively, to test the proposed damage mechanism under different types of loading.

The following section illustrates the FE modeling aspects.

4.5 Finite Element Modeling

Three-dimensional FE models were considered to assess further stress and strain-based damage initiation mechanisms as well as the proposed total SED damage mechanism. The first model is considering a uniaxial loading state of stress while the second is considering a combined state of stress that is of a prism under three-point bending. FE model geometries for tensile and bending specimens are based on the test samples prepared according to (ASTM D638-14, 2014) and (ASTM-D790-17, 2017), respectively. Schematic diagrams showing both test setups and loading conditions are provided in **Figure 4.3**. The arrows on the schematic diagrams indicate the applied displacement direction in each model. For the uniaxial loading model, the specimen was fixed at the lower end and displacement was applied to the top end. The two tabs of the specimens were constrained as rigid bodies. As for the prism under three-point bending, three rollers were defined to be rigid bodies. The bottom rollers were fixed in all directions while the top one was limited to move along the vertical direction only. The friction coefficient defining the contact property between the prism and rollers was taken 0.1 as recommended by the Abaqus manual (*Abaqus Documentation*, 2014). A general static analysis step was selected to perform the simulations in both models with automatic incrementation. The initial increment size was set to 0.1 with a minimum increment size of 1E-30.

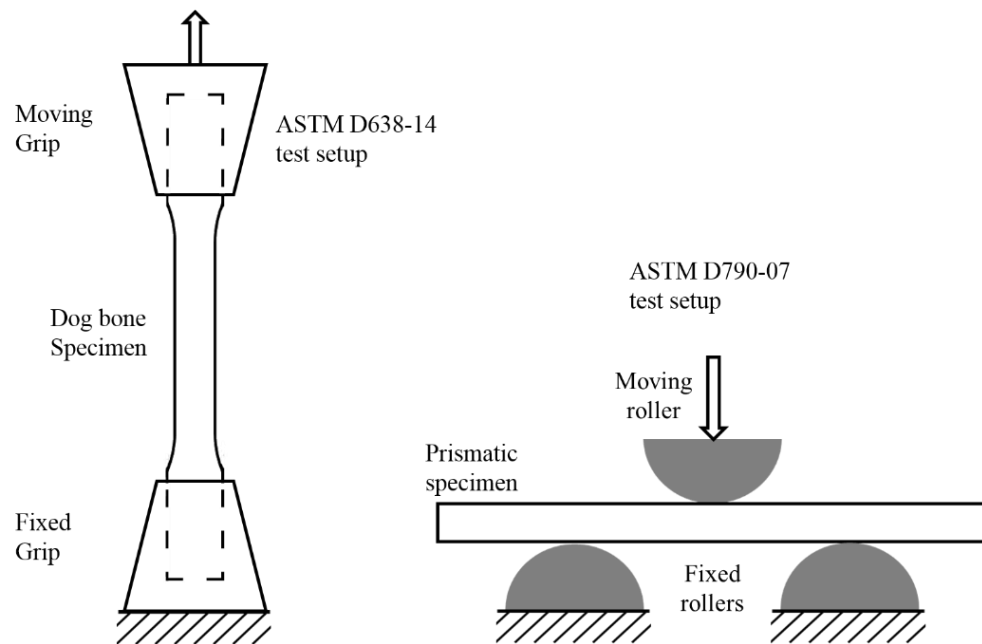


Figure 4.3 Tension test and three-point bending test schematic diagrams

The material linear behavior was defined by the elastic modulus E and the Poisson's ratio ν . The material module in Abaqus defines the plastic behavior using inelastic strains and their corresponding stresses. A solid homogeneous section was selected in both models with 8-noded linear three-dimensional brick elements, namely (C3D8R). The element uses reduced integration with hourglass control for optimizing computational efficiency with acceptable predictions accuracy. Based on displacements and stress convergence studies the sufficient mesh size was determined to be 4720 and 3275 elements for uniaxial and three point bending cases, respectively.

Analyses were performed with the intention to assess built-in failure mechanisms (section 4.3) together with the proposed SED mechanism compared to testing. In order to delineate the effect of damage initiation mechanisms on predictions results solely, the damage

evolution was controlled using fracture energy in all simulations to ensure a frame of reference for comparisons.

4.6 Material and Mechanical Testing

The epoxy material was obtained as neat resin epoxy plate from Polynt Composites Canada, Inc. The epoxy resin type was LamPoxy61 with a LamCat61 hardener. Both the resin and the hardener were mixed by a composition weight ratio of 6:1. The physical properties of the mixture are listed in **Table 4.2** as provided by the manufacturer.

Table 4.2. Polynt LAMPOXY61 physical properties at 25 °C

Lamination Epoxy properties	Resin material EPO-LAMPOXY 61	Hardener material EPO-LAMCAT 61
Viscosity (mPs)	1200-1400	25-50
Density (g/ml)	1.09-1.12	0.96-0.98
Weight (%)	85.72	14.28
Shelf life (days)	90	
Pot life (mins)	15-25	
Tack free (mins)	200-300	

In order to minimize surface flaws, the plate was milled down to the desired thickness of each test specimen. The profile geometries of the dog-bone and the prismatic specimens are shown in **Figure 2.4**. A set of six specimens was machined to the designated dimensions recommended by each ASTM standard. All the specimens were prepared from the same plate to ensure consistency of the tested material.

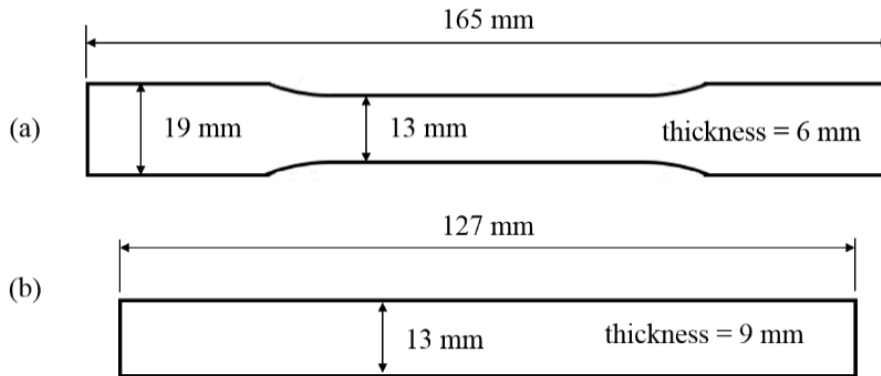


Figure 4.4 (a) Dog-bone specimen profile. (b) Prism specimen profile.

Assuring a high precision measurement method is indispensable dealing with a brittle material (i.e., low strain-to-failure) such as heavily cross-linked epoxy. Specimens were tested in an Instron E10000 load-frame employing an advanced video extensometer system for strain measurements. The system utilizes high precision non-contacting digital image correlation (DIC) displacement measurement with a resolution of 0.5 ± 0.01 microns. Furthermore, the full-field strain measurements were synchronized with video recordings to identify the onset of yielding as will be elaborated in the following section. The dog-bone specimens we marked with sets of two circles along the longitudinal and lateral directions, respectively. These markings were used by the video extensometer to measure strains in both directions as shown in **Figure 4.5a**. The correlation between the deformations along the two orthogonal directions results in the determination of Poisson's ratio. As for the prisms under three-point bending, the specimens were marked with a circle at the prism's center that is correlated to a fixed reference mark as shown in **Figure 4.5b**.

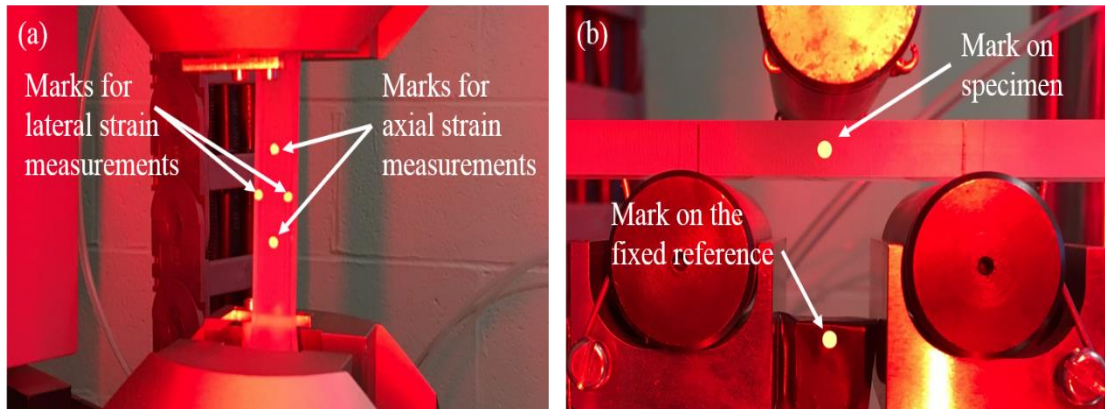


Figure 4.5 (a) Uniaxial test setup. (b) Three-point bending setup.

In the following section, results from testing are compared to those of FE modeling using conventional damage initiation mechanisms (subsection 4.3) and using the proposed user-defined damage initiation subroutine (subsection 4.4) based on total SED.

4.7 Results and Comparisons

4.7.1 Material Characterization

A set of six specimens were used for characterization of the heavily cross-linked plain epoxy. The tested material had a linear elastic behavior up to approximately 2.1% strain followed by nonlinear plastic deformation and sudden failure at approximately 2.4% strain. All fractured surfaces were normal to the load application direction (i.e., brittle failure). The testing results were averaged and used as material input parameters in FE models. The material averaged properties read as follows; the modulus of elasticity $E = 3.31$ GPa, the Poisson's ratio $\nu = 0.36$ and the fracture energy $G_f = 1.99$ N.m. The fracture energy was evaluated from area under load-displacement curves (D5045-99, 2013). Identifying the yield point of the highly cross-linked epoxy material is quite problematic due to low strain-to-failure capacity. To overcome this challenge, the entire loading procedures were video

recorded synchronically with the video extensometer testing measurements. The video data were analyzed by means of image processing to identify the yield point using the stress-whitening caused by plasticity. In other words, the first timeframe showing discoloration was considered as the onset of plastic deformation. Different images of the monochromic video at specific timeframes are portrayed in **Figure 4.6**. A gradual plastic deformation can be observed on the specimen going from one timeframe to another. The discoloration or the stress-whitening can be easily correlated to the onset of plastic deformation (yield point). The specimen started to undergo plastic deformation at the time frame of 225 sec. Synchronizing the test measurements with first timeframe image showing the stress whitening the yield point was efficiently indentified.

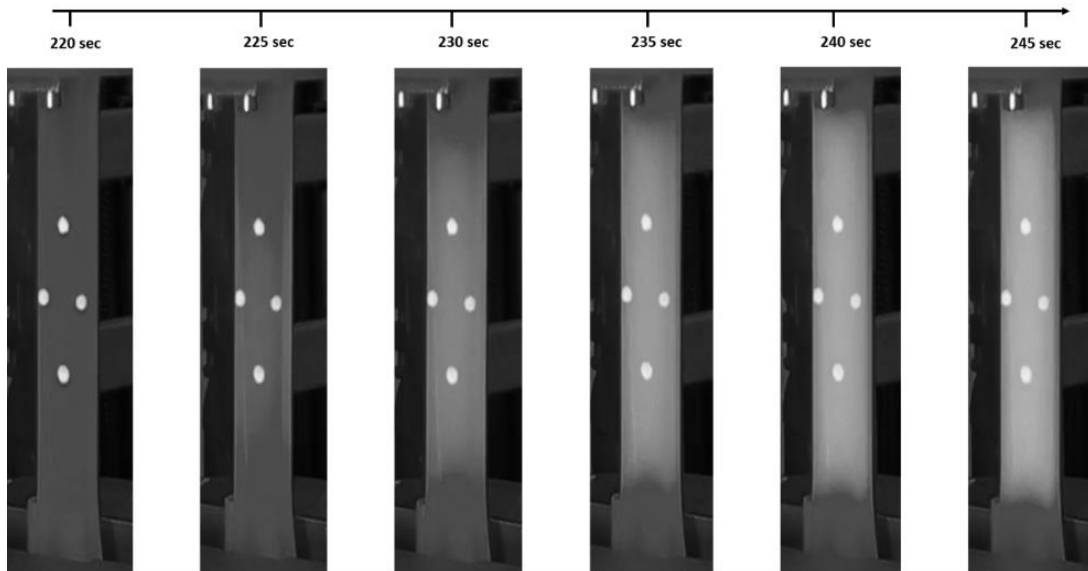


Figure 4.6 Discoloration caused by plasticity at different time frames for uniaxial testing

The following subsections are devoted for comparisons of testing measurements against FE predictions. The built-in damage initiation criteria together with the proposed total SED damage initiation mechanism were further assessed in the current work. Also, a fracture

surface investigation on failed specimens compared to FE predictions is provided. Finally, a closer investigation on the fractured surface is conducted using microscopic imaging is provided in following subsections.

4.7.2 Uniaxial loading

The epoxy dog-bone specimens were prepared for testing under tension according to ASTM D638-14. The specimens were fixed from both ends as shown in **Figure 4.5a**. Considering the brittleness of the heavily cross-linked epoxy the loading rate was set to 0.1 mm/min which is the minimum rate recommended by the testing standard. The distances between markings are based on the gauge lengths provided in the testing standard. Namely, 25 mm for markings along the longitudinal direction and 12 mm along the lateral direction. The local displacement between the markings was measured using the advanced video extensometer for axial strains while the lateral markings were used to measure lateral strains for Poisson's ratio evaluation. The axial load-displacement results are presented in **Figure 4.7**. As can be observed, the load-displacement curves hold a linear relation to approximately 90% of the failure load. The maximum and the minimum failure displacements had the values of 0.706 mm and 0.551 mm, respectively. Correspondingly, the peak of failure loads was 4734 N while the lowest was 4546 N.

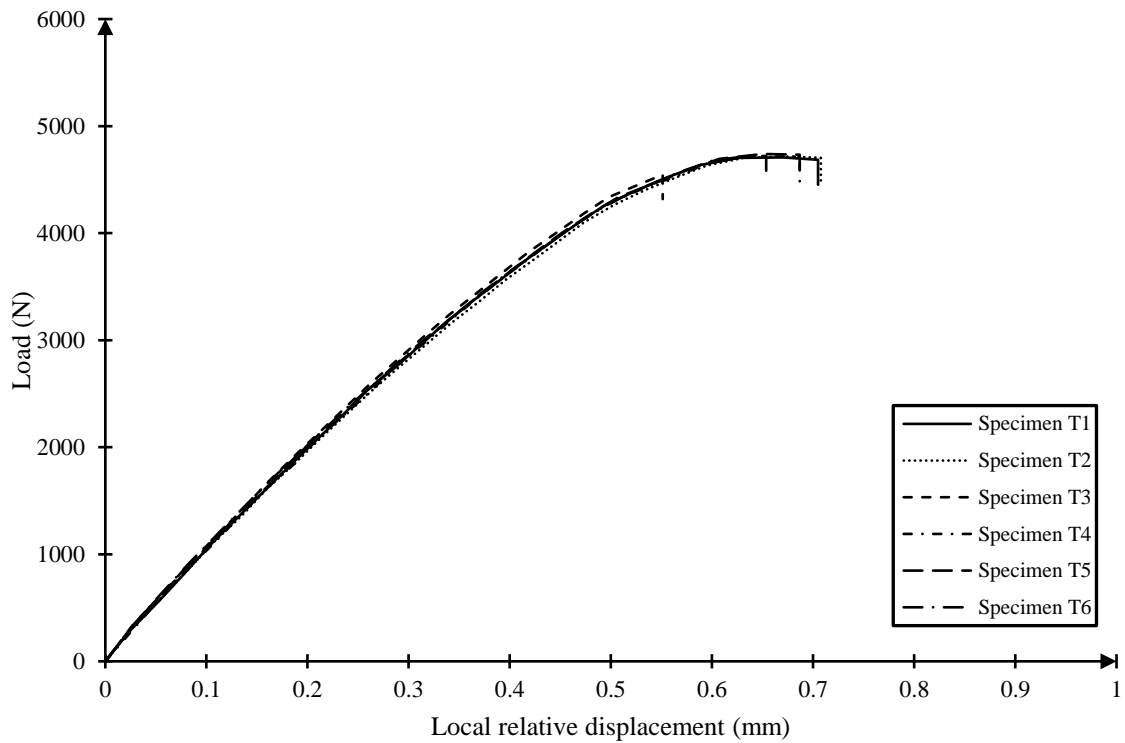


Figure 4.7 Load vs. relative displacement from video extensometer (uniaxial tension)

It can be noticed that the behavior of different specimens in the linear region is almost identical. Also, the plastic behavior of each specimen is following the same trend. All specimens had an unstable brittle failure with fractured surfaces normal to the load application direction. Observed failure loads had slight variations within approximately 5% while failure displacements had significant variations of approximately 20%. **Table 4.3** presents the mechanical failure properties, namely failure loads, tensile stresses and failure displacements.

Table 4.3. Failure limits for uniaxial tensile specimens

Specimen number	Failure Load (N)	Tensile stress (MPa)	Failure displacement (mm)
T1	4686	59.71	0.704
T2	4703	60.22	0.708
T3	4546	57.87	0.551

T4	4716	60.35	0.687
T5	4734	60.41	0.686
T6	4720	60.46	0.654

The FE predictions using currently available damage initiation criteria together with the proposed SED damage mechanism were compared against the averaged testing results from the uniaxial test. The comparison results in terms predicted load-displacement curves are presented in **Figure 4.8**. The average testing results are shown with markers while FE built-in damage mechanisms predictions are presented with different types of black lines. Finally, predictions using the proposed SED damage mechanism are presented using a dashed red line.

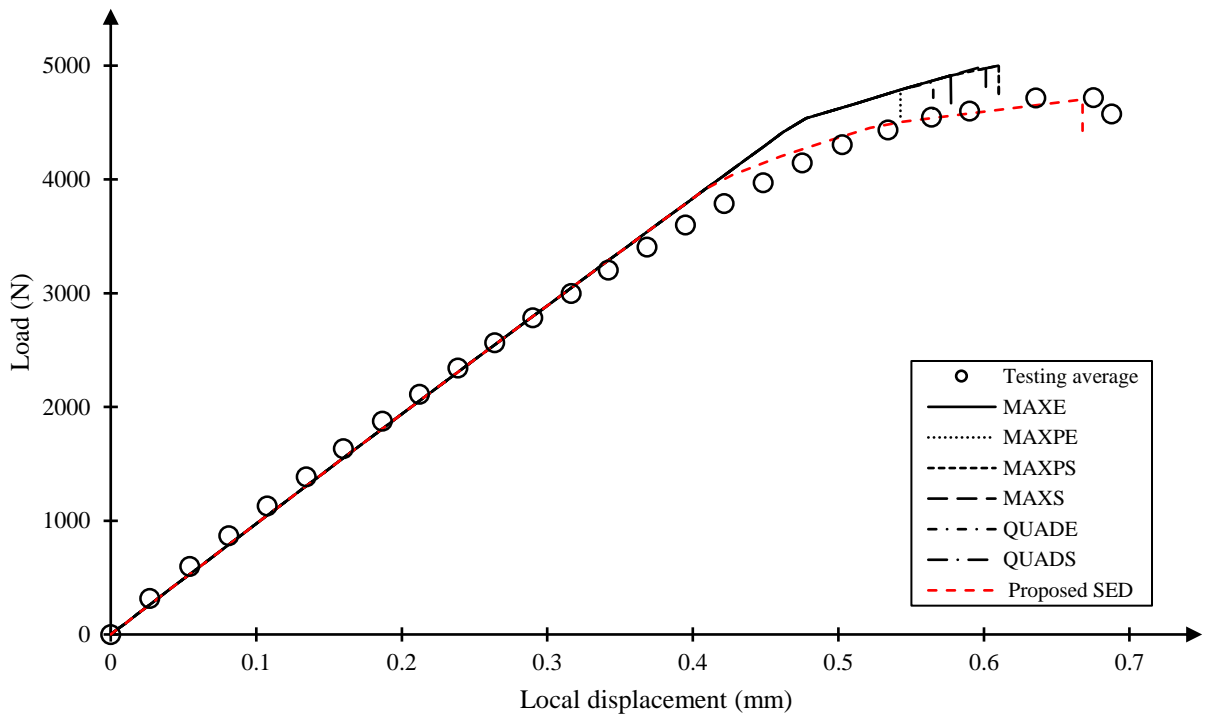


Figure 4.8. Load vs. relative displacement FE predictions compared to testing results

Currently, available damage initiation mechanisms showed an overestimation of failure loads while the failure displacements were underpredicted. The proposed SED damage

mechanism predicted both failure load and displacement with minimal error. A quantitative comparison between all failure mechanisms compared to the average testing data is documented in **Table 4.4**. The highest predicted failure loads were recorded by MAXPS and QUADS with 6% error from the testing data. The proposed SED damage mechanism slightly underpredicted the failure load with -0.4% error. Regarding failure displacements, all damage mechanisms underestimated the failure displacements. The maximum error, approximately -20%, was recorded by the MAXPE damage mechanism while the lowest, -1.5%, was recorded by the proposed SED damage mechanism.

Table 4.4. FE predictions (uniaxial): Failure loads, displacements and percentage error.

Damage Initiation Mechanism	Failure		Failure	
	Load (N)	Error %	displacement (mm)	Error %
MAXE	4914	4.1	0.565	-16.7
MAXPE	4788	1.5	0.543	-19.9
MAXPS	5000	6.0	0.610	-10.0
MAXS	4857	2.9	0.601	-11.4
QUADE	4950	4.9	0.577	-14.9
QUADS	5000	6.0	0.612	-9.7
Proposed SED	4702	-0.4	0.668	-1.5

Different damage initiation models were also compared by inspecting their associated failure surfaces together with the von Mises contour plots. Both stress-based damage initiation models, namely, MAXS and MAXPS showed fractured surfaces that are more like a cup and cone as depicted in **Figure 4.9a** and **Figure 4.9c** which was in contradiction with testing observations. The strain-based damage initiation models, namely, MAXE and MAXPE showed three parallel cracked surfaces normal to the load application direction as shown in **Figure 4.9b** while in fact, there is only one failure surface. The proposed SED

damage initiation model introduced in the current work showed a single fracture surface orthogonal to the load application direction as shown in **Figure 4.9d**. The proposed mechanism predicted a realistic failure surface matching experimental observation. As can be observed from **Figure 4.9**, there is a small variation in the von-Mises value for using each mechanism. The most conservative one is the SED mechanism, while the least conservative ones are MAXPS and QUADS. The proposed SED mechanism efficiently captured the residual stresses in the vicinity of the fractured surfaces while other built-in damage mechanisms failed to account for the same behavior.

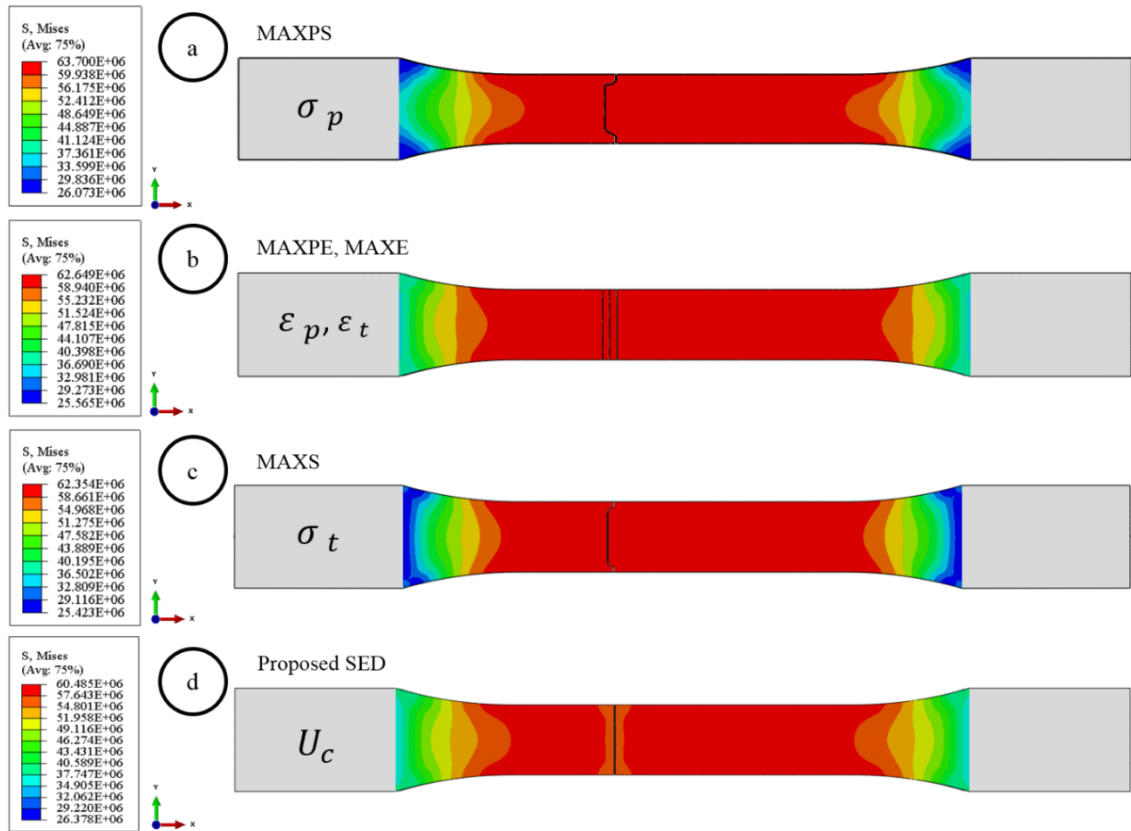


Figure 4.9 Failure surfaces profiles (a, b, and c) built-in mechanisms (d) the proposed SED mechanism.

The plastic deformations in specimens were efficiently captured using simple image processing. A monochromatic image of specimen number 4 (uniaxial loading) after failure is compared to a monochromatic contour plot of residual plastic strains using the proposed SED damage as presented in **Figure 4.10**. As can be seen, the residual plasticity predicted by the introduced damage model is in excellent agreement compared to discoloration resulting from plastic deformation in the specimen.

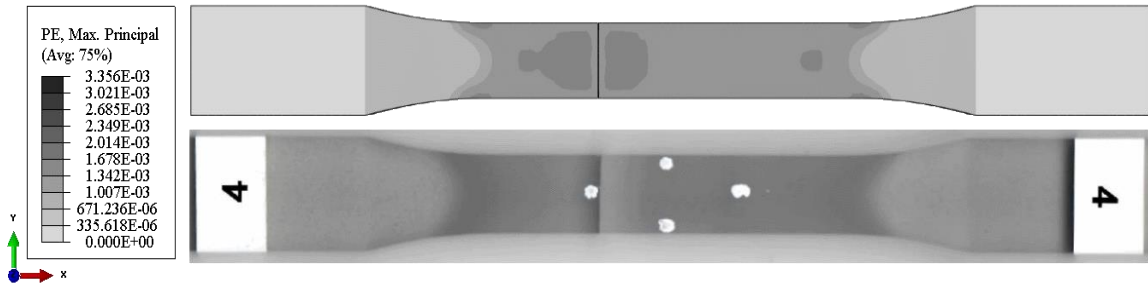


Figure 4.10 Plastic strains contour plot using proposed SED damage compared to discoloration from testing.

The failed specimens from uniaxial load testing were examined using optical microscopic imaging. The fractured surfaces showed crazes or cracks originating from micro-cavitation as presented in **Figure 4.11**. Micro-cavitation was observed towards the edges of the cross-section implying that the macroscopic crack moved from one side of the specimen inwards till fracture. Inspecting the micro-cavitation, their diameters were approximately 60~70 microns. The cracks were spread in a plane normal to the load application direction followed by rapid growth leading to the brittle failure. The direction of the crack growth is found to be in a plane normal to the applied load direction. This, in fact, emphasizes the importance of using a damage initiation criterion that accounts for the hydrostatic strain energy density component being the one dominating failure.

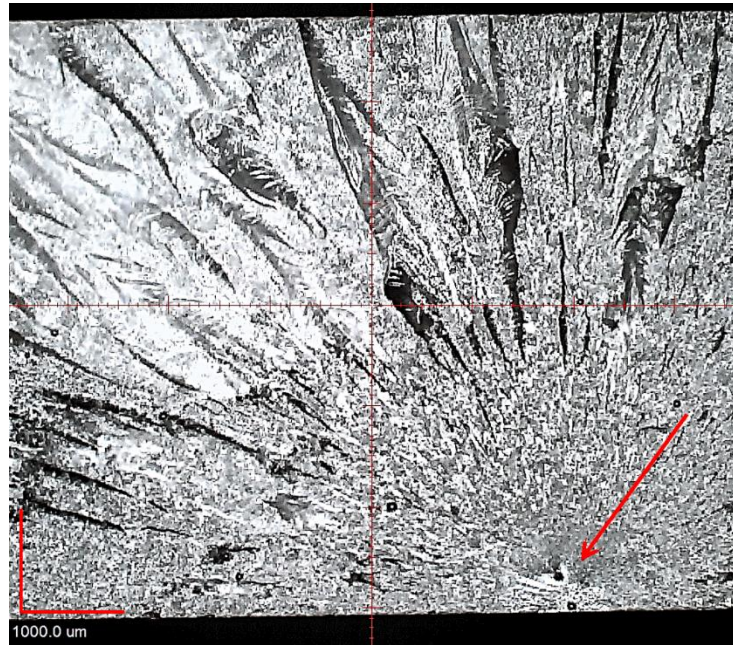


Figure 4.11 Specimen T1 Failure surface microscopic image

4.7.3 Three-point bending loading

To further investigate the heavily cross-linked epoxy, six prisms were tested under three-point loading according to ASTM D790-17. The loading rate was determined based on the specimen geometry as recommended by the testing standard (0.5 mm/min). Prismatic specimens were placed on standard roller supports attached to the load frame base. Same type of rollers was used for load application on top of the specimen mid-span. Center mark was placed on the specimen in addition to another on a fixed reference to measure the total relative deflection. The load-deflection testing results obtained from testing are provided in **Figure 4.12**. As can be observed, the linear relation dominates the behavior of all specimens. Some specimens showed almost brittle failure while the rest showed moderate plastic deformation before going into final failure. A peak failure load of approximately 1500 N was recorded by specimen B5 while the maximum failure displacement was 2.4

mm. on the other hand, the minimum failure load had a value of approximately 1200 N which was recorded by specimen B6 while the maximum failure displacement was 1.4 mm.

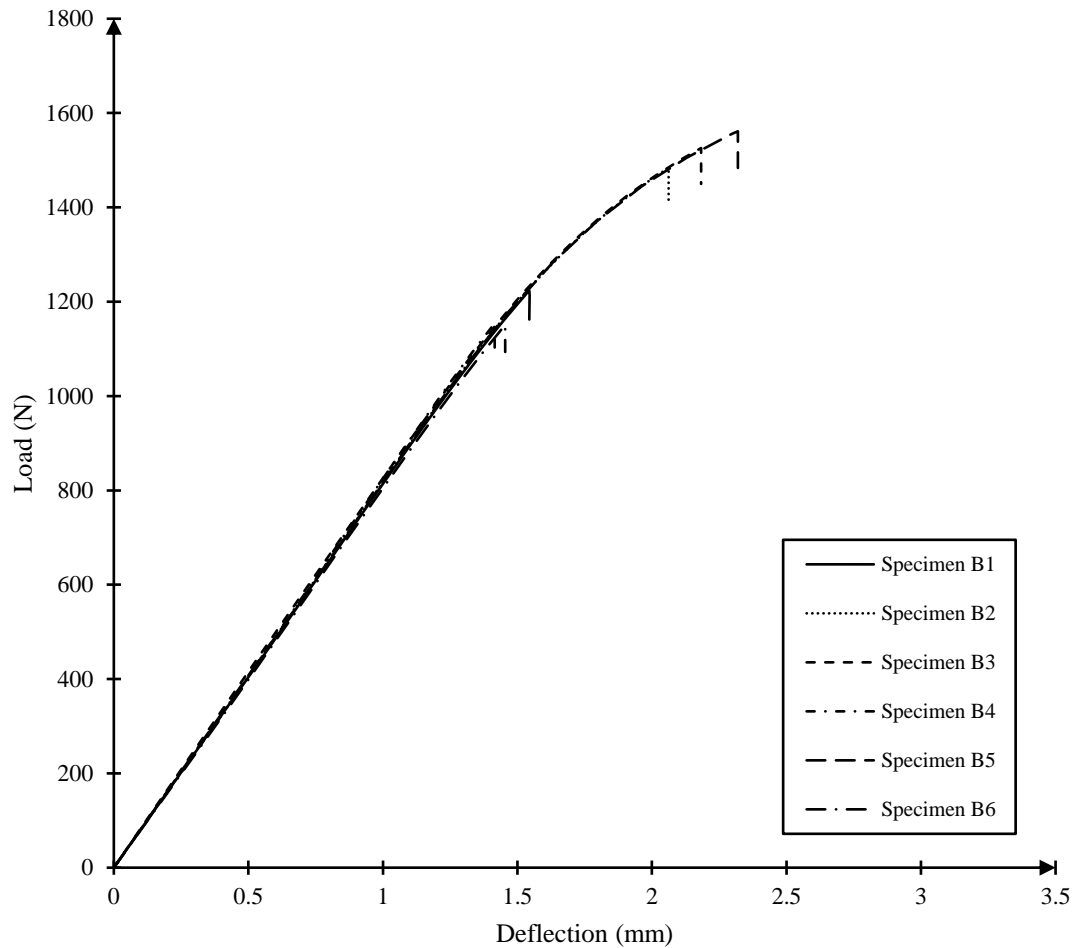


Figure 4.12 Load vs. relative displacement from video extensometer (three-point bending)

The variation of failure load is quite significant contradicting with the uniaxial loading case, approximately 25% which can be associated to the complex state of stress. Also, the failure displacement variation is more noticeable with approximately 40%, which rationalize the need of a failure criterion accounting for such performance. **Table 4.5** presents the mechanical failure properties, namely failure loads, flexural stresses and failure deflections.

Table 4.5. Failure limits for three-point loading specimens.

Specimen number	Failure load (N)	Flexural stress (MPa)	Failure Deflection (mm)
B1	1223	97.69	1.519
B2	1483	118.49	1.944
B3	1525	121.83	2.375
B4	1203	96.12	1.563
B5	1561	124.67	2.414
B6	1164	92.99	1.425

The FE predictions from the three-point bending model using the currently available damage initiation criteria together with the proposed SED damage mechanism are compared to the averaged testing results as depicted in **Figure 4.13**. As can be observed from the comparison, all built-in damage initiation mechanisms overestimated failure loads with errors varying from 2.9% to more than 10% error.

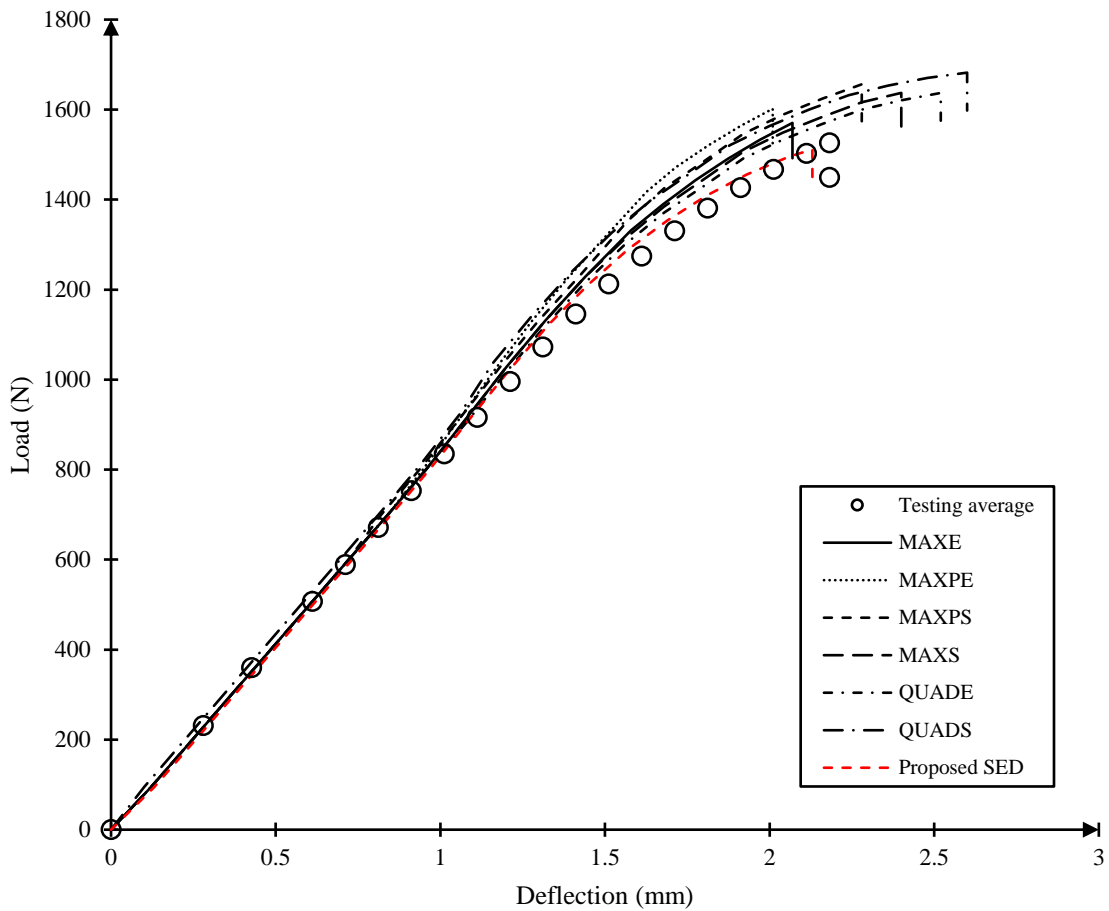


Figure 4.13 Load vs. deflection FE predictions compared to testing results.

Predicted failure deflections are compared against the average testing measurements. Two mechanisms underestimated the failure deflections, namely, MAXE and MAXPE with approximate errors of -5% and -8%, respectively. The proposed SED damage mechanism predicted both failure load and deflection with lower bounds. The percentage errors in failure load and deflection were -1% and -2.4%, respectively. Detailed failure loads and deflections with corresponding errors are documented in **Table 4.6**. The proposed SED damage mechanism is more conservative than the built-in damage mechanisms with lower errors in predicting both failure loads and deflections.

Table 4.6. FE predictions (three-point loading): Failure loads, deflections and percentage error.

Damage Initiation Mechanism	Failure load (N)	Error %	Failure deflection (mm)	Error %
MAXE	1570	2.9	2.069	-5.2
MAXPE	1602	5.0	2.009	-7.9
MAXPS	1656	8.5	2.280	4.5
MAXS	1637	7.3	2.400	10.0
QUADE	1637	7.3	2.520	15.5
QUADS	1682	10.2	2.600	19.1
Proposed SED	1511	-1.0	2.130	-2.4

Regarding the predicted failure surfaces using FE simulations, all built-in damage mechanisms together with the proposed mechanism efficiently predicted a failure surface parallel to the prismatic model cross-section. The lower mid-segment is the critical cross-section of a prism under three-point loading. The failure initiated in the lower mid-segment of the prism as can be observed from **Figure 4.14**.

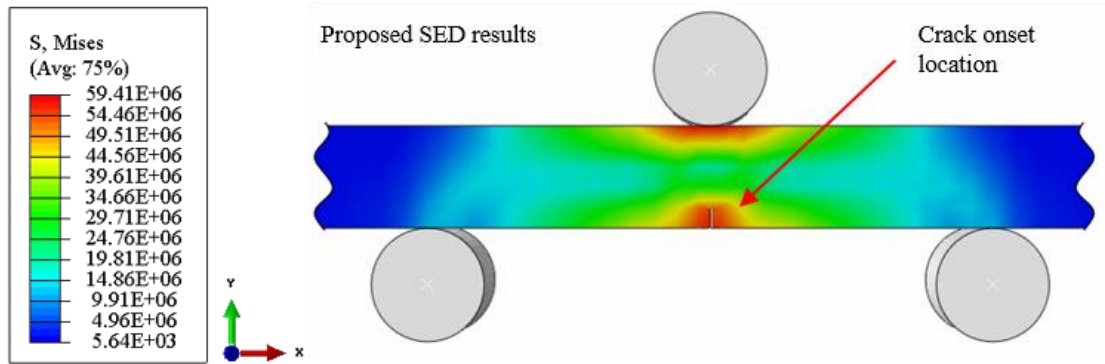


Figure 4.14 Von Mises contour plot and initiated crack location using proposed SED damage mechanism

The plastic strains contour plot from FE predictions using the proposed SED damage mechanism is presented in **Figure 4.15a** while the corresponding monochromic image of fracture specimen, B5, is presented in **Figure 4.15b**. As can be observed by simple

comparison, the proposed SED damage mechanism efficiently predicted plastic strains as well as the failed surface.

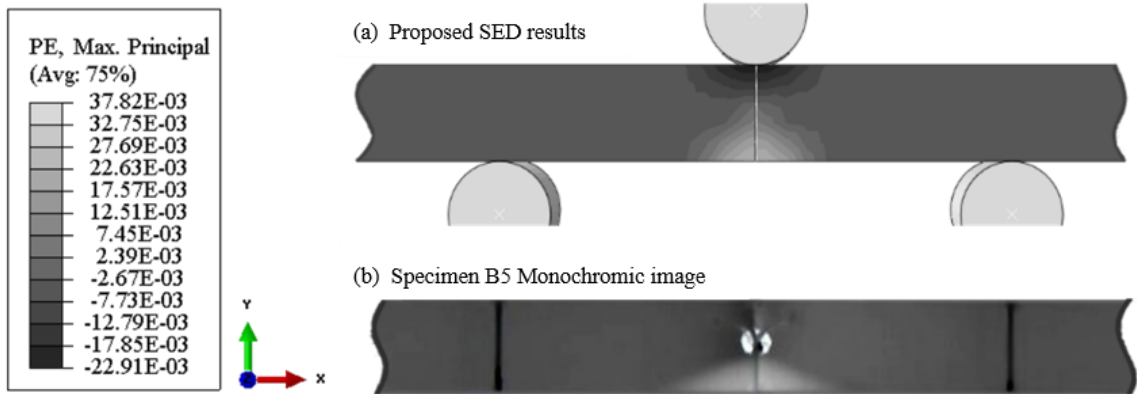


Figure 4.15 Plastic strains: (a) proposed SED results (b) Specimen B5 monochromatic image showing whitening.

The prismatic specimens under three-point loading had different failure behaviors. Three specimens had a linear behavior until failure. Namely, specimens 1, 4 and 6. The rest of the specimens manifested localized plastic deformation before failure as can be observed from **Figure 4.12**. To further investigate, the fractured surfaces were closely examined using optical microscopy. **Figure 4.16** portrays two of the fractured specimens (B3 and B4) and the corresponding fracture surface microscopic images. First, specimen B3 went through significant plastic deformation ahead of final failure. The plastically deformed region (whitened) can be observed from **Figure 4.16a**. Almost half the depth of the cross-section experienced a plastic deformation followed by crazes or cracking indicating that the final failure was of brittle manner. On the other hand, specimen B4 experienced a slight local plastic deformation originating from a micro-cavitation and expanding radially with many crazes or cracking initiating from the same locus. It can be said that the brittle behavior dominated the failure process from the beginning.

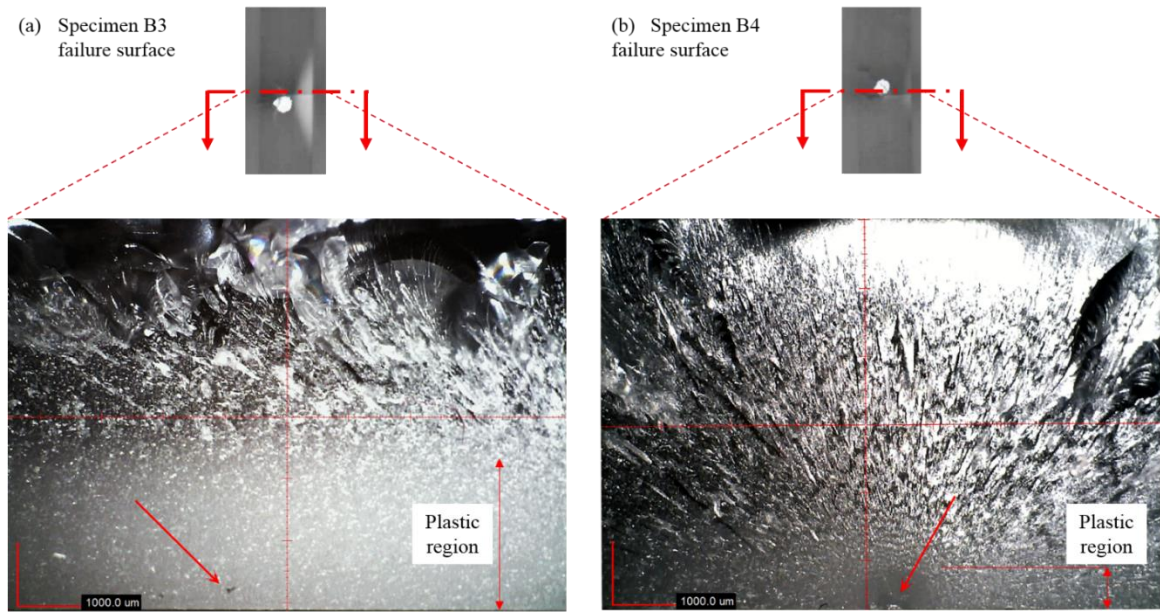


Figure 4.16 Failure surface microscopic image: (a) specimen B3 (b) specimen B4.

4.8 Conclusions

This paper proposed an improved damage model in the framework of XFEM to predict failure in heavily-cross linked epoxies. The SED based damage initiation criterion was developed and implemented in a UDMGINI subroutine. Comparisons against currently available damage initiation criteria in Abaqus were performed. For validation, a parallel experimental effort for both uniaxial and bending loading tests was conducted. Advanced techniques, precise measurements and post-failure analysis were also provided. In particular, high precision DIC system with synchronized monochromatic video recording enabled precise yielding identification.

Further inspection of failed specimens using fractographic analysis was conducted using optical microscopic imaging. The existence of micro-cavitation was reported in all specimens concurring with literature findings. Crazes or cracks were observed originating from micro-cavitation signifying brittle failure superiority and confirming the need to

account for dilatational SED component. Under a complex state of stress, a potential plastic zone was observed which highlights the importance of the distortional SED component as well. In turn, fractographic analysis emphasized the importance of using a damage initiation criterion that accounts for the hydrostatic as well as the distortional SED components.

From comparisons with testing, the proposed SED damage model demonstrated accurate prediction of damage initiation, propagation and the potential development of plastic strains. It can be concluded that the proposed SED damage in comparison to available damage criteria in Abaqus showed;

- Absolute minimum error in predictions when compared to both uniaxial and bending testing.
- Prediction results proved to be conservative under predicting both failure loads and displacements.
- Applicable to different loading scenarios and complex stress states accounting for total SED.
- Obtained results were accurately consistent in predicting both failure loads and displacements while built-in damage criteria reflected contradicting levels of accuracy in predicting loads versus those of displacements.
- In bending, all built-in criteria together with the proposed SED criterion predicted a realistic fracture surface. In uniaxial tension, built-in criteria failed to predict the correct fracture surface while the proposed SED criterion predicted a realistic fracture surface.

Therefore, the proposed model and its implementation is recommended for failure analysis of composites with heavily cross-linked epoxies. Also, it worth noting that the proposed model is applicable to brittle materials characterized by low strain-to-failure (i.e., less than 3% strain).

4.9 References

- Abaqus Documentation*. (2014). Providence, Rhode Island: Dassault Systèmes.
- Abdelaziz, Y., & Hamouine, A. (2008). A survey of the extended finite element. *Computers and Structures*, 86(11–12), 1141–1151. <https://doi.org/10.1016/j.compstruc.2007.11.001>
- Aho, T., Nerg, J., & Pyrhönen, J. (2007). Experimental and finite element analysis of solid rotor end effects. *IEEE International Symposium on Industrial Electronics*, 1242–1247. <https://doi.org/10.1109/ISIE.2007.4374776>
- Asp, L. E., Berglund, L. A., & Talreja, R. (1996). A criterion for crack initiation in glassy polymers subjected to a composite-like stress state. *Composites Science and Technology*, 56(11), 1291–1301. [https://doi.org/10.1016/S0266-3538\(96\)00090-5](https://doi.org/10.1016/S0266-3538(96)00090-5)
- Asp, Leif E., Berglund, L. A., & Gudmundson, P. (1995). Effects of a composite-like stress state on the fracture of epoxies. *Composites Science and Technology*, 53(1), 27–37. [https://doi.org/10.1016/0266-3538\(94\)00075-1](https://doi.org/10.1016/0266-3538(94)00075-1)
- ASTM-D790-17. (2017). Standard Test Methods for Flexural Properties of Unreinforced and Reinforced Plastics and Electrical Insulating Materials 1. *ASTM International. Designation: D*, 1–12. <https://doi.org/10.1520/D0790-17.2>
- ASTM D638-14. (2014). Standard test method for tensile properties of plastics. *ASTM International. Designation: D*, 08, 46–58. <https://doi.org/10.1520/D0638-14.1>
- Belytschko, T., & Black, T. (1999). Elastic crack growth in finite elements with minimal remeshing. *International Journal for Numerical Methods in Engineering*, 45(5), 601–620. [https://doi.org/10.1002/\(SICI\)1097-0207\(19990620\)45:5<601::AID-NME598>3.0.CO;2-S](https://doi.org/10.1002/(SICI)1097-0207(19990620)45:5<601::AID-NME598>3.0.CO;2-S)
- Belytschko, Ted, Gracie, R., & Ventura, G. (2009). A review of extended/generalized finite element methods for material modeling. *Modelling and Simulation in Materials Science and Engineering*, 17(4). <https://doi.org/10.1088/0965-0393/17/4/043001>
- Bressers, O. F. J. T. (2002). *Craze initiation in glassy polymer systems*. Technische Universiteit Eindhoven.
- Bauwens, Claude. Yield condition and propagation of Lüders' lines in tension–torsion experiments on poly(vinyl chloride). *Journal of Polymer Science Part A-2: Polymer Physics*, 1970(6), 893–901.
- D5045-99(2007). (2013). Standard Test Methods for Plane-Strain Fracture Toughness and Strain Energy Release Rate of Plastic Materials. *ASTM Book of Standards*, 99(Reapproved 2007), 1–9. <https://doi.org/10.1520/D5045-14.priate>
- Duarte, A. P. C., Díaz Sáez, A., & Silvestre, N. (2017). Comparative study between XFEM and Hashin damage criterion applied to failure of composites. *Thin-Walled Structures*, 115(October 2016), 277–288. <https://doi.org/10.1016/j.tws.2017.02.020>

- Elnekhaily, S. A., & Talreja, R. (2018). Damage initiation in unidirectional fiber composites with different degrees of nonuniform fiber distribution. *Composites Science and Technology*, 155. <https://doi.org/10.1016/j.compscitech.2017.11.017>
- Fries, T.-P., & Belytschko, T. (2010). The extended/generalized finite element method: An overview of the method and its applications. *International Journal for Numerical Methods in Engineering*, 84(April), 253–304. <https://doi.org/10.1002/nme>
- Hagstrand, P. O., Bonjour, F., & Månson, J. A. E. (2005). The influence of void content on the structural flexural performance of unidirectional glass fibre reinforced polypropylene composites. *Composites Part A: Applied Science and Manufacturing*, 36(5), 705–714. <https://doi.org/10.1016/j.compositesa.2004.03.007>
- Hencky, H. (1924). Zur Theorie plastischer Deformationen und der hierdurch im Material hervorgerufenen Nachspannungen. *ZAMM-Journal of Applied Mathematics and Mechanics/Zeitschrift Für Angewandte Mathematik Und Mechanik*, 4(4), 323–334.
- Jeong, H. Y., & Pan, J. (1995). A macroscopic constitutive law for porous solids with pressure-sensitive matrices and its implications to plastic flow localization. *International Journal of Solids and Structures*, 32(24), 3669–3691. [https://doi.org/10.1016/0020-7683\(95\)00009-Y](https://doi.org/10.1016/0020-7683(95)00009-Y)
- Kalantari, M., Dong, C., & Davies, I. J. (2017). Effect of matrix voids, fibre misalignment and thickness variation on multi-objective robust optimization of carbon/glass fibre-reinforced hybrid composites under flexural loading. *Composites Part B: Engineering*, 123, 136–147. <https://doi.org/10.1016/j.compositesb.2017.05.022>
- Knauss, W. G. (2012). On the importance of the dilatational component of the stress state in the uniaxial yield-like behavior of rate-dependent polymers: C. Bauwens-Crowet revisited. *Mechanics of Time-Dependent Materials*, 16(2), 223–240. <https://doi.org/10.1007/s11043-011-9149-6>
- Lachaud, F., Espinosa, C., Michel, L., Rahme, P., & Piquet, R. (2015). Modelling Strategies for Simulating Delamination and Matrix Cracking in Composite Laminates. *Applied Composite Materials*, 22(4), 377–403. <https://doi.org/10.1007/s10443-014-9413-4>
- Li, H., Li, J., & Yuan, H. (2018). A review of the extended finite element method on macrocrack and microcrack growth simulations. *Theoretical and Applied Fracture Mechanics*, 97(August), 236–249. <https://doi.org/10.1016/j.tafmec.2018.08.008>
- Liebig, W. V., Leopold, C., & Schulte, K. (2013). Photoelastic study of stresses in the vicinity of a unique void in a fibre-reinforced model composite under compression. *Composites Science and Technology*, 84, 72–77. <https://doi.org/10.1016/j.compscitech.2013.04.011>
- LS-DYNA. (2013). *LS-DYNA user's manual*. CA, USA: Livermore Software Technology Corporation.
- Melenk, J. M., & Babuška, I. (1996). The partition of unity finite element method: Basic

- theory and applications. *Computer Methods in Applied Mechanics and Engineering*, 139(1–4), 289–314. [https://doi.org/10.1016/S0045-7825\(96\)01087-0](https://doi.org/10.1016/S0045-7825(96)01087-0)
- Moës, N., & Belytschko, T. (2002). Extended finite element method for cohesive crack growth. *Engineering Fracture Mechanics*, 69(7), 813–833. [https://doi.org/10.1016/S0013-7944\(01\)00128-X](https://doi.org/10.1016/S0013-7944(01)00128-X)
- P.K. Mallick. (2007). Fiber-Reinforced Composites: Materials, Manufacturing, and Design. In *CRC Press*.
- Pawar, P. M., & Ganguli, R. (2006). Modeling progressive damage accumulation in thin walled composite beams for rotor blade applications. *Composites Science and Technology*, 66(13), 2337–2349. <https://doi.org/10.1016/j.compscitech.2005.11.033>
- Petrov, N. A., Gorbatiikh, L., & Lomov, S. V. (2018). A parametric study assessing performance of eXtended Finite Element Method in application to the cracking process in cross-ply composite laminates. *Composite Structures*, 187(July 2017), 489–497. <https://doi.org/10.1016/j.compstruct.2017.12.014>
- Pollayi, H., & Yu, W. (2014). Modeling matrix cracking in composite rotor blades within VABS framework. *Composite Structures*, 110(1), 62–76. <https://doi.org/10.1016/j.compstruct.2013.11.012>
- Pommier, S., Gravouil, A., & Combescure, A. (2013). Extended Finite Element Method X-FEM. In *Extended Finite Element Method for Crack Propagation*.
- Raghava, R., Caddell, R. M., & Yeh, G. S. Y. (1973). The macroscopic yield behaviour of polymers. *Journal of Materials Science*, 8(2), 225–232. <https://doi.org/10.1007/BF00550671>
- Sih, G. C. (1991). A three-dimensional strain energy density factor theory of crack propagation. *Mechanics of Fracture Initiation and Propagation*, 23–56.
- Song, J. H., Wang, H., & Belytschko, T. (2008). A comparative study on finite element methods for dynamic fracture. *Computational Mechanics*, 42(2), 239–250. <https://doi.org/10.1007/s00466-007-0210-x>
- Sukumar, N., Dolbow, J. E., & Moës, N. (2015). Extended finite element method in computational fracture mechanics: a retrospective examination. *International Journal of Fracture*, 196(1–2), 189–206. <https://doi.org/10.1007/s10704-015-0064-8>
- Talreja, R. (2014). Assessment of the fundamentals of failure theories for composite materials. *Composites Science and Technology*, 105, 190–201. <https://doi.org/10.1016/j.compscitech.2014.10.014>
- Timoshenko, S. P., & J. N. Goodier. (2010). *Theory of elasticity* (3rd ed.). Singapore: McGraw-Hill Ltd.
- Ukadgaonker, V. G., & Awasare, P. J. (1995). A new criterion for fracture initiation. *Engineering Fracture Mechanics*, 51(2), 265–274. [https://doi.org/10.1016/0013-7944\(94\)00265-J](https://doi.org/10.1016/0013-7944(94)00265-J)
- Uygunoglu, T. K. U., Gunes, I. K. U., & Brostov, W. of N. T. (2015). physical and

- Mechanical properties of polymer composite with high content. *Materials Research*, 18(6), 1188–1196. <https://doi.org/10.1590/1516-1439.009815>
- van Dongen, B., van Oostrum, A., & Zarouchas, D. (2018). A blended continuum damage and fracture mechanics method for progressive damage analysis of composite structures using XFEM. *Composite Structures*, 184(September 2017), 512–522. <https://doi.org/10.1016/j.compstruct.2017.10.007>
- von Mises, R. (1913). Mechanik der festen Körper im plastisch deformablen Zustand. *Göttin. Nachr. Math. Phys.*, 1, 582–592.
- Wang, Z., Liu, F., Liang, W., & Zhou, L. (2013). Study on tensile properties of nanoreinforced epoxy polymer: Macroscopic experiments and nanoscale FEM simulation prediction. *Advances in Materials Science and Engineering*, 2013. <https://doi.org/10.1155/2013/392450>
- Yamini, S., & Young, R. J. (1980). The mechanical properties of epoxy resins - Part 2 Effect of plastic deformation upon crack propagation. *Journal of Materials Science*, 15(7), 1823–1831. <https://doi.org/10.1007/BF00550603>
- Yazid, A., Abdelkader, N., & Abdelmadjid, H. (2009). A state-of-the-art review of the X-FEM for computational fracture mechanics. *Applied Mathematical Modelling*, 33(12), 4269–4282. <https://doi.org/10.1016/j.apm.2009.02.010>
- Yokozeki, T., Iwahori, Y., & Ishiwata, S. (2007). Matrix cracking behaviors in carbon fiber/epoxy laminates filled with cup-stacked carbon nanotubes (CSCNTs). *Composites Part A: Applied Science and Manufacturing*, 38(3), 917–924. <https://doi.org/10.1016/j.compositesa.2006.07.005>

5 Standard Mechanics Approach to Predict Effective Mechanical Behavior of Porous Sintered Steel Using Micromechanical RVE-based Finite Element Modeling

5.1 Abstract

This article proposes a standard approach Representative Volume Element (RVE)-based micromechanical model to predict effective elastic-plastic behavior of porous metals in the low range porosity, i.e. less than 10%. Three-dimensional RVE model was used to validate the proposed micromechanical modeling approach. The size effect of holes representing micro-porosity as well as the uniform and random distributions in RVEs were investigated. The results indicated the number of holes had a slight effect on predicting the linear behavior while in the plastic domain the influence was significant. Validation against testing results at three porosity fractions in the low range is provided. The proposed micromechanical model proved to be in excellent agreement with testing results from literature with maximum approximate errors of 2% and 4% in predicting the modulus of elasticity and the yield stress, respectively.

5.2 Introduction

Additive manufacturing (AM) or three-dimensional (3D) printing is a lay-up process of joining materials to construct parts from 3D modeling. Metallic 3D printing has been rapidly emerging in many engineering fields such as mechanical, aerospace and biomedical (Cheng & Ghosh, 2015; Mercelis & Kruth, 2006). The main advantage of 3D printing is manufacturing complex geometry parts while minimizing material waste (Attaran, 2017; Sercombe et al., 2015; B. Song et al., 2015; S. L. Su, Rao, & He, 2013; Szost et al., 2016).

However, this advanced manufacturing process results in decreased pore size to micro levels which may considerably influence the mechanical behavior (Attaran, 2017; Chawla & Deng, 2005; Frazier, 2014; R. A. Hardin & Beckermann, 2013; R. a Hardin & Beckermann, 2011; Richard A. Hardin & Beckermann, 2007; HASSELMAN, 1963; Jagota, Hui, & Dawson, 1987; P. Liu, Fu, Li, & Shi, 1999; Morin, Michel, & Leblond, 2017). Therefore, accounting for micro-porosity effect on the mechanical behavior is essential for design stages. As a result, the effective modulus of porous materials has been extensively studied in the literature, and many empirical models were developed (Debboub, Boumaiza, & Boudour, 2012; Dewey, 1947; MACKENZIE, 1949; Roberts & Garboczi, 2000; Saimoto & Thomas, 1986; S. L. Su et al., 2013; Sumitomo, Cáceres, & Veidt, 2002). However, most analytical models cannot account for geometrical variations at the microscale and are limited to linear behavior (Oliver, Caicedo, Huespe, Hernández, & Roubin, 2017; Omairey, Dunning, & Sriramula, 2018).

The commonly referenced model for porous metal plasticity is the Gurson-Tvergaard-Needleman (GTN) model which was originally proposed by Gurson (Gurson, 1977) and later extended by Tvergaard and Needleman (Tvergaard & Needleman, 1984). The model is micromechanically based on a cube with a central void to predict damage of porous metals in the low range porosity, i.e. less than 10% (*Abaqus Documentation*, 2014). GTN model can be used to study void growth and nucleation in porous metals however it requires the plastic behavior to be defined as a material input. Also, to predict nucleation and void growth nine material specific parameters are to be defined (*Abaqus Documentation*, 2014; R. A. Hardin & Beckermann, 2013; R. a Hardin & Beckermann, 2011; Richard A. Hardin

& Beckermann, 2007). Defining the material parameters entails substantial testing effort. Moreover, simulation runtime associated with a specimen sized model can be several days (R. A. Hardin & Beckermann, 2013). Nevertheless, the model does not predict the change in linear behavior due to micro-pores implying that further analysis is required to determine the effective modulus.

On the other hand, computational methods such as finite element analysis (FEA) have proven versatility in investigating mechanical behavior at different scales (e.g., micro, meso and macro) (Matouš, Geers, Kouznetsova, & Gillman, 2017). Rapidly emerging multiscale modeling techniques became indispensable for more precise and accurate predictions in material science (Leszczynski & Shukla, 2010). The multiscale modeling process is hierarchical by nature, aiming to study the material behavior at one scale (e.g., microscale) to predict the behavior at another (e.g., meso/macro-scale) (Collini, L., & Nicoletto, 2005; Dæhli, Faleskog, Børvik, & Hopperstada, 2016; GAO, WANG, LIU, & ZHUANG, 2017; Guidault, Allix, Champaney, & Cornuault, 2008; Leszczynski & Shukla, 2010; Matouš et al., 2017; Oliver, Caicedo, Roubin, Huespe, & Hernández, 2015; Schmitz & Horst, 2014; Schneider, Klusemann, & Bargmann, 2016; Talebi, Silani, Bordas, Kerfriden, & Rabczuk, 2014; Toro et al., 2016; J. Zhang, Koo, Subramanian, Liu, & Chattopadhyay, 2016). For example, Collini and Nicoletto (Collini, L., & Nicoletto, 2005) utilized an FEA model to determine the relationship between microstructural performance and the constitutive behavior of nodular cast iron. Also, micromechanical FE simulations were used to validate porous plasticity models for ductile materials as in the work of Morin et al. (Morin, Leblond, & Kondo, 2015; Morin et al., 2017) and Mbiakop et al. (Mbiakop,

Constantinescu, & Danas, 2015). All these studies commonly investigated the microstructural effect on mechanical behavior and reported satisfactory results. A commonly used micromechanical modeling approach is the representative volume element (RVE) homogenization method (Rodney Hill, 1963). The RVE is commonly defined as the smallest volume over which the material properties can be measured to represent the global properties (Elnekhaily & Talreja, 2018). The RVE-based FE simulations were used to predict effective behavior of solid materials with void inclusions (Babu, Mohite, & Upadhyay, 2018; Dong, 2016; Ghayoor, Hoa, & Marsden, 2018; Gitman, Askes, & Sluys, 2007; Hosseini-Toudeshky & Jamalain, 2015; Nguyen, Lloberas-Valls, Stroeven, & Sluys, 2011; Oliver et al., 2017). For example, RVE with spheroidal/spherical inclusions was proposed to model the micromechanical behavior of sintered produced porous titanium materials under compression (Soro et al., 2018). The predicted elastic properties were in good agreement with the Mori-Tanaka model (Mori & Tanaka, 1973), yet overestimating experimental results by approximately 20%. In general, RVE-based FE simulations have proven effectiveness in micromechanical investigations. However, RVE modeling process is time consuming and requires relatively high computational effort especially in three-dimensional domains (Elnekhaily & Talreja, 2018; Omairey et al., 2018). Also, prediction results are significantly influenced by microstructural representative size (Babu et al., 2018; Biswas & Poh, 2017; Cheng & Ghosh, 2015; Mirkhalaf, Andrade Pires, & Simoes, 2016; Yu et al., 2018). Besides, these simulation results are susceptible to mesh convergence as well as boundary conditions (BCs). These challenges motivated the current study to present

computationally effective micromechanical modeling approach emphasizing the RVE size and mesh quality effects.

Therefore, the effective macroscopic behavior of porous material is predicted from the material's microstructure. The computationally efficient standard mechanics approach is proposed to predict the mechanical behavior of porous materials using micromechanical RVE-based FEA. The proposed approach predicts the elastic-plastic behavior of porous material given the dense material behavior under the assumption of small deformations, i.e. less than 10%. A thorough investigation regarding the size and distribution of pores in the microstructure was conducted. Also, adequate structured meshing technique using different types of elements for RVE modeling is provided. The model requires minimal material parameters, i.e. dense material stress-strain curve, to predict effective elastic-plastic behavior of the porous one. FE predictions were validated against testing results at different volumetric porosity fractions in the low range porosity, i.e. less than 10%, results were in excellent agreement.

5.3 Theoretical Background

The RVE concept entails large enough volume representing the material and small enough to emulate the microstructure in consideration (Pelissou, Baccou, Monerie, & Perales, 2009). This concept can be achieved either by experimental observations or by validating numerical analysis with testing results (Liang, Li, Yu, Jiang, & Zhang, 2012). Also, the numerical response of the RVE must be independent of applied BC, i.e. uniform tractions or displacements. These homogenization requirements resulted in the development of the commonly used periodic boundary conditions (PBC). Usually, a node-to-node PBC is

applied in homogenization modeling to enable accurate predictions of the effective stiffness properties, i.e., linear behavior. Further details on PBCs application techniques can be found in (Gitman et al., 2007; Mirkhalaf et al., 2016; Omairey et al., 2018). An alternate approach for applying BCs on RVEs is the standard mechanics approach. This approach is utilized when both linear and plastic behaviors are anticipated. In the current work, RVE-based standard mechanics approach is used to estimate not only the effective stiffness but also, the entire effective stress-strain behavior in both linear and plastic domains.

5.3.1 Standard Mechanics Approach

The proposed RVE-based standard mechanics approach is analyzed using uniform displacement BC to produce an average strain within the homogenized material. The governing equation can be written using the divergence theorem (Rodney Hill, 1963) as

$$\bar{\varepsilon}_{ij} = \frac{1}{|V_{RVE}|} \int_{V_{RVE}} \varepsilon_{ij} dV_{RVE} = \int_{\Gamma_{RVE}} \frac{1}{2} (u_i n_j + u_j n_i) d\Gamma_{RVE} \quad (\text{Eq.5.1})$$

where $\bar{\varepsilon}_{ij}$ is the average strain tensor, V_{RVE} is the RVE volume, ε_{ij} is the local strain tensor, and Γ_{RVE} is the element boundary. u_i and u_j are the imposed displacements on the RVE boundary while n_i and n_j are the normal unit vectors. Similarly, the average stress relation to the imposed tractions reads as

$$\bar{\sigma}_{ij} = \frac{1}{|V_{RVE}|} \int_{V_{RVE}} \sigma_{ij} dV_{RVE} = \int_{\Gamma_{RVE}} \frac{1}{2} (t_i y_j + t_j y_i) d\Gamma_{RVE} \quad (\text{Eq.5.2})$$

where $\bar{\sigma}_{ij}$ is the average stress tensor, σ_{ij} is the local stress tensor, t_i and t_j are the imposed tractions while y_i and y_j are elemental boundary local coordinates. The imposed displacements or tractions defined by (Eq.5.1) and (Eq.5.2) are generally chosen to be uniform (Hollister & Kikuchi, 1992). Consequently, the local strain in RVE is evaluated using the standard weak formulation of equilibrium equations. The material behavior was defined for a general state of stress using the Ramberg-Osgood relationship (Ramberg & Osgood, 1943)

$$E \varepsilon_{ij} = (1 + \nu) \sigma_{Dev} - (1 - 2\nu) \sigma_{Hyd} I + \frac{3}{2} \alpha \left(\frac{\sigma_{Mises|eq}}{\sigma_y} \right)^{m-1} \sigma_{Dev} \quad (\text{Eq.5.3})$$

where E is the modulus of elasticity, ν is the Poisson's ratio and I represents the identity matrix. The hydrostatic stress, σ_{Hyd} , and the deviatoric stress, σ_{Dev} are defined by (Eq.5.4) and (Eq.5.5), respectively. The equivalent Mises stress is denoted by $\sigma_{Mises|eq}$ while the yield stress is denoted by σ_y . Finally, the yield offset is defined by α while m is the hardening exponent of the plastic region, i.e. $m > 1$).

$$\sigma_{Hyd} = \frac{1}{3} tr(\sigma_{ij}) \quad (\text{Eq.5.4})$$

$$\sigma_{Dev} = \sigma_{ij} - \sigma_{Hyd} I \quad (\text{Eq.5.5})$$

5.4 Micromechanical Finite Element Modeling

Micromechanical models are known for intensive computational efforts due to the required element size presenting micro-features. Consequently, leading to a large number of elements in a convergent mesh specifically in three-dimensional domains. Minimizing

computational effort while maintaining accurate results is targeted in the proposed work. Consider the infinitesimal element with micro-pores from a dog-bone specimen under uniaxial loading as shown in **Figure 5.1a**. This element is modeled using both three and two dimensional RVE models representing the total micro-porosity fraction using a center sphere and hole, respectively. Both three and two dimensional RVEs predictions were compared to validate plane stress/strain assumptions. The constructed three-dimensional RVE model cutaway is shown in **Figure 5.1b**. The cube side length is 100 microns while the void radius is approximately 28 microns which represents a 0.1 porosity fraction. Eight-noded linear hexahedral elements with reduced integration, namely C3D8R, were used for meshing the RVE model. Stress based mesh convergence study led to a mesh size of 103872 elements with a total number of unknowns 326832. On the other hand, the two-dimensional RVE had a side length of 100 microns with an 18 microns radius for the center hole corresponding to a 0.1 porosity fraction as shown in **Figure 5.1c**. The convergent mesh had 3076 quadrilateral elements which are approximately 3% of what is required by three-dimensional one, details of two-dimensional RVE meshing are discussed in the following paragraph. Average true stress-strain data from both models were compared, and results were in an excellent agreement. Therefore, the two-dimensional RVE modeling was adequate for the proposed micromechanical model based on their cost-effective characteristics.

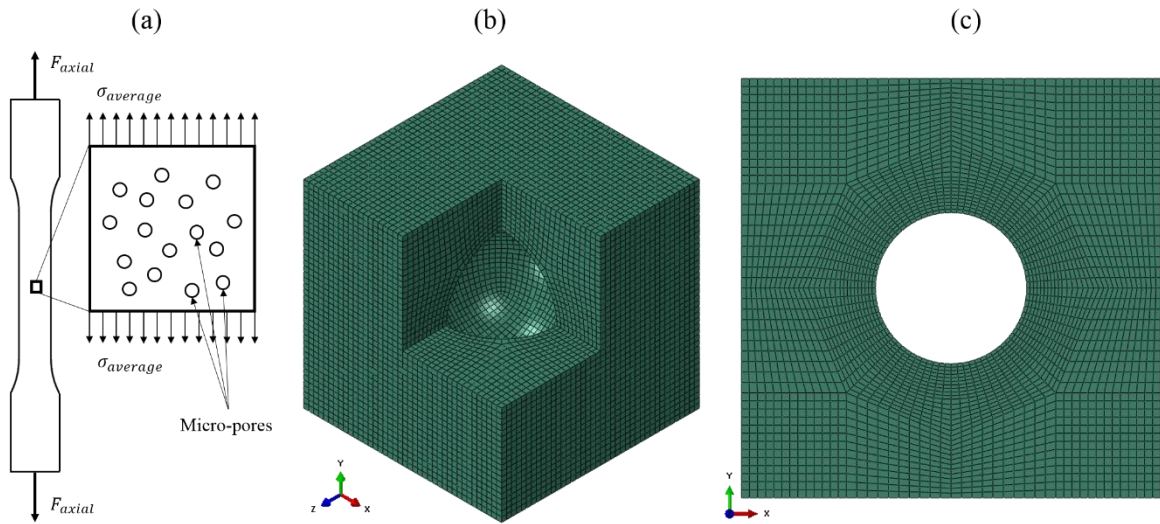


Figure 5.1 (a) Infinitesimal element with micro-pores (b) RVE mesh with single spherical void (c) RVE mesh with a center hole.

Plate with a center hole accounting for total microscopic porosity fraction was considered for modeling. Stresses in the vicinity of holes are significantly increased, given these stress concentration regions (Perumal, Tso, & Leng, 2016). Also, FEA predictions accuracy is strongly related to mesh size. Verification analysis was conducted regarding element type, aspect ratio and corner angles to ensure a high quality mesh. First, quadrilateral elements are known for better predictions compared to triangular ones (Reddy, 2014). Hence, it was attentively preferred for the current micro-structural analysis investigation. Two quadrilateral elements were compared based on plane stress/strain assumptions, namely CPS4R and CPE4R, respectively. Both elements follow the same formulation with a slight difference correlated to the associated assumption. The plane stress scenario neglects the out-of-plane stresses while the plane strain assumes zero out-of-plane relative displacements. The main challenge of using quadrilateral elements is conforming to complex geometries. To overcome this challenge, structured meshing technique was followed using appropriate partitions and manual seeds. As can be seen from **Figure 5.2a**,

a circular partition circumscribing the center hole enabled a high-quality mesh around the center hole. Smooth transition from the circular border to sharp corners of the RVE model was supported using an octagon shaped partition. Edges for each closed region were manually seeded the number of elements. Triangular elements were successfully avoided in meshing the all RVE-based models, **Figure 5.2b** shows the structured convergent mesh of 3076 quadrilateral elements with a total number of unknowns 7542. The average elemental aspect ratio along with the deviation from a right-angled corner were approximately 1.44 and 5° , respectively. Noteworthy to mention that the total number of unknowns in the two-dimensional model is approximately 2.3% of what is required by three-dimensional one. Consequently, the same methodology was followed in mesh generation for following RVEs.

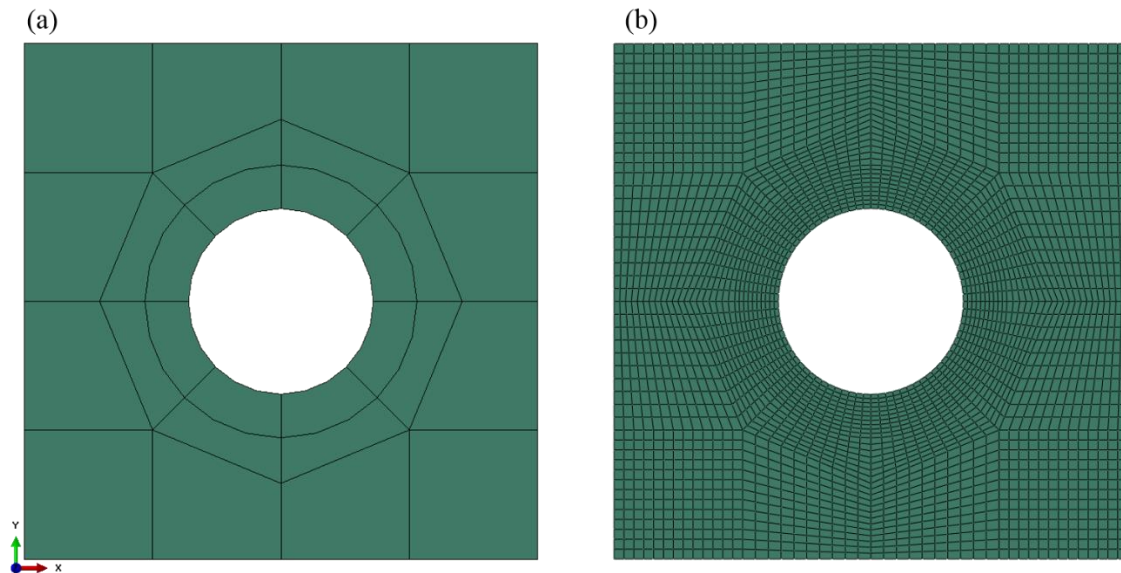


Figure 5.2 Center hole model: (a) partitioned RVE (b) convergent RVE mesh.

To investigate the influence of micro-porosity on effective material behavior, four uniform RVE models were used to simulate 10% total porosity fraction. The side length of each

model was maintained at 100 microns while the number of holes, n representing the total porosity fraction was varied, i.e. $n = 1, 4, 16, 64$. Partitioned RVE models together with their corresponding convergent meshes are presented in **Figure 5.3** and **Figure 5.4**, respectively.

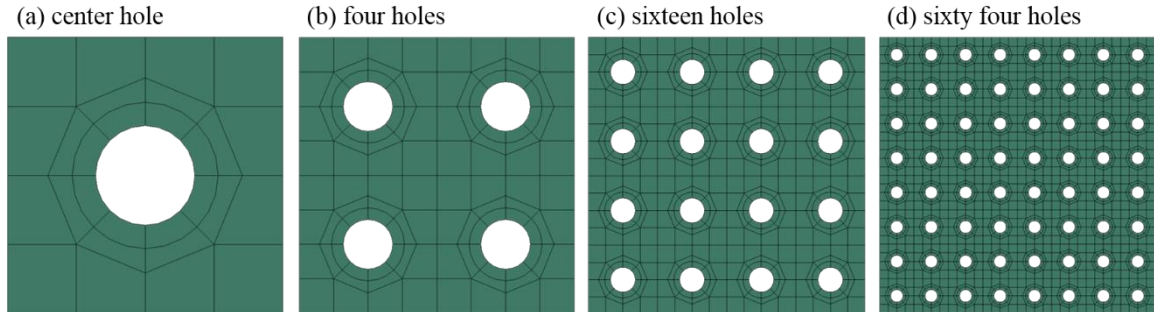


Figure 5.3 RVE models partitioning: (a) center hole (b) four holes (c) sixteen holes (d) sixty-four holes.

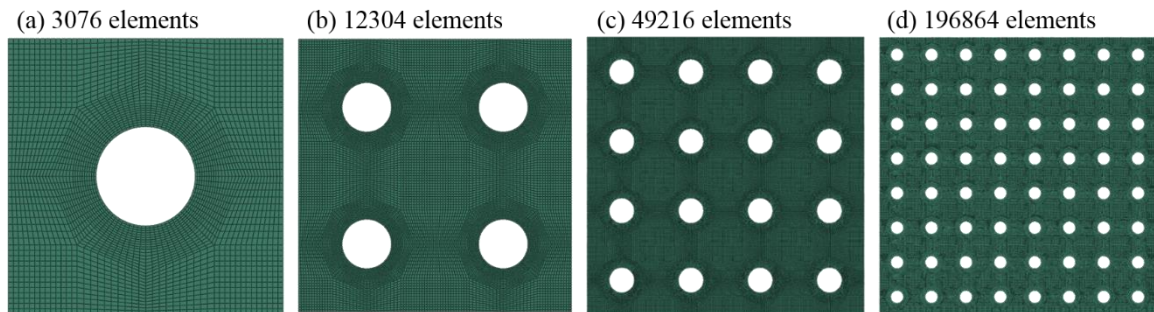


Figure 5.4 RVE models convergent mesh: (a) center hole (b) four holes (c) sixteen holes (d) sixty-four holes.

The Ramberg-Osgood relationship defined by (Eq.5.3) was used to calibrate the dense or sound material behavior. The resulted material properties were $E = 201$ GPa, $\sigma_y = 510$ MPa, and $\nu = 0.3$. The calibration process of the Ramberg-Osgood model led to an 8.5 hardening exponent and a 0.2% yield offset. A solid homogeneous section with plane stress/strain assumption was used. Each RVE was constrained from one edge while uniform-displacement was applied to the opposing edge. A general static step was chosen to perform the simulations with automatic incrementation. The initial increment size was

set to 0.01 with a minimum increment size of 1E-30 and a maximum of 0.02. Regarding the computational effort, the workstation used for running all simulations utilizes an Intel® Xeon® central processing unit E5-1603 v4 running at 2.80 GHz with 32 GB of RAM. A single processor was used to perform the simulations on Abaqus 2017.

5.5 Results and Discussion

Three different porosity fractions were investigated (i.e., low range <10%). Prediction results were validated against test data of Fe-0.85Mo-Ni powder metallurgy (P/M) steels reported by Chawla and Deng in (Chawla & Deng, 2003). Standard mechanics approach (subsection 5.3.1) was followed to predict the effective mechanical behavior from the microstructure. True-stress strain results were obtained based on the displacement approach from RVE models (subsection 4.5). The effective modulus was evaluated using the linear behavior slope while yield stress was defined using a 0.2% offset guided by calibration results of the sound material model. The results were quantitatively validated against testing results and corresponding errors were determined. Insights regarding the micromechanical local full-field predictions regarding von-Mises stresses and the total energy dissipation resulting from plastic deformations are provided.

5.5.1 Effective stress-strain results

Throughout the following figures, plane strain and stress predictions are presented using red and black lines, respectively, while reported testing results are presented with markers. Also, dense material behavior was predicted using a solid micromechanical RVE model. Prediction results using the CPE4R/CPS4R elements were validated against testing results reported by Chawla and Deng (Chawla & Deng, 2003) as shown in **Figure 5.5**. Plane strain

predictions have slightly overestimated the modulus of elasticity while in the plastic region significant deviation from testing can be observed. On the other hand, plane stress predictions proved to be in excellent agreement compared to testing results of dense material.

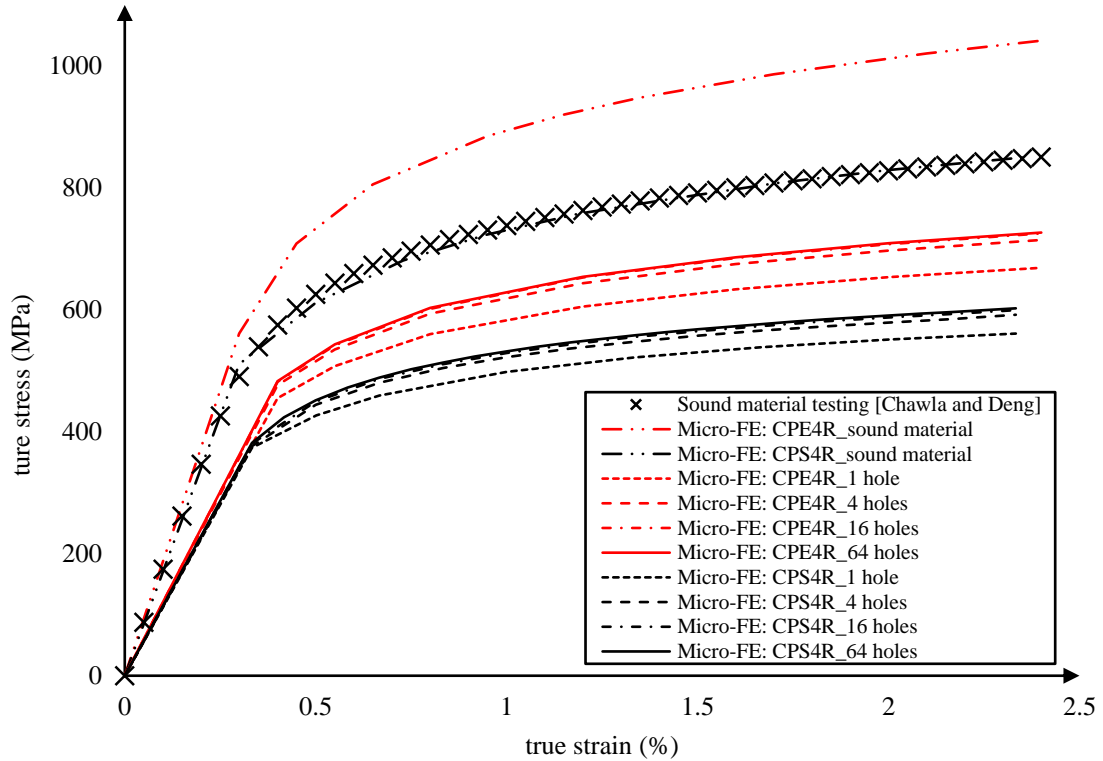


Figure 5.5 Predicted effective stress-strain curves for 10% porosity: CPE4R vs. CPS4R elements.

The three porosity fractions, i.e. 3.2%, 4.5% and 10.3%, were investigated thoroughly using four uniformly distributed RVE models discussed in subsection 4.5. Prediction results using the CPE4R and CPS4R elements at different porosity fractions were found to follow similar trends. For convenience, the maximum porosity fraction (i.e., 10%) was used to compare the plane strain/stress predictions. **Figure 5.5** illustrate the effect of 10% porosity on the true stress-strain behavior using the above types of elements. Also, the number of holes presenting the porosity in an RVE was varied. All predicted true stress-strain

behaviors captured the reduction in the modulus of elasticity, yield stress as well as the plastic flow compared to the dense material behavior. Increasing the number of holes in the RVE had an almost negligible effect on the linear region using both elements. It can be concluded that a center hole is sufficient to represent overall micro-porosity to estimate effective modulus. The predicted modulus of elasticity using plane strain elements was slightly higher than that obtained using plane stress ones. Contrarily, the onset of yielding was overestimated using plane strain elements. Similarly, a significant impact can be observed in the plastic region upon increasing number of holes. Both element types showed a convergence like behavior upon the increase of holes. For instance, increasing the number of holes from 16 to 64 holes had an infinitesimal effect on predicted results. In fact, following the same logic of mesh convergence the reader can conclude that the sufficient number of holes representing micro-porosity is 16.

To further investigate the suitable element for the proposed micro-structural analysis, 16 holes RVEs predictions were validated against reported testing results for different micro-porosity volumetric fractions. **Figure 5.6** shows that plane strain elements were consistent in overestimating moduli, yield stresses and plastic flow curves. The zero out-of-plane strains assumption resulted in an artificial in-plane stiffness leading to overestimated results. On the other hand, the plane stress elements predictions were in excellent agreement with testing results.

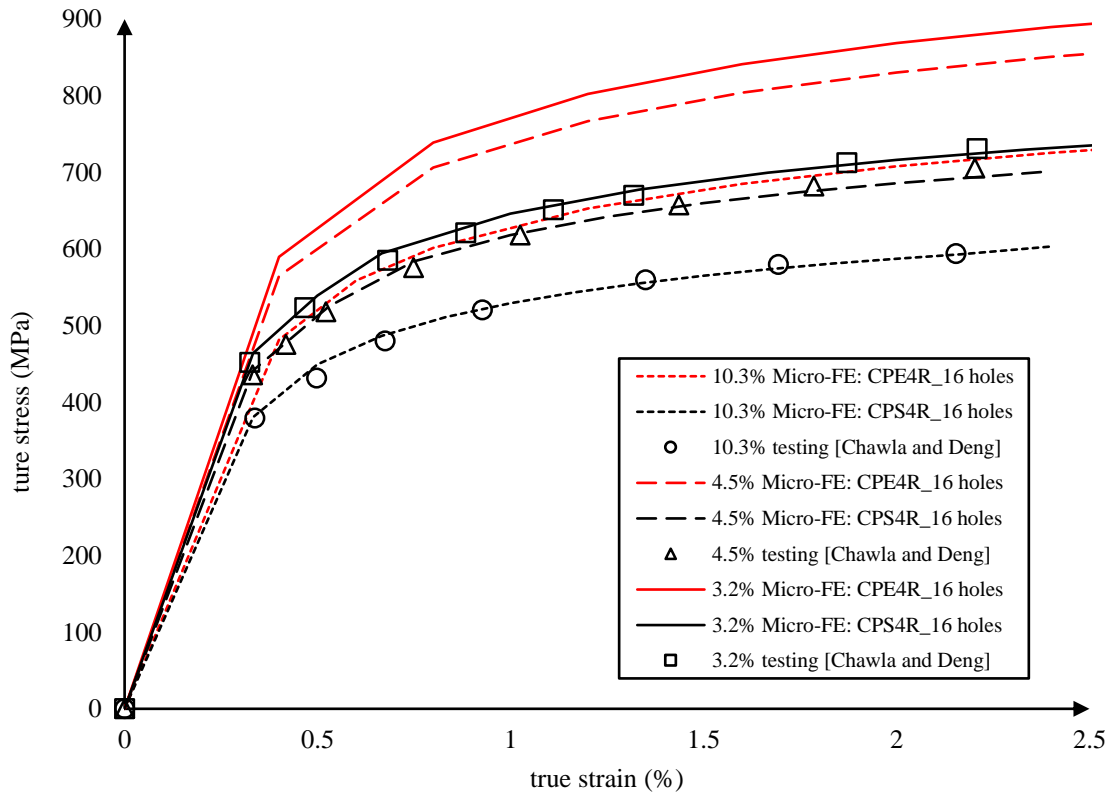


Figure 5.6 Predicted vs. testing (Chawla & Deng, 2003) stress-strain curves for 16 holes RVE.

Table 5.1 documents a quantitative comparison between predictions and testing results along with the percentage errors. As can be observed from comparisons, plane strain elements were consistent in over predicting both modulus as well as yield values. The maximum error in predicting the effective modulus of elasticity using plane strain elements was approximately less than 10%. On the other hand, the error in predicting yield stress was quite significant with minimum and maximum values of 17% and 24%, respectively. The plane stress elements showed an excellent agreement compared to testing results where the modulus of elasticity was efficiently predicted with a maximum error of -2.8%. Subsequently, the predicted yield stress results showed significant enhancement compared to plane strain elements with a maximum error of -4.39%.

Table 5.1 Prediction results and percentage errors compared to testing results.

Porosity fraction	number of holes	element type	E (GPa)	Error (%)	yield stress (MPa)	Error (%)	
Dense material	N/A	CPS4R	200.96	-0.50	574.36	-1.51	
		CPE4R	220.82	9.34	706.12	21.08	
3.20%	1	CPS4R	160.50	-2.48	498.31	-2.70	
	4		163.39	-0.72	504.13	-1.56	
	16		164.23	-0.21	508.37	-0.74	
	64		164.45	-0.08	509.07	-0.60	
	1	CPE4R	167.86	2.00	607.67	18.65	
	4		172.93	5.07	623.68	21.78	
	16		173.96	5.70	628.74	22.77	
	64		174.18	5.84	629.97	23.01	
	4.50%	1	CPS4R	152.97	-2.81	476.36	-4.39
		4		156.30	-0.70	486.52	-2.35
		16		156.85	-0.35	491.08	-1.44
		64		157.52	0.08	492.67	-1.12
		1	CPE4R	159.95	1.62	584.16	17.25
		4		165.44	5.11	605.46	21.52
		16		166.63	5.87	609.31	22.29
		64		166.87	6.02	610.02	22.44
10.30%		1	CPS4R	132.45	-0.24	402.63	-3.36
		4		133.37	0.45	409.98	-1.60
		16		134.72	1.46	418.58	0.47
		64		135.23	1.85	431.84	3.65
		1	CPE4R	134.35	1.19	489.76	17.55
		4		140.68	5.95	510.64	22.56
		16		142.15	7.06	516.42	23.95
		64		142.56	7.37	518.34	24.41

Effective mechanical behaviors of several random hole distributions were investigated. For demonstration purposes, three cases are illustrated for utilizing 16 holes RVE model, namely, uniform, random, and biased distributions. Holes were randomly distributed by deviating the center of each hole manually. Also, the last case shows the sixteen holes

locations biased towards the RVE edge. Predicted effective mechanical behaviors validated against test data of the corresponding porosity level are shown in **Figure 5.7** (i.e. RVE distributions are shown above the legend).

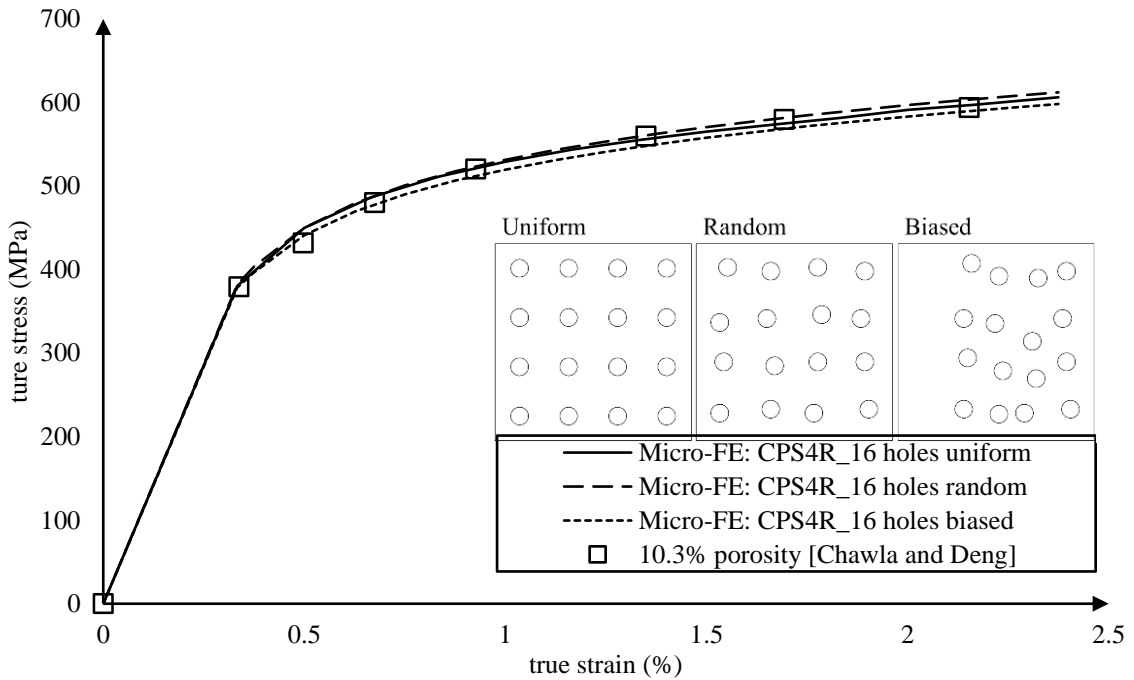


Figure 5.7 Predicted stress-strain curves for 16 holes RVE with different hole distributions.

It can be observed that the predicted behaviors using uniform, random and biased hole distribution are almost identical in the linear region as well as the onset of yielding. It can be observed that in the plastic region, there exists a slight difference between predicted curves. Noteworthy to mention that these slight differences in prediction results lie within the standard deviation of testing.

5.5.2 Microstructural local fields

Full-field contour plots were considered to investigate local microstructure behavior further. The von-Mises stresses at the final step of load application were used to compare different numbers of holes as presented in **Figure 5.8**. As can be seen, all evenly structured

RVEs showed localized stress concentration regions around holes with a maximum value towards the center and corners. Stresses were found to build up in a symmetric manner which can be correlated to the uniform distribution of holes. Also, along the diagonals between two holes at approximately at 45° , the highly localized stress concentration appeared to accumulate. Von-Mises values for relatively low deformations are significantly superior to predicted yield strength which anticipates localized plasticity in the vicinity of holes.

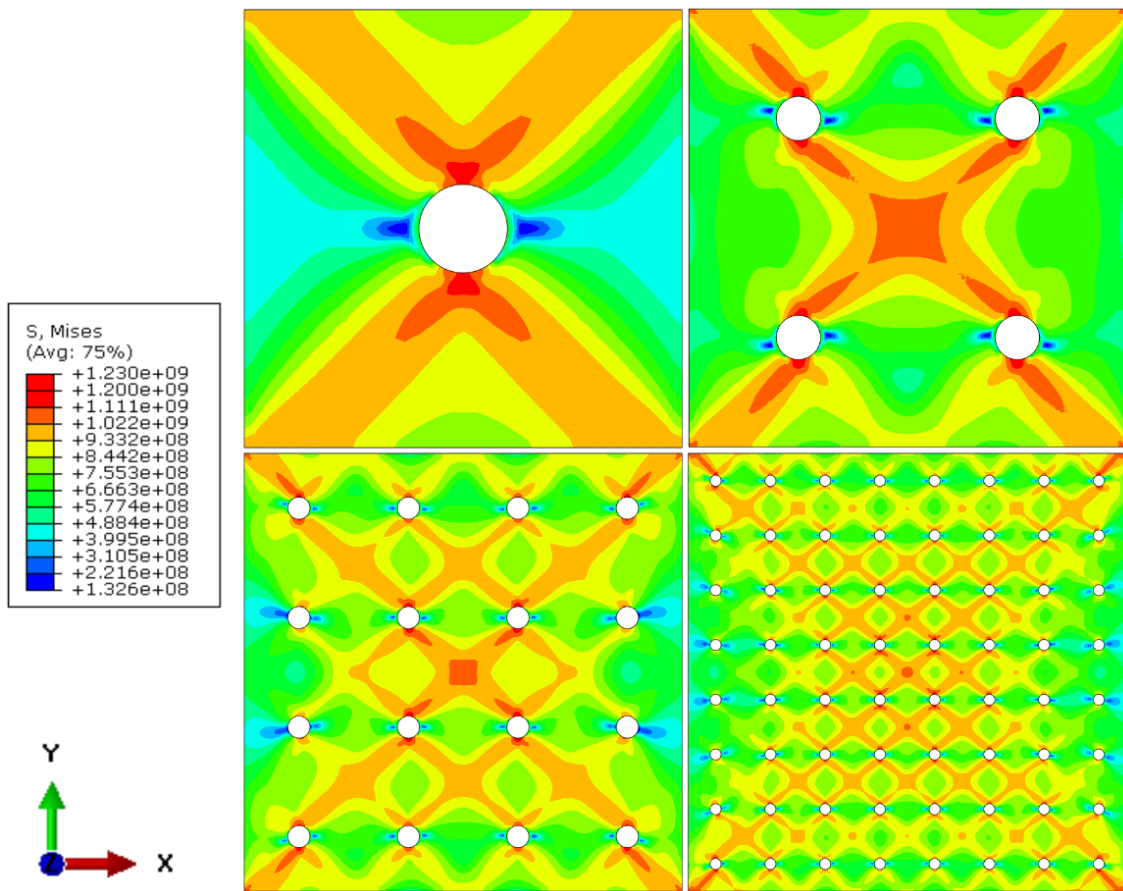


Figure 5.8 Von-Mises contour plots for RVEs with different holes number.

The stress field from both random and biased distributed RVEs are presented in **Figure 5.9**.

A substantial increase in stress concentration can be observed between holes in a closer

vicinity. Even though damage is not within the scope of current work, it is most likely to initiate at those regions where significantly localized plasticity occurs. In most cases, stresses around holes in the neighborhood of edges seemed to accumulate at approximately $\pm 45^\circ$. This may be correlated to the development of micromechanical slip bands in a ductile material.

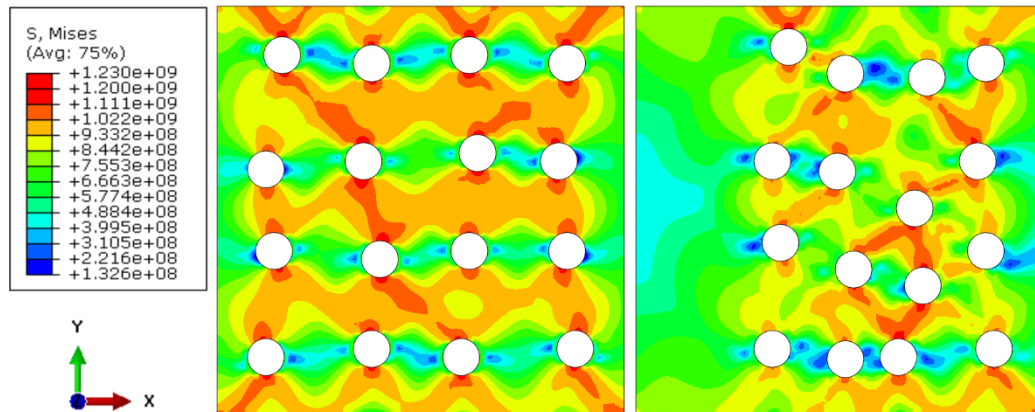


Figure 5.9 Von-Mises contour plots for 16 holes RVE with different hole distributions.

For potential extension of the current study to failure analysis, strain energy results are illustrated. Total plastic energy dissipation contour plots for uniform and random distributions are shown in **Figure 5.10** and **Figure 5.11**. Critical regions of plastically dissipated energy and von Mises stresses contours were consistent. Inspecting total energy dissipation in the microstructure suggests possible damage initiation regions. Closer micro-holes indicate a higher tendency to coalescence and merge into a single hole. This can be observed by the intense plastic energy dissipation between holes. This observation is in agreement with conclusions in (Chawla & Deng, 2003, 2005).

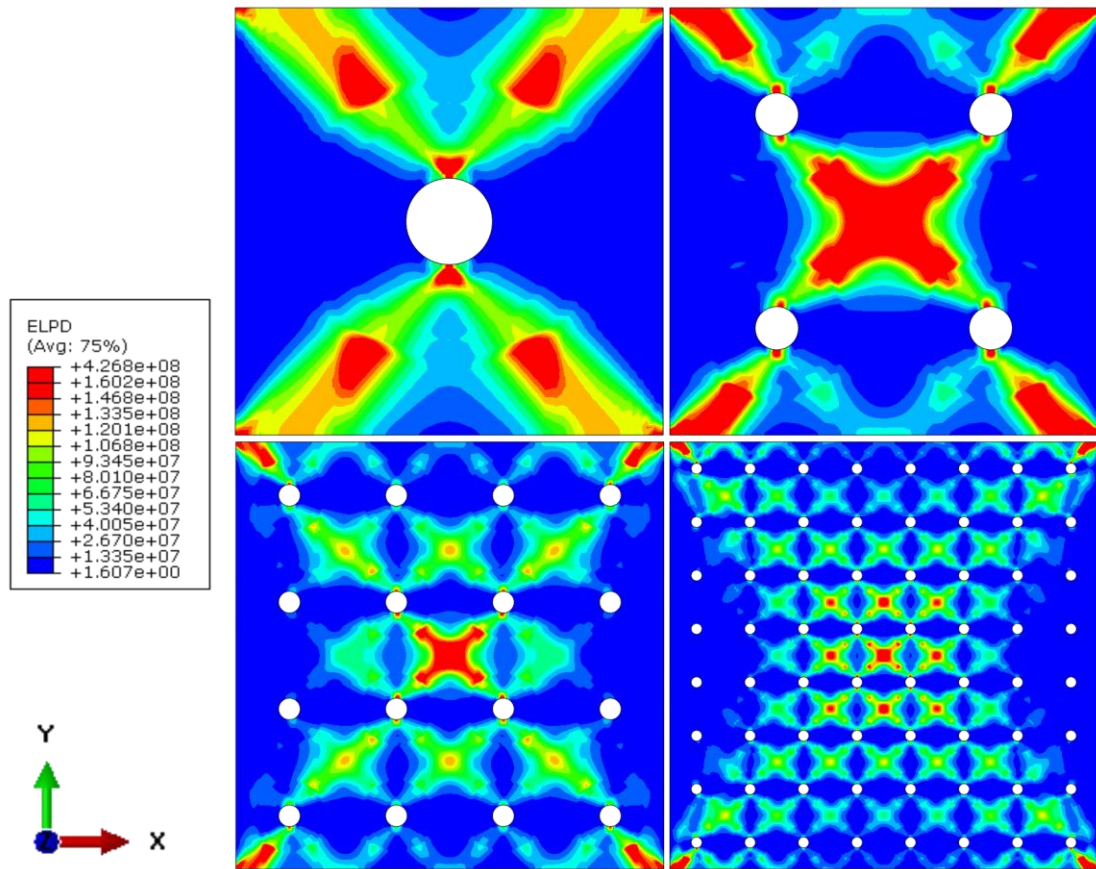


Figure 5.10 Total energy dissipated by plastic deformation in uniformly distributed holes RVEs.

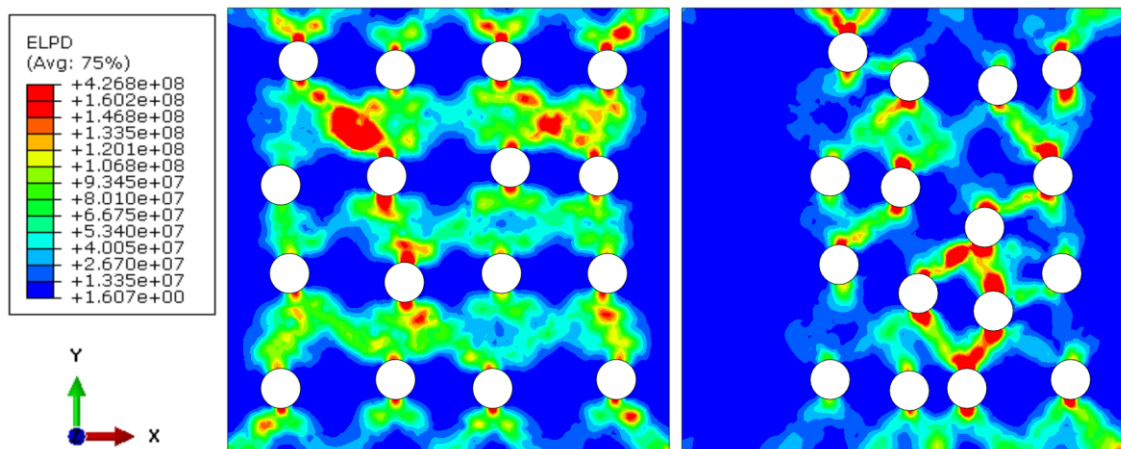


Figure 5.11 Total energy dissipated by plastic deformation in randomly distributed holes RVEs.

5.6 Conclusions

RVE-based micromechanical finite element simulations were proposed to predict the mechanical behavior of porous sintered steels under uniaxial loading in the low range (i.e., <10%). Three and Two-dimensional RVEs prediction results were compared, and the results were in excellent agreement. Two-dimensional RVEs requires a small fraction of computational effort compared to three-dimensional ones. The use of plane stress and strain elements was thoroughly investigated. Stress based convergent high quality meshes were ensured using appropriate partitioning and manual seeding. Four uniform distributions of holes/pores were investigated in addition to several random and biased distributions. The effective true stress-strain (linear and plastic behaviors) prediction results were validated against testing results from the literature. Predicted moduli together with yield stresses were compared to testing results and errors were documented. Local microstructural full-fields insights were also provided and discussed. From the presented work the following conclusions can be withdrawn

- Two-dimensional analysis proved the ability to efficiently capture effective behavior of porous material at significantly lower computational cost and can be utilized instead of three-dimensional one.
- Plane strain elements prediction results were found to overestimate modulus of elasticity with a relatively high error up to 10% while plane stress elements predicted the effective moduli with a maximum error of -2.81, i.e. lower bound.
- The predicted yield stresses using plane strain elements recorded errors varying from 17% to 24% consequently leading to a stiffer behavior causing a significant shift in the plastic flow curve. On the other hand, plane stress elements results were

in excellent agreement with testing results with a maximum error of -4.39% which lead to very close results in the plastic flow.

- Increasing number of holes in an RVE did not have a significant effect on predicted modulus. Therefore, using a center hole RVE is sufficient to estimate the micro-porosity effect on modulus. Contrarily, increasing the number of holes had a significant effect in plastic region predictions. Therefore, the center hole RVE model is not sufficient for predicting the effective plastic behavior as it leads to underestimated predictions.
- The current investigation identified the sufficient number of holes, $n = 16$, to accurately capture plastic behavior. There exist a minimum number of holes to represent the total porosity fraction in RVEs based on the actual size of micro-porosity in the material which confirms existing knowledge on general RVE modeling requirements.
- The local micromechanical von-Mises full-fields revealed stress concentration regions to be dependent on micro-holes distribution and locations.
- The total energy dissipated by plastic deformation full-fields provided insight into damage initiation and possible coalescence upon further loading. Higher energy dissipation was found in the neighborhood between closer holes.

5.7 References

- Abaqus Documentation*. (2014). Providence, Rhode Island: Dassault Systèmes.
- Attaran, M. (2017). The rise of 3-D printing: The advantages of additive manufacturing over traditional manufacturing. *Business Horizons*, 60(5), 677–688.
<https://doi.org/10.1016/j.bushor.2017.05.011>
- Babu, K. P., Mohite, P. M., & Upadhyay, C. S. (2018). Development of an RVE and its

- stiffness predictions based on mathematical homogenization theory for short fibre composites. *International Journal of Solids and Structures*, 130–131, 80–104. <https://doi.org/10.1016/j.ijsolstr.2017.10.011>
- Biswas, R., & Poh, L. H. (2017). A micromorphic computational homogenization framework for heterogeneous materials. *Journal of the Mechanics and Physics of Solids*, 102. <https://doi.org/10.1016/j.jmps.2017.02.012>
- Chawla, N., & Deng, X. (2003). Effect of Density on the Microstructure and Mechanical Behavior of Powder Metallurgy Fe-Mo-Ni Steels. ... in *Powder Metallurgy ...*, 6(March 2014), 7–257. Retrieved from <http://www.yunamedia.com/www.hoegtest.com/TechPapersv2/125.pdf>
- Chawla, N., & Deng, X. (2005). Microstructure and mechanical behavior of porous sintered steels. *Materials Science and Engineering A*, 390(1–2), 98–112. <https://doi.org/10.1016/j.msea.2004.08.046>
- Cheng, J., & Ghosh, S. (2015). A crystal plasticity FE model for deformation with twin nucleation in magnesium alloys. *International Journal of Plasticity*, 67, 148–170. <https://doi.org/10.1016/j.ijplas.2014.10.005>
- Collini, L., & Nicoletto, G. (2005). Determination of the relationship between microstructure and constitutive behaviour of nodular cast iron with a unit cell model. *The Journal of Strain Analysis for Engineering Design*, 40(2), 107–116. Retrieved from <https://doi.org/10.1243/030932405X7692>
- Dæhli, L. E. ., Faleskog, J., Børvik, T., & Hopperstada, O. S. (2016). Unit cell simulations and porous plasticity modelling for recrystallization textures in aluminium alloys. *Procedia Structural Integrity*, 2, 2535–2542. <https://doi.org/10.1016/j.prostr.2016.06.317>
- Debboub, S., Boumaiza, Y., & Boudour, A. (2012). Elasticity modulus evaluation for a porous material by acoustic methods. *IOP Conference Series: Materials Science and Engineering*, 28(1). <https://doi.org/10.1088/1757-899X/28/1/012009>
- Dewey, J. M. (1947). The elastic constants of materials loaded with non-rigid fillers. *Journal of Applied Physics*, 18(6), 578–581. <https://doi.org/10.1063/1.1697691>
- Dong, C. (2016). Effects of Process-Induced Voids on the Properties of Fibre Reinforced Composites. *Journal of Materials Science and Technology*, 32(7), 597–604. <https://doi.org/10.1016/j.jmst.2016.04.011>
- Elnekhaily, S. A., & Talreja, R. (2018). Damage initiation in unidirectional fiber composites with different degrees of nonuniform fiber distribution. *Composites Science and Technology*, 155. <https://doi.org/10.1016/j.compscitech.2017.11.017>
- Frazier, W. E. (2014). Metal additive manufacturing: A review. *Journal of Materials Engineering and Performance*, 23(6), 1917–1928. <https://doi.org/10.1007/s11665-014-0958-z>
- GAO, L., WANG, C., LIU, Z., & ZHUANG, Z. (2017). Theoretical aspects of selecting

- repeated unit cell model in micromechanical analysis using displacement-based finite element method. *Chinese Journal of Aeronautics*, 30(4), 1417–1426.
<https://doi.org/10.1016/j.cja.2017.05.010>
- Ghayoor, H., Hoa, S. V., & Marsden, C. C. (2018). A micromechanical study of stress concentrations in composites. *Composites Part B: Engineering*, 132.
<https://doi.org/10.1016/j.compositesb.2017.09.009>
- Gitman, I. M., Askes, H., & Sluys, L. J. (2007). Representative volume: Existence and size determination. *Engineering Fracture Mechanics*, 74(16), 2518–2534.
<https://doi.org/10.1016/j.engfracmech.2006.12.021>
- Guidault, P. A., Allix, O., Champaney, L., & Cornuault, C. (2008). A multiscale extended finite element method for crack propagation. *Computer Methods in Applied Mechanics and Engineering*, 197(5), 381–399.
<https://doi.org/10.1016/j.cma.2007.07.023>
- Gurson, A. L. (1977). Continuum Theory of Ductile Rupture by Void Nucleation and Growth: Part I—Yield Criteria and Flow Rules for Porous Ductile Media. *Journal of Engineering Materials and Technology*, 99(1), 2. <https://doi.org/10.1115/1.3443401>
- Hardin, R. A., & Beckermann, C. (2013). Effect of porosity on deformation, damage, and fracture of cast steel. *Metallurgical and Materials Transactions A: Physical Metallurgy and Materials Science*, 44(12), 5316–5332.
<https://doi.org/10.1007/s11661-013-1669-z>
- Hardin, R. a, & Beckermann, C. (2011). Measurement and Prediction of Mechanical Behavior of Cast Steel Plates with Centerline Porosity. *Proceedings of the 65th SFSA Technical and Operating Conference*, (5.4). Chicago, IL: Steel Founders' Society of America.
- Hardin, Richard A., & Beckermann, C. (2007). Effect of porosity on the stiffness of cast steel. *Metallurgical and Materials Transactions A: Physical Metallurgy and Materials Science*, 38 A(12), 2992–3006. <https://doi.org/10.1007/s11661-007-9390-4>
- HASSELMAN, D. P. H. (1963). Relation Between Effects of Porosity on Strength and on Young's Modulus of Elasticity of Polycrystalline Materials. *Journal of the American Ceramic Society*, 46(11), 564–565. <https://doi.org/10.1111/j.1151-2916.1963.tb14615.x>
- Hill, R. (1963). Elastic properties of reinforced solids: some theoretical principles. *Journal of the Mechanics and Physics of Solids*, 11(5), 357–372.
- Hollister, S. J., & Kikuchi, N. (1992). A comparison of homogenization and standard mechanics analyses for periodic porous composites. *Computational Mechanics*, 10(2), 73–95. <https://doi.org/10.1007/BF00369853>
- Hosseini-Toudeshky, H., & Jamalain, M. (2015). Simulation of micromechanical damage to obtain mechanical properties of bimodal Al using XFEM. *Mechanics of Materials*, 89, 229–240. <https://doi.org/10.1016/j.mechmat.2015.06.015>

- Jagota, A., Hui, C. Y., & Dawson, P. R. (1987). The determination of fracture toughness for a porous elastic-plastic solid. *International Journal of Fracture*, 33(2), 111–124. <https://doi.org/10.1007/BF00033743>
- Leszczynski, J., & Shukla, M. (2010). *Practical Aspects of Computational Chemistry*. Springer.
- Liang, X., Li, H., Yu, W., Jiang, X., & Zhang, Z. (2012). A numerical approximation to the elastic properties of hollow particle filled composites. *ICIC Express Letters*, 6(6), 1549–1554. [https://doi.org/10.1016/S0022-5096\(02\)00021-2](https://doi.org/10.1016/S0022-5096(02)00021-2)
- Liu, P., Fu, C., Li, T., & Shi, C. (1999). Relationship between tensile strength and porosity for high porosity metals. *Science in China, Series E: Technological Sciences*, 42(1), 100–107. <https://doi.org/10.1007/BF02917065>
- MACKENZIE, J. K. (1949). The elastic constants of a material containing spherical coated holes. *Arch. Mech.*, 47, 223–246.
- Matouš, K., Geers, M. G. D., Kouznetsova, V. G., & Gillman, A. (2017). A review of predictive nonlinear theories for multiscale modeling of heterogeneous materials. *Journal of Computational Physics*, 330, 192–220. <https://doi.org/10.1016/j.jcp.2016.10.070>
- Mbiakop, A., Constantinescu, A., & Danas, K. (2015). An analytical model for porous single crystals with ellipsoidal voids. *Journal of the Mechanics and Physics of Solids*, 84, 436–467. <https://doi.org/10.1016/j.jmps.2015.07.011>
- Mercelis, P., & Kruth, J. P. (2006). Residual stresses in selective laser sintering and selective laser melting. *Rapid Prototyping Journal*, 12(5), 254–265. <https://doi.org/10.1108/13552540610707013>
- Mirkhalaf, S. M., Andrade Pires, F. M., & Simoes, R. (2016). Determination of the size of the Representative Volume Element (RVE) for the simulation of heterogeneous polymers at finite strains. *Finite Elements in Analysis and Design*, 119, 30–44. <https://doi.org/10.1016/j.finel.2016.05.004>
- Mori, T., & Tanaka, K. (1973). Average stress in matrix and average elastic energy of materials with misfitting inclusions. *Acta Metallurgica*, 21(5), 571–574. [https://doi.org/10.1016/0001-6160\(73\)90064-3](https://doi.org/10.1016/0001-6160(73)90064-3)
- Morin, L., Leblond, J. B., & Kondo, D. (2015). A Gurson-type criterion for plastically anisotropic solids containing arbitrary ellipsoidal voids. *International Journal of Solids and Structures*, 77, 86–101. <https://doi.org/10.1016/j.ijsolstr.2015.05.021>
- Morin, L., Michel, J. C., & Leblond, J. B. (2017). A Gurson-type layer model for ductile porous solids with isotropic and kinematic hardening. *International Journal of Solids and Structures*, 118–119, 167–178. <https://doi.org/10.1016/j.ijsolstr.2017.03.028>
- Nguyen, V. P., Lloberas-Valls, O., Stroeven, M., & Sluys, L. J. (2011). Homogenization-based multiscale crack modelling: From micro-diffusive damage to macro-cracks. *Computer Methods in Applied Mechanics and Engineering*, 200(9–12), 1220–1236.

- <https://doi.org/10.1016/j.cma.2010.10.013>
- Oliver, J., Caicedo, M., Huespe, A. E., Hernández, J. A., & Roubin, E. (2017). Reduced order modeling strategies for computational multiscale fracture. *Computer Methods in Applied Mechanics and Engineering*, 313, 560–595.
<https://doi.org/10.1016/j.cma.2016.09.039>
- Oliver, J., Caicedo, M., Roubin, E., Huespe, A. E., & Hernández, J. A. (2015). Continuum approach to computational multiscale modeling of propagating fracture. *Computer Methods in Applied Mechanics and Engineering*, 294, 384–427.
<https://doi.org/10.1016/j.cma.2015.05.012>
- Omairey, S. L., Dunning, P. D., & Sriramula, S. (2018). Development of an ABAQUS plugin tool for periodic RVE homogenisation. *Engineering with Computers*, 0(0), 1–11. <https://doi.org/10.1007/s00366-018-0616-4>
- Pelissou, C., Baccou, J., Monerie, Y., & Perales, F. (2009). Determination of the size of the representative volume element for random quasi-brittle composites. *International Journal of Solids and Structures*, 46(14–15), 2842–2855.
<https://doi.org/10.1016/j.ijsolstr.2009.03.015>
- Perumal, L., Tso, C. P., & Leng, L. T. (2016). Analysis of thin plates with holes by using exact geometrical representation within XFEM. *Journal of Advanced Research*, 7(3), 445–452. <https://doi.org/10.1016/j.jare.2016.03.004>
- Ramberg, W., & Osgood, W. R. (1943). Description of stress-strain curves by three parameters. In *National Advisory Committee for Aeronautics*.
<https://doi.org/10.1016/j.matdes.2009.07.011>
- Reddy, J. N. (2014). *An Introduction to Nonlinear Finite Element Analysis: with applications to heat transfer, fluid mechanics, and solid mechanics*. Oxford: OUP.
- Roberts, a P., & Garboczi, E. J. (2000). Elastic properties of model porous ceramics. *Journal of the American Ceramic Society*, 83(12), 3041–3048.
<https://doi.org/10.1111/j.1151-2916.2000.tb01680.x>
- Saimoto, S., & Thomas, D. R. M. (1986). A novel method to measure the elastic modulus of polymers as a function of tensile deformation. *Journal of Materials Science*, 21(10), 3686–3690. <https://doi.org/10.1007/BF02403022>
- Schmitz, A., & Horst, P. (2014). A finite element unit-cell method for homogenised mechanical properties of heterogeneous plates. *Composites Part A: Applied Science and Manufacturing*, 61, 23–32. <https://doi.org/10.1016/j.compositesa.2014.01.014>
- Schneider, K., Klusemann, B., & Bargmann, S. (2016). Automatic three-dimensional geometry and mesh generation of periodic representative volume elements for matrix-inclusion composites. *Advances in Engineering Software*, 99, 177–188.
<https://doi.org/10.1016/j.advengsoft.2016.06.001>
- Sercombe, T. B., Xu, X., Challis, V. J., Green, R., Yue, S., Zhang, Z., & Lee, P. D. (2015). Failure modes in high strength and stiffness to weight scaffolds produced by

- Selective Laser Melting. *Materials and Design*, 67(November), 501–508.
<https://doi.org/10.1016/j.matdes.2014.10.063>
- Song, B., Zhao, X., Li, S., Han, C., Wei, Q., Wen, S., ... Shi, Y. (2015). Differences in microstructure and properties between selective laser melting and traditional manufacturing for fabrication of metal parts: A review. *Frontiers of Mechanical Engineering*, 10(2), 111–125. <https://doi.org/10.1007/s11465-015-0341-2>
- Soro, N., Brassart, L., Chen, Y., Veidt, M., Attar, H., & Dargusch, M. S. (2018). Finite element analysis of porous commercially pure titanium for biomedical implant application. *Materials Science and Engineering A*, 725(April), 43–50.
<https://doi.org/10.1016/j.msea.2018.04.009>
- Su, S. L., Rao, Q. H., & He, Y. H. (2013). Theoretical prediction of effective elastic constants for new intermetallic compound porous material. *Transactions of Nonferrous Metals Society of China (English Edition)*, 23(4), 1090–1097.
[https://doi.org/10.1016/S1003-6326\(13\)62570-4](https://doi.org/10.1016/S1003-6326(13)62570-4)
- Sumitomo, T., Cáceres, C. H., & Veidt, M. (2002). The elastic modulus of cast Mg-Al-Zn alloys. *Journal of Light Metals*, 2(1), 49–56. [https://doi.org/10.1016/S1471-5317\(02\)00013-5](https://doi.org/10.1016/S1471-5317(02)00013-5)
- Szost, B. A., Terzi, S., Martina, F., Boisselier, D., Prytuliak, A., Pirling, T., ... Jarvis, D. J. (2016). A comparative study of additive manufacturing techniques: Residual stress and microstructural analysis of CLAD and WAAM printed Ti-6Al-4V components. *Materials and Design*, 89, 559–567. <https://doi.org/10.1016/j.matdes.2015.09.115>
- Talebi, H., Silani, M., Bordas, S. P. A., Kerfriden, P., & Rabczuk, T. (2014). A computational library for multiscale modeling of material failure. *Computational Mechanics*, 53(5), 1047–1071. <https://doi.org/10.1007/s00466-013-0948-2>
- Toro, S., Sánchez, P. J., Blanco, P. J., De Souza Neto, E. A., Huespe, A. E., & Feijóo, R. A. (2016). Multiscale formulation for material failure accounting for cohesive cracks at the macro and micro scales. *International Journal of Plasticity*, 76, 75–110.
<https://doi.org/10.1016/j.ijplas.2015.07.001>
- Tvergaard, V., & Needleman, A. (1984). Analysis of the cup-cone fracture in a round tensile bar. *Acta Metallurgica*, 32(1), 157–169. [https://doi.org/10.1016/0001-6160\(84\)90213-X](https://doi.org/10.1016/0001-6160(84)90213-X)
- Yu, H., Hou, Z., Guo, X., Chen, Y., Li, J., Luo, L., ... Yang, T. (2018). Finite element analysis on flexural strength of Al₂O₃-ZrO₂ composite ceramics with different proportions. *Materials Science and Engineering A*, 738(May), 213–218.
<https://doi.org/10.1016/j.msea.2018.05.075>
- Zhang, J., Koo, B., Subramanian, N., Liu, Y., & Chattopadhyay, A. (2016). An optimized cross-linked network model to simulate the linear elastic material response of a smart polymer. *Journal of Intelligent Material Systems and Structures*, 27(11), 1461–1475. <https://doi.org/10.1177/1045389X15595292>

6 Extending the Ramberg-Osgood relationship to Account for Metal Porosity

6.1 Abstract

This article proposes an extended Ramberg-Osgood (R-O) relationship accounting for the effect of porosity on porous metals behavior under tension. Initially, microstructural unit cells satisfying continuity boundary conditions was employed to account for pores intensity and their effect on elastic-plastic behavior. Results obtained from micromechanical simulations coupled with regression analyses were utilized to express elastic-plastic behavior as a function of porosity. Therefore, mathematical relationships were successfully developed to extend the R-O model to account for porosity. Finally, for validation and assessment of developed relation, analytical and macro-mechanical finite element (FE) results were compared to those of testing. Comparisons at low porosity range, i.e. less than 10% proved an excellent agreement. It is concluded that multiscale FE analyses conducted successively in micro and macro scales efficiently delineated the effect of porosity on mechanical behavior. Moreover, these analyses enabled extending R-O relationship for accurate modeling of porous metals in low range porosity

6.2 Introduction

Additive manufacturing (AM) or three-dimensional (3D) printing has been rapidly emerging in many fields such as automotive, aerospace and biomedical. A paramount advantage of 3D printing over subtractive manufacturing is fabricating complex shaped components directly from computer-aided design (CAD) models while minimizing material waste (Allison et al., 2013; Attaran, 2017; Frazier, 2014). Fabricated components

vary from aircraft structural components to biomedical implants (Choren, Heinrich, & Silver-Thorn, 2013; Frazier, 2014; Soro et al., 2018; Zaharin et al., 2018). In AM processes materials are joined together using layering to form an object. For example, laser sintering (LS) methods produce metallic objects from powder metallurgy (PM) using laser(s) to selectively fuse or melt material locally in a layer by layer series (Gibson, Rosen, & Stucker, 2013). Layering process usually results in undesired material imperfections such as lack of fusion, micro-cracks and high porosity levels (R. A. Hardin & Beckermann, 2013; Szost et al., 2016; F. Wang, Williams, Colegrove, & Antonysamy, 2013). Most of the material defects especially residual porosity may be minimized but not avoided (Cao, Shen, Shao, & Burlion, 2018; R. a Hardin & Beckermann, 2011; Polasik, Williams, & Chawla, 2002).

Therefore, accounting for the porosity effect on material behavior is essential for early design stages. As a result, many relationships correlating the so-called effective modulus of elasticity to total porosity level have been proposed for various materials. For example, the work by Dewey (Dewey, 1947) proposed an extension to the early work of Goodier (GOODIER & N., 1933) by solving linear equations describing small deformations of a medium containing single spherical inclusion for any elastic constant. In his work, a linear relation was proposed correlating effective modulus to that of fully dense material. Similarly, Hasselman and Fulrath (HASSELMAN, 1962, 1963) proposed first-order relationships on elastic moduli dependency on the porosity of polycrystalline refractory materials. Power laws were also proposed to estimate moduli of elasticity as reported in the work of Phani et al. and Bert (Bert, 1985; Phani, 1986). Also, exponential laws were

proposed by Spriggs and Panakkal et al. in references (Panakkal, Willems, & Arnold, 1990; SPRIGGS, 1961) to estimate elastic modulus given total porosity fraction. Also, an exponential law for the dependence of mechanical strength on porosity was proposed by Knudsen (KNUDSEN, 1959). All these relations were developed to account for porosity on material deterioration from the linear regime to failure limits. However, these models focus on discretized material parameters as modulus of elasticity (i.e., linear behavior) and few of them predicts effective yield strength. Even though available relations provide an insight into the effective material properties compared to testing results of different materials, the precise accuracy of predictions may fail to reach a substantial confidence degree (Choren et al., 2013). Besides, most of analytical relations are based on a single inclusion assumption representing total volumetric porosity. In other words, microstructural features were marginally considered. Regarding plastic behavior, most commonly referenced is the Gurson-Tvergaard-Needleman (GTN) model which was initially proposed by Gurson (Gurson, 1977) and later extended by Tvergaard and Needleman (Tvergaard & Needleman, 1984). The original micromechanical model is based on spherically symmetric deformations of a single spherical inclusion representing total porosity in metals. GTN model implementation in mainstream FE codes is referred to as porous plasticity model (*Abaqus Documentation*, 2014). It can be used to study void growth and nucleation assuming a single void, and it is applicable to low porosity range (i.e., less than 10%). While the GTN model can be utilized to study localized plasticity and failure analysis, the model possesses a strict requirement for defining porous material elastic-plastic behavior. Moreover, nine material-specific parameters are to be determined from

substantial testing effort and model calibration (R. A. Hardin & Beckermann, 2013; R. a Hardin & Beckermann, 2011; Oh, Nam, Kim, & Miura, 2018; Schiavone, Abeygunawardana-Arachchige, & Silberschmidt, 2016). Finally, simulation runtime using the GTN model for a specimen sized domain would be in the order of several days (R. A. Hardin & Beckermann, 2013; R. a Hardin & Beckermann, 2011).

Similarly, parallel efforts utilizing multiscale FE modeling is widely used as versatile tool for different scale investigations on material behavior (e.g., micro/macro) (Oliver et al., 2017; Roters et al., 2010). For example, representative volume element (RVE) FE-based analyses have been widely used to predict elastic constants for anisotropic composites (Gusev, 1997). Usually, RVE is used to predict effective stiffness properties for anisotropic materials such as composites or a solid matrix with inclusion(s) (Miled, Sab, & Le Roy, 2011; Mori & Tanaka, 1973; Omairey et al., 2018). While RVE presents a solid foundation for predicting stiffness properties, homogenization results are limited to stiffness properties which are utilized to predict elastic properties (Elnekhaily & Talreja, 2018; Hollister & Kikuchi, 1992; Miled et al., 2011; Trofimov, Abaimov, Akhatov, & Sevostianov, 2018). In a recent study, porous plasticity modeling was combined with unit cell (UC) simulations for modeling recrystallization textures in aluminum alloys (Dæhli et al., 2016). UC analyses were used to calibrate the porous plasticity model, and results showed predictive capabilities (Dæhli et al., 2016). Also, another study proposed UC modeling using porous plasticity model for strongly anisotropic face-centered cubic (FCC) metals (Bryhni Dæhli, Faleskog, Børvik, & Hopperstad, 2017). A sequential least-square optimization was applied

on a single void UC, and numerical results were utilized to calibrate two out of nine material parameters regarding porous plasticity model (Bryhni Dæhli et al., 2017).

In the current work, the well-known Ramberg-Osgood (R-O) relationship is extended to account for porosity effect on elastic-plastic behavior. An extended R-O relationship would be of a primary benefit for early design stages utilizing AM technologies in manufacturing. Micromechanical investigations utilizing UC method to predict effective mechanical behavior of porous materials were conducted. UC models were implemented to study pore intensity, shape and distribution effect(s) on mechanical behavior. Numerically obtained stress-strain curves from micromechanical models were validated against relevant testing results reported in the literature for two types of steel. Upon validation, UC models were exploited to generate a sufficient number of stress-strain curves for regression analysis. Effective material behaviors at various levels of porosity factor were used to establish mathematical relationships. Following literature findings, regression analysis yielded exponential expressions as a function of porosity for both effective modulus and yield strength. Developed expressions were employed to modify the original R-O model to account for porosity. Extended R-O enabled capturing the effect of porosity on complete elastic-plastic behavior of porous metals. Effective behaviors at different levels of porosity factor were generated using the proposed R-O extension. Analytically generated curves were utilized to evaluate porous material parameters used in macroscale (specimen sized) FE models. Finally, numerically obtained results were validated against testing results.

6.3 Theoretical Background

The porosity fraction is usually evaluated from relative density which can be defined as the density ratio of porous material to that of the fully dense, i.e. sound material. Some of existing mathematical relationships correlating total volumetric porosity fraction, p to mechanical properties are emphasized to substantiate the proposed work. Several forms of mathematical expressions were available in literature such as power laws, linear and exponential relationships. Most of the mathematical expressions are similar where material constants vary depending on material behavior as well as being applicable to limited porosity ranges. For brevity purpose, only a few of available relationships considering different mathematical expressions are discussed. As an example on power laws, Eudier (Eudier, 1962) proposed a simple power law based on stress intensity factors of an infinite plate with a spherical pore/hole reading as

$$E_p \cong E_o \left(1 - 1.19p^{\frac{2}{3}} \right) \quad \text{(Eq.6.1)}$$

where E_p is the effective modulus of elasticity, E_o is modulus of elasticity of sound (i.e., fully dense) material. The validity range for Eudier's expression 0-35% porosity range. However, assessment against testing results of several sintered metals showed that errors tend to increase by approaching high levels of porosity factor, i.e. greater than 25%. Similarly, Bert (Bert, 1985) proposed a semi-empirical approach to accurately derive an effective modulus relationship as a function of porosity. The developed power included stress intensity factor K_o depending on inclusion, i.e. pore, shape (i.e. $K_o = 2$ for spherical inclusion) as

$$E_p \equiv E_o \left(1 - \left(\frac{p}{P_{max}} \right) \right)^{K_o P_{max}} \quad \text{(Eq.6.2)}$$

where P_{max} defines the maximum possible volumetric fraction of porosity depending on the inclusion shape. The expression was validated against available experimental results at the time of proposing work and showed good agreement for 0-20% porosity range. Noteworthy to mention, Bert (Bert, 1985) concluded that effective yield strength relationship could be similarly derived.

As an example on linear relationships, Dewey (Dewey, 1947) analytically derived linear relationships to evaluate effective modulus elasticity and yield strength and of a porous medium loaded with non-rigid fillers (gas), for derivation details the reader is referred to read the original article by Dewey (Dewey, 1947). The porosity dependent mathematical expressions read as

$$E_p = E_o(1 - ap) \quad \text{(Eq.6.3)}$$

$$\sigma_p = \sigma_o(1 - bp) \quad \text{(Eq.6.4)}$$

where σ_p is the effective yield stress, a and b are constants depending on dense materials parameters in addition to the gas pressure. Typical values for a and b assuming zero gas pressure are 0.25 and 0.75, respectively. Dewey's work was purely mathematical by providing a solution for linear equations describing elastic deformations of a medium containing spherical void of any elastic constants (Dewey, 1947). Similar relationship to (Eq.6.3) was proposed by Fryxell and Chandler (FRYXELL & CHANDLER, 1964) for a

2-17% porosity range and the material constant was independent of the pressure with a value of approximately 1.9. Also, Hasselman and Fultrath (HASSELMAN & FULRATH, 1964) proposed a similar linear relationship with the material constant, a as a function of Poisson's ratio of the dense material. In their work, the range of validity was fairly narrow (i.e., less than 2.5%). Other researchers proposed exponential equations such as the work by Knudsen (KNUDSEN, 1959) to predict the porosity dependent strength, S_p from the nominal material strength S_o as

$$S_p = S_o \exp(-mp) \quad (\text{Eq.6.5})$$

where m is the exponential constant and the negative sign signifies the deteriorating effect. (Eq.6.5) was found to be independent of pore size validated against their presented experimental data and it is valid for a moderate porosity range of 5-31% (KNUDSEN, 1959). Similar exponent based formula was proposed by Spriggs (SPRIGGS, 1961) to predict porosity dependent modulus reading as

$$E_p = E_o \exp(-mp) \quad (\text{Eq.6.6})$$

Validation against several reported experimental data for polycrystalline alumina was conducted by Spriggs (SPRIGGS, 1961). Exponential constant values were reported to vary between 2.7 to 4.3. Noteworthy to mention that (Eq.6.6) is valid for open as well as closed pores in addition to applicability to a wide range of porosity (0-37%). As can be observed that several models were developed either analytically and/or empirically with the objective of expressing effective elastic constants as a function of total volumetric porosity. It was

also demonstrated that each relationship is valid for a class of material(s) as well as certain porosity range(s) with the exception of Spriggs work which is valid to moderately wide porosity range (SPRIGGS, 1961). It seems that exponential laws are more accurate and their range of validity is moderately wider. The scope of current work lies within low porosity range, i.e. less than 10% for metals under tensile loads. An extension to the R-O relationship to account for porosity is the main objective of the current work. Hence, the R-O model for a general state of stress is briefly reviewed. The tensorial notation for general state of stress as per R-O model (Ramberg & Osgood, 1943) reads as

$$E \varepsilon_{ij} = (1 + \nu) \sigma_{Dev} - (1 - 2\nu) \sigma_{Hyd} I + \frac{3}{2} \alpha \left(\frac{\sigma_{Mises|eq}}{\sigma_y} \right)^{n-1} \sigma_{Dev} \quad (\text{Eq.6.7})$$

where ε_{ij} represents the strain tensor, σ_{ij} is the stress tensor, I is the identity matrix while σ_{Dev} and σ_{Hyd} are deviatoric and hydrostatic stresses as defined by (Eq.6.8) and (Eq.6.9), respectively. Finally, the equivalent Mises stress is denoted by $\sigma_{Mises|eq}$ and defined using (Eq.6.10).

$$\sigma_{Hyd} = -\frac{1}{3} \sigma_{ij} : I \quad (\text{Eq.6.8})$$

$$\sigma_{Dev} = \sigma_{ij} + \sigma_{Hyd} I \quad (\text{Eq.6.9})$$

$$\sigma_{Mises|eq} = \sqrt{\frac{3}{2} \sigma_{Dev} : \sigma_{Dev}} \quad (\text{Eq.6.10})$$

The relationship was originally developed by Ramberg and Osgood (Ramberg & Osgood, 1943) to describe stress-strain curves using three material dependent parameters. To better understand the R-O relationship, (Eq.6.7) for a uniaxial state of stress reads as

$$E\varepsilon = \sigma + \alpha\sigma \left(\frac{|\sigma|}{\sigma_y} \right)^{n-1} \quad \text{(Eq.6.11)}$$

where E is Young's modulus, ε is the strain, σ is uniaxial stress and the subscript y represents the yield stress. α is the yield offset while n is the hardening exponent, i.e. $n > 1$. In fact, R-O relationship is nonlinear at all stress levels where the nonlinearity becomes significant (for $n \geq 5$) upon reaching the yield stress σ_y . In other words, second term on the RHS of **(Eq.6.11)** will only start becoming significantly valued at stress levels close to yield strength. Otherwise, the term will approximately become minor resulting in a close to linear relationship (Hooke's law). The nonlinear relationship tends to behave as a linearly elastic perfectly plastic material for very high values of the hardening exponent, $n \geq 50$. For elaboration, consider a steel material with 196000 MPa modulus of elasticity and a yield stress of 400 MPa. **Figure 6.1** shows the effect of increasing n on stress-strain behavior of **(Eq.6.11)**. For better illustration, non-dimensional stress values are defined relative to the yield stress. Therefore, the onset of yielding corresponds to a unity value on the vertical axis. Strains are represented on the horizontal axis which is limited to 0.5% strain to provide a zoomed-in view on the onset of yielding region.

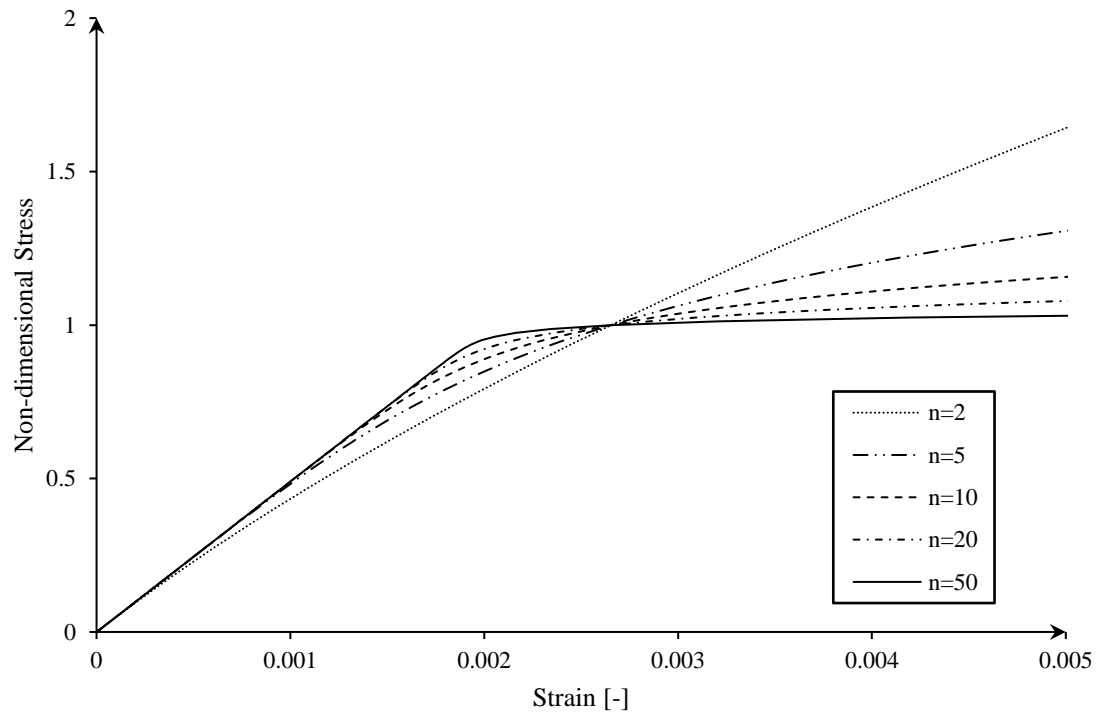


Figure 6.1 Non-dimensional stress vs. non-dimensional strain showing the effect of increasing the hardening exponent n .

R-O model lends itself supremacy being a single relationship describing mechanical behavior in linear elastic, non-linear elastic and plastic regimes, however it does not account for porosity. Therefore, current work proposes an extension to the original R-O relationship to account for porosity as will be explained in subsection 6.5.

6.4 Micromechanical investigations for model development

As reported in literature, porosity is well-known for deteriorating material behavior in both linear and non-linear regimes. Several porosity features can be used in microstructural characterization of porosity (e.g. shape, size and location). Micromechanical investigations are required to assess and evaluate effective mechanical behavior relying on pores intensity/shapes. Multiscale FE analysis framework was used for developing representative

UC models accounting for porosity. Applying necessary boundary conditions on continuum enabled predicting global macromechanical behavior. **Figure 6.2** shows a schematic diagram to elaborate FE modeling at different scales. For this purpose, microstructural representative UCs were implemented to study the effect of porosity on material behavior. To determine pore shape effect on predicted mechanical behavior, both regular circular and irregular pore shapes were used. Also, uniform and non-uniform pore distributions were used to investigate the effect of their locations. UCs predicted effective behaviors were validated against test data for two types of steel at different levels of porosity factor. Micromechanical UCs were used to determine the effective behaviors for porosity levels varying from 0-10%.

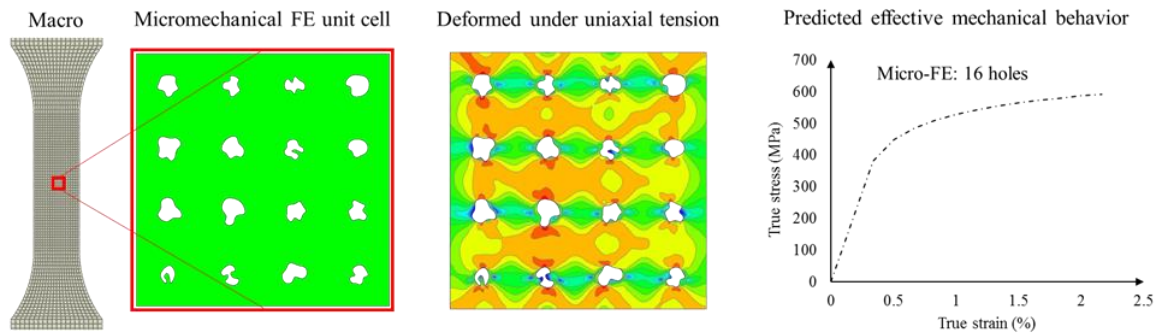


Figure 6.2 Schematic diagram showing finite element modeling at different scales.

To enable accurate representation of effective behavior using a micromechanical unit cells a minimum number of pores is required (Elnekhaily & Talreja, 2018; Ghayoor et al., 2018; Gusev, 1997). Convergence study should be conducted to determine the satisfactory number depending on the problem of interest. In the current work, convergence study on microstructure and associated effect on mechanical behavior led to a minimum number of 16 pores. Initial configuration showing geometry of each unit cell is shown in **Figure 6.3**

.Each UC had a side length of 100 microns and pores were uniformly distributed along each side. Uniform holes of circular cross-section were used to represent micro-porosity. Total area of 16 pores were used to calculate the radii for each porosity level.

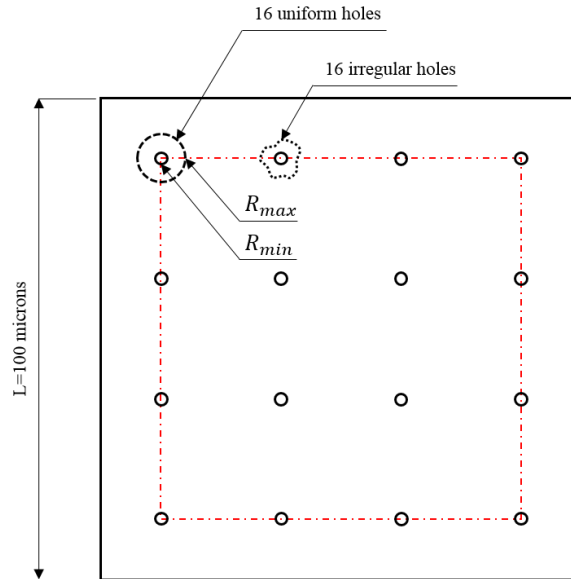


Figure 6.3 Unit cell geometry showing initial configuration (uniform distribution) of pore locations.

A chief objective of the proposed work is to analytically predict complete mechanical behavior of porous metals given the sound material behavior only. Hence, all micromechanical investigations were based on the material definition using calibration of sound materials. Calibration processes was performed on a solid (i.e. without pores) unit cell models and corresponding material parameters are documented in **Table 6.1**.

Table 6.1 Micromechanical unit cell models material parameters.

Material	E [GPa]	ν	σ_y [MPa]	n	α
Low strength steel	198	0.3	490	7.41	0.2
High strength steel	196	0.3	1462	9.31	0.1

The vicinity of pores is known to act as a stress concentrator, infinitesimal elements of very small characteristic lengths are required in those regions. Stress convergence mesh analysis

was conducted on each UC yielding an average mesh size of 20000 elements with slight variations depending on pores geometries. Elemental lengths varied from 0.18 μm to a maximum of 1 μm , infinitesimal elements were associated towards pores and gradually increased reaching its maximum value towards UC edges. This meshing technique was necessary to satisfactorily capture microstructural effect of porosity on mechanical behavior. A general static step was used to simulate load application of uniaxial state of stress. To ensure continuity of different scales and smoothness of predicted effective mechanical behaviors essential Dirichlet and Neumann boundary conditions were applied on each unit cell. One edge was constrained with zero degrees of freedom (Dirichlet type) while a uniform displacement boundary condition (Neumann type) was enforced on the opposing edge (Chawla & Deng, 2005). Nodes on both edges were constrained to be rigid to avoid local stress concentrations. These boundary conditions produce an average strain within the homogenized material.

To complicate matters, pore shapes are not necessary circular nor uniform as reported in references (Chawla, Williams, & Saha, 2003; Deng, Piotrowski, Chawla, & Narasimhan, 2008; Richard A. Hardin & Beckermann, 2007; Nimmo, 2004; Soro et al., 2018). Therefore, irregular random geometries were used to delineate whether the global mechanical behavior is going to be influenced or not. Irregular geometries were manually constructed assuring that pore area percentage is representative of the total porosity level investigated. In addition, the locations of pores were biased towards the right side of a UC.

Figure 6.4 presents numerical results in terms of stress-strain curves for a total porosity of 8%. For better demonstration of results, stress values were normalized by division on

maximum stress value at 5% strain. In addition, von Mises stress contour plots from different unit cell models are portrayed above the figure legend. Contour plots shows high stress concentrations in micro-pores vicinities which tend to intensify with irregular geometries and biased pore locations. Despite that pore shapes/distributions may significantly influence stress localization and hypothetically local plasticity, numerically evaluated mechanical behaviors proved to be identical in the linear region while there is negligible deviation in plastic regions. Also, uniformly distributed circular pores numerical results present the mean value of plastic flows.

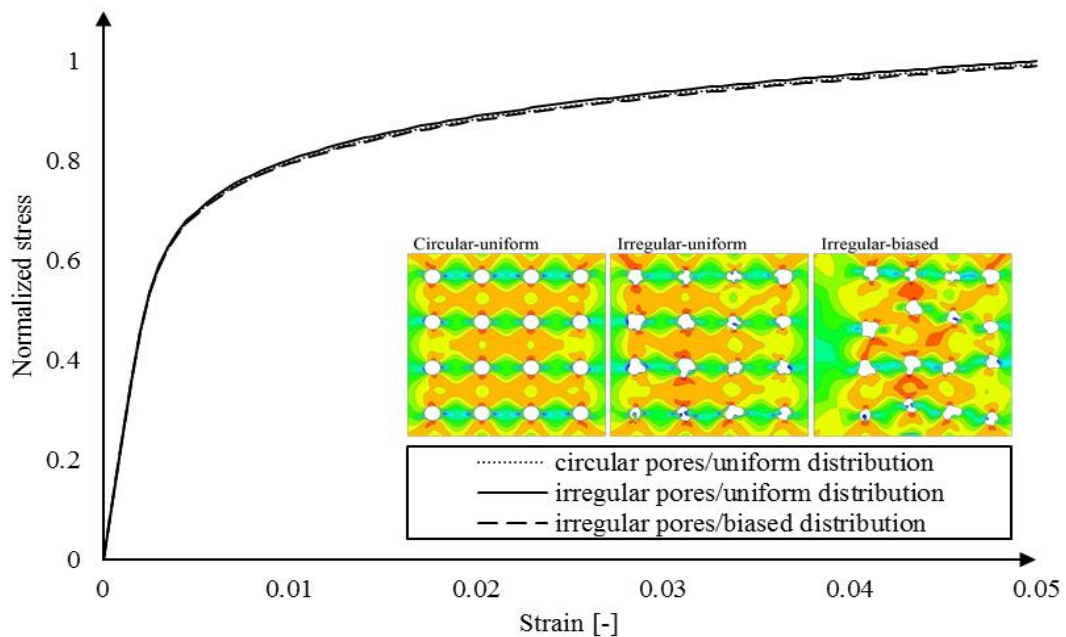


Figure 6.4 Pore shape/distribution effect on mechanical behavior.

For purpose of initial assessment of the proposed work, numerically obtained behaviors using micromechanical UCs were validated against testing results reported in literature. Test data regarding two types of powder metal (P/M) steel alloys produced using sintering manufacturing techniques were found relevant for comparisons. First, testing results of low

strength steel (Fe-0.85Mo-Ni P/M) reported by Chawla and Deng (Chawla & Deng, 2005). Second, are testing results of high strength steel (FL4405 P/M) reported by Stephens et al. (Stephens, Horn, Poland, & Sager, 1998b). Detailed material composition and specifications are found in references (Chawla & Deng, 2005; Stephens et al., 1998b). **Figure 6.5** shows the stress-strain curves of reproduced uniaxial tension testing data from reference (Chawla & Deng, 2005) against numerically obtained micromechanical results. Testing results are presented using different markers while prediction results are presented with different line types. The deteriorating effect of porosity can be observed starting with the linear region. Variation in modulus of elasticity was efficiently captured even for moderately low porosity level (e.g. 3.2%). For the 10.3% porosity, a significant drop in the modulus can be observed by a change of slope in the linear region. Also, the predicted plastic behaviors are in excellent agreement with test data of low strength steel. On the other hand, comparisons with reproduced testing results of high strength steel from reference (Stephens et al., 1998b) against corresponding UCs numerical results are presented in **Figure 6.6**. Beginning with the sound material behavior, micromechanical model efficiently captured effective stress-strain curve in both linear and plastic domains. At moderately small porosity level of 2.5%, numerically obtained effective behavior shown to be in excellent agreement compared to testing. Finally, at a porosity level of 10.1% the overall predicted behavior is in a very good agreement with test data. Inspecting numerically obtained behaviors for more than 10.0% porosity, **Figure 6.5** and **Figure 6.6**, a slight deviancy from testing data can be observed approximately at the onset of yielding.

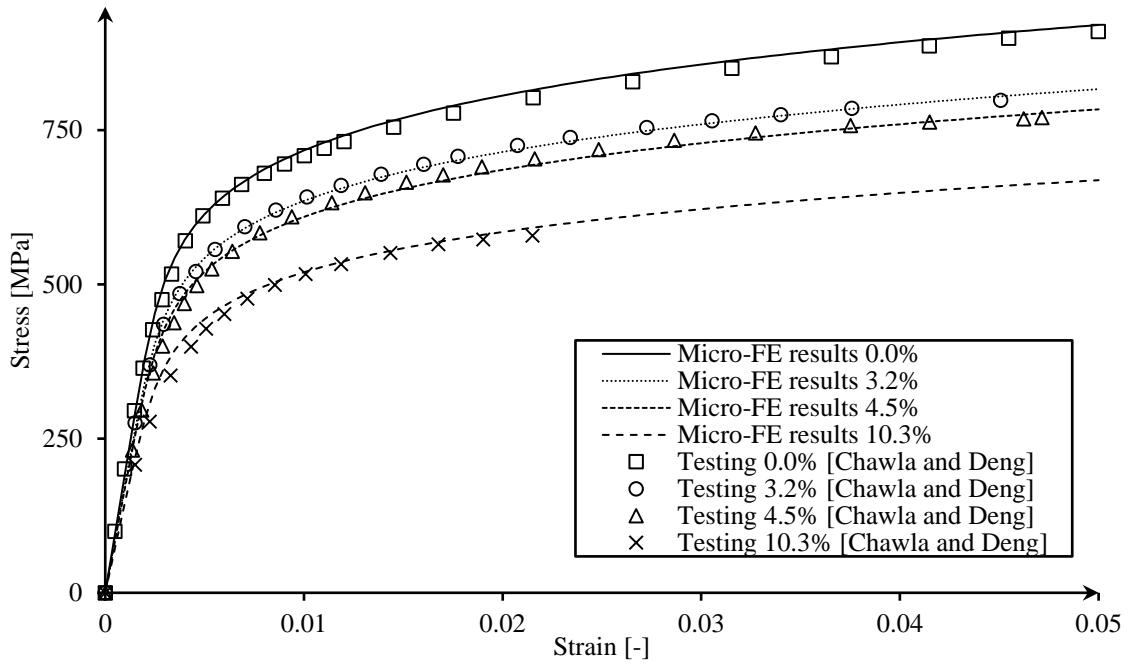


Figure 6.5 Low strength steel stress-strain curves: Micromechanical FE results vs testing (Chawla & Deng, 2005).

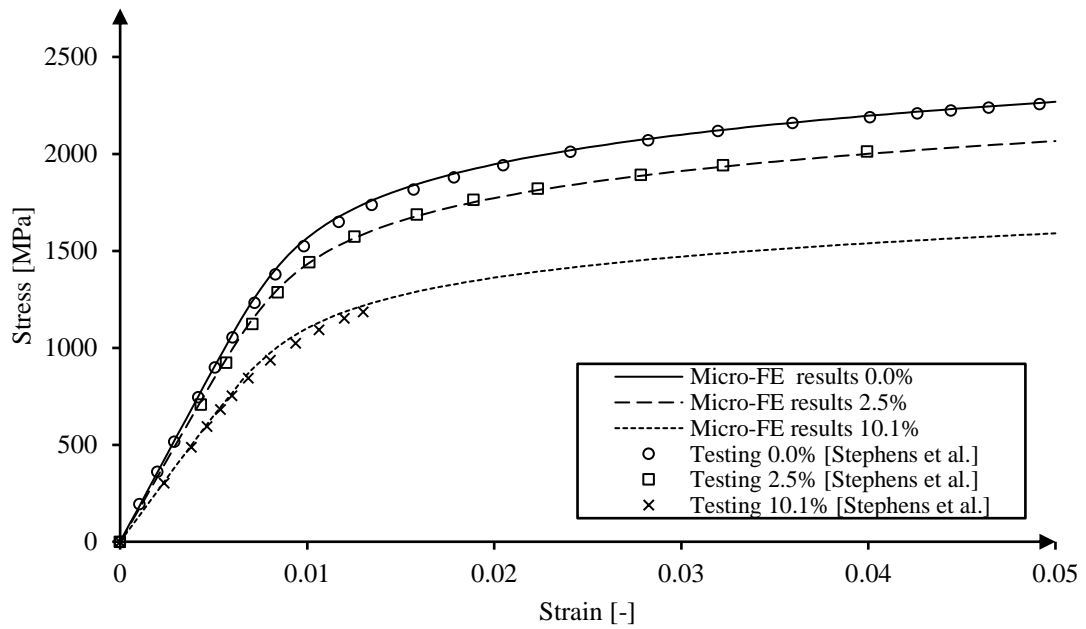


Figure 6.6 High strength steel stress-strain curves: Micromechanical FE results vs testing (Stephens et al., 1998b).

Noteworthy to mention that defining material behaviors using Ramberg-Osgood relationship enabled smooth predicted curves avoiding sharp transitions from linear to non-linear regions. This can be observed from comparisons with test data of low and high strength steels. To this end, micromechanical UCs were deemed sufficient for capturing the effect of microstructural porosity on material's mechanical behavior.

As discussed in literature, micro-porosity has proven to deteriorate the overall mechanical behavior of a porous material. Most of studies have shown that material deterioration in the linear region can be accounted for using an effective modulus. A relationship correlating total micro-porosity level is attainable based on analytical modeling and/or empirical data. Most of empirically based relationship are limited to the modulus of elasticity (i.e. linear behavior). Few studies proposed relationships to predict effective yield strength as a function of porosity. In fact, these empirical models remain limited to discrete values (e.g. E_{eff} or $\sigma_{y,eff}$) in addition to requiring numerous testing results. According to the authors' best of knowledge, none of available empirical models predicts complete (elastic-plastic) behavior for a porous material. Moreover, controlling porosity level during manufacturing process is one way or another challenging which resulted in insufficient testing results in literature. Hence, micromechanical UCs are used to numerically predict various effective behaviors at different porosity levels. In doing so, several numerically acquired effective mechanical behaviors will be obtainable saving time, effort and testing costs. Relying on which will enable development of statistically representative equations.

Consequently, same parameters for low strength steel micromechanical modeling documented in **Table 6.1** were used with 10 equally sized UCs with different pores radii.

The minimum and maximum radii were evaluated as 1.41 μm and 4.46 μm corresponding to total porosity levels of 1% and 10%, respectively. Details of each porosity level and corresponding pore radius are documented in **Table 6.2**. Numerically obtained stress-strain results corresponding to each porosity level are shown in **Figure 6.7**.

Table 6.2 Different levels of porosity factor and corresponding pore radii.

Porosity [%]	1	2	3	4	5	6	7	8	9	10
Pore radius [μm]	1.41	1.99	2.44	2.82	3.15	3.45	3.73	3.99	4.23	4.46

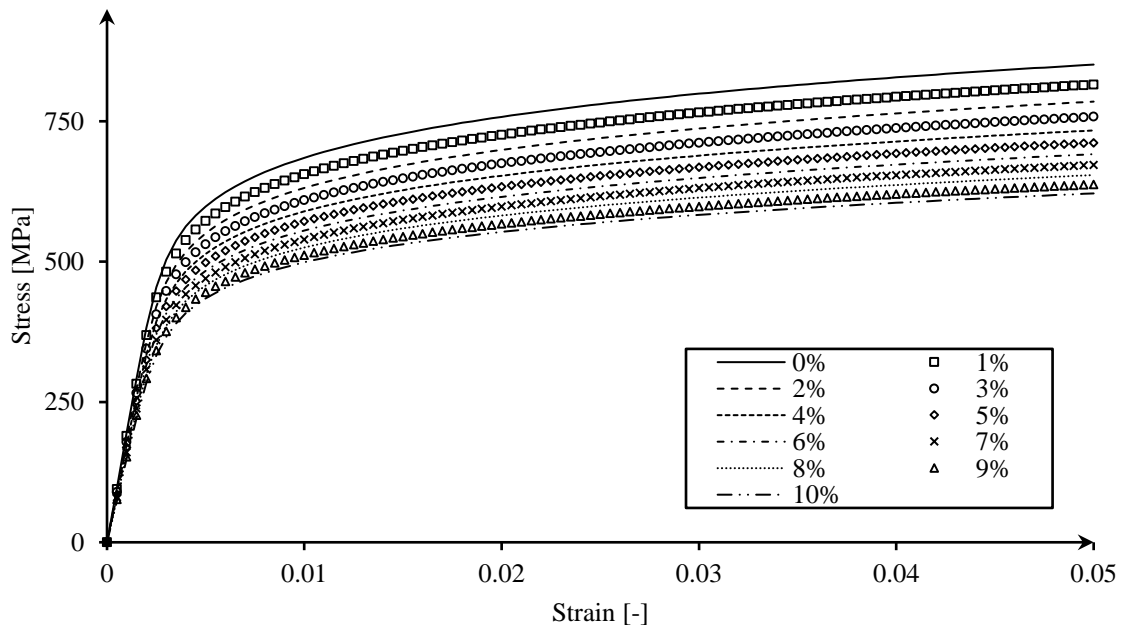


Figure 6.7 Low strength steel predicted stress-strain curves at 10 porosity levels.

As can be observed, stress-strain curves at different levels of porosity shows varying moduli and onset of plastic behavior while similar behaviors can be observed in the plastic region. This similarity indicates that the hardening exponent is almost unaltered. In other words, the significant change is limited to modulus of elasticity and the onset of plastic behavior. Hence, effective elastic moduli together with effective yield stresses at 0.2%

offset were evaluated from stress-strain curves and documented in **Table 6.3**. These results were used to construct relationship(s) between nominal values of the sound material and effective ones as a function of porosity.

Table 6.3 Effective material properties at different levels of porosity factor.

Porosity [%]	1	2	3	4	5	6	7	8	9	10
E_{eff} [GPa]	189.2	183.9	178.7	173.8	169.2	164.8	160.5	156.4	152.6	148.8
$\sigma_{y,eff}$ [MPa]	520.6	501.2	483.9	468.2	454.2	441.1	428.7	417.2	406.4	396.1

The effective material properties at 10 levels of porosity were adequate to construct statistically accurate governing relationships between nominal values of sound material and effective properties that of a porous one (Cain, 2017). **Figure 6.8** presents the statistical data used in constructing governing equations as a function of the porosity factor p . Also, governing equations for low strength steel together with corresponding root mean squared errors are shown on **Figure 6.8**.

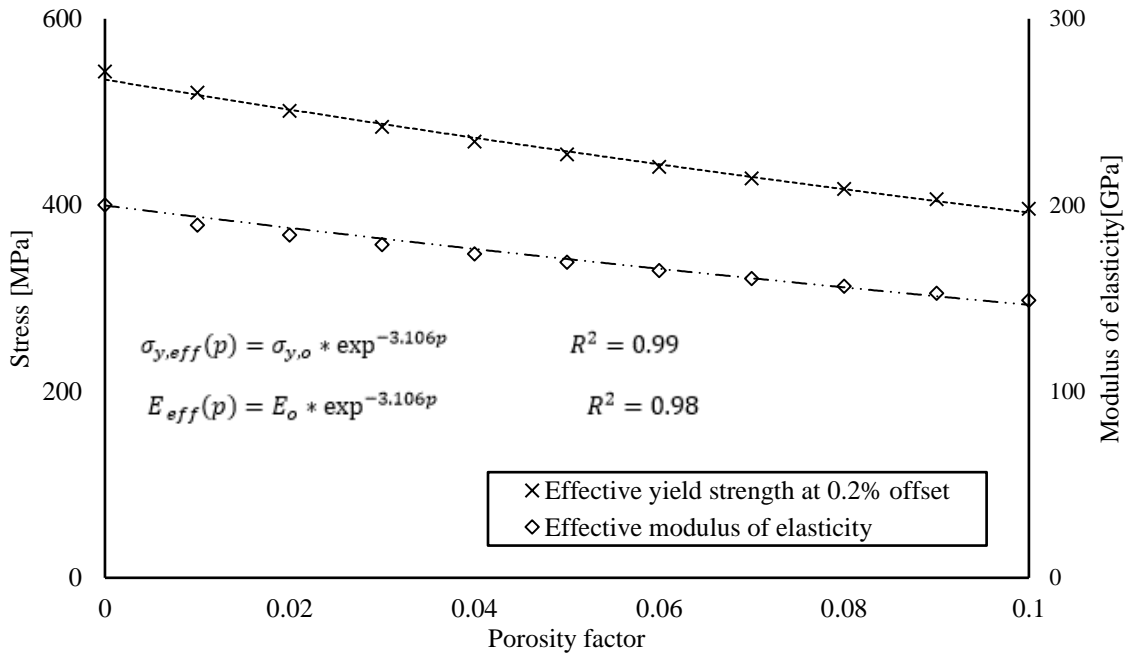


Figure 6.8 Effect of porosity on modulus of elasticity and yield strength.

Regression analyses yielded two exponential laws as a function of porosity fraction, p with root mean squared values of approximately 0.98 and 0.99 for effective modulus and yield, respectively. Both exponential constants had same negative value which can be attributed to the deteriorating effect of porosity. Noteworthy to mention that developed equations are in excellent agreement with the work proposed by Spriggs (SPRIGGS, 1961) as discussed in subsection 6.3. Produced exponential laws are valid for low range porosity, i.e. $\leq 10\%$ and can be written in a generic form as

$$E_{eff} = E_o e^{-mp} \quad \text{(Eq.6.12)}$$

$$\sigma_{y,eff} = \sigma_{y_o} e^{-mp} \quad \text{(Eq.6.13)}$$

where E_{eff} is the effective modulus of the porous material, $\sigma_{y,eff}$ represents the effect yield strength, m is the exponential constant while E_o and σ_{y_o} are the nominal values of a

non-porous material. To this end, the governing equation law was developed correlating effect of micro-porosity on effective mechanical behavior regarding linear region as well as the onset of plastic deformation. The following section is devoted for proposed extension of R-O relationship as a function of the porosity factor.

6.5 Extended Ramberg-Osgood relationship

Following the current study findings via micromechanical modeling both modulus of elasticity as well as yield stress have proven dependency on material's total porosity fraction. Modulus of elasticity defines linear region behavior while yield stress initiates plastic deformation. An extension to the R-O relationship to account for porosity effect on overall mechanical behavior is proposed. Supremacy of R-O relationship is that the full behavior is described using a single relationship which is not the case for most of available material models. The majority of available material models deals either with the linear behavior or plastic behavior. A combined model to describe the complete behavior does not exist. Therefore, proposing a single relationship depending on minimum number of material parameters would be of chief advantage for early design stages. Knowing which, an extension of R-O relationship is proposed. Inserting the effective properties relationships defined by (Eq.6.12) and (Eq.6.13) into (Eq.6.11) we get

$$E e^{-mp} \varepsilon = \sigma + \alpha \sigma \left(\frac{|\sigma|}{\sigma_y e^{-mp}} \right)^{n-1} \quad (\text{Eq.6.14})$$

(Eq.6.14) represents the foundation of a porosity dependent R-O relationship that can be used as a single relationship describing mechanical behavior of a porous material in both

elastic and plastic regimes. Noteworthy to mention that this extension depends on a single additional material parameter, m , to be calibrated from testing data and/or micromechanical modeling. To illustrate effect of porosity on stress-strain behavior using the developed extension of R-O relationship, total porosity was varied from zero to 10% and corresponding stress-strain curves are presented in **Figure 6.9**.

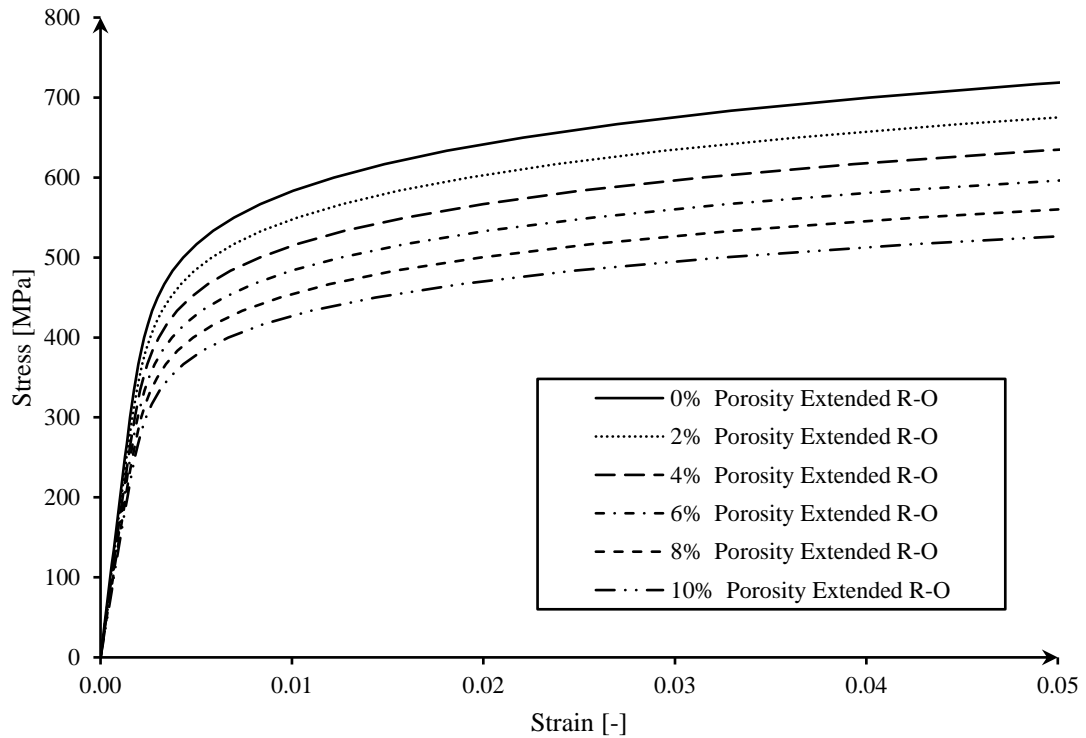


Figure 6.9 Effect of total porosity on stress-strain behavior using (Eq.6.14).

A slope change can be observed in the linear region at different levels of porosity which can be attributed to a reduction in modulus of elasticity. The deterioration effect of porosity on modulus of elasticity was efficiently captured using the exponential law defined by (Eq.6.12). Also, onset of non-linearity appears to vary as well as the onset of yielding or plastic flow depending on effective yield strength defined by (Eq.6.13). It is noteworthy to

mention that the developed relationship is smooth throughout both linear and plastic regimes in addition to the transition in between. In order to validate the proposed extension, (Eq.6.14) was used to generate various stress-strain behaviors at different levels of porosity matching relevant testing data. Effective mechanical behaviors were analytically generated at reported levels of porosity for low and high strength steels, corresponding results are presented in **Figure 6.10** and **Figure 6.11**, respectively.

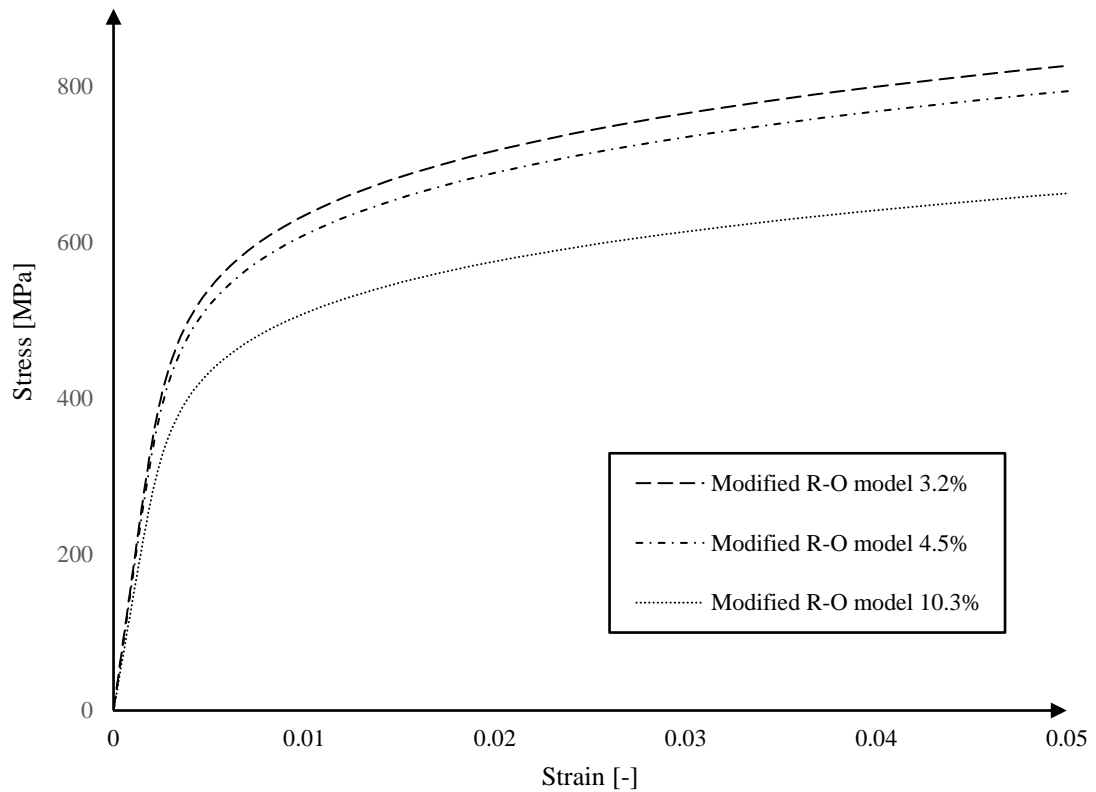


Figure 6.10 Predicted effective behavior using (Eq.6.14) for low strength steel at reported levels of porosity.

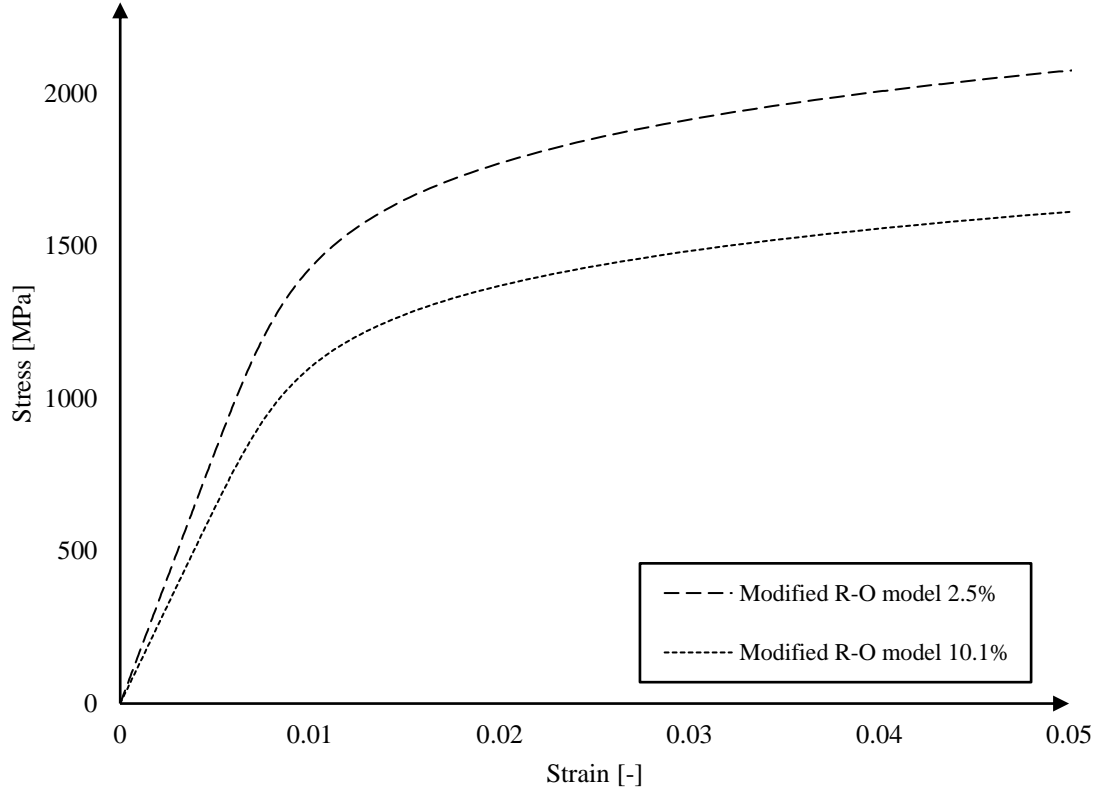


Figure 6.11 Predicted effective behavior using (Eq.6.14) for high strength steel at reported levels of porosity.

Generated curves were used to evaluate material parameters to be used in macroscale (specimen sized) modeling, obtained material parameters are documented in **Table 6.4**.

Table 6.4 Material parameters evaluated from extended R-O results at reported levels of porosity.

Material parameters	Model	P [%]	E_{eff} [GPa]	$\sigma_{y_{eff}}$ [MPa]	n [-]	α [-]	m [-]
Low strength steel	A	3.2	176.5	443.6	7.4	0.2	3.106
		4.5	169.6	426.1			
		10.3	141.6	355.8			
High strength steel	B	2.5	164.9	1380.0	9.3	0.1	3.106
		10.1	130.8	1048.0			

Two dumbbell were constructed in three dimensional finite element models corresponding to their relevant experimental results from literature (Chawla & Deng, 2005; Stephens et al., 1998b). A schematic diagram showing the profile of specimens used to construct both models along with loading conditions and the deformed models are shown in **Figure 6.12**. For convenience, the major geometric parameters for both models A and B are also provided in **Figure 6.12**.

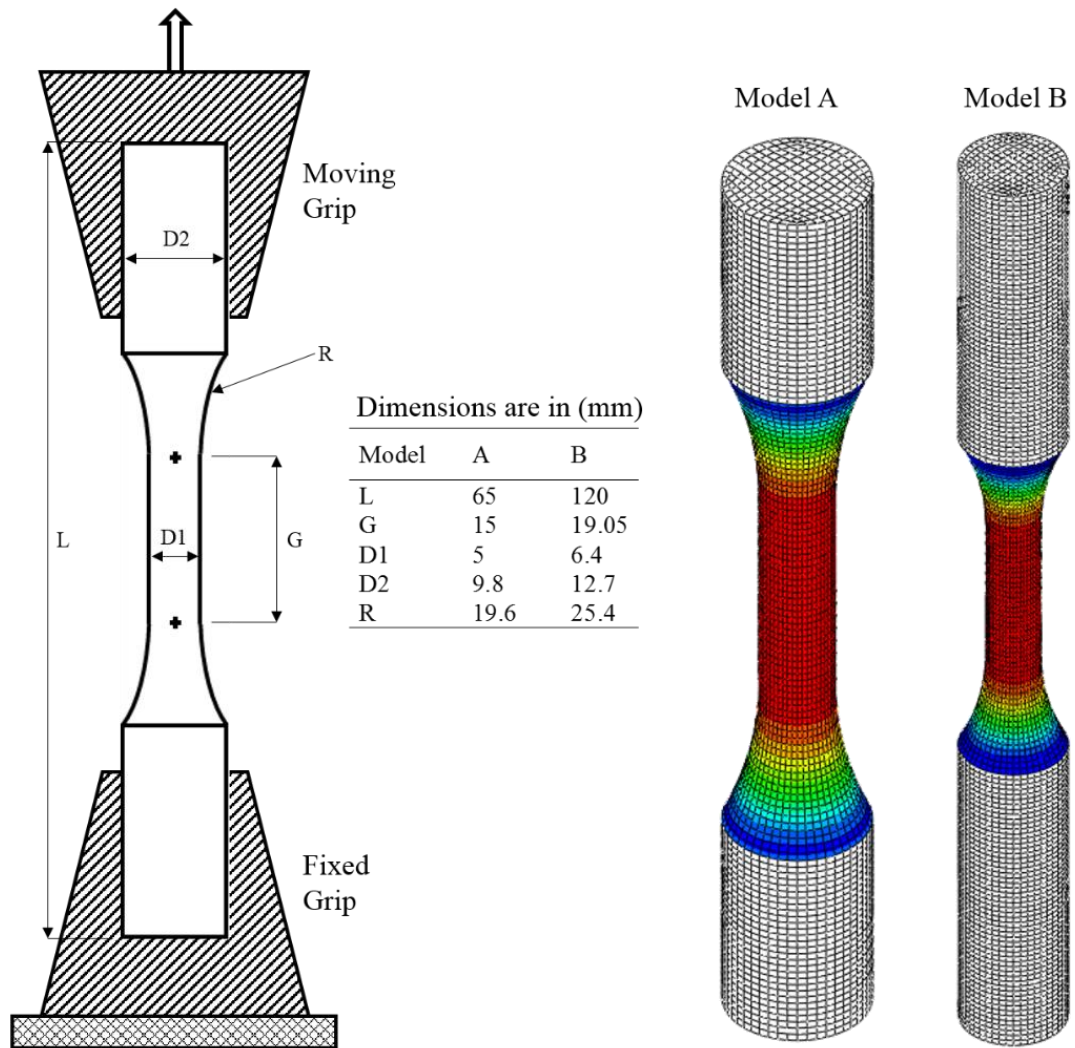


Figure 6.12 Specimen geometry and three-dimensional finite element models (not to scale).

Solid homogeneous section was defined for both models with 20-node quadratic brick elements, namely C3D20R to ensure precise results at each material point. Stress convergence analysis resulted in a mesh sizes of approximately 26000 and 33000 elements for models A and B, respectively. Following standard testing procedures specimens were fixed from one end while a monotonic displacement was applied on the other. Macromechanical numerically obtained stress-strain behaviors are plotted against corresponding testing results in **Figure 6.13** and **Figure 6.14**, respectively. As can be seen, numerical predictions at a macroscale based on the proposed Ramberg-Osgood extension are generally in excellent agreement with testing results. A chief advantage of numerical results is continuity of predicted behaviors which is attributed to the nature of Ramberg-Osgood model. The proposed extension shows an extended capability to account for effect of micro-porosity. Given that the extension is purely analytical, precise effective material properties were obtained which enabled accurate macromechanical numerical results.

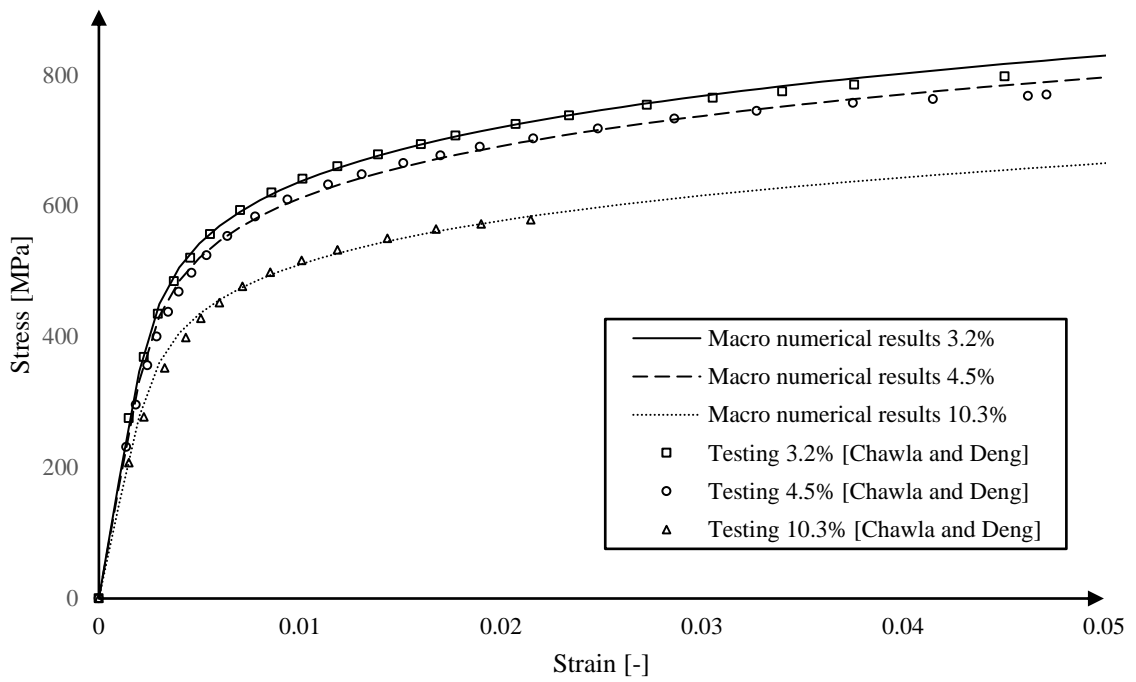


Figure 6.13 Low strength steel stress-strain curves: Macro numerical results vs testing (Chawla & Deng, 2005).

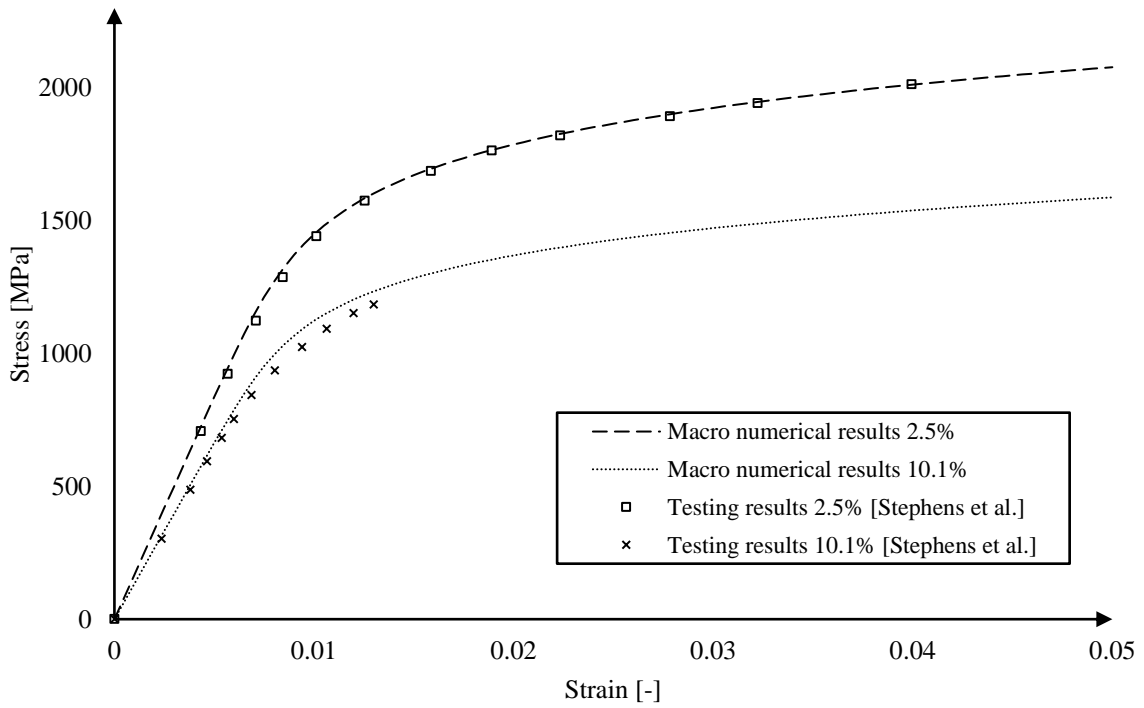


Figure 6.14 High strength steel stress-strain curves: Macro numerical results vs testing (Stephens et al., 1998b).

6.6 Conclusions

An extended Ramberg-Osgood (R-O) relationship accounting for effect of porosity on behavior of porous metals under tension was proposed. Micromechanical modeling utilizing unit cell (UC) method was employed to investigate pore intensity, shape and distribution effect(s) on elastic-plastic behaviors. Numerically obtained UC results were validated against testing results of low and high strength steels from literature. UC results proven predictive capabilities regarding porous materials behavior (i.e. elastic-plastic). Sufficient set of numerically obtained stress-strain data (i.e. 10 curves) were employed to generate effective material parameters for regression analysis. Two mathematical expressions correlating effective modulus and yield strength as a function of porosity were efficiently developed enabling the proposed R-O extension to account for porosity. The resulting relationship defined by **(Eq.6.14)** presents the proposed R-O extension accounting for porosity in elastic-plastic behavior. To assess and validate proposed extension, analytically obtained stress-strain curves at different levels of porosity were used to generate mechanical properties. Macroscale (specimen sized) FE models utilizing analytically generated properties were also provided. Noteworthy to mention that all provided comparisons within the context are were on elastic-plastic behavior basis rather than discrete points. Finally, macromechanical results were validated against those of testing. From the current work the following can be concluded;

- Micromechanical modeling using UC method proven to capture effect of micro-porosity on mechanical behavior given practical representative UC size and sufficient intensity of pores, see **Figure 6.5** and **Figure 6.6**.

- The pore shape/distribution effect on effective mechanical behavior under tension is negligible on linear behavior while a minor slight deviation from plastic region occurred in extreme cases, see **Figure 6.4**.
- Developed porosity mathematical expressions were in excellent agreement with the work by Spriggs. Also, both developed expressions yielded same exponential constant values which may signify that both material constants are similarly deteriorating, at least for presented validation with experimental data.
- A single relationship (extended R-O) was proposed to capture effect of porosity on complete elastic-plastic behavior relying on single additional parameter to be calibrated from testing and/or micromechanical modeling
- The extended R-O relationship, (**Eq.6.14**) has proven excellent analytical predictions capabilities compared with both macroscale numerical results and testing from literature.

6.7 References

- Abaqus Documentation*. (2014). Providence, Rhode Island: Dassault Systèmes.
- Allison, P. G., Grewal, H., Hammi, Y., Brown, H. R., Whittington, W. R., & Horstemeyer, M. F. (2013). Plasticity and Fracture Modeling/Experimental Study of a Porous Metal Under Various Strain Rates, Temperatures, and Stress States. *Journal of Engineering Materials and Technology*, 135(4), 041008. <https://doi.org/10.1115/1.4025292>
- Attaran, M. (2017). The rise of 3-D printing: The advantages of additive manufacturing over traditional manufacturing. *Business Horizons*, 60(5), 677–688. <https://doi.org/10.1016/j.bushor.2017.05.011>
- Bert, C. W. (1985). Prediction of elastic moduli of solids with oriented porosity. *Journal of Materials Science*, 20(6), 2220–2224. <https://doi.org/10.1007/BF01112307>
- Bryhni Dæhli, L. E., Faleskog, J., Børvik, T., & Hopperstad, O. S. (2017). Unit cell simulations and porous plasticity modelling for strongly anisotropic FCC metals.

- European Journal of Mechanics, A/Solids*, 65, 360–383.
<https://doi.org/10.1016/j.euromechsol.2017.05.004>
- Cain, J. W. (2017). Mathematics of Fitting Scientific Data. *Molecular Life Sciences*, 1–7.
https://doi.org/10.1007/978-1-4614-6436-5_560-1
- Cao, Y. J., Shen, W. Q., Shao, J. F., & Burlion, N. (2018). European Journal of Mechanics / A Solids Influences of micro-pores and meso-pores on elastic and plastic properties of porous materials. *European Journal of Mechanics / A Solids*, 72(March), 407–423. <https://doi.org/10.1016/j.euromechsol.2018.06.003>
- Chawla, N., & Deng, X. (2005). Microstructure and mechanical behavior of porous sintered steels. *Materials Science and Engineering A*, 390(1–2), 98–112.
<https://doi.org/10.1016/j.msea.2004.08.046>
- Chawla, N., Williams, J. J., & Saha, R. (2003). *Mechanical behavior and microstructure characterization of sinter-forged SiC particle reinforced aluminum matrix composites*. 2(2002), 215–227. [https://doi.org/10.1016/S1471-5317\(03\)00005-1](https://doi.org/10.1016/S1471-5317(03)00005-1)
- Choren, J. A., Heinrich, S. M., & Silver-Thorn, M. B. (2013). Young’s modulus and volume porosity relationships for additive manufacturing applications. *Journal of Materials Science*, 48(15), 5103–5112. <https://doi.org/10.1007/s10853-013-7237-5>
- Dæhli, L. E. ., Faleskog, J., Børvik, T., & Hopperstada, O. S. (2016). Unit cell simulations and porous plasticity modelling for recrystallization textures in aluminium alloys. *Procedia Structural Integrity*, 2, 2535–2542.
<https://doi.org/10.1016/j.prostr.2016.06.317>
- Deng, X., Piotrowski, G., Chawla, N., & Narasimhan, K. S. (2008). *Fatigue crack growth behavior of hybrid and prealloyed sintered steels Part I. Microstructure characterization*. 491, 19–27. <https://doi.org/10.1016/j.msea.2008.05.009>
- Dewey, J. M. (1947). The elastic constants of materials loaded with non-rigid fillers. *Journal of Applied Physics*, 18(6), 578–581. <https://doi.org/10.1063/1.1697691>
- Elnekhaily, S. A., & Talreja, R. (2018). Damage initiation in unidirectional fiber composites with different degrees of nonuniform fiber distribution. *Composites Science and Technology*, 155. <https://doi.org/10.1016/j.compscitech.2017.11.017>
- Eudier, M. (192AD). The Mechanical Properties of Sintered Low-Alloy Steels. *Otolaryngology–Head and Neck Surgery*, 9(1), 278–290.
<https://doi.org/10.1177/019459988609500112>
- Frazier, W. E. (2014). Metal additive manufacturing: A review. *Journal of Materials Engineering and Performance*, 23(6), 1917–1928. <https://doi.org/10.1007/s11665-014-0958-z>
- FRYXELL, R. E., & CHANDLER, B. A. (1964). Creep, Strength, Expansion, and Elastic Moduli of Sintered BeO As a Function of Grain Size, Porosity, and Grain Orientation. *Journal of the American Ceramic Society*, 47(6), 283–291.
<https://doi.org/10.1111/j.1151-2916.1964.tb14417.x>

- Ghayoor, H., Hoa, S. V., & Marsden, C. C. (2018). A micromechanical study of stress concentrations in composites. *Composites Part B: Engineering*, 132. <https://doi.org/10.1016/j.compositesb.2017.09.009>
- Gibson, I., Rosen, D., & Stucker, B. (2013). Standard Terminology for Additive Manufacturing Technologies. *Rapid Manufacturing Association*, 10–12. <https://doi.org/10.1520/F2792-12A.2>
- GOODIER, & N., J. (1933). Concentration of Stress around Spherical and Cylindrical Inclusions and Flaws. *T. A. S. M. E.*, 55, 39. Retrieved from <http://ci.nii.ac.jp/naid/20000117887/en/>
- Gurson, A. L. (1977). Continuum Theory of Ductile Rupture by Void Nucleation and Growth: Part I—Yield Criteria and Flow Rules for Porous Ductile Media. *Journal of Engineering Materials and Technology*, 99(1), 2. <https://doi.org/10.1115/1.3443401>
- Gusev, A. A. (1997). Representative volume element size for elastic composites: A numerical study. *Journal of the Mechanics and Physics of Solids*, 45(9), 1449–1459. [https://doi.org/10.1016/S0022-5096\(97\)00016-1](https://doi.org/10.1016/S0022-5096(97)00016-1)
- Hardin, R. A., & Beckermann, C. (2013). Effect of porosity on deformation, damage, and fracture of cast steel. *Metallurgical and Materials Transactions A: Physical Metallurgy and Materials Science*, 44(12), 5316–5332. <https://doi.org/10.1007/s11661-013-1669-z>
- Hardin, R. a, & Beckermann, C. (2011). Measurement and Prediction of Mechanical Behavior of Cast Steel Plates with Centerline Porosity. *Proceedings of the 65th SFSA Technical and Operating Conference*, (5.4). Chicago, IL: Steel Founders' Society of America.
- Hardin, Richard A., & Beckermann, C. (2007). Effect of porosity on the stiffness of cast steel. *Metallurgical and Materials Transactions A: Physical Metallurgy and Materials Science*, 38 A(12), 2992–3006. <https://doi.org/10.1007/s11661-007-9390-4>
- HASSELMAN, D. P. H. (1962). On the Porosity Dependence of the Elastic Moduli of Polycrystalline Refractory Materials. *Journal of the American Ceramic Society*, 45(9), 452–453. <https://doi.org/10.1111/j.1151-2916.1962.tb11191.x>
- HASSELMAN, D. P. H. (1963). Relation Between Effects of Porosity on Strength and on Young's Modulus of Elasticity of Polycrystalline Materials. *Journal of the American Ceramic Society*, 46(11), 564–565. <https://doi.org/10.1111/j.1151-2916.1963.tb14615.x>
- HASSELMAN, D. P. H., & FULRATH, R. M. (1964). Effect of Small Fraction of Spherical Porosity on Elastic Moduli of Glass. *Journal of the American Ceramic Society*, 47(1), 52–53. <https://doi.org/10.1111/j.1151-2916.1964.tb14644.x>
- Hollister, S. J., & Kikuchi, N. (1992). A comparison of homogenization and standard mechanics analyses for periodic porous composites. *Computational Mechanics*, 10(2), 73–95. <https://doi.org/10.1007/BF00369853>

- KNUDSEN, F. P. (1959). Dependence of Mechanical Strength of Brittle Polycrystalline Specimens on Porosity and Grain Size. *Journal of the American Ceramic Society*, 42(8), 376–387. <https://doi.org/10.1111/j.1151-2916.1959.tb13596.x>
- Miled, K., Sab, K., & Le Roy, R. (2011). Effective elastic properties of porous materials: Homogenization schemes vs experimental data. *Mechanics Research Communications*, 38(2), 131–135. <https://doi.org/10.1016/j.mechrescom.2011.01.009>
- Mori, T., & Tanaka, K. (1973). Average stress in matrix and average elastic energy of materials with misfitting inclusions. *Acta Metallurgica*, 21(5), 571–574. [https://doi.org/10.1016/0001-6160\(73\)90064-3](https://doi.org/10.1016/0001-6160(73)90064-3)
- Nimmo, J. R. (2004). Porosity and pore size distribution. *Encyclopedia of Soils in the Environment*, 295–303. <https://doi.org/10.1016/B978-0-12-409548-9.05265-9>
- Oh, Y., Nam, H., Kim, Y., & Miura, N. (2018). International Journal of Pressure Vessels and Piping Application of the GTN model to ductile crack growth simulation in through-wall cracked pipes. *International Journal of Pressure Vessels and Piping*, 159(November 2017), 35–44. <https://doi.org/10.1016/j.ijpvp.2017.11.006>
- Oliver, J., Caicedo, M., Huespe, A. E., Hernández, J. A., & Roubin, E. (2017). Reduced order modeling strategies for computational multiscale fracture. *Computer Methods in Applied Mechanics and Engineering*, 313, 560–595. <https://doi.org/10.1016/j.cma.2016.09.039>
- Omairey, S. L., Dunning, P. D., & Sriramula, S. (2018). Development of an ABAQUS plugin tool for periodic RVE homogenisation. *Engineering with Computers*, 0(0), 1–11. <https://doi.org/10.1007/s00366-018-0616-4>
- Panakkal, J. P., Willems, H., & Arnold, W. (1990). Nondestructive evaluation of elastic parameters of sintered iron powder compacts. *Journal of Materials Science*, 25(2), 1397–1402. <https://doi.org/10.1007/BF00585456>
- Phani, K. K. (1986). Elastic-constant-porosity relations for polycrystalline thoria. *Journal of Materials Science Letters*, 5(7), 747–750. <https://doi.org/10.1007/BF01730236>
- Polasik, S. J., Williams, J. J., & Chawla, N. (2002). *Fatigue Crack Initiation and Propagation of Binder-Treated Powder Metallurgy Steels*. 33(January), 73–81.
- Ramberg, W., & Osgood, W. R. (1943). Description of stress-strain curves by three parameters. In *National Advisory Committee for Aeronautics*. <https://doi.org/10.1016/j.matdes.2009.07.011>
- Roters, F., Eisenlohr, P., Hantcherli, L., Tjahjanto, D. D., Bieler, T. R., & Raabe, D. (2010). Overview of constitutive laws, kinematics, homogenization and multiscale methods in crystal plasticity finite-element modeling: Theory, experiments, applications. *Acta Materialia*, 58(4), 1152–1211. <https://doi.org/10.1016/j.actamat.2009.10.058>
- Schiavone, A., Abeygunawardana-Arachchige, G., & Silberschmidt, V. V. (2016). Crack

- initiation and propagation in ductile specimens with notches: experimental and numerical study. *Acta Mechanica*, 227(1), 203–215. <https://doi.org/10.1007/s00707-015-1425-0>
- Soro, N., Brassart, L., Chen, Y., Veidt, M., Attar, H., & Dargusch, M. S. (2018). Finite element analysis of porous commercially pure titanium for biomedical implant application. *Materials Science and Engineering A*, 725(April), 43–50. <https://doi.org/10.1016/j.msea.2018.04.009>
- SPRIGGS, R. M. (1961). Expression for Effect of Porosity on Elastic Modulus of Polycrystalline. *Journal of The American Ceramic Society-Discussions and Notes*, 28(1), 1960–1961.
- Stephens, R. I., Horn, J. J., Poland, D. D., & Sager, E. A. (1998). Influence of Density and Porosity Size and Shape on Fatigue and Fracture Toughness of High Strength FL4405 P/M Steel. *Effects of Product Quality and Design Criteria on Structural Integrity, STP1337-EB*, 72–101. Retrieved from <https://doi.org/10.1520/STP12343S>
- Szost, B. A., Terzi, S., Martina, F., Boisselier, D., Prytuliak, A., Pirling, T., ... Jarvis, D. J. (2016). A comparative study of additive manufacturing techniques: Residual stress and microstructural analysis of CLAD and WAAM printed Ti-6Al-4V components. *Materials and Design*, 89, 559–567. <https://doi.org/10.1016/j.matdes.2015.09.115>
- Trofimov, A., Abaimov, S., Akhatov, I., & Sevostianov, I. (2018). On the bounds of applicability of two-step homogenization technique for porous materials. *International Journal of Engineering Science*, 123, 117–126. <https://doi.org/10.1016/j.ijengsci.2017.11.017>
- Tvergaard, V., & Needleman, A. (1984). Analysis of the cup-cone fracture in a round tensile bar. *Acta Metallurgica*, 32(1), 157–169. [https://doi.org/10.1016/0001-6160\(84\)90213-X](https://doi.org/10.1016/0001-6160(84)90213-X)
- Wang, F., Williams, S., Colegrove, P., & Antonysamy, A. A. (2013). Microstructure and mechanical properties of wire and arc additive manufactured Ti-6Al-4V. *Metallurgical and Materials Transactions A: Physical Metallurgy and Materials Science*, 44(2), 968–977. <https://doi.org/10.1007/s11661-012-1444-6>
- Zaharin, H., Abdul Rani, A., Azam, F., Ginta, T., Sallih, N., Ahmad, A., ... Zulkifli, T. Z. A. (2018). Effect of Unit Cell Type and Pore Size on Porosity and Mechanical Behavior of Additively Manufactured Ti6Al4V Scaffolds. *Materials*, 11(12), 2402. <https://doi.org/10.3390/ma11122402>

7 Two-stage finite element modeling procedure to predict elastoplastic behavior and damage of porous metals

7.1 Abstract

The current article presents two-stage finite element analysis procedures employing micro/macromechanical models to predict the effective mechanical behavior of porous metals in addition to its final failure under tension. Micromechanical three-dimensional representative volume elements (RVEs) with single ellipsoidal void were employed to predict effective elastic-plastic behaviors. Python script was developed and implemented in the commercial finite element software Abaqus to analyze the effect of pore shape on mechanical behaviors. Post-processing for micromechanical modeling results was automated to generate material parameters for macroscale modeling. Three user-defined subroutines were developed and implemented in Abaqus using Fortran to enable macromechanical failure predictions utilizing the framework of XFEM. Strain energy density (SED) based damage model was employed to simulate the damage process. Proposed procedure results were validated against reported testing results from literature regarding low and high strength steels at different volumetric porosity levels, i.e. low range porosity ($\cong 10\%$). Proposed modeling procedure proven excellent agreement with testing results.

7.2 Introduction

Metal additive manufacturing (AM) techniques are widely used to produce high quality final parts in many engineering fields such as biomedical, aerospace and automotive industries (Attaran, 2017; Frazier, 2014). Selective laser sintering (SLS) is one of the most eminent techniques utilized to generate complex geometry metallic parts consolidating

successive layers of powder materials (Kruth, Mercelis, Van Vaerenbergh, Froyen, & Rombouts, 2005). This procedure involves complex thermal cycles resulting from subsequent melting/solidification of each successive layer (Zheng, Zhou, Smugeresky, Schoenung, & Lavernia, 2008). Melting and solidification progression results in microstructural features such as micro-pores (Choren et al., 2013; Gao et al., 2015; Pabst & Gregorová, 2015; B. Song et al., 2015). Mechanical behavior as well as load-bearing capacity are strongly related to porosity level of the manufactured material (Chawla & Deng, 2005; Deng et al., 2008; Stephens, Horn, Poland, & Sager, 1998a). Accounting for microstructural features effect on the mechanical behavior is of paramount significance for early design stages (Allison et al., 2013).

Several research addressing the effect of total volumetric porosity on material properties such Young's modulus and material strength were proposed in literature. Choren et al. (Choren et al., 2013) provided a comprehensive review on available relationships correlating total volumetric porosity to effective modulus of elasticity from 1947 until 2007. In their work, available linear and non-linear relationships were summarized based on the applicable porosity ranges. They concluded that while many relationships are available to predict porous materials mechanical properties particularly Young's modulus, there remains an absence of "perfect-association" regarding micro-structural porosity and corresponding effective moduli (Choren et al., 2013). The material strength dependency on volumetric porosity was correlated to that of non-porous material utilizing power and exponential laws as in the work of Bal'shin (Bal'shin, 1949) and Knudsen (KNUDSEN, 1959), respectively. The exponential law proposed by Knudsen was validated against wide

variety of metals for moderate porosity range, i.e. less than 30%. Regarding plastic behavior, the Gurson-Tvergaard-Needleman (GTN) model (Gurson, 1977; Tvergaard & Needleman, 1984) is commonly referenced for studying ductile behavior of porous metals in the low range porosity, i.e. less than 10%. This model defines a yield potential based on single isolated spherical void in an infinite continuum based on the early work of Gurson (Gurson, 1977). The GTN model constructs the basis for many available porous plasticity models (Besson, 2010; Jeong & Pan, 1995; Leblond, 2014; Mbiakop et al., 2015; Morin et al., 2015, 2017; Vadillo, Reboul, & Fern, 2016). Also, the GTN model is currently implemented in commercial finite element analysis (FEA) software Abaqus. GTN model requires the definition of nine parameters (*Abaqus V6.14– Documentation, Dassault Systèmes Simulia Corporation, 2013*); several of which are material specific and rely on the best fitting of experimental stress-strain data of porous materials (Rousselier, 2001; Trillat & Pastor, 2005; Weinberg, Mota, & Ortiz, 2006). Also, GTN model does not deal with linear elastic behavior which implies that the effective modulus of elasticity remains to be user-defined (*Abaqus V6.14– Documentation, Dassault Systèmes Simulia Corporation, 2013*). In addition, the GTN model does not predict actual macroscopic failure besides demanding considerable computational effort as pointed out by Hardin and Beckermann (R. A. Hardin & Beckermann, 2013; Richard A. Hardin & Beckermann, 2007) that a specimen sized model may require several days of computational runtime. Therefore, practical challenges are associated with GTN model when analyzing full-scale models as it can be deemed unattainable. Also, GTN model requires explicit definition of porous

material behavior regarding both linear and non-linear plastic behaviors (*Abaqus V6.14–Documentation, Dassault Systèmes Simulia Corporation, 2013*).

Alternatively, homogenization methods can be utilized to predict the effective stiffness properties of anisotropic materials (Leclerc, Karamian-Surville, & Vivet, 2015; Pontefisso, Zappalorto, & Quaresimin, 2015; Shan & Gokhale, 2002; Xu, Sun, Li, Ryu, & Khaleel, 2013). Among the commonly referenced homogenization techniques is the representative volume element (RVE) or the unit cell (UC) method. The term RVE was coined by Hill (R. Hill, 1963) which can be defined as the smallest volume element capable of representing microstructural features while being macroscopically representative of continuum (Elnekhaily & Talreja, 2018; Ma, Liu, & Hu, 2006; Omairey et al., 2018; Salahouelhadj & Haddadi, 2010). In other words, to predict continuum constitutive properties accounting for structural properties of microconstituents (Siavouche & Hori, 1993). The RVE method has been widely used in past two decades to predict effective elastic properties of heterogeneous materials such as composite materials (Elnekhaily & Talreja, 2018; Omairey et al., 2018; Shan & Gokhale, 2002; Siavouche & Hori, 1993; Trias, Costa, Turon, & Hurtado, 2006), multi-phase materials (Gaudig, Mellert, Weber, & Schmauder, 2003; Xu et al., 2013; C. Zhang, Gong, Deng, & Wang, 2017) and porous materials (Guo et al., 2017; Han, Tang, Kou, Li, & Feng, 2015; Saby, Bernacki, Roux, & Bouchard, 2013; Sladek, Sladek, Krahulec, & Song, 2016; Dawei Song & Ponte Castañeda, 2017). To enable RVE predictions of effective elastic properties, uniform stress/strain should be imposed on the micromechanical RVE ensuring uniform deformations and satisfying equilibrium (Siavouche & Hori, 1993). For that purpose, usually periodic boundary conditions (PBC)

are employed to ensure that deformed boundaries remain periodic (Elnekhaily & Talreja, 2018; Leclerc et al., 2015; Omairey et al., 2018; Pontefisso et al., 2015; Salahouelhadj & Haddadi, 2010). There exist two main types of RVEs, first type is real microstructure or voxel based RVEs (Leclerc et al., 2015; Mignone et al., 2017; Saby et al., 2013) in which microstructural features are characterized and modeled. Second type is of a unit cell nature, in which each RVE can be repeated indefinitely in all directions to construct the periodic structure (Asim, Siddiq, & Kartal, 2018; Ravi, Seefeldt, Van Bael, Gawad, & Roose, 2019; Dawei Song & Ponte Castañeda, 2017). The main advantage of RVE homogenization is that the periodic system is usually simulated utilizing a single step to obtain anisotropic stiffness matrix representing material's elastic behavior (Ghayoor et al., 2018; Omairey et al., 2018). To overcome analysis limited to elastic behavior, continuum mechanics approach applying special deformation boundary conditions is alternatively utilized if the anticipated result is the mechanical behavior, i.e. elastic-plastic behavior (Hollister & Kikuchi, 1992; Rashid & Nemat-Nasser, 1992; Siavouche & Hori, 1993; Danlong Song et al., 2016). For example, Soro et al. (Soro et al., 2018) utilized RVE homogenization technique to study the behavior of porous titanium produced by sintering used in biomedical implants under compressive loads. Their results showed good agreement in the linear behavior and demonstrated better predictive capabilities compared to semi-analytical model of Mori-Tanaka (Mori & Tanaka, 1973). Regarding plastic behavior, there were uncertainties in reported numerical stress-strain behavior when compared to testing (Soro et al., 2018). The predicted yield strengths showed up to 23% error which can be attributed

to moderately high porosity levels (up to 36% porosity) and random pore size/location contributing to localized stress concentrations.

In the current work, continuum mechanics approach RVE method is employed to generate micromechanical models predicting effective mechanical behavior of porous metals under tension. Micromechanical RVE models with center oblate spheroidal void representing total volumetric porosity are generated using Python scripting in Abaqus. Non-porous material behavior is used to define voided RVE matrix material. Post-processing of numerically obtained effective behaviors is performed to automatically generate macromechanical modeling material properties. User-defined material model accounting for linear, plastic and final failure behaviors of porous materials is developed using Fortran in Abaqus. The macromechanical model employs material properties generated from RVE post-processing to precisely define elastic-plastic behavior. Also, a strain energy density (SED) based damage model was developed and implemented to predict macroscopic cracks and final failure. Numerically obtained results were validated against independent testing results regarding low and high strength steel materials reported in literature.

7.3 Material model and methods

7.3.1 Proposed modeling procedure overview

The main objective of proposed procedure is to predict elastic-plastic behavior of porous metals as well as its final failure given the mechanical behavior of the non-porous one and total volumetric porosity. For that purpose, a two-stage finite element procedure employing micro and macro mechanical modeling is proposed. First stage is dealing with micromechanical modeling utilizing three-dimensional RVE method based on continuum

mechanics approach. Micromechanical RVEs utilizing single spheroidal void are used to predict effective elastic-plastic behavior of porous materials. The matrix material in all RVE simulations is defined using the mechanical behavior of fully dense material, i.e. non-porous. Post-processing of numerically obtained effective stress-strain behaviors is automated to generate macromechanical material properties. Second stage deals with macromechanical specimen sized models utilizing the framework of extended finite element method (XFEM) in Abaqus for macroscopic failure predictions. XFEM was originally proposed by Belytschko and Black (T. Belytschko & Black, 1999) and later developed by Moës et al. (Moës et al., 1999). XFEM has superior advantage over conventional finite element method enabling crack onset as well as final failure without the need of remeshing (Duarte et al., 2017; Fries & Belytschko, 2010; Yazid et al., 2009). References (Abdelaziz & Hamouine, 2008; Ted Belytschko et al., 2009a; Fries & Belytschko, 2010; Yazid et al., 2009) provide comprehensive details on XFEM mathematical formulation and applications. The framework of XFEM in Abaqus is used to develop the user-defined damage model. A flowchart outlining the two-stage modeling procedure at different scales is provided in **Figure 7.1**. A Python script was developed in Abaqus to automatically perform three major tasks. First task is the automatic generation of micromechanical RVE with single oblate ellipsoidal void representing the total volumetric porosity. The second task deals with extracting the effective elastic-plastic behavior of the RVE at a given porosity level. Third task is post-processing the effective behavior to automatically generate material parameters used in user-defined subroutines of the second stage, i.e. macromechanical.

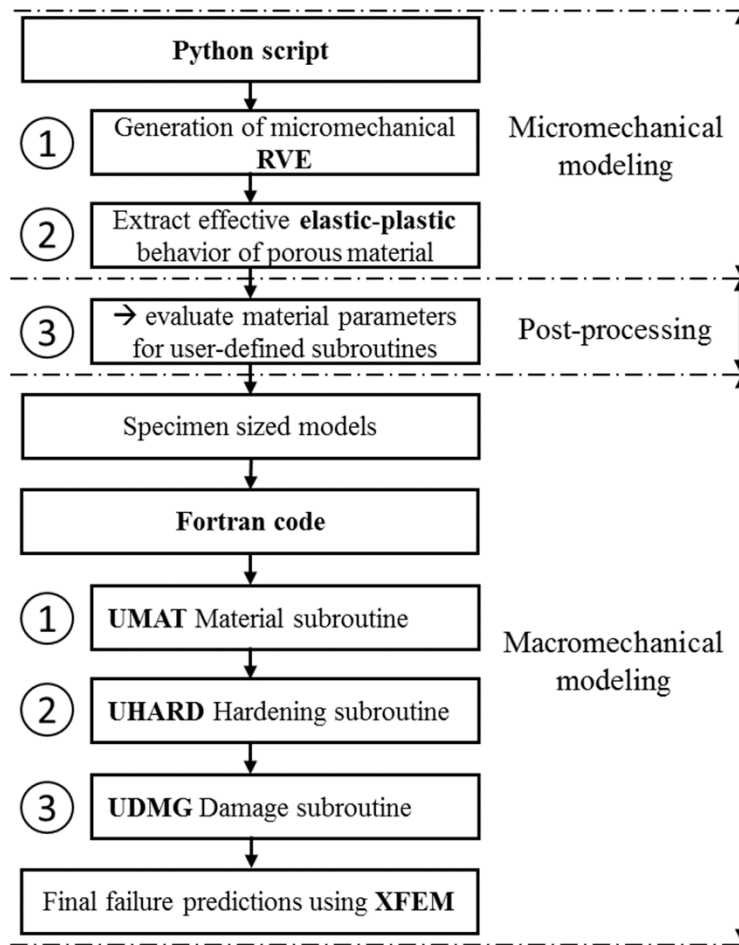


Figure 7.1 Flowchart showing the scope of work at different scales (micro/macro).

The second stage involves specimen sized models' generation along with developing user-defined subroutines to define mechanical and failure behavior of the porous material. Three subroutines were developed and implemented using Fortran in Abaqus to enable accurate material definition regarding elastic-plastic behavior as well as predicting final failure. User-defined material (UMAT) together user-defined hardening (UHARD) deals with the elastic-plastic behavior while user-defined damage (UDMG) utilizing the framework of XFEM controls material degradation and predicts final failure. The material model is explained in subsection 7.3.2 while particular details of micromechanical and

macromechanical methods are discussed in subsections 7.3.3 and 7.3.4, respectively. subsection 7.4 illustrates finite element modeling details on both micro and macro scales. Numerical results using the proposed procedure are reported and discussed in subsection 7.5.

7.3.2 Material model

The material model of RVE matrix material is defined utilizing the deformation plasticity theory in Abaqus (*Abaqus V6.14– Documentation, Dassault Systèmes Simulia Corporation, 2013*) which is based on the Ramberg-Osgood (RO) relationship (Ramberg & Osgood, 1943). The material model for a generalized case of stress state reads as

$$E\varepsilon_{ij} = (1 + \nu)\sigma_{dev} - (1 - 2\nu)\sigma_{hyd}I + \frac{3}{2}\alpha\left(\frac{\sigma_{mises}}{\sigma_y}\right)^{n-1}\sigma_{dev} \quad (\text{Eq.7.1})$$

where E is the young's modulus, ν is the Poisson's ratio, σ_y is yield stress while α is the yield offset and n is the hardening exponent for the non-linear term, i.e. $n \geq 1$. ε_{ij} and σ_{ij} define the strain and the stress tensors, respectively. I is the identity matrix, σ_{dev} is the stress deviator tensor while σ_{hyd} is the equivalent hydrostatic stress and σ_{mises} defines the Mises flow stress. (Eq.7.2) to (Eq.7.4) define the stress invariants.

$$\sigma_{Hyd} = -\frac{1}{3}\sigma_{ij}:I \quad (\text{Eq.7.2})$$

$$\sigma_{Dev} = \sigma_{ij} + \sigma_{Hyd}I \quad (\text{Eq.7.3})$$

$$\sigma_{Mises|eq} = \sqrt{\frac{3}{2} \sigma_{Dev} : \sigma_{Dev}} \quad (\text{Eq.7.4})$$

The model is assumed to be compressible in the linear region and incompressible in the non-linear one where the plastic flow is normal to Mises stress (*Abaqus V6.14–Documentation, Dassault Systèmes Simulia Corporation, 2013*). Currently, microstructural RVE is utilized to predict the effective elastic-plastic behavior of porous metals under tension, hence the assumption is valid for the scope of work. Uniaxial tension testing results of low and high strength steel materials from literature were found adequate for validation purposes. First, is a set of uniaxial tension testing results regarding low strength steel at different porosity fractions reported by Chawla and Deng (Chawla & Deng, 2005). Second, is a set of testing results of high strength steel at different porosity fractions reported by Stephens et al. (Stephens et al., 1998b). To determine RVE matrix material parameters, the RO relationship presented by (Eq.7.1) is reduced to uniaxial state of stress as

$$E\varepsilon = \sigma_i + \alpha \sigma_i \left(\frac{\sigma_i}{\sigma_y} \right)^{n-1} \quad (\text{Eq.7.5})$$

Where σ_i represents the stress component along the i^{th} direction. The above relationship is nonlinear at all stress values where the non-linearity becomes significant at stress values approaching/exceeding σ_y . The non-porous mechanical behavior of low and high strength steels were used to identify material parameters of (Eq.7.5). **Table 7.1** documents the resulting material parameters from calibration processes which are used in material definition of RVE models.

Table 7.1. Material properties of the non-porous metals.

Material	E [GPa]	σ_y [MPa]	ν	n	α
Low strength steel	201.2	480.4	0.3	7.55	0.2
High strength steel	186.8	1449.3	0.3	8.47	0.1

7.3.3 Representative volume element (RVE) method

Hill (Rodney Hill, 1963) defined RVE to be typical of microstructural features such as inclusions or voids yet large enough to evaluate effective material properties. This can be enabled by proper sizing of RVEs in addition to applying necessary boundary conditions to produce an average uniform strain/traction within the homogenized element (Babu et al., 2018; Elnekhaily & Talreja, 2018; Mirkhalaf et al., 2016; Omairey et al., 2018). Homogenization methods are usually utilized when the material behavior is of heterogeneous nature. The homogenization method yields effective stiffness properties which are then employed to evaluate elastic constants of anisotropic behavior. RVE can be also analyzed in continuum mechanics approach using either uniform tractions or displacements (Salahouelhadj & Haddadi, 2010; N. K. Sharma, Mishra, & Sharma, 2016; Siavouche & Hori, 1993). The type of utilized boundary conditions in this approach is selected to produce an average stress/strain within the homogeneous matrix material of RVE. In the current work, displacement boundary conditions were employed where the averaged strain can be correlated to displacements via the divergence theorem (Hashin & Rotem, 1973; Rodney Hill, 1963; Siavouche & Hori, 1993) as

$$\bar{\varepsilon}_{ij} = \frac{1}{|V_{RVE}|} \int_{V_{RVE}} \varepsilon_{ij}^{local} dV_{RVE} = \int_{\Gamma_{RVE}} \frac{1}{2} (u_i n_j + u_j n_i) d\Gamma_{RVE} \quad (\text{Eq.7.6})$$

where $\bar{\varepsilon}_{ij}$ is the averaged strain tensor, V_{RVE} is the RVE volume, ε_{ij}^{local} is the local strain tensor, and Γ_{RVE} is the element boundary. u_i and u_j are the imposed displacements on the RVE boundary while n_i and n_j are the normal unit vectors. Similarly, the averaged stress relation to the imposed tractions reads as

$$\bar{\sigma}_{ij} = \frac{1}{|V_{RVE}|} \int_{V_{RVE}} \sigma_{ij}^{local} dV_{RVE} = \int_{\Gamma_{RVE}} \frac{1}{2} (t_i y_j + t_j y_i) d\Gamma_{RVE} \quad (\text{Eq.7.7})$$

where $\bar{\sigma}_{ij}$ is the average stress tensor, σ_{ij}^{local} is the local stress tensor, t_i and t_j are the imposed tractions while y_i and y_j are elemental boundary local coordinates. The imposed displacements or tractions defined by (Eq.7.6) and (Eq.7.7) are generally chosen to be uniform (R Hill, 2006; Mori & Tanaka, 1973; Nemat-Nasser & Taya, 1981). Consequently, the local strain in RVE is evaluated using the standard weak formulation of equilibrium equations. In case of displacement boundary conditions, the weak form of RVE equilibrium equations is

$$\int_{V_{RVE}} C_{ijkl} \varepsilon_{ij}^{(virtual)} \varepsilon_{kl}^{(total)} dV_{RVE} = \int_{\Gamma_{RVE}} C_\varepsilon v_i^{(virtual)} (u_i - g_i) d\Gamma_{RVE} \quad (\text{Eq.7.8})$$

Where C_{ijkl} is the stiffness tensor, $\varepsilon_{ij}^{(virtual)}$ is the virtual strain tensor and $\varepsilon_{kl}^{(total)}$ is the total microstructural strain tensor. The displacements are imposed using a penalty method where C_ε represents a correction factor (*Abaqus V6.14– Documentation, Dassault Systèmes Simulia Corporation*, 2013). $v_i^{(virtual)}$ is the virtual displacement while the term $(u_i - g_i)$ represents the imposed displacements boundary conditions to generate averaged uniform

strain, $\bar{\varepsilon}_{kl}$ within the homogenised matrix material. Note that total strain, $\varepsilon_{kl}^{(total)}$, is decomposed into $\varepsilon_{kl}^{(elastic)}$ and $\varepsilon_{kl}^{(plastic)}$ representing the elastic and plastic strain components, respectively. Strain states are obtained from finite element simulations and local microstructural strains are correlated to the average strains via local structure tensor, M_{ijkl} . Assuming small deformations, i.e. less than 10% strain, the local strain at any point in the RVE can be evaluated as

$$\varepsilon_{ij} = M_{ijkl}\bar{\varepsilon}_{kl} \quad (\text{Eq.7.9})$$

The averaged stress tensor can be readily obtained using the effective stiffness tensor, \bar{C}_{ijkl} which correlates average stress to average strains reading as

$$\bar{\sigma}_{ij} = \bar{C}_{ijkl}\bar{\varepsilon}_{kl} \quad (\text{Eq.7.10})$$

The same relationship can be written to determine stresses at macroscopic levels

$$\sigma_{ij} = C_{ijkl}\varepsilon_{kl} \quad (\text{Eq.7.11})$$

Integrating both sides of over the RVE volume and dividing by the total RVE volume, V_{RVE} we get

$$\frac{1}{|V_{RVE}|} \int_{V_{RVE}} \sigma_{ij} dV_{RVE} = \frac{1}{|V_{RVE}|} \int_{V_{RVE}} C_{ijkl}\varepsilon_{kl} dV_{RVE} \quad (\text{Eq.7.12})$$

Substituting (Eq.7.10) into (Eq.7.12) and recalling (Eq.7.6) and (Eq.7.7) the effective stiffness tensor can be defined as

$$\bar{C}_{ijkl} = \frac{1}{|V_{RVE}|} \int_{V_{RVE}} C_{ijkl} M_{klij} dV_{RVE} \quad (\text{Eq.7.13})$$

In this approach, the equilibrium equations have to be solved once for each component of the stress/strain tensor unlike periodic boundary conditions which usually enables solving the analysis in a single step for all components. The major advantage of utilizing the continuum approach relies in the ability to predict the complete elastic-plastic behavior of the RVE material. Hence, it is adopted for the analysis of the proposed micromechanical models.

To this end, the main role of the micromechanical RVE simulations is almost accomplished. The next step is a post-processing step in which predicted behaviors are employed to evaluate macromechanical material model properties. User-defined material and damage subroutines parameters are automatically generated from effective stress-strain data. For illustration of post-processing step, consider the schematic diagram of an effective behavior as presented by **Figure 7.2**. Once the effective stress-strain behavior is predicted, the script will generate a ‘strain vs. stress’ dataset using numerically obtained values. The process begins with evaluating effective modulus of elasticity, E_{eff} which can be readily available from the slope of the linear region. Generated dataset is used for that purpose utilizing first five rows (strain vs. stress) to evaluate the effective modulus. Second, step is the evaluation of yield stress and total elastic strains. The yield stress, σ_y can be defined as the onset of plastic deformation while corresponding strain is considered as the magnitude of total elastic strain ε_t .

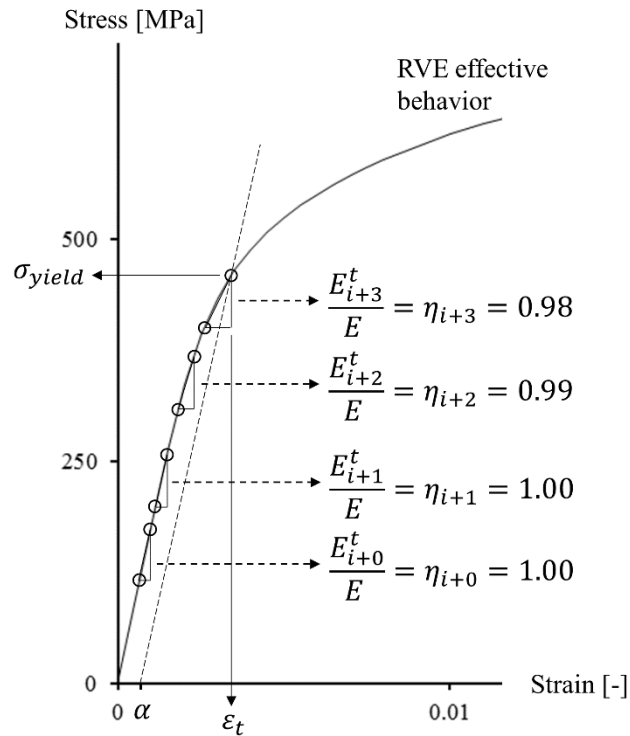


Figure 7.2 Material properties evaluation from effective stress-strain curves.

Tangential moduli E_i^t through each successive data entries are evaluated as pointed out on **Figure 7.2** where the subscript i denotes the current data entry. Each tangential modulus E_i^t is compared to the effective modulus, E_{eff} as shown on **Figure 7.2**. A factor η is defined as the ratio between tangential and young's moduli where η is equal to unity if the data belongs to the linear region. Once the behavior deviates from linearity, η will be less than unity. A predefined tolerance is set to control yield identification process based on the exact yield offset α of the non-porous material. Upon reaching the tolerance, the stress-strain curve is deemed yielding at the interpolation point between the last successive entries. Finally, the plastic strains are isolated from elastic ones and corresponding stresses are determined. This step is essential to define the plastic behavior in the user-defined subroutine as will be discussed in subsection 7.3.4.

7.3.4 Macromechanical modeling and failure

Macromechanical material behavior is defined using three user-defined subroutines using Fortran in Abaqus. User-defined material (UMAT) subroutine is developed to define the linear elastic behavior of the porous material as well as calling the hardening behavior (UHARD) subroutine. Finally, to predict final failure of material a user-defined damage (UDMG) is developed based on strain energy density (SED) as will be discussed shortly. The frame work of extended finite element method (XFEM) is utilized for macroscopic failure predictions. XFEM was originally proposed by Belytschko and Black (T. Belytschko & Black, 1999) and later developed by Moës et al. (Moës et al., 1999). XFEM has superior advantage over conventional finite element method regarding predicting crack onset as well as final failure without the need of remeshing (Duarte et al., 2017; Fries & Belytschko, 2010; Yazid et al., 2009). XFEM works by enriching the domain of conventional finite element mesh with special enrichments function to account for crack onset as well as propagation (V. Gupta & Duarte, 2016). The standard Abaqus notation is followed throughout the following subsections.

7.3.4.1 User-defined material (UMAT)

The linear behavior is defined using generalized Hooke's law in terms of elastic strains while stresses beyond yielding are correlated to total strains. The UMAT subroutine utilizes material behavior predicted using the micromechanical RVE simulations stage. Input material parameters are read from the automatically generated text file as discussed in subsection 7.3.3. For elaboration purpose, the subroutine properties and their equivalent mechanical properties are presented in **Table 7.2**. First two properties PROPS(1) and

PROPS(2) define effective elastic modulus, E_{eff} and Poisson's ratio, respectively, while PROPS(3) and PROPS(4) present the first yield stress, σ_{y0} and corresponding zero plastic strain, ε_{pl0} . Remaining table entries PROPS(...) are dedicated for stress vs. plastic strain data.

Table 7.2. User-defined material (UMAT) subroutine properties.

Subroutine property	Mechanical property	property symbol
PROPS(1)	Effective modulus	E_{eff}
PROPS(2)	Poisson's ratio	ν
PROPS(3), PROPS(4)	Yield stress, plastic strain	$\sigma_{y0}, \varepsilon_{pl0}$
PROPS(...)	Table for yield stress, plastic strain	$\sigma_{y...}, \varepsilon_{pl...}$

The linear behavior is defined using generalized Hooke's law $\boldsymbol{\sigma} = \mathbf{C}\boldsymbol{\varepsilon}$ where \mathbf{C} presents the constitutive matrix. Effect of porosity on linear behavior is accounted for using Lamé's parameters λ and μ as a function of effective modulus reading as

$$\lambda = \frac{E_{eff}\nu}{(1 + \nu)(1 - 2\nu)} \quad (\text{Eq.7.14})$$

$$\mu = \frac{E_{eff}}{2(1 + \nu)} \quad (\text{Eq.7.15})$$

Afterwards, the hardening subroutine (UHARD) is called to check if the material is undergoing plastic deformation which is achieved by checking the stress value for the current load increment compared to first yield stress, σ_{y0} or PROPS(3) in strain vs. stress dataset. If the material is actively yielding, then the material is flowing inelastically. Incremental plasticity theory is adopted where total strain rates $d\varepsilon_t$ are assumed to be decomposed into elastic $d\varepsilon_{el}$ and inelastic components $d\varepsilon_{pl}$ (Abaqus V6.14–

Documentation, Dassault Systèmes Simulia Corporation, 2013). Inelastic deformation is defined in terms of scalar value of equivalent plastic strain rate $d\bar{\varepsilon}_{pl}$ as

$$d\varepsilon_{pl} = d\bar{\varepsilon}_{pl} \left(\frac{3}{2} \frac{\sigma_{dev}}{q} \right) \quad (\text{Eq.7.16})$$

where deviatoric stress σ_{dev} has been already defined by (Eq.7.2). For a general state of stress $q = \sigma_{mises}$ as defined by (Eq.7.4). For a uniaxial tension case and a rate independent material, the yield condition reduces to $q = \sigma_{y_i}$ where yield stresses σ_{y_i} are defined as a function of inelastic strain components ε_{pl_i} . The sub-subscript i denotes the i^{th} entry in the plastic behavior table depending on the table length.

7.3.4.2 User-defined damage (UDMG)

A traction separation was is utilized to define an enriched element damage within the framework of XFEM. To illustrate the damage process, consider the schematic diagram in **Figure 7.3** showing the undamaged and damaged material behaviors. If no damage model is utilized, the material response is going to be similar to the undamaged behavior presented by the solid line in **Figure 7.3**. Correspondingly if a damage model is utilized, the material behavior will show degradation at some point and will continue to degrade until final failure as shown by the dashed line path. Material failure may be defined as the total loss of load-bearing capability as a result of progressive deterioration in the material stiffness. A damage factor D is useful to define the deterioration process of an enriched element where $D = 0$ prior to damage initiation. If the damage initiation criterion is encountered, the damage factor will have a value between zero and unity as shown in **Figure 7.3** signifying

partially damaged elements. Finally, a unity damage factor signifies final failure and separation of material. During the analysis at any step, damaged stress tensor is evaluated for enriched elements by $\sigma_{ij}^D = (1 - D)\sigma_{ij}$.

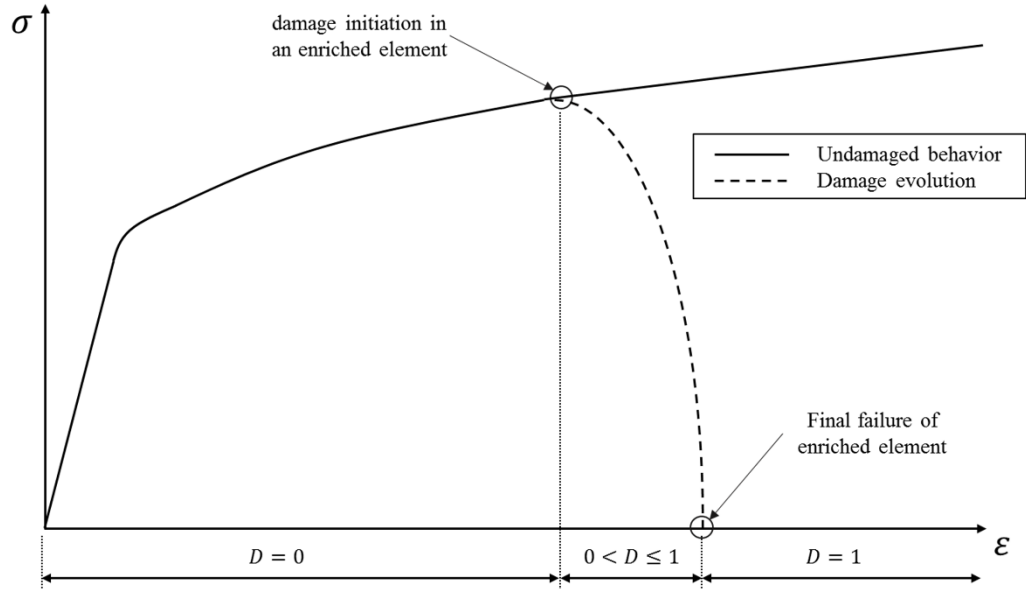


Figure 7.3 Schematic diagram showing damaged and undamaged material behaviors for metals.

In the current work, a user-defined damage subroutine is developed and implemented to predict final failure of porous metals. In which, the damage factor, D is controlled based on critical strain energy density (SED). Assuming small deformations, i.e. less than 10%, the SED for the material model defined by (Eq.7.1) can be obtained as

$$W = \int_0^{\sigma_f} \sigma_{ij} d\varepsilon_{ij} = \frac{(1 + \nu)(\sigma_{mises})^2}{3E} + \frac{3(1 - 2\nu)(\sigma_{hyd})^2}{2E} + \frac{n\alpha(\sigma_{mises})^{n+1}}{E(n + 1)(\sigma_y)^{n-1}} \quad (\text{Eq.7.17})$$

The expression enables evaluating SED for a general state of stress at enriched elements. Noteworthy to mention that SED is invariant under rotation of coordinates (Jones, 2009;

Shames, 1997). Therefore, damage initiation condition in the developed UDMG subroutine reads

$$f = \frac{\langle W \rangle}{W_{critical}} \quad (\text{Eq.7.18})$$

where $f = 1$ signifies onset of damage within an enriched element. The Macaulay brackets $\langle \cdot \rangle$ signifies that pure compressive state of stress does not initiate damage. $W_{critical}$ represents the critical value of SED which can be evaluated from area under the load-displacement curve of a uniaxial tension test (R. Hill, 1998; Jones, 2009; Shames, 1997). SED expressed by (Eq.7.17) can be rewritten for a uniaxial state of stress after some manipulation as

$$W_{critical} = \frac{\sigma_f^2}{E} \left(\frac{\alpha n}{n+1} + \frac{1}{2} \right) \quad (\text{Eq.7.19})$$

where σ_f is the failure stress, E and ν are material constants. The hardening exponent n and the yield offset α can be calibrated from stress-strain curve of the non-porous material. (Eq.7.19) was used to evaluate the critical SEDs of non-porous material defined in Table 7.1 yielding 6.8 MPa and 3.0 MPa for high and low strength steels, respectively. The main objective of defining the damage behavior is to enable accurate failure predictions for porous materials. To achieve this objective, the failure stress should be expressed as a function of porosity. For that purpose, a relationship correlating failure stress of porous metals to that of non-porous one is utilized. The exponential relationship was originally developed and validated by Knudsen (KNUDSEN, 1959) reading as

$$\sigma_f^{eff} = \sigma_f^o e^{-m\phi} \quad (\text{Eq.7.20})$$

where σ_f^{eff} is the effective failure stress of the porous material, σ_f^o presents the failure stress of the fully-dense material and e is the Napierian constant (2.71828..). m is an empirical constant while ϕ is total volumetric porosity factor and the exponent negative sign implies the deteriorating effect. The relationship is valid for moderate porosity ranges up to 30% (Choren et al., 2013; KNUDSEN, 1959) which is adequate for the current work. Inserting (Eq.7.20) into (Eq.7.19) will result in an expression for the critical SED as a function of porosity reading as

$$W_{critical}^{eff} = \frac{(\sigma_f^o e^{-m\phi})^2}{E_{eff}} \left(\frac{\alpha n}{n+1} + \frac{1}{2} \right) \quad (\text{Eq.7.21})$$

(Eq.7.21) was implemented in the Python script as the final post-processing step to evaluate the critical SED for the porous material. To this end the proposed modeling procedure details at micro and macro scales were illustrated. Finite element models particulars are discussed in subsection 7.4 while subsection 7.5 is devoted for validating micro/macro numerical results against reported testing results from literature.

7.4 Finite Element Modeling

7.4.1 Micromechanical RVE models

Micromechanical RVE models were automatically generated using the developed Python script. Also, numerically obtained results from RVE simulations are post-processed using the same script for automatic generation of macromechanical material properties as

illustrated earlier in subsection 7.3.3. Single spheroidal voided RVE similar to references (Asim et al., 2018; Danas & Aravas, 2012; Huang & Talreja, 2005; Mbiakop et al., 2015; Saby et al., 2013; Spaggiari & O’Dowd, 2012b) was utilized in the current work to predict the effective elastic-plastic behavior of porous metals. RVE size was optimized to be small enough to capture microscopic features (e.g. micro-porosity), yet large enough to support accurate predictions of effective macroscopic behavior. The size analysis of representative volume for the current study yielded a unit length, $l_{RVE} = 100 \mu m$ for the RVE. The cubic RVE model geometry showing center oblate ellipsoidal void is presented in **Figure 7.4**. Total volume of a fully dense cube is represented by V_{RVE} which can be evaluated as $(l_{RVE})^3$.

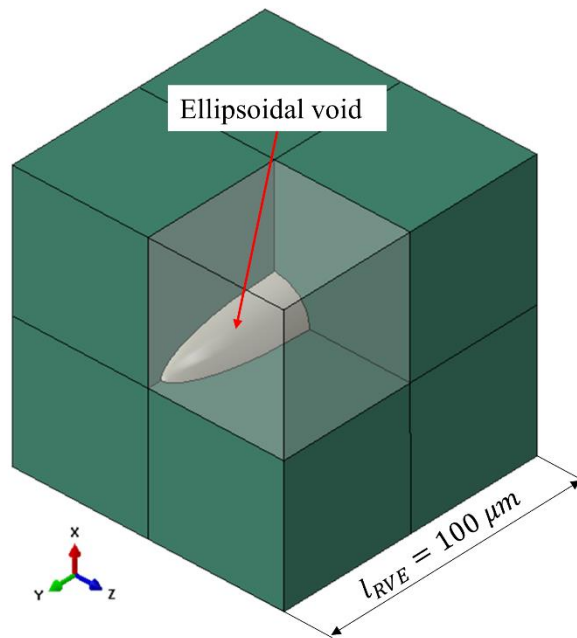


Figure 7.4 Single ellipsoidal RVE model cutaway and void geometry.

Total volumetric porosity factor, ϕ is evaluated using density ratio as

$$\phi = \left(1 - \frac{\rho_{porous}}{\rho_{non-porous}}\right) \quad (\text{Eq.7.22})$$

where ρ_{porous} is the density of porous material while $\rho_{non-porous}$ represents the density of non-porous material, i.e. sound material. Ellipsoidal void volume, V_{void} is then determined by utilizing the porosity factor ϕ and total volume, V_{RVE} . The embedded ellipsoidal void geometric parameters are shown in **Figure 7.5**. The ellipsoidal shapes utilized for current analyses has an equal minor radius, r along the x and z axes while R represents the major radius along the y -axis.

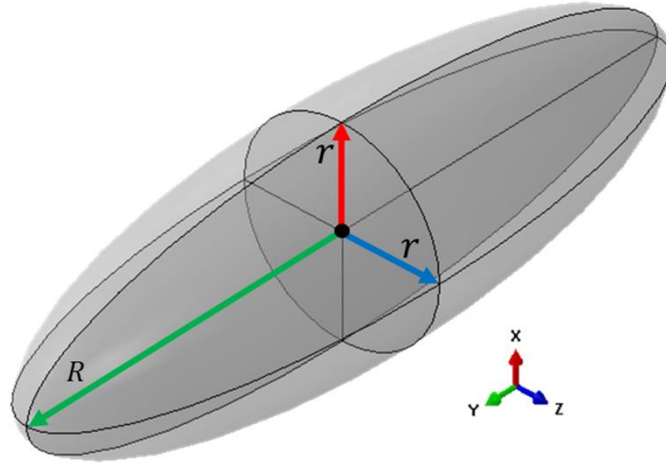


Figure 7.5 Ellipsoidal void shape and geometric parameters.

Ellipsoidal three-dimensional surface expression can be written as

$$\frac{x^2}{R^2} + \frac{y^2 + z^2}{r^2} = 1 \quad (\text{Eq.7.23})$$

where x , y and z represent the Cartesian coordinates along the three orthogonal directions, respectively. To parametrize ellipsoid volume, a non-dimensional aspect ratio between major and minor axes, $a = R/r$ was utilized to express the ellipsoidal volume as

$$V_{void} = \frac{4}{3} \pi a r^3 \quad (\text{Eq.7.24})$$

Note that a unity aspect ratio yields a perfect spherical void with three identical radii. In the current work different aspect ratios are considered to investigate the void shape effect on predicted mechanical behaviors. **Figure 7.6** presents different ellipsoids utilizing aspect ratios greater than or equal to unity.

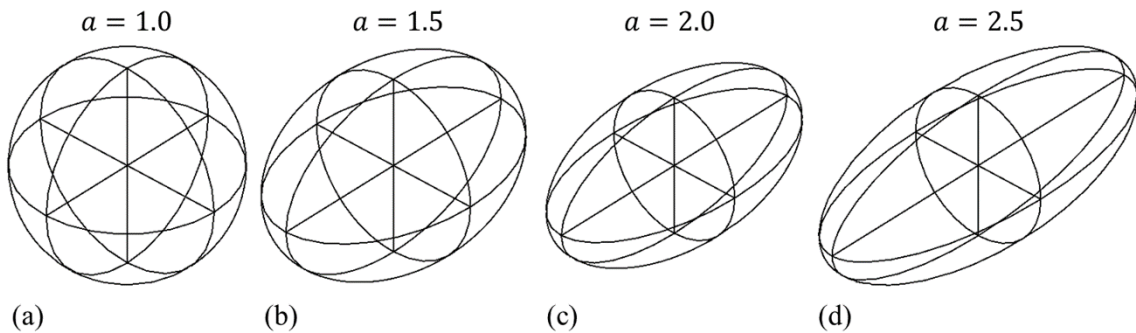


Figure 7.6 Ellipsoidal shapes at different aspect ratios: (a) $a=1.0$, (b) $a=1.5$, (c) $a=2.0$, (d) $a=2.5$.

Each ellipsoid is aligned at RVE centroid and Boolean geometric subtraction operation is utilized to generate the final voided RVE model as shown in **Figure 7.7**. In order to attain better mesh conformation to the curved boundaries of ellipsoids, the developed python script was used to enable automatic partitioning to each generated RVE. The partitioning process results in eight symmetric subdivisions of the three-dimensional cube. To enable structured meshing technique, geometric edges of each sub-division including ellipsoidal edges were seeded the same number of nodes. As a result, only brick elements were used

in meshing, namely C3D8R, which are eight-noded elements with reduced integration. **Figure 7.7a** and **Figure 7.7b** shows the automatically partitioned RVE model and the resulting high-quality structured mesh, respectively. The final convergent meshes for generated RVEs had average size of 60,000 elements with a minimum and a maximum elemental length of $1\mu\text{m}$ and $2.5\mu\text{m}$, respectively.

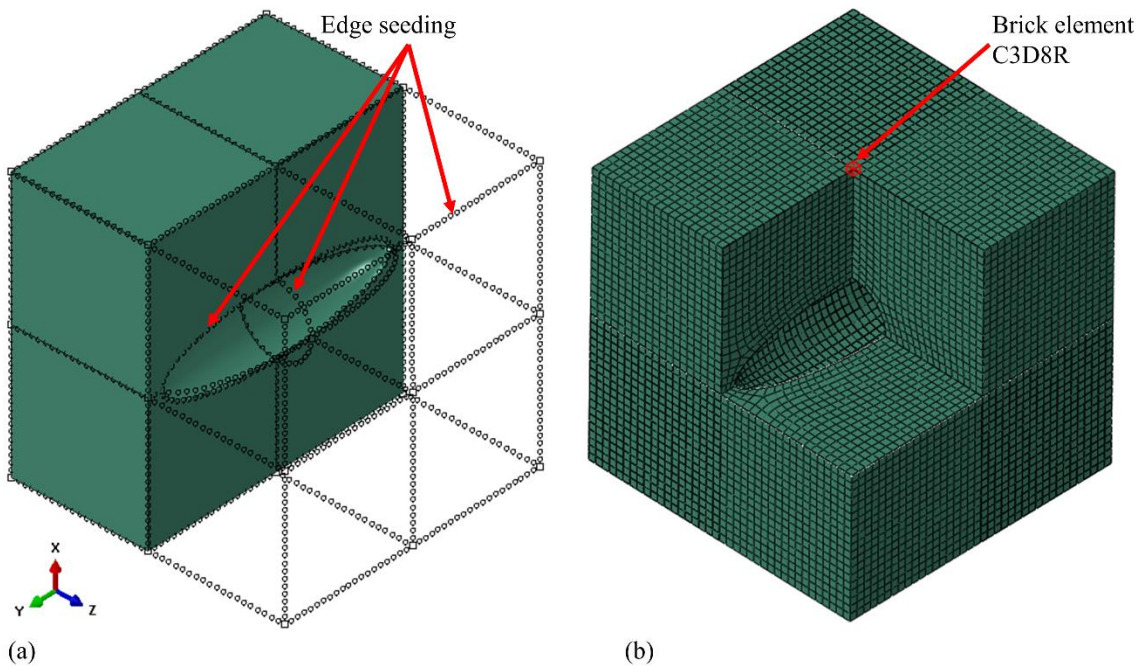


Figure 7.7 (a) Automatically partitioned RVE model showing edge seeding, (b) resulting high quality structured mesh.

Micromechanical modeling is focused on effective behavior of porous metals under tension. Therefore, the continuum mechanics approach is adopted to enable predictions of a complete mechanical behavior. To enable homogenization of the microstructure, it is necessary to produce an average strain within the homogenized material. Necessary set of Neumann and Dirichlet boundary conditions should be precisely applied (Siavouche & Hori, 1993). For this purpose, two faces of the RVE are associated with three-dimensional rigid nodes, namely RNODE3D as shown in **Figure 7.8**. These nodes constraint faces from

deforming during the analysis as well as being used to apply necessary set of boundary conditions. The face highlighted in red is constrained with a fixed boundary condition (Dirichlet type) while the face highlighted in blue is set to uniform displacement (Neumann type) ramped at 100 equal steps to generate a uniform strain within the homogenized material. The peak value of applied displacement is limited to produce 5% strains to conform to the small deformation's assumption, i.e. less than 10%.

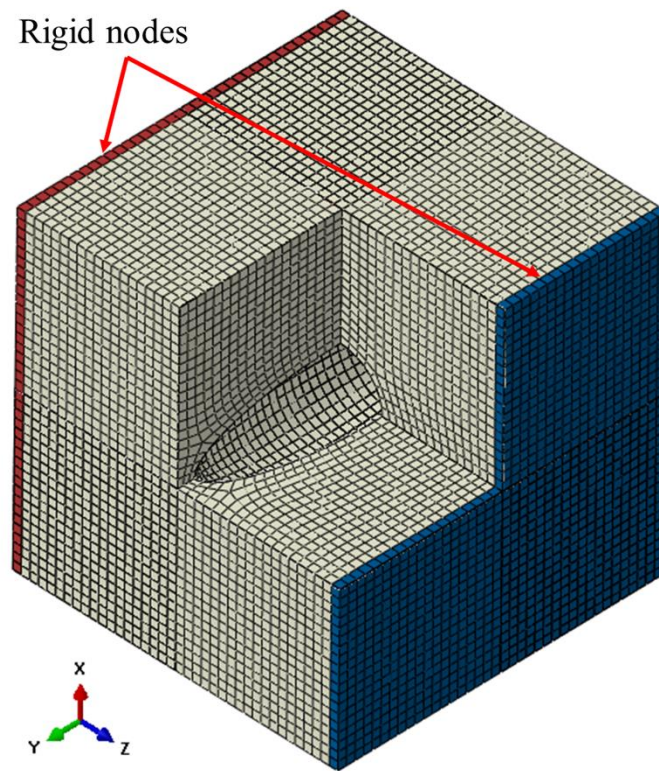


Figure 7.8 RVE model showing rigid node faces highlighted in blue and red.

7.4.2 Macromechanical modeling and failure

Macromechanical material behavior is defined using the three user-defined subroutines UMAT, UHARD and UDMG as discussed in subsection 7.3.4. Material properties were automatically generated using the Python script by post-processing micromechanical RVE

output as illustrated in subsection 7.3.3. Three-dimensional specimen sized models were considered for macromechanical models. Loading conditions and geometric parameters are presented by **Figure 7.9**. Models representing the low and high strength steel specimens are named model A and B, respectively.

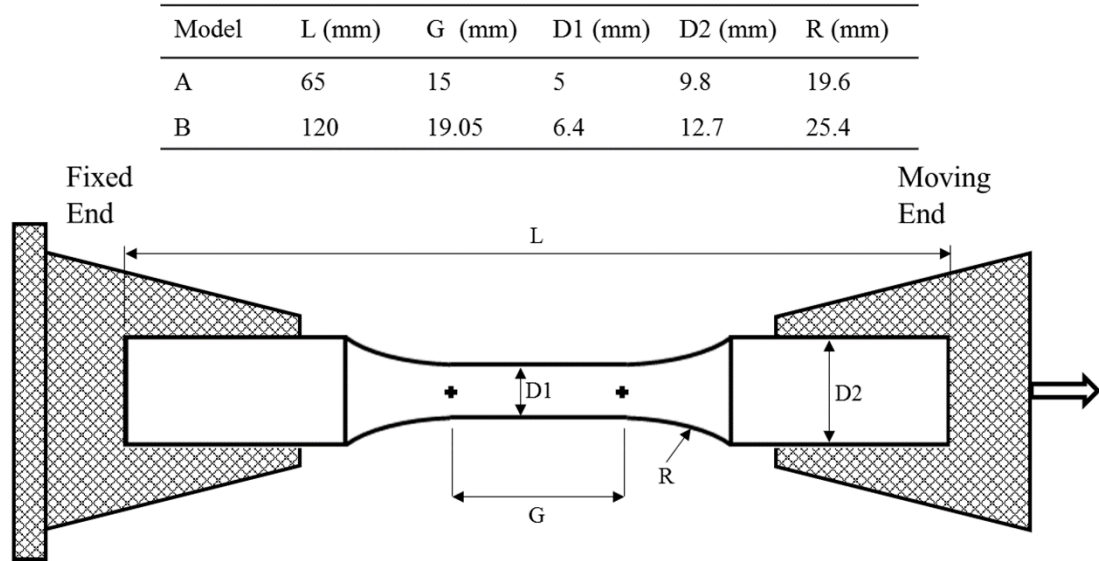


Figure 7.9 Finite element models geometry and loading conditions.

Specimens end tabs should be constrained as undeformable sections to avoid biasing numerical results. Therefore, corresponding elements were chosen of a rigid type. The left tab was fixed in all degrees of freedom using the ENCASTRE boundary condition in Abaqus, while the right tab was constrained to move along the specimen's vertical axis only to mimic the test conditions. A solid homogeneous section was selected for all specimen sized models with an eight-noded linear three-dimensional brick element, namely (C3D8R). The element utilizes reduced integration technique to reduce computational effort with hourglass control for better prediction results. Based on displacements and stress convergence studies the sufficient mesh size was determined to be 8000 and 10000

elements for models A and B, respectively. XFEM enrichments were utilized in the narrow section of each model to allow for damage initiation and evolution. The displacement was linearly ramped until final failure. A general static analysis step was selected to perform the simulations with automatic incrementation. The initial increment size was set to 0.005 with a while the maximum was set to 0.01. Nonlinear geometric behavior was allowed during the analysis. Regarding the computational effort, the workstation used for running all simulations utilizes an Intel® Xeon® central processing unit E5-1603 v4 running at 2.80 GHz with 32 GB of RAM. A single processor was used to perform the simulations on Abaqus 2017.

7.5 Results and Discussion

7.5.1 Micromechanical RVE results

To assess the effect of oblate ellipsoidal void, four aspect ratios were considered as shown in **Figure 7.6**. Starting with a unity ratio to generate a perfect spherical void and increasing the aspect ratio up to 2.5. Obtained micromechanical numerical results were used to extract effective elastic-plastic behavior of the voided material. Effective behaviors for same volumetric porosity, i.e. 4.5% at different aspect ratios compared to that of testing reported by Chawla and Deng (Chawla & Deng, 2005) are presented in **Figure 7.10**.

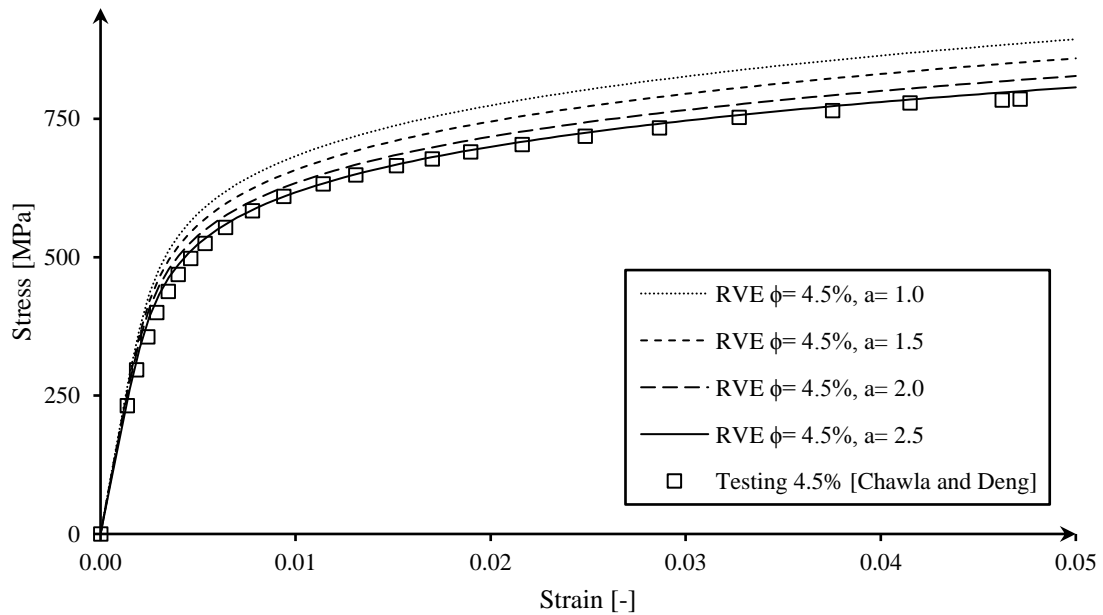


Figure 7.10 RVE effective stress-strain behaviors for 4.5% porosity low strength steel at different aspect ratios.

As can be observed that a perfect spherical void, i.e. $a = 1$ is showing larger slope in the linear region followed by a significant deviation in non-linear region as well as the plastic flow. The numerically obtained stress-strain curve is similar in nature to that of testing, yet there is a major deviation from testing curve specifically in the non-linear region and plastic flow. As the aspect ratio was increased, the numerically obtained effective behaviors had a tendency of approaching the testing results. This can be observed from the effective behaviors of aspect ratios 1.5 and 2.0. A perfect agreement can be observed between numerically obtained stress-strain behaviors utilizing an aspect ratio of 2.5 when compared to testing. Increasing the aspect ratio above 2.5 did not seem to have an effect on prediction results and stress-strain curves were unaltered. In fact, this signifies that an optimum aspect ratio may exist depending on material type of interest. To further assess this claim, the aspect ratio was set to 2.5 while total volumetric porosity percentage was varied. Chawla

and Deng (Chawla & Deng, 2005) reported testing results regarding three total volumetric percentages of porosity regarding low strength sintered steel. The developed Python script was used to generate effective behaviors of these percentages and numerical results were compared to those of testing as shown in **Figure 7.11**. Numerical results are presented with different line types while corresponding testing data are presented with different marker types. Upon varying only one factor, i.e. total volumetric porosity ϕ , a change in the slope of the linear region as well as a variation regarding the onset of plastic deformation can be observed similar to testing behaviors. Finally, predicted behaviors were able to capture differences regarding plastic flows at each porosity percentage where there is drop in the curve owed to the onset of yielding. For low strength steel, the proposed micromechanical RVE results showed excellent agreement with those of testing at different porosity percentages.

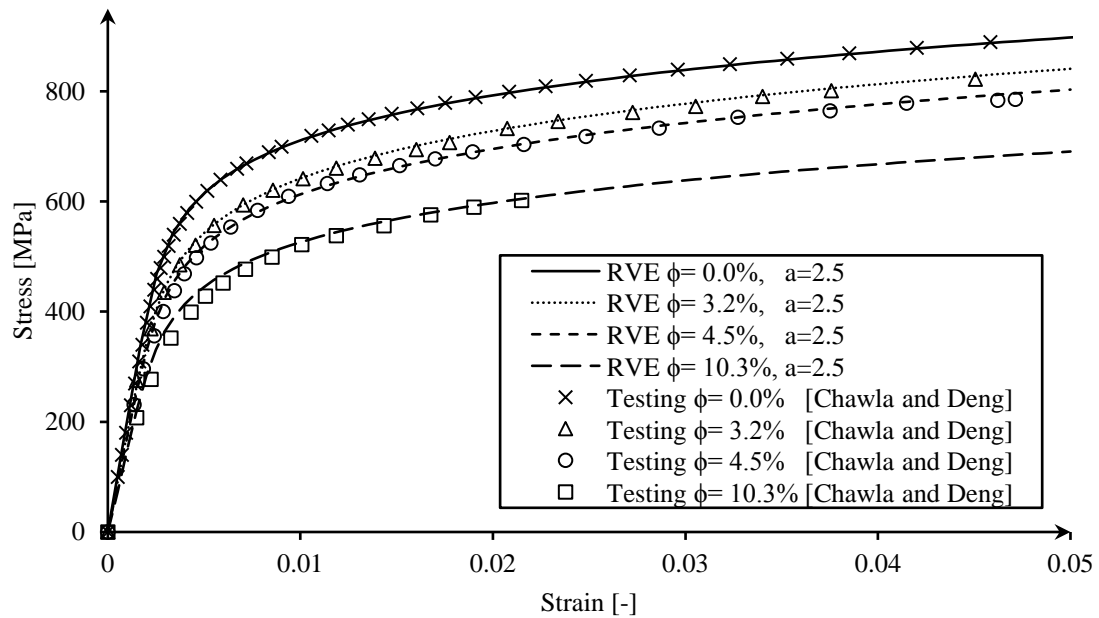


Figure 7.11 RVE effective elastic-plastic behavior vs low strength steel testing (Chawla & Deng, 2005).

To further validate the proposed modeling approach, the micromechanical RVE script was used to obtain stress-strain behaviors of high strength steel. Two porosity percentages were reported by Stephens et al. (Stephens et al., 1998b) regarding the mechanical behavior of high strength steel. The developed Python script was used to generate effective behaviors at reported porosity percentages. Numerically obtained stress-strain curves from RVE simulations are compared to those of testing as shown in **Figure 7.12**. The proposed RVE approach proven predictive capabilities regarding the effective mechanical behavior. This can be demonstrated by a change of slope in linear region, alteration in onset of yielding as well as the plastic flow curves. Excellent agreement was consistently observed between numerical predictions when compared to testing results of high strength steel.

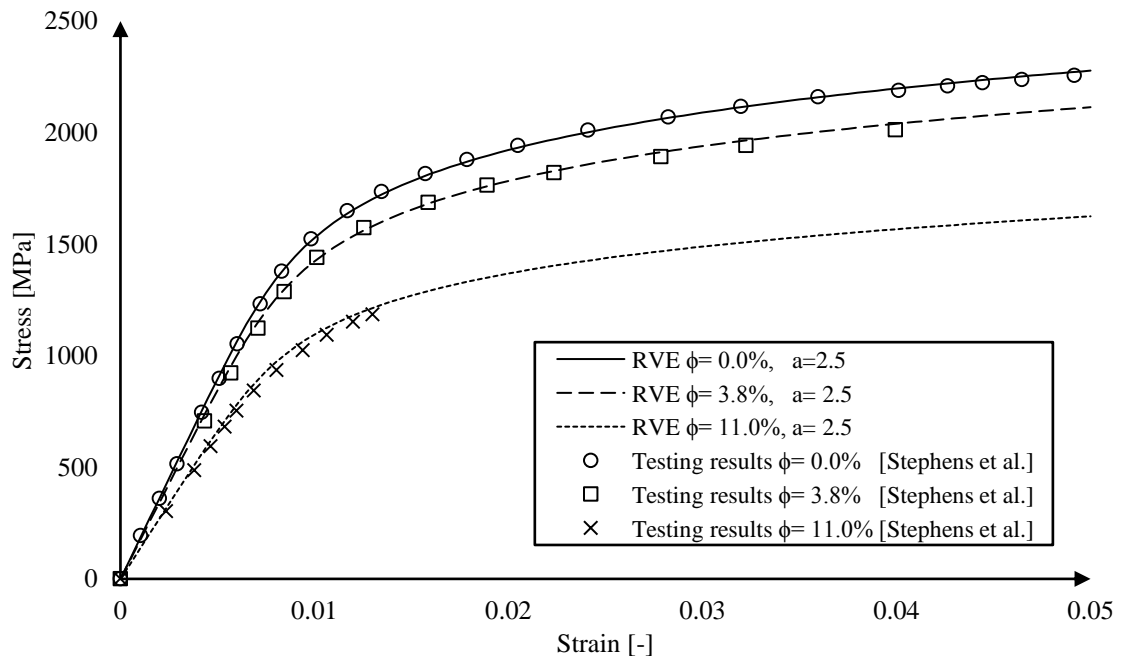


Figure 7.12 RVE effective elastic-plastic behavior vs strength steel testing (Stephens et al., 1998b).

Noteworthy to mention, that the selected material model, i.e. defined by (Eq.7.1) enabled predicting precise continuous stress-strain curves as can be observed from comparisons

with two independent sets of reported testing results. To this end, anticipated outcome from micromechanical modeling stage is accomplished. The proposed macromechanical material model results are discussed in the following subsection.

7.5.2 Macromechanical modeling results

Numerical results obtained using the proposed user-defined subroutines are demonstrated. For brevity purposes, only model A results are shown in full-field results (i.e. at 4.5% volumetric porosity). Meanwhile numerically obtained stress-strain curves are compared to those of testing and presented for both models, A and B, respectively, and for all specimens at different porosity levels. Also, quantitative comparisons based on discrete material properties are provided. In the following comparisons, UMDMG denotes the developed subroutine numerical results. The elastic strain energy density (ESEDEN) contour plot was extracted at different load increments, and the corresponding results are depicted in **Figure 7.13**. As can be observed, the critical cross-section existed towards the lower end of the specimen. The critical cross-section is the one experiencing a maximum value of strain energy density, elements belonging to this region are highlighted in red in **Figure 7.13**.

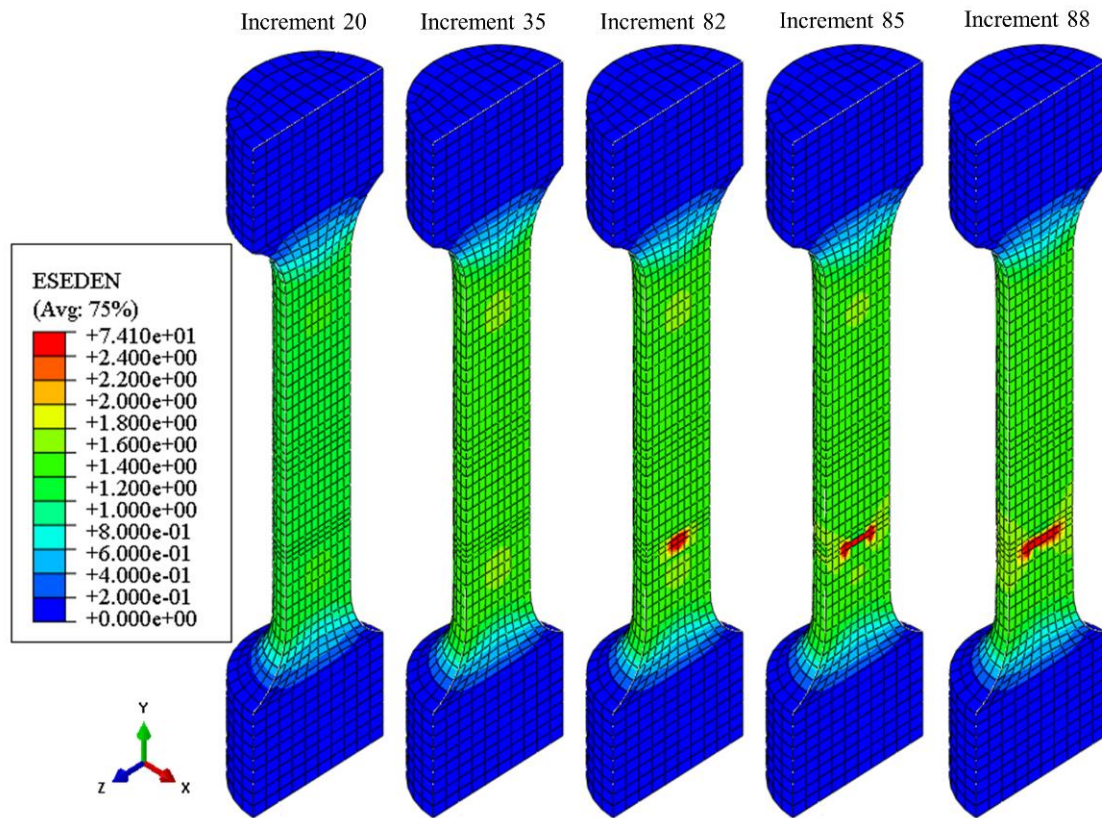


Figure 7.13 Elastic SED contour plot at different load increments

The plastic dissipation of SED (EPDDEN) at the particular load increments are portrayed in **Figure 7.14**. The plastic energy dissipation represents the amount of energy required to permanently deform the material. The same critical cross-section location was observed to be in consistency with the critical cross-section from **Figure 7.13**.

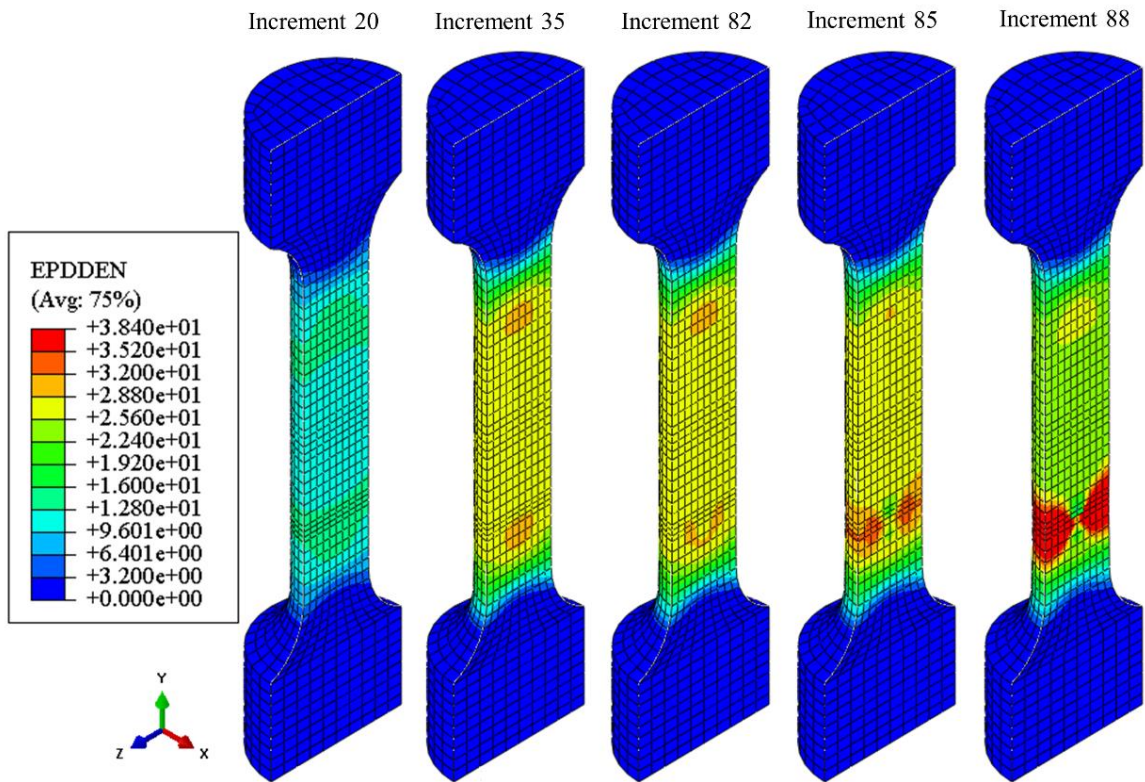


Figure 7.14 Total plastic dissipation of SED contour plots

The total SED combining both elastic and plastic contributions is depicted in **Figure 7.15**. The mesh gridlines were removed from the model for better viewing. As can be seen, the combined SED results validates the previous results reported in both **Figure 7.13** and **Figure 7.14**. The damage initiation location, as well as the damage evolution direction, can be anticipated by inspecting the SED at different load increments, **Figure 7.15**.

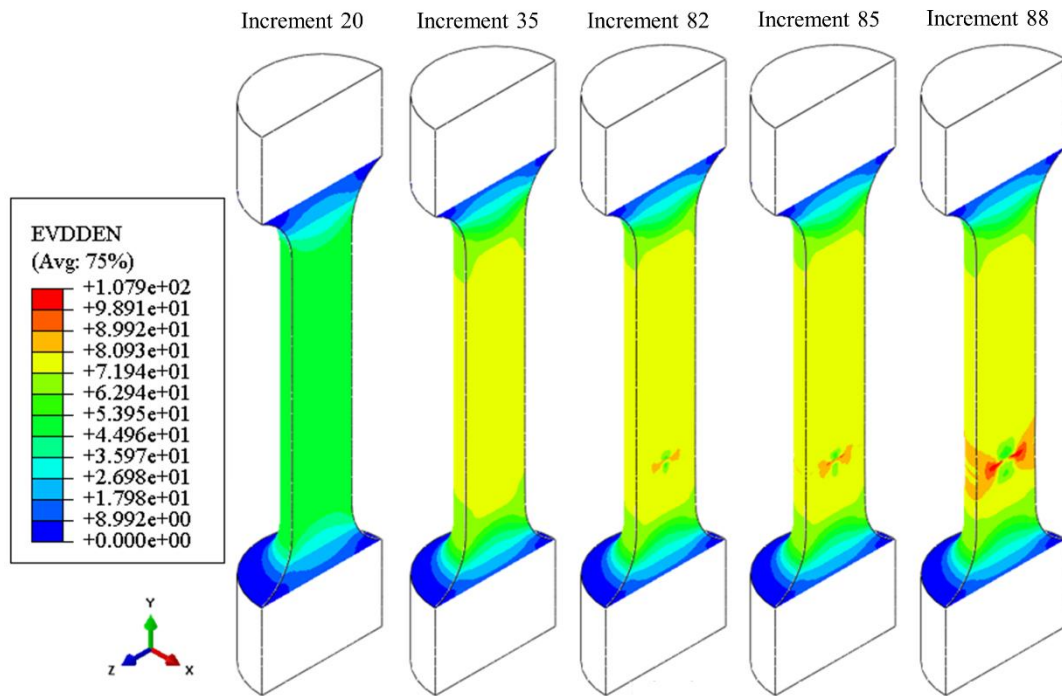


Figure 7.15 SED contour plots at different load increments

Figure 7.16 presents predicted damage initiation and evolution using the proposed UMDMG at different step increments. A cutout through the specimen cross-section is used to better visualize the damage process. As can be seen, damage initiation was in the center of the specimen where 4 elements were subject to approximately 10% damage according to the damage factor scale. Upon increasing the load more elements were subject to the same percentage of damage. It can be observed that damage was expanding radially with the increase of loading. At increment 82 a change in color for some elements with more intensity towards the center can be observed signifying more loss of stiffness. Starting from increment 85, material degradation was rapid where two elements in the center showed a complete loss of stiffness signified by the red color which corresponds to a damage factor of unity. At increment 88 the center elements shown by the grey color have already

exhibited separation. Finally, the final fractured surface can be anticipated from the contour plot at increment 93.

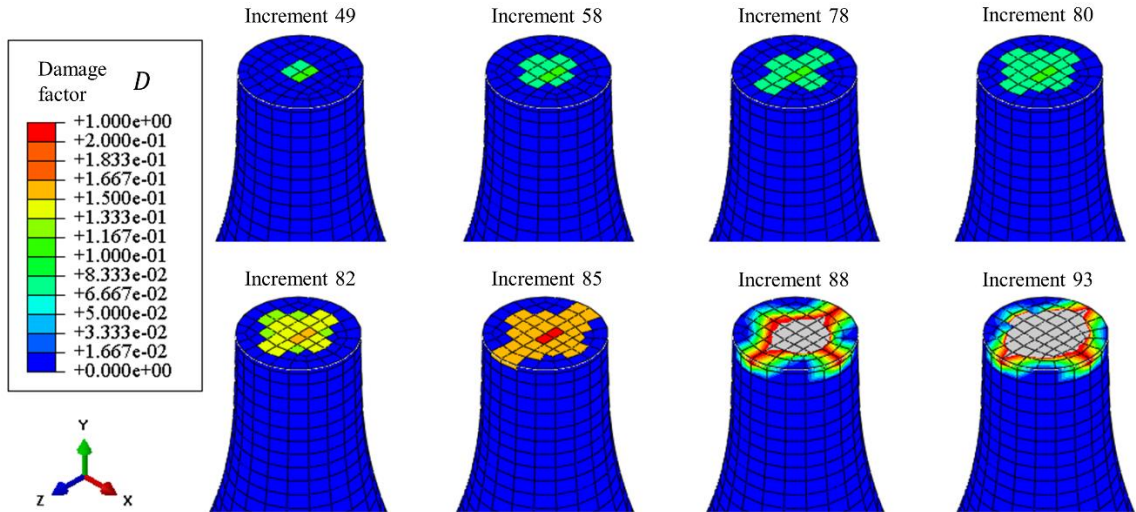


Figure 7.16 UMDMG results showing damage initiation and evolution at different increments.

Stress-strain results utilizing UMDMG subroutine are presented against reported testing data from literature. Throughout the following comparisons, reported testing results are presented with different types of markers while UMDMG numerical results are presented with different line types. **Figure 7.17** presents numerical results simulating the low strength steel behavior. As can be seen, numerical results are in excellent agreement with testing behaviors starting with the sound material and up to 10.3% total volumetric porosity. Also, the developed damage model showed prediction capabilities regarding macroscopic failure. Noteworthy to mention that prediction results were consistently conservative. **Table 7.3** provides a quantitative comparison between predicted and reported testing regarding mechanical properties of low strength steel. The predicted moduli of elasticity were in excellent agreement when compared to those of testing with minimum and maximum errors of -0.25% and 4.48%, respectively. The maximum error was recorded by the 10.3%

porosity level while lower porosity levels showed less errors. Regarding failure limits, the maximum recorded error was -2.13% recorded by the predicted strain at failure of the 4.5% total volumetric porosity material. Failure limits were in excellent agreement which can be attributed to strain energy density-based damage model.

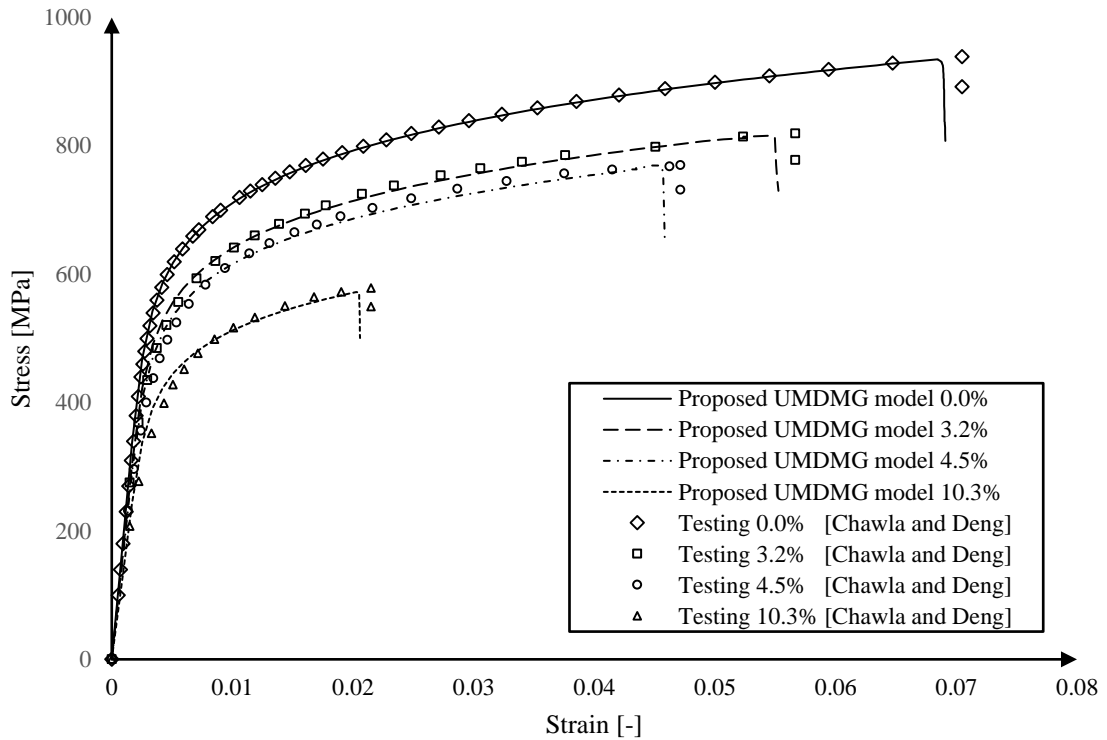


Figure 7.17 Stress-strain results of low strength steel at different volumetric porosity: UDMG vs Testing (Chawla & Deng, 2005).

Table 7.3. Low strength steel mechanical properties: predicted vs testing.

Total volumetric porosity	Mechanical property	Testing results (Chawla & Deng, 2005)	UDDMG predictions	Percentage error (%)
0.0%	E (GPa)	201.2	200.7	-0.25
	σ_f (MPa)	939.1	934.7	-0.47
	ε_f (%)	7.0	6.9	-1.43
3.2%	E (GPa)	183.7	180.9	-1.52
	σ_f (MPa)	819.0	816.0	-0.37
	ε_f (%)	5.6	5.5	-1.79

4.5%	E (GPa)	169.7	173.8	2.42
	σ_f (MPa)	770.1	769.4	-0.10
	ε_f (%)	4.7	4.6	-2.13
10.3%	E (GPa)	138.5	144.7	4.48
	σ_f (MPa)	578.6	572.3	-1.07
	ε_f (%)	2.2	2.1	-4.54

Figure 7.18 presents a similar comparison for high strength steel at different total volumetric porosity. As can be observed, the proposed UMDMG subroutine results are in excellent agreement with reported testing behaviors which can be observed for the sound material behavior as well as the porous materials behaviors. It can be said that the material behaviors were precisely captured beginning with the linear region, yielding as well as the plastic flow. Also, regarding failure, consistency was observed in conservative predictions. This can be attributed to the adopted failure mechanism in the proposed model. Energy based criteria are by far more accurate compared to simple stress/strain criteria. **Table 7.4** provides a quantitative comparison between predicted and reported testing regarding mechanical properties of high strength steel. As can be observed the maximum error in Young's modulus is 1.25% which was reported by the 11.0% porosity material. The maximum errors in predicting failure stress and strain were 1.06% and -1.55%, respectively. As can be observed from both comparisons with testing results of low and high strength steels, the proposed procedure proven excellent prediction capabilities in linear, non-linear as well as final failure of porous materials. Noteworthy to mention that only required material input for the analyses was the behavior of the fully dense materials as reported in Table 7.1.

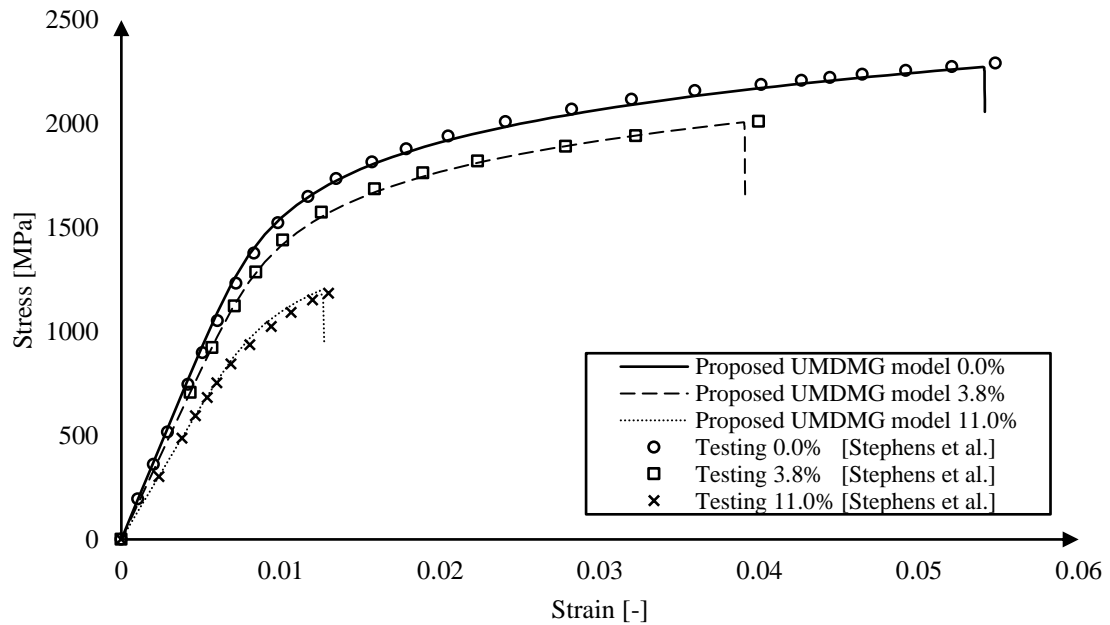


Figure 7.18 Stress-strain results of high strength steel at different volumetric porosity: UDMGM vs Testing (Stephens et al., 1998b).

Table 7.4. High strength steel mechanical properties: predicted vs testing.

Total volumetric porosity	Mechanical property	Testing results (Stephens et al., 1998b)	UDMGM predictions	Percentage error (%)
0.0%	E (GPa)	186.8	184.6	-1.18
	σ_f (MPa)	2293.3	2274.6	-0.82
	ε_f (%)	5.47	5.40	-1.28
3.8%	E (GPa)	163.4	164.2	0.49
	σ_f (MPa)	2012.8	2008.5	-0.21
	ε_f (%)	3.99	3.90	-2.26
11.0%	E (GPa)	128.4	130.0	1.25
	σ_f (MPa)	1185.0	1197.6	1.06
	ε_f (%)	1.29	1.27	-1.55

7.6 Conclusions

Two-stage finite element procedure was provided to predict effective elastic-plastic behavior as well as final failure of porous metals under tension. Micromechanical modeling utilizing RVE method was used for the first stage to predict the effective mechanical

behavior given the fully dense material behavior. A python script was developed to fully automate RVE generation, boundary conditions application and high-quality mesh generation. Also, post-processing of micromechanical results was implemented in the same script. Second stage provided macromechanical modeling utilizing automatically generated material parameters to be used in Fortran user-defined subroutine, i.e. UMDMG. A strain energy density (SED) based damage model was utilized to predict final failure at macroscopic levels within the framework of XFEM. Finally, proposed work was validated against two independent sets of testing results of porous metals, namely low and high strength steels. Noteworthy to mention that validation was limited to low range porosity, i.e. $\cong 10\%$. From the presented work, the following can be concluded

- Micromechanical RVE representing total volumetric porosity by a single oblate spheroidal void proven excellent predictive capabilities regarding elastic-plastic behavior of porous metals under tension.
- The RVE size and ellipsoidal void aspect ratio were found to be dominant parameters controlling numerical predictions accuracy.
- A major contribution of the proposed work is automatic post-processing of micromechanical modeling results enabling precise definition of macromechanical modeling material properties while alleviating user-intervention.
- For macroscale level, the proposed user-defined subroutines employing automatically generated material properties enabled accurate definition of elastic-plastic behavior of porous materials.

- Critical strain energy density (SED) as a function of total volumetric porosity presented by (Eq.7.21) was developed in the proposed work and proven excellent predictive capabilities.
- SED damage model utilizing the framework of XFEM enabled predicting final failure precisely. Also, the damage model proven to be consistent providing conservative failure limits.
- The proposed two-stage finite element procedure running time for (micro-macro models) was in the order of minutes. Therefore, computational effort is a fraction of multiscale modeling techniques requirements where the overall simulation time is in the order of days, e.g. GTN model.

7.7 References

- Abaqus V6.14– Documentation, Dassault Systèmes Simulia Corporation, Providence, Rhode Island (2013).
- Abdelaziz, Y., & Hamouine, A. (2008). A survey of the extended finite element. *Computers and Structures*, 86(11–12), 1141–1151.
<https://doi.org/10.1016/j.compstruc.2007.11.001>
- Allison, P. G., Grewal, H., Hammi, Y., Brown, H. R., Whittington, W. R., & Horstemeyer, M. F. (2013). Plasticity and Fracture Modeling/Experimental Study of a Porous Metal Under Various Strain Rates, Temperatures, and Stress States. *Journal of Engineering Materials and Technology*, 135(4), 041008.
<https://doi.org/10.1115/1.4025292>
- Asim, U. B., Siddiq, M. A., & Kartal, M. (2018). Representative Volume Element (RVE) based Crystal Plasticity study of Void Growth on Phase Boundary in Titanium alloys. *28th International Workshop on Computational Mechanics of Materials (IWCM28)*, 161(December 2018), 346–350.
<https://doi.org/10.1016/j.commatsci.2019.02.005>
- Attaran, M. (2017). The rise of 3-D printing: The advantages of additive manufacturing over traditional manufacturing. *Business Horizons*, 60(5), 677–688.
<https://doi.org/10.1016/j.bushor.2017.05.011>
- Babu, K. P., Mohite, P. M., & Upadhyay, C. S. (2018). Development of an RVE and its

- stiffness predictions based on mathematical homogenization theory for short fibre composites. *International Journal of Solids and Structures*, 130–131, 80–104. <https://doi.org/10.1016/j.ijsolstr.2017.10.011>
- Bal'shin, M. Y. (1949). Dependence of the mechanical properties of porous materials on their porosity and the limiting properties of porous sintered materials. *Dokl. Akad. Nauk SSSR*, 67(5), 831–834.
- Belytschko, T., & Black, T. (1999). Elastic crack growth in finite elements with minimal remeshing. *International Journal for Numerical Methods in Engineering*, 45(5), 601–620. [https://doi.org/10.1002/\(SICI\)1097-0207\(19990620\)45:5<601::AID-NME598>3.0.CO;2-S](https://doi.org/10.1002/(SICI)1097-0207(19990620)45:5<601::AID-NME598>3.0.CO;2-S)
- Belytschko, T., Gracie, R., & Ventura, G. (2009). A review of extended/generalized finite element methods for material modeling. *Modelling and Simulation in Materials Science and Engineering*, 17(4). <https://doi.org/10.1088/0965-0393/17/4/043001>
- Besson, J. (2010). *Continuum models of ductile fracture: A review*. *International Journal of Damage Mechanics* (Vol. 19). <https://doi.org/10.1177/1056789509103482>
- Chawla, N., & Deng, X. (2005). Microstructure and mechanical behavior of porous sintered steels. *Materials Science and Engineering A*, 390(1–2), 98–112. <https://doi.org/10.1016/j.msea.2004.08.046>
- Choren, J. A., Heinrich, S. M., & Silver-Thorn, M. B. (2013). Young's modulus and volume porosity relationships for additive manufacturing applications. *Journal of Materials Science*, 48(15), 5103–5112. <https://doi.org/10.1007/s10853-013-7237-5>
- Danas, K., & Aravas, N. (2012). Numerical modeling of elasto-plastic porous materials with void shape effects at finite deformations. *Composites Part B: Engineering*, 43(6), 2544–2559. <https://doi.org/10.1016/j.compositesb.2011.12.011>
- Deng, X., Piotrowski, G., Chawla, N., & Narasimhan, K. S. (2008). Fatigue crack growth behavior of hybrid and prealloyed sintered steels Part I. Microstructure characterization, 491, 19–27. <https://doi.org/10.1016/j.msea.2008.05.009>
- Duarte, A. P. C., Díaz Sáez, A., & Silvestre, N. (2017). Comparative study between XFEM and Hashin damage criterion applied to failure of composites. *Thin-Walled Structures*, 115(October 2016), 277–288. <https://doi.org/10.1016/j.tws.2017.02.020>
- Elnekhaily, S. A., & Talreja, R. (2018). Damage initiation in unidirectional fiber composites with different degrees of nonuniform fiber distribution. *Composites Science and Technology*, 155. <https://doi.org/10.1016/j.compscitech.2017.11.017>
- Frazier, W. E. (2014). Metal additive manufacturing: A review. *Journal of Materials Engineering and Performance*, 23(6), 1917–1928. <https://doi.org/10.1007/s11665-014-0958-z>
- Fries, T.-P., & Belytschko, T. (2010). The extended/generalized finite element method: An overview of the method and its applications. *International Journal for Numerical Methods in Engineering*, 84(April), 253–304. <https://doi.org/10.1002/nme>

- Gao, W., Zhang, Y., Ramanujan, D., Ramani, K., Chen, Y., Williams, C. B., ...
Zavattieri, P. D. (2015). The status, challenges, and future of additive manufacturing in engineering. *CAD Computer Aided Design*, 69, 65–89.
<https://doi.org/10.1016/j.cad.2015.04.001>
- Gaudig, W., Mellert, R., Weber, U., & Schmauder, S. (2003). Self-consistent one-particle 3D unit cell model for simulation of the effect of graphite aspect ratio on Young's modulus of cast-iron. *Computational Materials Science*, 28(3–4 SPEC. ISS.), 654–662. <https://doi.org/10.1016/j.commat.2003.08.021>
- Ghayoor, H., Hoa, S. V., & Marsden, C. C. (2018). A micromechanical study of stress concentrations in composites. *Composites Part B: Engineering*, 132.
<https://doi.org/10.1016/j.compositesb.2017.09.009>
- Guo, Z., Wang, L., Chen, Y., Zheng, L., Yang, Z., & Dong, L. (2017). A universal model for predicting the effective shear modulus of two-dimensional porous materials. *Mechanics of Materials*, 110, 59–67. <https://doi.org/10.1016/j.mechmat.2017.04.006>
- Gupta, V., & Duarte, C. A. (2016). On the enrichment zone size for optimal convergence rate of the Generalized/Extended Finite Element Method. *Computers and Mathematics with Applications*, 72(3), 481–493.
<https://doi.org/10.1016/j.camwa.2016.04.043>
- Gurson, A. L. (1977). Continuum Theory of Ductile Rupture by Void Nucleation and Growth: Part I—Yield Criteria and Flow Rules for Porous Ductile Media. *Journal of Engineering Materials and Technology*, 99(1), 2. <https://doi.org/10.1115/1.3443401>
- Han, F., Tang, B., Kou, H., Li, J., & Feng, Y. (2015). Experiments and crystal plasticity finite element simulations of nanoindentation on Ti-6Al-4V alloy. *Materials Science and Engineering A*, 625, 28–35. <https://doi.org/10.1016/j.msea.2014.11.090>
- Hardin, R. A., & Beckermann, C. (2007). Effect of porosity on the stiffness of cast steel. *Metallurgical and Materials Transactions A: Physical Metallurgy and Materials Science*, 38 A(12), 2992–3006. <https://doi.org/10.1007/s11661-007-9390-4>
- Hardin, R. A., & Beckermann, C. (2013). Effect of porosity on deformation, damage, and fracture of cast steel. *Metallurgical and Materials Transactions A: Physical Metallurgy and Materials Science*, 44(12), 5316–5332.
<https://doi.org/10.1007/s11661-013-1669-z>
- Hashin, Z., & Rotem, A. (1973). A Fatigue Failure Criterion for Fiber Reinforced Materials. *Journal of Composite Materials*, 7(4), 448–464.
<https://doi.org/10.1177/002199837300700404>
- Hill, R. (1963). Elastic properties of reinforced solids: some theoretical principles. *Journal of the Mechanics and Physics of Solids*, 11(5), 357–372.
- Hill, R. (1963). Elastic properties of reinforced solids: Some theoretical principles. *Journal of the Mechanics and Physics of Solids*, 11(5), 357–372.
[https://doi.org/10.1016/0022-5096\(63\)90036-X](https://doi.org/10.1016/0022-5096(63)90036-X)

- Hill, R. (1998). *The mathematical theory of plasticity* (11th ed.). Oxford university press.
- Hill, R. (2006). The elastic field of an inclusion in an anisotropic medium. *Proceedings of the Royal Society of London. Series A. Mathematical and Physical Sciences*, 300(1461), 270–289. <https://doi.org/10.1098/rspa.1967.0170>
- Hollister, S. J., & Kikuchi, N. (1992). A comparison of homogenization and standard mechanics analyses for periodic porous composites. *Computational Mechanics*, 10(2), 73–95. <https://doi.org/10.1007/BF00369853>
- Huang, H., & Talreja, R. (2005). Effects of void geometry on elastic properties of unidirectional fiber reinforced composites. *Composites Science and Technology*, 65(13), 1964–1981. <https://doi.org/10.1016/j.compscitech.2005.02.019>
- Jeong, H. Y., & Pan, J. (1995). A macroscopic constitutive law for porous solids with pressure-sensitive matrices and its implications to plastic flow localization. *International Journal of Solids and Structures*, 32(24), 3669–3691. [https://doi.org/10.1016/0020-7683\(95\)00009-Y](https://doi.org/10.1016/0020-7683(95)00009-Y)
- Jones, R. M. (2009). *Deformation theory of plasticity*. Bull Ridge Corporation.
- KNUDSEN, F. P. (1959). Dependence of Mechanical Strength of Brittle Polycrystalline Specimens on Porosity and Grain Size. *Journal of the American Ceramic Society*, 42(8), 376–387. <https://doi.org/10.1111/j.1151-2916.1959.tb13596.x>
- Kruth, J. P., Mercelis, P., Van Vaerenbergh, J., Froyen, L., & Rombouts, M. (2005). Binding mechanisms in selective laser sintering and selective laser melting. *Rapid Prototyping Journal*, 11(1), 26–36. <https://doi.org/10.1108/13552540510573365>
- Leblond, J. (2014). An improved description of spherical void growth in plastic porous materials with finite porosities, 3(2013), 1232–1237. <https://doi.org/10.1016/j.mspro.2014.06.200>
- Leclerc, W., Karamian-Surville, P., & Vivet, A. (2015). An efficient and automated 3D FE approach to evaluate effective elastic properties of overlapping random fibre composites. *Computational Materials Science*, 99, 1–15. <https://doi.org/10.1016/j.commatsci.2014.10.047>
- Ma, H., Liu, X., & Hu, G. (2006). Overall elastoplastic property for micropolar composites with randomly oriented ellipsoidal inclusions. *Computational Materials Science*, 37(4), 582–592. <https://doi.org/10.1016/j.commatsci.2005.12.016>
- Mbiakop, A., Constantinescu, A., & Danas, K. (2015). An analytical model for porous single crystals with ellipsoidal voids. *Journal of the Mechanics and Physics of Solids*, 84, 436–467. <https://doi.org/10.1016/j.jmps.2015.07.011>
- Mignone, P. J., Echlin, M. P., Pollock, T. M., Finlayson, T. R., Riley, D. P., Sesso, M. L., & Franks, G. V. (2017). Modelling the elastic properties of bi-continuous composite microstructures captured with TriBeam serial-sectioning. *Computational Materials Science*, 131, 187–195. <https://doi.org/10.1016/j.commatsci.2017.01.026>
- Mirkhalaf, S. M., Andrade Pires, F. M., & Simoes, R. (2016). Determination of the size of

- the Representative Volume Element (RVE) for the simulation of heterogeneous polymers at finite strains. *Finite Elements in Analysis and Design*, 119, 30–44. <https://doi.org/10.1016/j.finel.2016.05.004>
- Moës, N., Dolbow, J., & Belytschko, T. (1999). A finite element method for crack growth without remeshing. *International Journal for Numerical Methods in Engineering*, 46(1), 131–150. [https://doi.org/10.1002/\(SICI\)1097-0207\(19990910\)46:1<131::AID-NME726>3.0.CO;2-J](https://doi.org/10.1002/(SICI)1097-0207(19990910)46:1<131::AID-NME726>3.0.CO;2-J)
- Mori, T., & Tanaka, K. (1973). Average stress in matrix and average elastic energy of materials with misfitting inclusions. *Acta Metallurgica*, 21(5), 571–574. [https://doi.org/10.1016/0001-6160\(73\)90064-3](https://doi.org/10.1016/0001-6160(73)90064-3)
- Morin, L., Leblond, J. B., & Kondo, D. (2015). A Gurson-type criterion for plastically anisotropic solids containing arbitrary ellipsoidal voids. *International Journal of Solids and Structures*, 77, 86–101. <https://doi.org/10.1016/j.ijsolstr.2015.05.021>
- Morin, L., Michel, J. C., & Leblond, J. B. (2017). A Gurson-type layer model for ductile porous solids with isotropic and kinematic hardening. *International Journal of Solids and Structures*, 118–119, 167–178. <https://doi.org/10.1016/j.ijsolstr.2017.03.028>
- Nemat-Nasser, S., & Taya, M. (1981). On effective moduli of an elastic body containing periodically distributed voids. *Quarterly of Applied Mathematics*, 39(1), 43–59. <https://doi.org/10.1090/qam/99626>
- Omairey, S. L., Dunning, P. D., & Sriramula, S. (2018). Development of an ABAQUS plugin tool for periodic RVE homogenisation. *Engineering with Computers*, 0(0), 1–11. <https://doi.org/10.1007/s00366-018-0616-4>
- Pabst, W., & Gregorová, E. (2015). Critical Assessment 18: Elastic and thermal properties of porous materials -rigorous bounds and cross-property relations. *Materials Science and Technology (United Kingdom)*, 31(15), 1801–1808. <https://doi.org/10.1080/02670836.2015.1114697>
- Pontefisso, A., Zappalorto, M., & Quaresimin, M. (2015). An efficient RVE formulation for the analysis of the elastic properties of spherical nanoparticle reinforced polymers. *Computational Materials Science*, 96(PA), 319–326. <https://doi.org/10.1016/j.commatsci.2014.09.030>
- Ramberg, W., & Osgood, W. R. (1943). *Description of stress-strain curves by three parameters. National Advisory Committee for Aeronautics.* <https://doi.org/10.1016/j.matdes.2009.07.011>
- Rashid, M. M., & Nemat-Nasser, S. (1992). A constitutive algorithm for rate-dependent crystal plasticity. *Computer Methods in Applied Mechanics and Engineering*, 94(2), 201–228. [https://doi.org/10.1016/0045-7825\(92\)90147-C](https://doi.org/10.1016/0045-7825(92)90147-C)
- Ravi, S. K., Seefeldt, M., Van Bael, A., Gawad, J., & Roose, D. (2019). Multi-scale material modelling to predict the material anisotropy of multi-phase steels. *Computational Materials Science*, 160(September 2018), 382–396.

- <https://doi.org/10.1016/j.commatsci.2019.01.028>
- Rousselier, G. (2001). Dissipation in porous metal plasticity and ductile fracture. *Journal of the Mechanics and Physics of Solids*, 49(8), 1727–1746.
[https://doi.org/10.1016/S0022-5096\(01\)00013-8](https://doi.org/10.1016/S0022-5096(01)00013-8)
- Saby, M., Bernacki, M., Roux, E., & Bouchard, P. O. (2013). Three-dimensional analysis of real void closure at the meso-scale during hot metal forming processes. *Computational Materials Science*, 77, 194–201.
<https://doi.org/10.1016/j.commatsci.2013.05.002>
- Salahouelhadj, A., & Haddadi, H. (2010). Estimation of the size of the RVE for isotropic copper polycrystals by using elastic-plastic finite element homogenisation. *Computational Materials Science*, 48(3), 447–455.
<https://doi.org/10.1016/j.commatsci.2009.12.014>
- Shames, I. H. (1997). *Elastic and inelastic stress analysis*. CRC Press.
- Shan, Z., & Gokhale, A. M. (2002). Representative volume element for non-uniform micro-structure. *Computational Materials Science*, 24(3), 361–379.
[https://doi.org/10.1016/S0927-0256\(01\)00257-9](https://doi.org/10.1016/S0927-0256(01)00257-9)
- Sharma, N. K., Mishra, R. K., & Sharma, S. (2016). 3D micromechanical analysis of thermo-mechanical behavior of Al₂O₃/Al metal matrix composites. *Computational Materials Science*, 115, 192–201. <https://doi.org/10.1016/j.commatsci.2015.12.051>
- Siavouche, N.-N., & Hori, M. (1993). *Micromechanics: overall properties of heterogeneous materials*. (J. D. Achenbach, B. Budiansky, H. A. Lauwerier, P. G. Saffman, L. Van Wijngaarden, & J. R. Willis, Eds.) ((Vol. 37)). Elsevier B.V.
- Sladek, J., Sladek, V., Krahulec, S., & Song, C. (2016). Micromechanics determination of effective properties of voided magnetoelastic materials. *Computational Materials Science*, 116, 103–112. <https://doi.org/10.1016/j.commatsci.2015.05.015>
- Song, B., Zhao, X., Li, S., Han, C., Wei, Q., Wen, S., ... Shi, Y. (2015). Differences in microstructure and properties between selective laser melting and traditional manufacturing for fabrication of metal parts: A review. *Frontiers of Mechanical Engineering*, 10(2), 111–125. <https://doi.org/10.1007/s11465-015-0341-2>
- Song, D., Li, Y., Zhang, K., Cheng, H., Liu, P., & Hu, J. (2016). Micromechanical analysis for microscopic damage initiation in fiber/epoxy composite during interference-fit pin installation. *Materials and Design*, 89, 36–49.
<https://doi.org/10.1016/j.matdes.2015.09.118>
- Song, D., & Ponte Castañeda, P. (2017). A finite-strain homogenization model for viscoplastic porous single crystals: I – Theory. *Journal of the Mechanics and Physics of Solids*, 107(3), 560–579. <https://doi.org/10.1016/j.jmps.2017.06.008>
- Soro, N., Brassart, L., Chen, Y., Veidt, M., Attar, H., & Dargusch, M. S. (2018). Finite element analysis of porous commercially pure titanium for biomedical implant application. *Materials Science and Engineering A*, 725(April), 43–50.

- <https://doi.org/10.1016/j.msea.2018.04.009>
- Spaggiari, A., & O'Dowd, N. (2012). The influence of void morphology and loading conditions on deformation and failure of porous polymers: A combined finite-element and analysis of variance study. *Computational Materials Science*, *64*, 41–46. <https://doi.org/10.1016/j.commatsci.2011.12.022>
- Stephens, R. I., Horn, J. J., Poland, D. D., & Sager, E. A. (1998a). FATIGUE AND FRACTURE TOUGHNESS OF HIGH STRENGTH FL4405 Materials / Specimens, 72–101.
- Stephens, R. I., Horn, J. J., Poland, D. D., & Sager, E. A. (1998b). Influence of Density and Porosity Size and Shape on Fatigue and Fracture Toughness of High Strength FL4405 P/M Steel. *Effects of Product Quality and Design Criteria on Structural Integrity, STP1337-EB*, 72–101. Retrieved from <https://doi.org/10.1520/STP12343S>
- Trias, D., Costa, J., Turon, A., & Hurtado, J. E. (2006). Determination of the critical size of a statistical representative volume element (SRVE) for carbon reinforced polymers. *Acta Materialia*, *54*(13), 3471–3484. <https://doi.org/10.1016/j.actamat.2006.03.042>
- Trillat, M., & Pastor, J. (2005). Limit analysis and Gurson's model. *European Journal of Mechanics, A/Solids*, *24*(5), 800–819. <https://doi.org/10.1016/j.euromechsol.2005.06.003>
- Tvergaard, V., & Needleman, A. (1984). Analysis of the cup-cone fracture in a round tensile bar. *Acta Metallurgica*, *32*(1), 157–169. [https://doi.org/10.1016/0001-6160\(84\)90213-X](https://doi.org/10.1016/0001-6160(84)90213-X)
- Vadillo, G., Reboul, J., & Fern, J. (2016). European Journal of Mechanics A / Solids A modi fi ed Gurson model to account for the in fl uence of the Lode parameter at high triaxialities, *56*, 31–44. <https://doi.org/10.1016/j.euromechsol.2015.09.010>
- Weinberg, K., Mota, A., & Ortiz, M. (2006). A variational constitutive model for porous metal plasticity. *Computational Mechanics*, *37*(2), 142–152. <https://doi.org/10.1007/s00466-005-0685-2>
- Xu, W., Sun, X., Li, D., Ryu, S., & Khaleel, M. A. (2013). Mechanism-based representative volume elements (RVEs) for predicting property degradations in multiphase materials. *Computational Materials Science*, *68*, 152–159. <https://doi.org/10.1016/j.commatsci.2012.10.026>
- Yazid, A., Abdelkader, N., & Abdelmadjid, H. (2009). A state-of-the-art review of the X-FEM for computational fracture mechanics. *Applied Mathematical Modelling*, *33*(12), 4269–4282. <https://doi.org/10.1016/j.apm.2009.02.010>
- Zhang, C., Gong, B., Deng, C., & Wang, D. (2017). Computational prediction of mechanical properties of a C-Mn weld metal based on the microstructures and micromechanical properties. *Materials Science and Engineering A*, *685*(November 2016), 310–316. <https://doi.org/10.1016/j.msea.2017.01.023>

Zheng, B., Zhou, Y., Smugeresky, J. E., Schoenung, J. M., & Lavernia, E. J. (2008). Thermal behavior and microstructural evolution during laser deposition with laser-engineered net shaping: Part I. Numerical calculations. *Metallurgical and Materials Transactions A: Physical Metallurgy and Materials Science*, 39(9), 2228–2236. <https://doi.org/10.1007/s11661-008-9557-7>

8 Automating XFEM Modeling Process for Optimal Failure Predictions

8.1 Abstract

The eXtended Finite Element Method (XFEM) is a versatile method for solving crack propagation problems. Meanwhile, XFEM predictions for crack onset and propagation rely on the stress field which tends to converge at a slower rate than that of displacements, making it challenging to capture critical load at crack onset accurately. Furthermore, identifying the critical region(s) for XFEM nodal enrichments is user dependent. The identification process can be straightforward for small scale test specimen while in other cases such as complex structures it can be unmanageable. In this work a novel approach is proposed with three major objectives; (1) alleviate user-dependency (2) enhance predictions accuracy (3) minimize computational effort. An automatic critical region(s) identification based on material selected failure criterion is developed. Moreover, the approach enables the selection of optimized mesh necessary for accurate prediction of failure loads at crack initiation. Also, optimal enrichment zone size determination is automated. The proposed approach was developed as an iterative algorithm and implemented in ABAQUS using Python scripting. The proposed algorithm was validated against own test data of un-notched specimens as well as relevant test data from the literature. The results of the predicted loads/displacements at failure are in excellent agreement with measurements. Crack onset locations were in very good agreement with observations from testing. Finally, the proposed algorithm has shown a significant enhancement in the overall computational efficiency compared to the conventional XFEM. The proposed algorithm can be easily implemented into user-built or commercial finite element codes.

8.2 Introduction

Stress concentrations may cause the initiation of a fatigue crack in a structure (Sumi, 2014). It arises mainly by either a concentrated force acting on a body or a geometrical discontinuity such as holes, a sharp geometrical change or a cracked surface. Finite Element Method (FEM) has proven to be a versatile analysis technique in solving structural engineering problems. Meanwhile, problems involving discontinuities or singularities such as crack onset/propagation problems, are quite problematic (Pommier et al., 2013). One Major challenge in the conventional FEM is the need for mesh regeneration (Sumi, 2014) to align the mesh with crack boundaries. Moreover, stress concentration at the crack-tip requires mesh refinement for accurate representation (Moës et al., 1999). Mesh alignment and refinement operations negatively affect computational efficiency and accuracy of predictions (Dolbow, Moës, & Belytschko, 2001). The eXtended Finite Element Method (XFEM) initially proposed by Belytschko and his collaborators (T. Belytschko & Black, 1999; Moës et al., 1999). Belytschko and Black (T. Belytschko & Black, 1999) introduced a new technique for solving crack growth problems with minimal remeshing. Their methodology was developed based on the work by Melenk and Babuška (BABUŠKA & MELENK, 1997; Melenk & Babuška, 1996). The method provided an application of the partition of unity theorem to conventional FEM. XFEM works by enriching the nodes of the traditional finite element mesh by special shape functions to account for the displacement field discontinuities which are present in the case of a macro-crack. Hence, in XFEM domain remeshing is no longer needed to account for the crack presence and its propagation. The method is well suited for crack propagation (Ted Belytschko et al., 2009b), and it was implemented in commercial Finite Element Analysis (FEA) codes such

as ABAQUS and ANSYS (*Abaqus Documentation*, 2014; Radhakrishnan, 2011). Meanwhile, the current implementation of XFEM in commercial finite element code has its challenges (L. Wu, Zhang, & Guo, 2013). The primary problem is related to the need of embedding an initial crack a priori into the finite element mesh to trigger crack propagation. Inserting a crack raises the need for an expert user to identify the crack location. Alternatively, critical region(s) which are more likely to fail has to be determined for XFEM nodal enrichments. Hence without an expert user, enriching nodes of the entire domain of a finite element mesh becomes a general practice, which in turn results in more runtime and reduced computational efficiency. Heavily tied to the primary challenge comes a second one resulting from the dependency of prediction accuracy on mesh quality; more specifically the prediction of crack onset being dependent on mesh quality and density. XFEM predictions applied to composites has been on rapid development by researchers. For example, Grogan et al. (Grogan, Leen, & O. Brádaigh, 2014) proposed a methodology for simulating thermal fatigue delamination in FRP composites using the framework of XFEM. Their methodology was used for the safe design of composite cryogenic fuel tanks. The proposed model predictions were validated with measurements from static and fatigue test methods. In their models, initial cracks were embedded to trigger crack propagation till failure. Duarte et al. (Duarte et al., 2017) provided a comparative study between XFEM and the Hashin's damage criterion applied to the failure of composites. They concluded that the XFEM solution of the problem dealing with laminated composites overestimated failure loads at smaller deformations, suggesting that further investigation is required since XFEM predicted stiffer behavior. Petrov et al. (Petrov et al., 2018) presented a parametric

study for assessing the performance of XFEM applied to cross-ply composite laminates cracking. In their conclusions, XFEM predictions overestimated the number of cracks as well as corresponding strains and stresses. Bobiński and Tejchman (Bobinski & Tejchman, 2012; Tejchmann & Bobinski, 2015) used XFEM to study cracked concrete elements. In their work, they compared XFEM predictions to testing measurements of double-notched specimens reported by Nooru-Mohamed (Nooru-Mohamed, M. B. "Mixed-mode Fracture of Concrete: An Experimental Approach." Delft University of Technology, 1992). Load-deflection curves in (Bobinski & Tejchman, 2012; Tejchmann & Bobinski, 2015) reflected over-predictions of approximately 20% when compared to measurements. In review article on recent developments in damage modeling methodologies for composites (P. F. Liu & Zheng, 2010), the multiscale modeling technique was highlighted as promising technique and promoted further investigation. Meanwhile Liu and Zheng (P. F. Liu & Zheng, 2010) identified multiscale modeling computational challenges in incorporating microscopic modeling and macroscale failure mechanisms. As an example on multiscale modeling, Unger and Eckardt (Unger & Eckardt, 2011) presented multiscale modeling of concrete by coupling a homogeneous macroscale model with a heterogeneous mesoscale one. Their results were in a good agreement compared to testing results, but the multiscale modeling approach required long computational time (45000 ~ 64000 sec) for solving 2-D problems. In the same review article Liu and Zheng (P. F. Liu & Zheng, 2010) pointed out the advantages as well as the promising outcomes of XFEM which is the focus of the current research.

Therefore, in the current work, a novel approach is developed with the objectives (1) Automatic identification of critical region(s) to alleviate user-dependency, (2) rigorous automatic mesh refinement based on stress convergence within these region(s) to ensure accurate predictions and (3) automatically enriching critical region(s) for optimal XFEM execution. The main aim of current work is to eliminate the reliance on an expert user in identifying the critical region(s) and mesh refinement to enhance predictions accuracy at failure onset (damage initiation). For this purpose, an automation algorithm is developed to enable automatic identification of critical region(s) location/size and performing optimal mesh refinement procedure. The algorithm enriches only necessary nodes corresponding to the critical region(s) for XFEM modeling to predict the crack onset failure load and location. For the purpose of validating the current methodology, notched specimens were excluded since they are mainly used to study crack propagation rather than its onset. It is noteworthy to mention that the scope of the current work is predicting failure onset location together with failure loads/displacements with minimal user intervention to allow analyzing a real-life structure. To this end, a set of six un-notched concrete prismatic specimens were prepared and tested for validation. In addition, further comparisons were established with relevant test data of un-notched specimens from the literature.

8.3 Research Significance

In the current work, some of XFEM implementation challenges are considered. The first challenge is the method dependency on user skills for critical region(s) identification for nodal enrichments. The second challenge stems from the high dependency of predictions accuracy on mesh quality and density. The proposed approach overcomes both challenges

by automating the XFEM modeling process to arrive at a convergent mesh as well as potential (crack onset) zone without user intervention, hence allowing regular users to predict failure onset accurately. Another chief advantage of the proposed methodology is eliminating the need to embed initial cracks when analyzing crack propagation problems. This provides further advantages when the analysis is not limited to propagation and damage onset prediction is of primary importance. Critical load predictions at crack initiation facilitated by the current approach proved to be in excellent agreement with measurements obtained when testing un-notched specimens as well as relevant test data from the literature. Therefore, the proposed method allows accurate prediction of failure onset and eliminates the need for biasing specimens by introducing notches or first cracks. Furthermore, the proposed approach enables efficient mesh optimization and optimal enrichments which in turn enhances the overall computational efficiency. In conclusion, applying the proposed approach have significant effects on providing accurate and computationally efficient analysis of complex structures where critical region(s) identification can be challenging even for an expert user.

8.4 XFEM Fundamentals and ABAQUS Implementation

8.4.1 Mathematical Formulation

In the current section, the mathematical aspects of XFEM are briefly presented as in (Moës et al., 1999). Consider a finite element mesh of a two-dimensional cracked body as shown in **Figure 8.1a**, in which a crack is shown using a dashed line, finite element mesh by solid lines and nodes are represented by black filled circles (set I). As can be seen, in XFEM the crack is surrounded by two types of nodes. The first type is the ‘Heaviside’ enrichment

nodes which are illustrated using square shapes (set J). The second type is the ‘Crack-tip’ nodes which are presented using red circles (set K). The formulation of the XFEM problem is similar to that of conventional FEM formulation where both are based on standard Galerkin’s formulation with a slight difference in the former (*Abaqus Documentation*, 2014). XFEM utilizes the global shape functions of conventional FEM throughout all nodes in the mesh (set I). A subset of the elemental nodes is referred to as ‘enriched nodes’ (set J and K) where extra terms are added to the global shape function to account for discontinuities in the displacement field (e.g., crack jump) in addition to the crack-tip singularities.

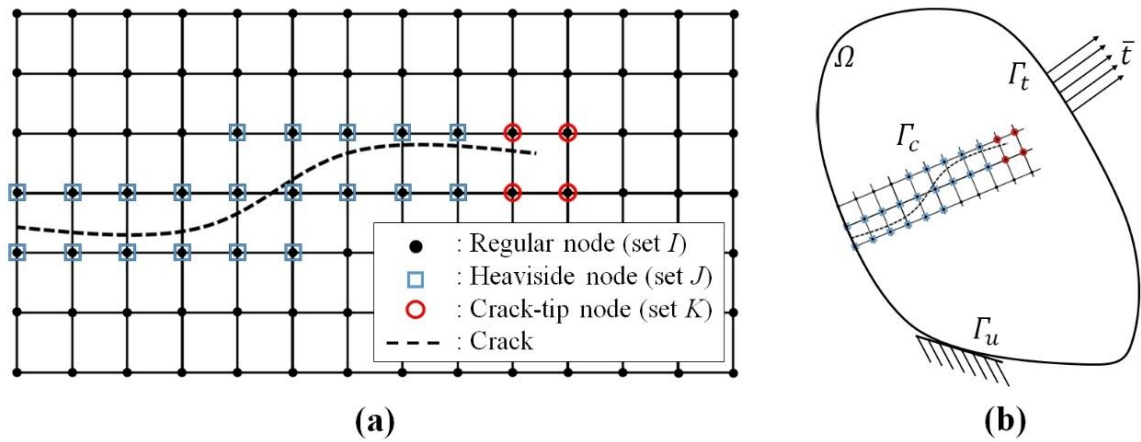


Figure 8.1 (a) 2-D finite element mesh of a cracked body. (b) 2-D linear elastic boundary value problem with a crack

Therefore, general shape function for all nodes in the domain takes the form of **(Eq.8.1)**.

$$u^h(x) = \sum_{i \in I} u_i N_i + \sum_{j \in J} b_j N_j H(x) + \sum_{k \in K} N_k \left[\sum_{l=1}^4 c_k^l F_l(x) \right] \quad \text{(Eq.8.1)}$$

where x presents the global coordinates, N_i are shape functions of i and u_i are the degrees of freedom of node i . $H(x)$ is the Heaviside function or the jump function, N_j are the shape

functions related to the discontinuity at node j , while b_j are the additional degrees of freedom associated to the jump function. $F_l(x)$ are the crack-tip enrichment functions, N_k are the shape functions related to the crack-tip functions at node k and c_k^l are the additional degrees of freedom related to the elastic asymptotic crack-tip enrichment functions. For 2-D elasticity problem, the crack-tip enrichment functions are given by

$$\{F_l(r, \theta)\}_{l=1}^4 = \left\{ \sqrt{r} \cos\left(\frac{\theta}{2}\right), \sqrt{r} \sin\left(\frac{\theta}{2}\right), \sqrt{r} \sin\left(\frac{\theta}{2}\right) \sin \theta, \sqrt{r} \cos\left(\frac{\theta}{2}\right) \sin \theta \right\} \quad (\text{Eq.8.2})$$

where (r, θ) represent the polar coordinate system with the origin at the crack-tip as shown in **Figure 8.2**. The tangent s is at $\theta = 0$, and the outward normal at $\theta = 90$, is denoted by n .

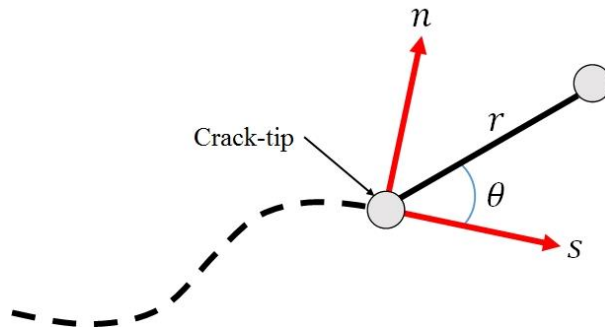


Figure 8.2 Crack-tip representation showing the outward normal and the tangent.

Throughout the domain of the problem, nodes which are not enriched by a Heaviside function nor a crack-tip asymptotic function are associated with the conventional shape functions of FEM. Hence, **(Eq.8.1)** can be simplified to include only the first summation term on RHS leading to the traditional formulation of FEM reading as

$$u^h(x) = \sum_{i \in I} u_i N_i \quad (\text{Eq.8.3})$$

For the region which is cut by the crack (crack domain), the displacement approximation function of XFEM can be reduced to only include both first and second summation terms of **(Eq.8.1)** and can be written as

$$u^h(x) = \sum_{i \in I} u_i N_i + \sum_{j \in J} b_j N_j H(x) \quad (\text{Eq.8.4})$$

Finally, to account for the crack-tip singularities as well as its propagation **(Eq.8.1)** can be reduced to only include first and third summation terms on the RHS which takes the form of **(Eq.8.5)** as follows

$$u^h(x) = \sum_{i \in I} u_i N_i + \sum_{k \in K} N_k \left[\sum_{l=1}^4 c_k^l F_l(x) \right] \quad (\text{Eq.8.5})$$

As can be observed from the previous equations, the computational effort required for the solution of XFEM is higher than that needed for conventional FEM, because XFEM accounts for more degrees of freedom to capture crack behavior using the same number of nodes leading to an increased problem size; demanding more computational effort.

8.4.2 Enrichment Zone Sizing

In a 2D linear elastic boundary value problem shown in **Figure 8.1b**, the crack domain is denoted by Ω while the boundary is presented by Γ . The boundary conditions Γ is composed of three sets, namely, Γ_u , Γ_t and Γ_c such that $\Gamma = \Gamma_u \cup \Gamma_t \cup \Gamma_c$. The displacements are

imposed on Γ_u , while tractions are imposed on Γ_t . The crack surface represented by Γ_c which is assumed to be traction-free. The equilibrium equations and the constitutive relationships are given by

$$\nabla \cdot \boldsymbol{\sigma} = 0 \quad \boldsymbol{\sigma} = \mathbf{C} : \boldsymbol{\varepsilon} \quad \text{in } \Omega \quad (\text{Eq.8.6})$$

where ∇ is the gradient operator, $\boldsymbol{\sigma}$ is Cauchy's stress tensor, \mathbf{C} represents Hooke's tensor and $\boldsymbol{\varepsilon}$ is the strain tensor. The prescribed tractions are

$$\boldsymbol{\sigma} \cdot \mathbf{n} = \bar{\mathbf{t}} \quad \text{on } \Gamma_t \quad (\text{Eq.8.7})$$

where \mathbf{n} is the outward unit normal vector to Γ_t . Consequently, for traction free crack surface $\boldsymbol{\sigma} \cdot \mathbf{n} = 0$. Under the assumptions of small strains and displacements, the kinematic equations read

$$\boldsymbol{\varepsilon} = \frac{1}{2} (\nabla \mathbf{u} + \nabla^T \mathbf{u}) \equiv \boldsymbol{\varepsilon}(\mathbf{u}) \quad \text{on } \Omega \quad (\text{Eq.8.8})$$

where $\boldsymbol{\varepsilon}(\mathbf{u})$ is the linearized strains and \mathbf{u} is the displacement field. **(Eq.8.6)** and **(Eq.8.7)** represents the strong form of the governing equations. In order to transform strong formulation of the problem into the weak form which is better suited for finite element computations (Moës & Belytschko, 2002), the displacement \mathbf{u} must belong to a set of kinematically admissible displacement fields (BABUŠKA & MELENK, 1997; T. Belytschko & Black, 1999; Melenk & Babuška, 1996; Pommier et al., 2013). The weak form of the equilibrium equations is given by **(Eq.8.9)**, which is solved using the Galerkin's method.

$$\int_{\Omega} \sigma(u^h) : \varepsilon(v^h) d\Omega = \int_{\Gamma_t} \bar{t} \cdot (v^h) d\Gamma \quad (\text{Eq.8.9})$$

Based on the weak form in **(Eq.8.9)**, the error in the energy norm can be calculated (Moës & Belytschko, 2002; Strouboulis, Copps, & Babuška, 2011). Gupta and Duarte (V. Gupta & Duarte, 2016) utilized the expression of the error in the energy norm to develop a priori estimate for the enrichment zone size. In their work, they explained that the error in the element located immediately outside a distance d from the crack-tip is to remain bounded for optimal convergence. Under this condition and accounting for displacement field u^h near the crack-tip, they developed an expression for optimal zone enrichment reading as follows

$$d^{-2p}h \leq C \quad (\text{Eq.8.10})$$

where d is the minimal enrichment zone size for optimal convergence, p is the polynomial degree of interpolation functions and h is the characteristic length of the element. To attain the optimal rate of convergence the left-hand side of **(Eq.8.10)** is to remain less than or equal to a constant C . This equation was extensively studied in (P. Gupta, Pereira, Kim, Duarte, & Eason, 2012; V. Gupta, 2014; V. Gupta & Duarte, 2016) proving its validity.

8.4.3 XFEM in ABAQUS

Modeling process using XFEM for crack initiation in ABAQUS involves several steps. First, selection of regions that are more likely to fail or initiate a crack (*Abaqus Documentation*, 2014). As an illustration, let us consider the Koyna dam problem shown in **Figure 8.3**, the Koyna dam survived an earthquake of magnitude 6.5 on the Richter scale

on December 11, 1967 (*Abaqus Documentation*, 2014). The quake did not cause significant damage, but it triggered the initiation of some cracks in the dam.

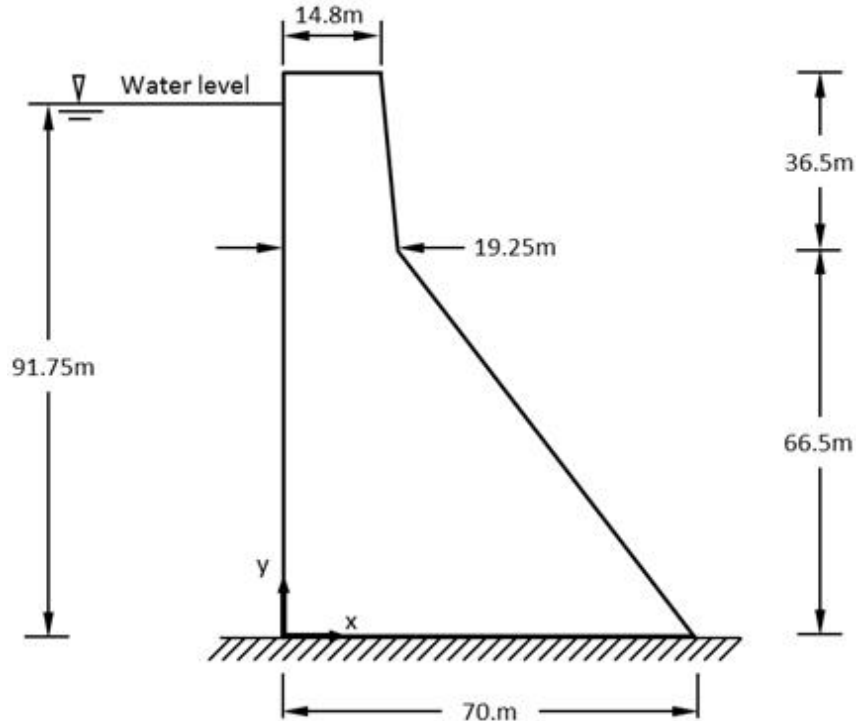


Figure 8.3 The Koyna dam two-dimensional profile reproduced from (*Abaqus V6.14– Documentation, Dassault Systèmes Simulia Corporation, 2013*).

There exist two approaches to analyze this problem using XFEM. The first approach is to embed an initial crack in the critical region to trigger crack propagation analysis as shown in **Figure 8.4a**. Merely this is done to study crack propagation rather than its onset. Embedding initial cracks reduce the accuracy of predicted failure limits, which is detrimental in the case of brittle materials as their failure is said to be catastrophic; Once the damage is initiated, it will rapidly propagate under various types of loading till fracture. In the second approach, the user is required to identify potential failure region(s) which might be a straightforward task for a small structure (e.g., specimen). On the other hand, it might become a very challenging task dealing with large structures. Upon identifying the

critical region(s), the user would select this region(s) as shown in **Figure 8.4b**. Corresponding nodes for this region(s) are enriched with XFEM unique shape functions to account for crack onset. Failing to identify the critical region(s) will potentially lead to the enrichment of the entire domain of the problem. Full domain enrichment results in a drastic increase of required computational requirements and there is a possibility of an ill-conditioned system of equations that may cause convergence problems.



Figure 8.4: Koyuna dam 2-D problem. (a) Initially embedded crack. (b) User-defined critical region for XFEM enrichment.

Initiation of a crack depends on a selected failure criterion for damage, typically stress or strain-based failure criterion. Accurate and efficient evaluation of the stress/strain fields for critical regions is dominant to precisely encounter crack initiation criterion. It is known that stresses in finite elements tend to converge at a slower rate than that of displacements which prompts the need of using refined and optimal mesh throughout the critical region(s) to

precisely capture stress/strain fields (*Abaqus Documentation*, 2014). Mesh refinement and optimization process is a user-dependent process relying on the user's experience. Therefore, the lack of expert user insight entails enriching the entire domain of the problem and raises the potential of using less than optimal mesh, leading to a drastic increase in computational requirements along with lower predictions accuracy. Hence, overcoming the previously mentioned challenges is the primary objective of the current work. The following section devoted to present and discuss the proposed approach by emphasizing the role of each module.

8.5 The Proposed Approach

In the current work, a novel method is proposed to overcome XFEM modeling challenges in ABAQUS. The main aim is to automate the modeling process to predict failure onset (damage initiation) while maintaining optimal computational efficiency. It worth noting that the primary interest of current work is predicting failure onset without biasing or introducing any initial cracks a priori. The proposed algorithm was implemented using Python scripting in ABAQUS with three main tasks to be performed. First, automatic identification of critical region(s). Second, mesh optimization for precise predictions. Third, optimal XFEM execution for predicting crack onset location together with the corresponding load. A typical four-point bending problem was used as an example to demonstrate the algorithm procedures. A two-dimensional model was used throughout this section. The flowchart of the proposed algorithm is shown in **Figure 8.5**.

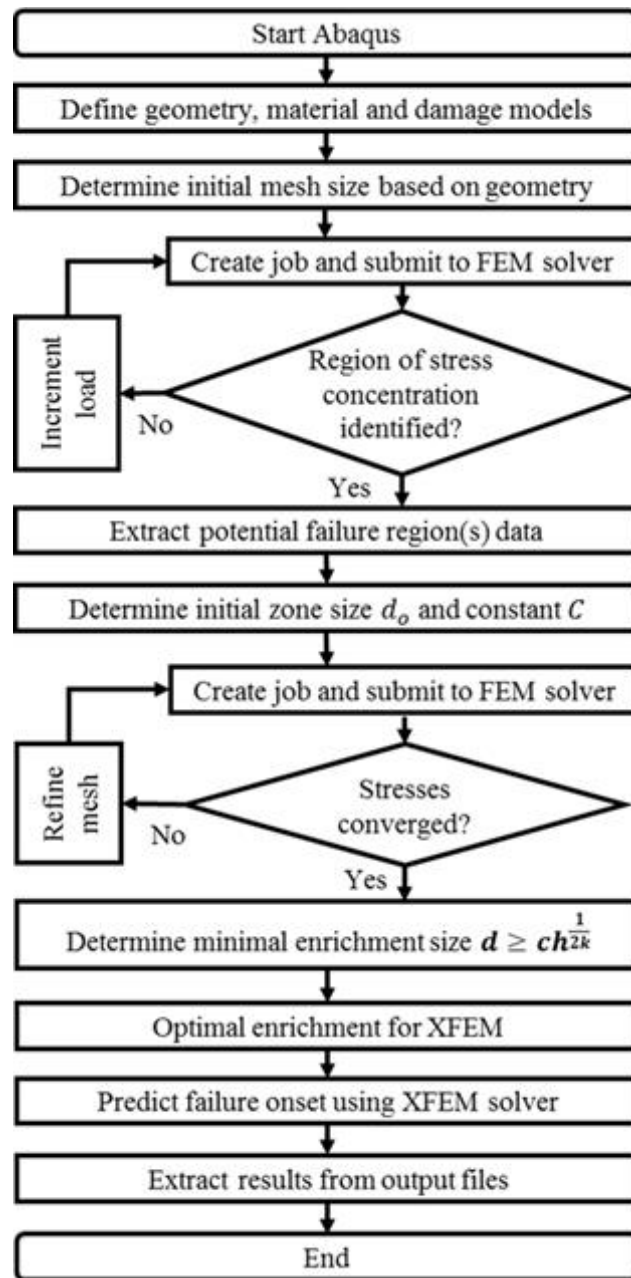


Figure 8.5: The proposed algorithm flowchart

The main algorithm starts with reading geometric parameters, material properties and loading conditions as user input parameters. The first primary step is an automatic determination of mesh size. For this purpose, a subroutine was implemented into the main algorithm to correlate the model geometry to the initial mesh size. A stress convergence

condition was utilized for mesh refinement and optimization to ensure accurate predictions.

Figure 8.6 illustrates the stress convergence performed by the optimal mesh subroutine for the problem in hand.

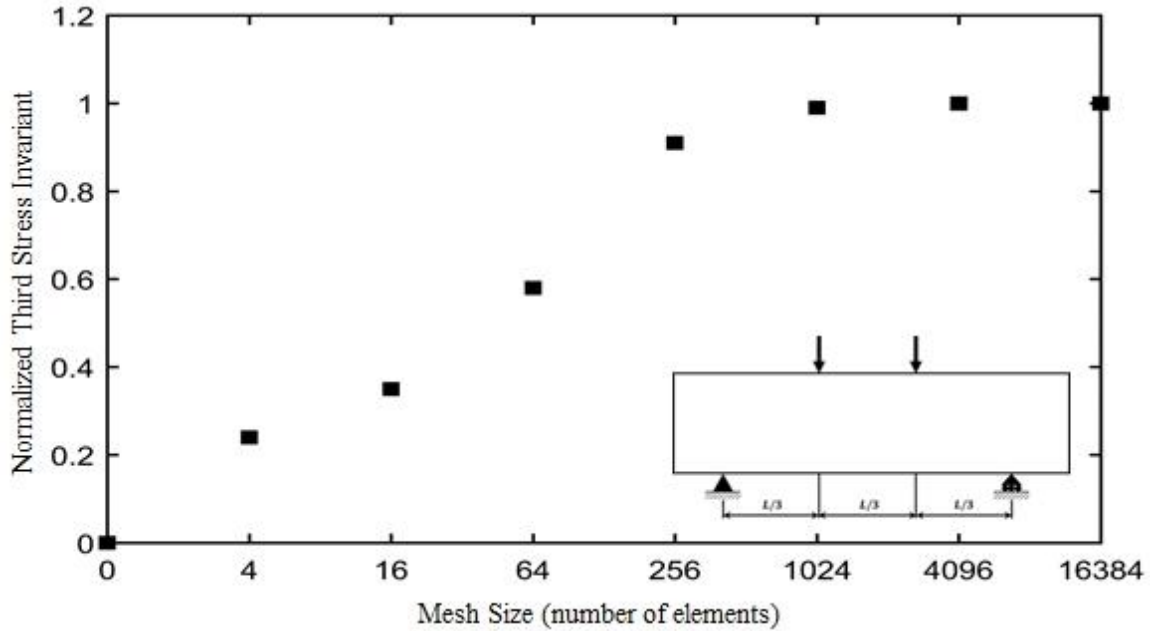


Figure 8.6: Mesh convergence (normalized stress invariant vs. mesh size)

The second step is the essential one, where the algorithm is to check the model to identify the potential region(s) for crack onset. Predictions accuracy relies mainly on the proper selection of failure criterion which is strongly related to the material behavior. In the current work, brittle and quasi-brittle materials are the ones of interest. Hence, the failure criterion was chosen based on the third stress invariant I_3 . The work of Papadopoulos (Papadopoulos, 1987) concluded fracture would occur when the stress tensor determinant reaches a critical value. The evaluation of a stress tensor will result in the same value independent of the material orientation, which can be considered as a material property

(Papadopoulos, 1987). The third stress invariant equation assuming zero out of plane stresses can be expressed as

$$I_3 = \det(\sigma_{ij}) = \sigma_{11}\sigma_{22} - \sigma_{12}^2 \quad (\text{Eq.8.11})$$

where σ_{11} and σ_{22} are the normal stress components, while σ_{12} is the shear stress component. The subroutine initiates iterations by incrementing loading magnitude while checking if failure criterion was encountered. During each iteration, the algorithm extracts data related to the most possible regions to fail. **Figure 8.7** presents the third invariant stress field from the finite element simulation showing the critical region experiencing the maximum values.

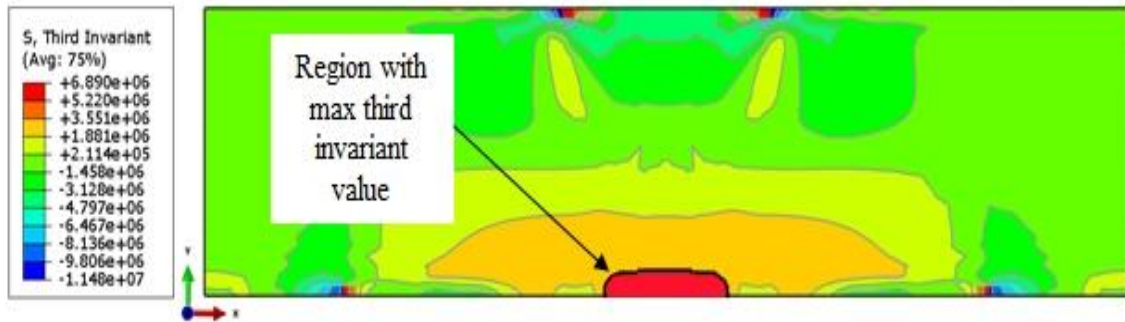


Figure 8.7: Third Invariant stress field from FE simulations

Once the failure criterion is encountered, the algorithm automatically highlights critical zone(s) for crack initiation as depicted in **Figure 8.8**.

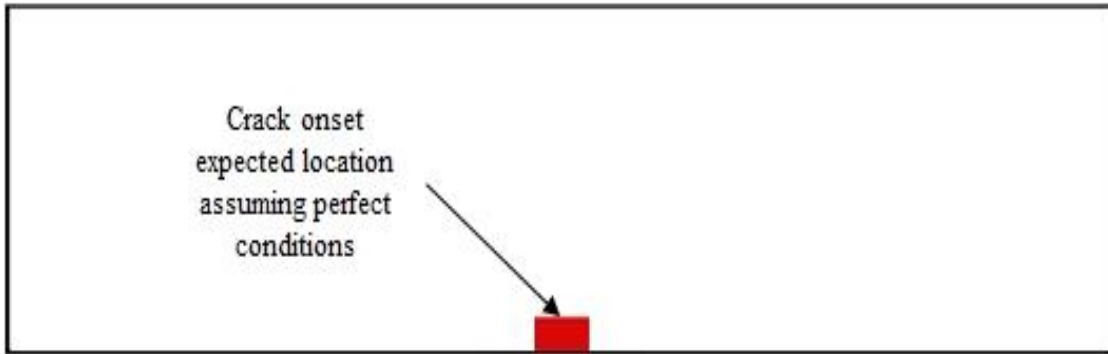


Figure 8.8: 2-D FE model of the beam showing critical zone identification based on a perfect case scenario

As can be seen from Figure 8.8, the algorithm highlighted a small zone of the beam's lower mid-segment. By comparison with **Figure 8.7**, this zone is the one suffering maximum third invariant stress. The location is identified assuming perfect loading and boundary conditions. The critical region identification subroutine can also account for imperfect scenarios in load application/boundary conditions resulting from misalignments. In this case, the subroutine expands the critical zone to include its neighborhood. Critical zone(s) for crack onset are expanded to include regions of potential crack propagation direction. It worth noting that the crack propagation process is proven to be accurate in the standard XFEM method and consequently current implementation in ABAQUS. Meanwhile, without identifying a crack onset zone, the entire domain of the problem becomes a potential region for enrichment. It can be concluded that the region identification subroutine predicts the critical region(s) based on loading levels and imperfections. **Figure 8.9** provides the final critical zone(s) as identified by the subroutine.

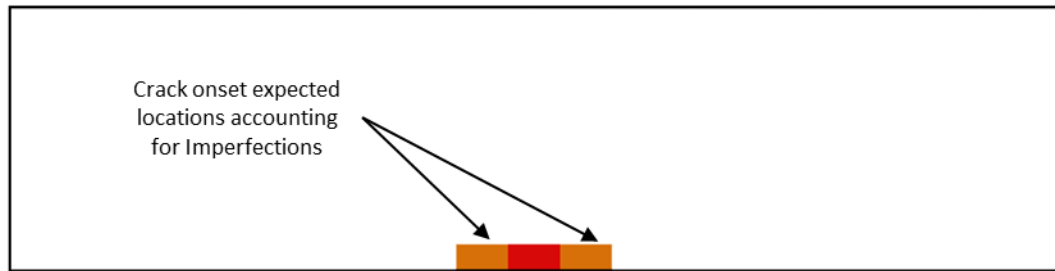


Figure 8.9: Beam FE model showing critical zone identification based on imperfections

In the final step of the algorithm for optimal XFEM execution, a dedicated subroutine performs a mesh refinement to the automatically identified critical region(s). **Figure 8.10** shows the refined mesh for the problem in hand. Subsequently, critical region's nodes are enriched, and the algorithm solves for crack onset.

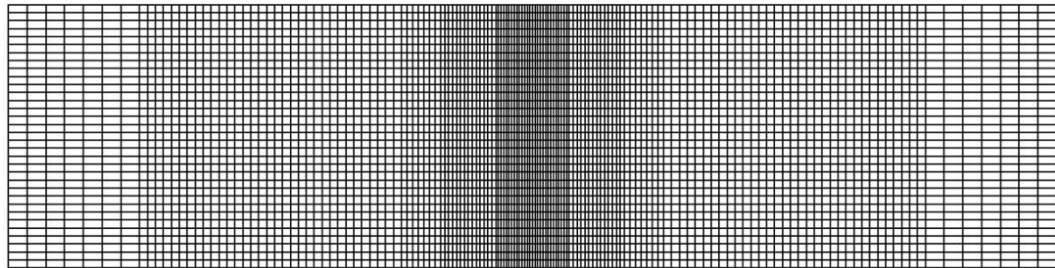


Figure 8.10: FE refined mesh based on the automatically identified critical region

Figure 8.11 shows the enriched nodes of the model highlighted in red. The algorithm submits a new job to the ABAQUS solver, in which the critical region(s) have already been identified for nodal enrichments and the critical region mesh is optimized without user intervention.

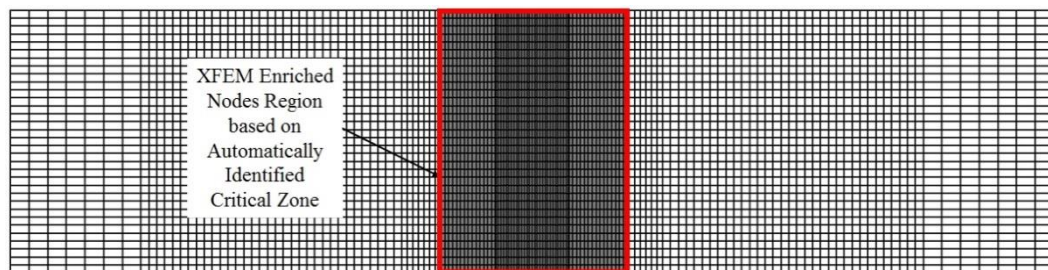


Figure 8.11: FE mesh showing the enriched nodes of the automatically determined critical region

8.6 Numerical Modeling

As discussed in subsection 8.4.3, embedding a notch (crack) in the finite element model or the tested specimens may bias crack onset predictions. Therefore, to test and validate the proposed algorithm, a problem of an un-notched prism under four-point bending was selected. The problem geometry along with the loading conditions as per the American Standard for Testing and Materials (ASTM) designation for the selected problem is shown in **Figure 8.12**. For the detailed specifications of the problem, the reader is referred to ASTM C78 (*C78/C78M-16: Standard Test Method for Flexural Strength of Concrete (Using Simple Beam with Third-Point Loading)*), 2010).

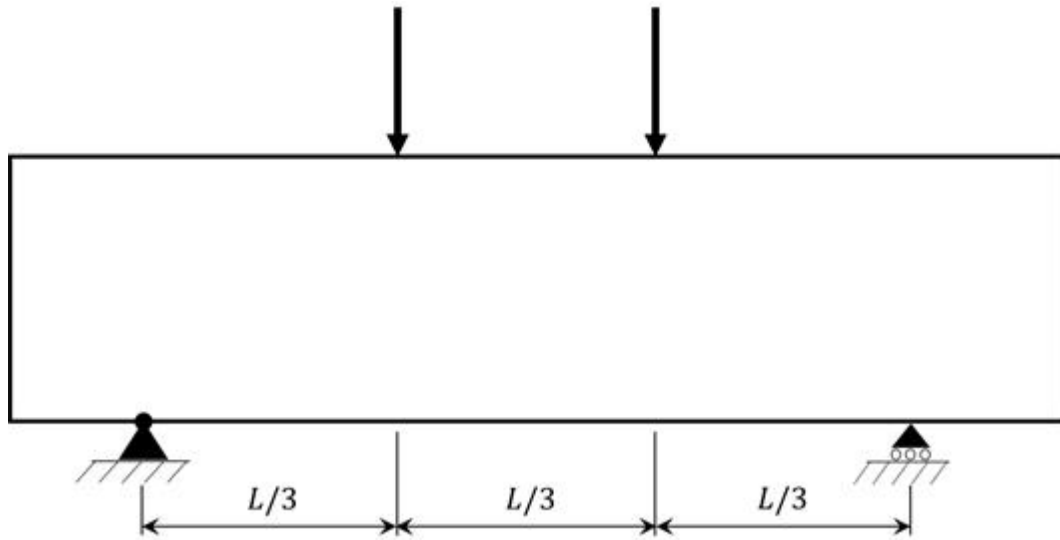


Figure 8.12: A two-dimensional model of the beam under four-point bending

The total length of the beam is 400 mm centrally position on two supports spanned 300 mm apart. The beam is of square cross-section with a side length of 100 mm. The load consists of two concentrated forces applied at the edges of the mid-segment of supported span allowing the beam to experience a uniform bending moment in this segment. It is noteworthy to mention; there is no need for a prior definition of the crack location as in the

case of a notched beam. The crack location is to be identified automatically using the proposed algorithm. The current test is conducted on a beam of brittle material, i.e., concrete. Brittle materials are said to undergo catastrophic failure due to their low strain to failure capacity. In other words, once a crack is initiated, it propagates under various levels of loading until fracture. The material model for concrete is chosen to be linearly elastic in compression and tension until failure. For failure initiation, a traction separation law based on maximum principal stress is adopted taking into consideration the ease of determining the maximum tensile strength for concrete by testing. The damage evolution was selected based on the fracture energy of concrete rather than the critical crack opening displacement. Fracture energy results in better accuracy due to the difficulty of capturing a crack behavior after being initiated for a brittle material (Lee & Lopez, 2014), in addition to, the availability of detailed data on concrete fracture energy in the literature. A general static step was chosen for the analysis, and 4-noded bilinear plane strain quadrilateral element (CPE4R) with reduced integration is selected for meshing. The model is meshed using structured meshing control.

8.7 Specimens Preparation and Testing

General use Portland cement similar to ASTM (2012b) C150 Type I (*ASTM C150/C150M-12*, “*Standard specification for Portland cement.*”, Philadelphia, PA: American Society for Testing and Materials, 2012, n.d.) was used to produce mixtures. Natural crushed stone was used as a coarse aggregate with a maximum size of 10 mm while natural sand was used as a fine aggregate. Both types of aggregates had a specific gravity of 2.6 and absorption of 1%. Several trial mixtures were cast to determine the water/cement ratio and coarse/fine

aggregate ratio. Based on the trial mixtures stage, the optimized flowability of mixtures and enhanced mechanical properties were achieved by using a coarse to fine aggregate weight ratio of 0.7 and 0.9. Meanwhile, the water to cement ratios of 0.4, 0.45, and 0.5 were used.

Table 8.1 provides the details of the mix designs used to build test specimens.

Table 8.1: Mix design for tested specimens

Mixture	Cement (kg/m ³)	Coarse to fine aggregate ratio	Water to cement ratio
Mix #1	550	0.9	0.50
Mix #2	550	0.7	0.40
Mix #3	550	0.7	0.45
Mix #4	550	0.9	0.40
Mix #5	550	0.9	0.45
Mix #6	550	0.7	0.50

The material mechanical properties namely compressive strength, flexural strength, splitting tensile strength and the modulus of elasticity for each mixture were measured from standard testing. First, the compressive strength was measured according to ASTM C39 standard testing (ASTM C39, 2016). Second, the flexural strength was measured according to ASTM C78 (*C78/C78M-16: Standard Test Method for Flexural Strength of Concrete (Using Simple Beam with Third-Point Loading)*), 2010). Third, splitting tensile strength was measured according to ASTM C496 (ASTM C496/C496M – 17, 2011). Finally, the modulus of elasticity was measured according to ASTM C469 (ASTM Standard C469/C469M, 2014). The load cell accuracy of the testing machine was $\pm 0.062\%$ according to the last calibration report of the load-frame. The measured mechanical properties associated with each mixture are recorded in **Table 8.2**.

Table 8.2: Mechanical properties from testing the six concrete specimens.

Concrete Mixture Number	Compressive Strength (MPa)	Flexural Strength (MPa)	Splitting Tensile Strength (MPa)	Modulus of Elasticity (MPa)	Fracture Energy (N/M)	Poisson's Ratio (—)
Mix #1	60.08	8.40	3.43	32010	90.13	0.2
Mix #2	51.16	8.31	3.07	30910	80.54	0.2
Mix #3	45.90	5.40	3.20	29300	74.65	0.2
Mix #4	81.09	10.56	5.41	34060	111.18	0.2
Mix #5	74.07	9.66	3.91	35500	104.36	0.2
Mix #6	41.49	6.57	3.32	27470	69.55	0.2

All mechanical properties were measured except for Poisson's ratio which was assumed to be 0.2 (Unger & Eckardt, 2011) and fracture energy which is dependent on two main parameters, namely, size of aggregate used and compressive strength of the mixture. Given the knowledge of the maximum aggregate size and measuring the compressive strength, the fracture energy of concrete G_f was calculated using (Eq.8.12) and (Eq.8.13) provided by Comité Euro-International du Béton (CEB) (*MC90 CEB. Comité Euro-International du Béton, CEB-FIP Model Code 1990. Bulletin D'Information. 1993(215), n.d.*).

$$G_f = G_{f_0} \left(\frac{f_c}{10} \right)^{0.7} \quad (\text{Eq.8.12})$$

$$G_{f_0} = 0.0469 D_{max}^2 - \frac{D_{max}}{2} + 26 \quad (\text{Eq.8.13})$$

where G_f is the calculated fracture energy, f_c is the compressive strength of mixture and G_{f_0} is a factor accounting for the maximum aggregate size D_{max} used in the preparation of concrete mixtures.

8.8 Results and Discussion

This section is devoted to discussing the results from testing un-notched concrete prisms. The corresponding results predicted by the proposed algorithm are compared to those of testing for the validation purposes. Assessments are introduced delineating two significant aspects, namely, the critical load causing crack onset and corresponding crack location. Also, the proposed approach is compared to the conventional XFEM regarding computational efficiency. The failure loads measured from testing of the six concrete prisms are reported in **Table 8.3**. Correspondingly, predicted values using the automation algorithm in addition to the percentage error are provided. As can be seen from the results, predictions compared to measurements, indicated percentage error from 1.91% to 1.96%. The algorithm was able to precisely predicted failure loads with a relatively minimal error.

Table 8.3: Failure load: Testing, predictions and relative error.

Concrete Mixture Number	F_{Measured} (N)	$F_{\text{Predicted}}$ (N)	Error (%)
Mix #1	28000	28542	1.94
Mix #2	27700	28238	1.94
Mix #3	18000	18343	1.91
Mix #4	35200	35883	1.94
Mix #5	32200	32832	1.96
Mix #6	21900	22326	1.95

Finally, comparisons were conducted regarding computational efficiency for proposed algorithm. Correlations assumed the absence of an expert user hence conventional XFEM required enriching the entire domain. Since the proposed algorithms automatically arrives at convergent mesh, the same exact mesh was used for conventional XFEM assuming an expert user has arrived at this convergent mesh. Therefore, identical mesh size (i.e., the

same number of elements) was utilized for the comparison purposes as shown in Table 8.4. The proposed algorithm enabled optimal enrichment of nodes in the critical region only. The total number of enriched nodes by the algorithm is 53% less than those of conventional XFEM. Consequently, the total number of unknowns in the system is 33% less than conventional XFEM requirements. **Table 8.4** shows the detailed computational effort comparison. As can be seen from the comparison, the conventional implementation of XFEM results in almost doubling the total number of enriched nodes. Meanwhile, a minimal increase in the enrichment unknowns was enabled through the proposed approach resulting in runtime reduction by 39% and enhancing overall computational efficiency. Through this simple example, the reader can conclude the high potential of the current approach when applied to problems of complex geometry and combined loading scenarios. Furthermore, minimizing computational effort is significant in the case of dynamic analysis and 3-D problems.

Table 8.4: Computational effort comparison: conventional XFEM vs. proposed approach.

Item of Comparison	Conventional XFEM	Proposed Algorithm
Number of elements	1860	1860
Number of Nodes	2268	2268
Number of Enriched nodes	2268	1066
Total number of unknowns	7696	5200
Increments to solve	14	6
Iterations	46	13
Runtime (sec)	14.8	9.1

The following section is dedicated for comparisons with relevant test data (plain concrete testing) from the literature. The same aspects of comparisons outlined in Section 7 were used.

8.9 Algorithm Validation with Test Data from Literature

The proposed algorithm was tested for validation purposes against relevant test data from the literature. Only test data for un-notched specimens were compared with the algorithm predictions in the current section. Comparisons were based on damage initiation loads and/or displacements (if available). The first case adopted from literature for validation is from the work of Unger and Eckardt (Unger & Eckardt, 2011). Their work presented adaptive multiscale modeling for concrete combining two different scale models, namely, mesoscale and macroscale. Non-Linear analysis of an L-shaped large-scale panel was provided using multiscale modeling. Their results were validated with specimens prepared and tested by Winkler et al. (Winkler, Hofstetter, & Niederwanger, 2001). The mechanical properties as reported in (Unger & Eckardt, 2011) are reproduced in **Table 8.5**. The mechanical properties required for the current analysis are minimal compared to multiscale modeling techniques.

Table 8.5: L-shaped specimen mechanical properties as reported in (Unger & Eckardt, 2011).

Concrete Mixture	Flexural Strength (MPa)	Modulus of Elasticity (MPa)	Fracture Energy (N/M)	Poisson's Ratio (—)
Plain	2.60	18500	140	0.18

The problem geometry together with the loading conditions are shown in **Figure: 8.13a**.

The proposed algorithm was used to analyze the L-shaped problem using the methodology illustrated in subsection 8.5. The third stress invariant contour plot identifying the potential region for crack onset is shown in **Figure: 8.13b**.

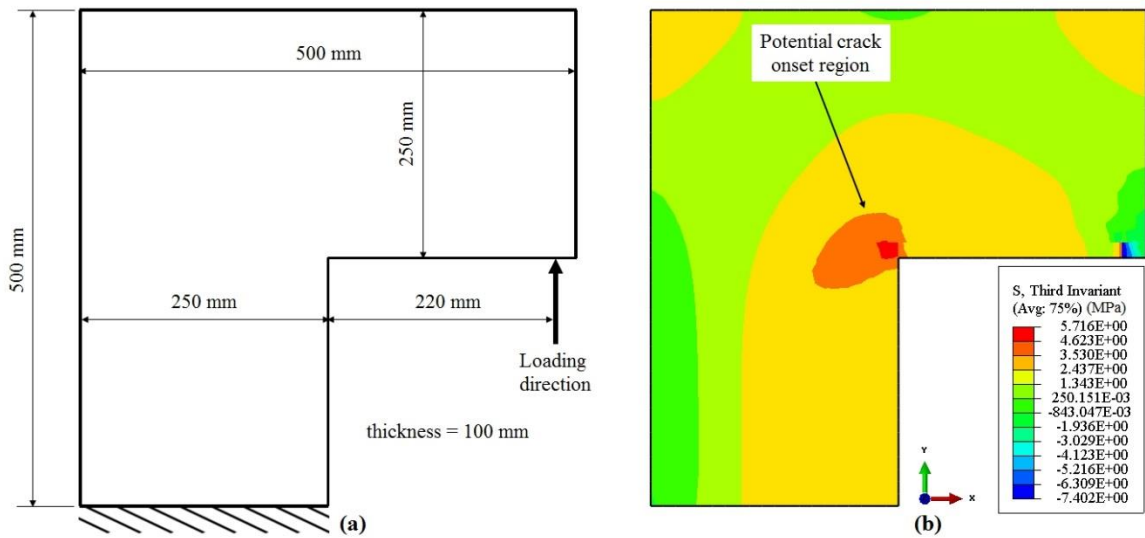


Figure: 8.13: (a) Specimen geometry and loading conditions. (b) Contour plot of third stress invariant showing potential region for crack onset.

Based on the maximum value of the third stress invariant, the algorithm automatically identified the potential region for XFEM enrichment. The critical region mesh is refined to ensure accurate failure predictions. Finally, the optimal enriched zone size is determined. The optimized final mesh along with the optimal enrichment zone constructed automatically by the proposed algorithm are shown in **Figure 8.14a**. The crack onset location predicted using the proposed algorithm is shown in **Figure 8.14b**.

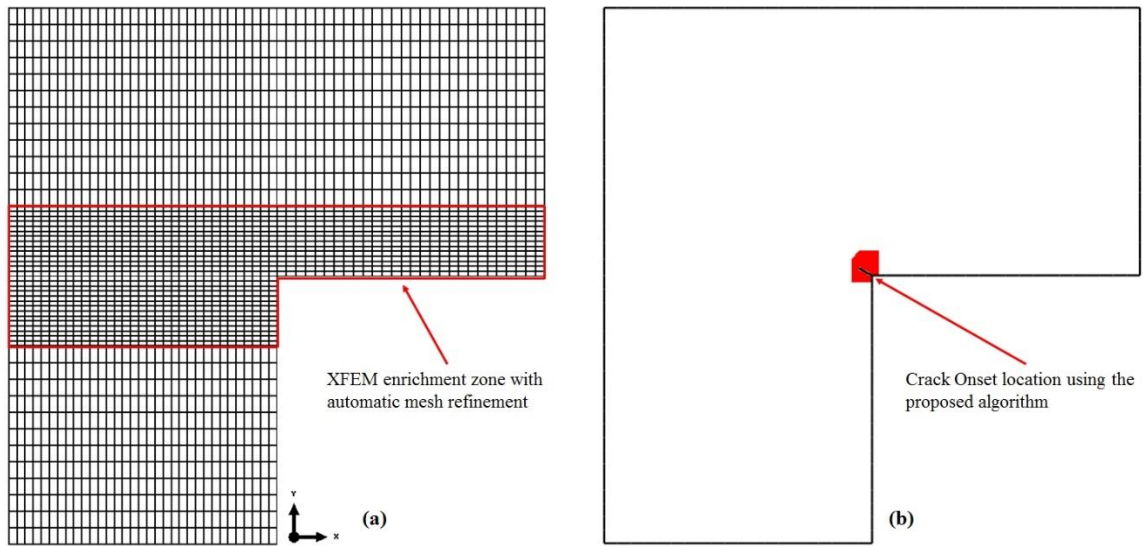


Figure 8.14: (a) Optimized mesh and enrichment zone. (b) Predicted crack onset location using the proposed algorithm

The onset location is in excellent agreement with the test data reported in (Unger & Eckardt, 2011). **Table 8.6** shows the predicted failure load and displacement using the mesoscale-macroscale coupled model from (Unger & Eckardt, 2011) in addition to the predicted values using the proposed algorithm. The proposed algorithm recorded excellent agreement with measurements from testing in predicting both failure load as well as failure displacement. As can be observed from **Table 8.6**, the percentage error of the proposed algorithm shows enhanced predictions on both failure loads and displacements.

Table 8.6: Proposed Algorithm versus experimental data from testing.

Item of Comparison	Failure Load [N]	Load Error [%]	Displacement [mm]	Displacement Error [%]
Experimental data	6933	–	0.163	–
Coupled Model (Unger & Eckardt, 2011)	6789	2.1	0.180	10.4
Proposed Algorithm	6960	0.4	0.169	3.7

For completeness, the proposed algorithm was also compared to the conventional XFEM regarding computational efficiency as shown in **Table 8.7**. It can be observed that same meshes were used for the sake of comparison assuming the user of conventional XFEM has performed mesh convergence analysis which was automatically performed using the current algorithm.

Table 8.7. Computational effort comparison (L-Shape): conventional XFEM vs. proposed approach.

Item of Comparison	Conventional XFEM	Proposed Algorithm
Number of elements	1700	1700
Number of Nodes	1798	1798
Number of Enriched nodes	1798	840
Total number of unknowns	9022	4232
Increments to solve	19	11
Iterations	43	17
Runtime (sec)	6.3	2.7

The algorithm enabled enriching less than 47% of the nodes in the entire domain for the current problem, in turn reducing the total number of unknowns in the system. Consequently, the total number of required increments and iterations to solve using the proposed algorithm is significantly less than that required by conventional XFEM. It can be observed that the total runtime of the proposed algorithm is 42% in comparison to that of conventional XFEM. It can be concluded from **Table 8.6** and **Table 8.7**, that the proposed algorithm enhanced the overall predictions while minimizing computational effort.

The second case for comparison is a large-scale T-section adopted from (AbdelAleem & Hassan, 2017). The specimen geometry and the loading conditions are presented in **Figure 8.15a**. The section has a total height of 1 m and a hanging span of 0.6 m with a uniform

thickness of 0.25 m. A concentrated tip load is applied to the free end of the hanging span. The proposed algorithm was utilized for analyzing the T-section problem following the same methodology discussed in subsection 8.5. The contour plot of the third stress invariant is shown in **Figure 8.15b**, based on its maximum values the potential region for crack onset is automatically identified. The mechanical properties for the plain concrete mix as reported in (AbdelAleem & Hassan, 2017) are reproduced in **Table 8.8**.

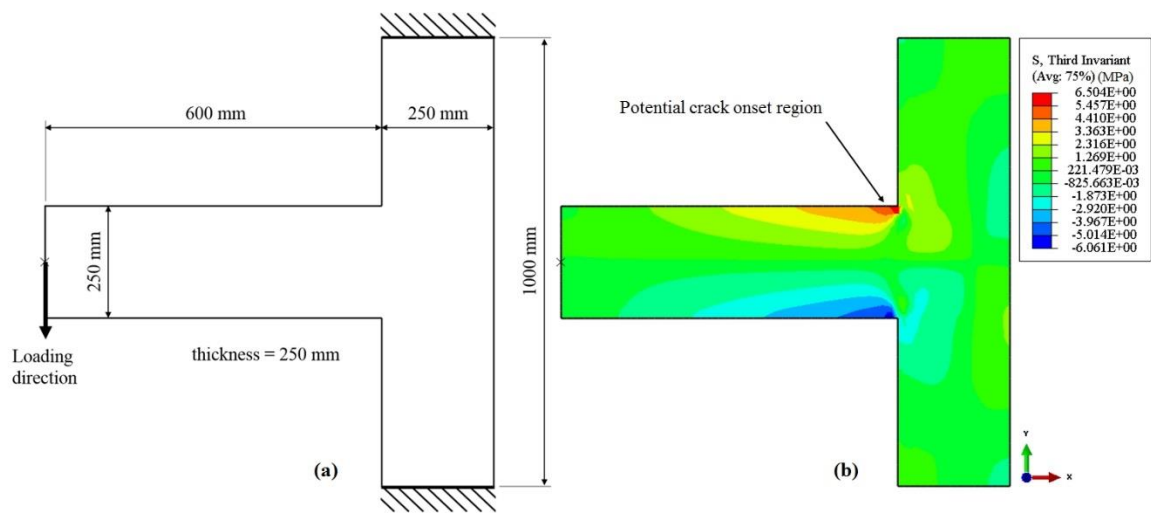


Figure 8.15: (a) Specimen geometry and loading conditions. (b) Contour plot of third stress invariant showing potential region for crack onset.

Table 8.8: T-section specimen mechanical properties as reported in (AbdelAleem & Hassan, 2017).

Concrete Mix	Flexural Strength (MPa)	Modulus of Elasticity (MPa)	Fracture Energy (N/M)	Poisson's Ratio (—)
Plain concrete	4.5	29400	114.70	0.18

As per the current algorithm, the initial enrichment zone identification is followed by an automatic mesh refinement for the critical region. The final optimized mesh is shown in **Figure 8.16a**, the automatically optimized enrichment zone is highlighted in red. The crack onset location as predicted by the proposed algorithm is shown in **Figure 8.16b**.

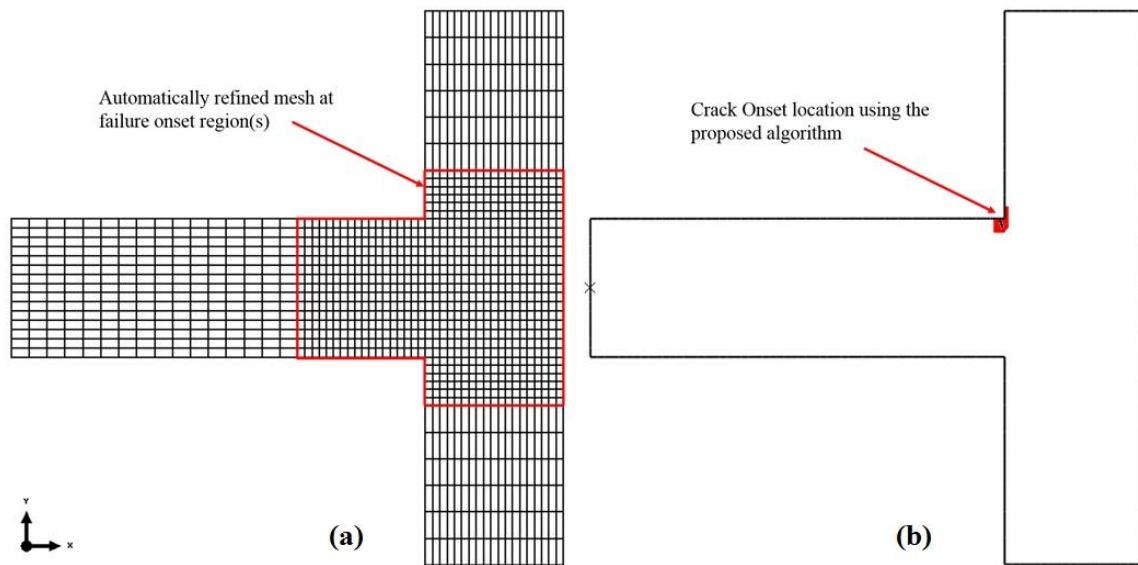


Figure 8.16: (a) Optimized mesh and enrichment zone. (b) Predicted crack onset location using the proposed algorithm.

The crack onset location is in excellent agreement with testing results from (AbdelAleem & Hassan, 2017). The failure load causing the first crack from testing was reported to be (30.9 KN), whereas the proposed algorithm predicted the first crack to occur at (30.6 KN). It can be concluded that the proposed algorithm is in excellent agreement with testing for both predicting the crack location and the failure load causing the first crack. Regarding computational efficiency, the proposed algorithm is compared to conventional XFEM as shown in Table 8.9.

Table 8.9. Computational effort comparison (T-section): conventional XFEM vs. proposed approach.

Item of Comparison	Conventional XFEM	Proposed Algorithm
Number of elements	1828	1828
Number of Nodes	1936	1936
Number of Enriched nodes	1936	980
Total number of unknowns	9712	4932
Increments to solve	39	7
Iterations	103	15
Runtime (sec)	15.2	5.4

The proposed algorithm was able to enrich approximately 50% of the entire domain resulting in a 50% reduction in the total number of unknowns. The required runtime to analyze this problem using the proposed algorithm was 36% of the runtime required by conventional XFEM.

8.10 Conclusions

In the presented work, a novel technique is proposed for automating XFEM implementation in user-built and commercial FE codes with minimal user-intervention. The proposed technique was developed to overcome XFEM existing challenges related to prediction accuracy and to enhance computational efficiency. The novel technique was developed into an algorithm which was implemented using Python scripting in mainstream FE code ABAQUS performing three major tasks; (1) Automatic identification of critical region(s) based on material-specific failure criterion, (2) Automatic mesh refinement based on stress convergence for accurate predictions, and (3) Optimal enrichment for identified critical region(s).

Three different problems were used for validation of prediction accuracy, namely, beam under four-point bending, L-shaped and T-section problems. Furthermore, regarding computational efficiency, the performance of the implemented algorithm was compared to that of conventional XFEM. The following observations were recorded in these comparisons; (1) Predicted failure loads/displacements corresponding to damage initiation were in excellent agreement with measurements of un-notched specimens obtained from literature and in-house testing, (2) Crack onset location predictions showed excellent agreement with observations from different geometries/loading-conditions, and (3)

significant reduction in all model parameters in terms of total number of enriched nodes, number of unknowns, increments and iterations when compared to conventional XFEM. It is notable to mention that the runtime for three different problems under diverse loading conditions was in the order of seconds. Therefore, and based on these observations it can be concluded that the proposed algorithm:

- Alleviated the user-dependency for identifying the critical region(s).
- Enabled accurate predictions due to rigorous and automatic mesh-refinement.
- Enhanced the overall computational efficiency.

In conclusion, applying the proposed approach was proven to have significant effects on providing accurate and computationally efficient analysis. Therefore, this approach is recommended for analysis of complex structures and combined loading scenarios where critical region(s) identification can be challenging even for an expert user. Moreover, the approach possesses high potential of minimizing computational effort in the case of dynamic and 3-D analyses.

8.11 References

- Abaqus Documentation*. (2014). Providence, Rhode Island: Dassault Systèmes.
- Abaqus V6.14– Documentation, Dassault Systèmes Simulia Corporation*. (2013). Providence, Rhode Island.
- AbdelAleem, B. H., & Hassan, A. A. A. (2017). Influence of rubber content on enhancing the structural behaviour of beam–column joints. *Magazine of Concrete Research*, 1–13. <https://doi.org/10.1680/jmacr.17.00323>
- ASTM C150/C150M-12, “Standard specification for Portland cement.”*, Philadelphia, PA: American Society for Testing and Materials, 2012.
- ASTM C39. (2016). Standard Test Method for Compressive Strength of Cylindrical Concrete Specimens. *American Society for Testing and Materials*, 1–7. <https://doi.org/10.1520/C0039>

- ASTM C496/C496M – 17. (2011). Standard Test Method for Splitting Tensile Strength of Cylindrical Concrete Specimens ASTM C-496. *ASTM International*, 1–5. <https://doi.org/10.1520/C0496>
- ASTM Standard C469/C469M. (2014). Standard Test Method for Static Modulus of Elasticity and Poisson's Ratio of Concrete in Compression. *ASTM International*, 1–5. <https://doi.org/10.1520/C0469>
- BABUŠKA, I., & MELENK, J. M. (1997). the Partition of Unity Method. *International Journal for Numerical Methods in Engineering*, 40(4), 727–758. [https://doi.org/10.1002/\(SICI\)1097-0207\(19970228\)40:4<727::AID-NME86>3.0.CO;2-N](https://doi.org/10.1002/(SICI)1097-0207(19970228)40:4<727::AID-NME86>3.0.CO;2-N)
- Belytschko, T., & Black, T. (1999). Elastic crack growth in finite elements with minimal remeshing. *International Journal for Numerical Methods in Engineering*, 45(5), 601–620. [https://doi.org/10.1002/\(SICI\)1097-0207\(19990620\)45:5<601::AID-NME598>3.0.CO;2-S](https://doi.org/10.1002/(SICI)1097-0207(19990620)45:5<601::AID-NME598>3.0.CO;2-S)
- Belytschko, Ted, Gracie, R., & Ventura, G. (2009). A Review of Extended / Generalized Finite Element Methods for Material Modelling. *Modelling and Simulation in Materials Science and Engineering*, 17.4, 0430(4). <https://doi.org/10.1088/0965-0393/17/4/043001>
- Bobinski, J., & Tejchman, J. (2012). Application of Extended Finite Element Method to Cracked Concrete Elements – Numerical Aspects. *Archives of Civil Engineering*, LVIII(4), 409–431. <https://doi.org/10.2478/v.10169-012-0022-z>
- C78/C78M-16: Standard Test Method for Flexural Strength of Concrete (Using Simple Beam with Third-Point Loading)*. , (2010).
- Dolbow, J., Moës, N., & Belytschko, T. (2001). An extended finite element method for modeling crack growth with frictional contact. *Computer Methods in Applied Mechanics and Engineering*, 190(51–52), 6825–6846. [https://doi.org/10.1016/S0045-7825\(01\)00260-2](https://doi.org/10.1016/S0045-7825(01)00260-2)
- Duarte, A. P. C., Díaz Sáez, A., & Silvestre, N. (2017). Comparative study between XFEM and Hashin damage criterion applied to failure of composites. *Thin-Walled Structures*, 115(October 2016), 277–288. <https://doi.org/10.1016/j.tws.2017.02.020>
- Grogan, D. M., Leen, S. B., & O. Brádaigh, O. C. M. (2014). An XFEM-based methodology for fatigue delamination and permeability of composites. *Composite Structures*, 107(1). <https://doi.org/10.1016/j.compstruct.2013.07.050>
- Gupta, P., Pereira, J. P., Kim, D.-J., Duarte, C. A., & Eason, T. (2012). Analysis of three-dimensional fracture mechanics problems: A non-intrusive approach using a generalized finite element method. *Engineering Fracture Mechanics*, 90, 41–64. <https://doi.org/10.1016/j.engfracmech.2012.04.014>
- Gupta, V. (2014). *Improved conditioning and accuracy of a two-scale generalized finite element method for fracture mechanics*. University of Illinois at Urbana-Champaign.

- Gupta, V., & Duarte, C. A. (2016). On the enrichment zone size for optimal convergence rate of the Generalized/Extended Finite Element Method. *Computers and Mathematics with Applications*, 72(3), 481–493.
<https://doi.org/10.1016/j.camwa.2016.04.043>
- Lee, J., & Lopez, M. M. (2014). An Experimental Study on Fracture Energy of Plain Concrete. *International Journal of Concrete Structures and Materials*, 8(2), 129–139. <https://doi.org/10.1007/s40069-014-0068-1>
- Liu, P. F., & Zheng, J. Y. (2010). Recent developments on damage modeling and finite element analysis for composite laminates: A review. *Materials and Design*, 31(8), 3825–3834. <https://doi.org/10.1016/j.matdes.2010.03.031>
- MC90 CEB. Comité Euro-International du Béton, CEB-FIP Model Code 1990. *Bulletin D'Information*. 1993(215).
- Melenk, J. M., & Babuška, I. (1996). The partition of unity finite element method: Basic theory and applications. *Computer Methods in Applied Mechanics and Engineering*, 139(1–4), 289–314. [https://doi.org/10.1016/S0045-7825\(96\)01087-0](https://doi.org/10.1016/S0045-7825(96)01087-0)
- Moës, N., & Belytschko, T. (2002). Extended finite element method for cohesive crack growth. *Engineering Fracture Mechanics*, 69(7), 813–833.
[https://doi.org/10.1016/S0013-7944\(01\)00128-X](https://doi.org/10.1016/S0013-7944(01)00128-X)
- Moës, N., Dolbow, J., & Belytschko, T. (1999). A finite element method for crack growth without remeshing. *International Journal for Numerical Methods in Engineering*, 46(1), 131–150. [https://doi.org/10.1002/\(SICI\)1097-0207\(19990910\)46:1<131::AID-NME726>3.0.CO;2-J](https://doi.org/10.1002/(SICI)1097-0207(19990910)46:1<131::AID-NME726>3.0.CO;2-J)
- Papadopoulos, G. A. (1987). The stationary value of the third stress invariant as a local fracture parameter (Det.-criterion). *Engineering Fracture Mechanics*, 27(6), 643–652. [https://doi.org/10.1016/0013-7944\(87\)90156-1](https://doi.org/10.1016/0013-7944(87)90156-1)
- Petrov, N. A., Gorbatikh, L., & Lomov, S. V. (2018). A parametric study assessing performance of eXtended Finite Element Method in application to the cracking process in cross-ply composite laminates. *Composite Structures*, 187(July 2017), 489–497. <https://doi.org/10.1016/j.compstruct.2017.12.014>
- Pommier, S., Gravouil, A., & Combescure, A. (2013). Extended Finite Element Method X-FEM. In *Extended Finite Element Method for Crack Propagation*.
- Radhakrishnan, H. (2011). *ANSYS Mechanical Tips & Tricks*.
- Strouboulis, T., Copps, K., & Babuška, I. (2011). The generalized finite element method. *Computer Methods in Applied Mechanics and Engineering*, 190(32–33), 4081–4193.
- Sumi, Y. (2014). *Mathematical and Computational Analyses of Cracking Formation* (Vol. 2). <https://doi.org/10.1007/978-4-431-54935-2>
- Tejchmann, J., & Bobinski, J. (2015). *Continuous and Discontinuous Modelling of Fracture in Concrete Using FEM* (Vol. 1). <https://doi.org/10.1007/978-3-642-28463-2>

- Unger, J. F., & Eckardt, S. (2011). Multiscale Modeling of Concrete. *Archives of Computational Methods in Engineering*, 18(3), 341–393.
<https://doi.org/10.1007/s11831-011-9063-8>
- Winkler, B., Hofstetter, G., & Niederwanger, G. (2001). Experimental verification of a constitutive model for concrete cracking. *Proceedings of the Institution of Mechanical Engineers, Part L: Journal of Materials: Design and Applications*, 2015(2), 75–86. <https://doi.org/https://doi.org/10.1177/146442070121500202>
- Wu, L., Zhang, L. X., & Guo, Y. K. (2013). A Review of the Extended Finite Element for Fracture Analysis of Structures. *Applied Mechanics and Materials*, 444–445, 96–102. <https://doi.org/10.4028/www.scientific.net/AMM.444-445.96>

9 Conclusions and Future Work

In the current thesis, micro/macro investigations on material mechanical behaviors were investigated. The framework of extended finite element method (XFEM) was employed in most of numerical models. Also, the unit cell (UC) method as well as the representative volume element (RVE) methods were used for micromechanical modeling. Different material behaviors were investigated, namely plain epoxy, plain concrete and steel materials. A general algorithm was proposed for optimal failure predictions using the framework of XFEM. The modeling process was automated and optimized to minimize computational effort and user-intervention. For plain epoxy and concrete, the specimens were tested at Memorial University's laboratories while testing results regarding different types of steel and large-scale concrete structures were obtained from the literature.

First, a comprehensive study on plain epoxy resin was conducted. Plain epoxy was prepared and tested under different types of loading utilizing digital image correlation (DIC) for displacement measurements. Fractographic analyses were performed using three different methods, namely, optical microscopy (OM), scan electron microscopy (SEM), and computed tomography (CT). Numerical modeling at different scales (micro/macro) were provided. Numerical results were validated against testing results proving excellent agreements. Fractographic analyses revealed better understanding of failure mechanism at different scales. Also, consistent results were obtained from different fractographic analyses. Novel modeling procedures were proposed accounting for microscopic features (i.e., micro-voids). Besides, user-defined damage driven by microstructural voids effect

was developed and implemented in user-defined Fortran subroutines in Abaqus. Numerically obtained results were validated with measurements from standard testing.

Second, is the ductile behavior of porous metals which was extensively investigated from numerical point of view while the testing was acquired from the literature due to limited resources and the challenges associated with manufacturing. The UC method was used to predict elastic plastic behavior of porous metals under tension. Numerical predictions were in excellent agreement with the reported testing results which motivated and triggered the proposed extended Ramberg-Osgood (ERO) relationship. The proposed ERO relationship has proven its validity to account for metal porosity in the low range porosity (i.e., less than 10%). Notably, the ERO employed a single extra parameter to the original three parameters of Ramberg-Osgood relationship. The proposed ERO relationship can be considered as an asset for early design stages specially for being representative of the complete elastoplastic behavior of porous metals. Noteworthy, to the author best of knowledge there exists no relationship that can predict the elastic-plastic behavior of porous metals. For completeness, a two-stage finite element procedure was provided mainly to predict the final failure of porous metals. Single spheroidal RVE was employed in micromechanical models to predict the elastic plastic behavior of the porous metal. At macro scale, a strain energy density (SED)-based user-defined material model was developed and implemented for final failure prediction within the framework of XFEM. A similar porosity dependent relationship to evaluate the critical SED of porous metals was proposed and validated with reported testing results proving excellent agreement and conservative predictions.

Third, the modeling process of XFEM was automated to alleviate the user-dependency and minimize computational effort. Initial validation with specimen sized models proven excellent agreement for two-dimensional domains. Also, full-scale structures were numerically investigated using the proposed automating algorithm. Validation against the reported testing results from the literature showed excellent predictive capabilities. Finally, the experimental/numerical investigations conducted in the abovementioned work led to the following conclusions:

Brittle behavior (epoxy):

- Micro-voids were observed in plain epoxy resin which is most probably resulting from the curing process and the exothermic chemical reaction (i.e., polymerization). These voids were characterized by shape, size and intensity and were found to be a major reason for damage initiation at microscales.
- A novel testing procedure was proposed to experimentally identify yielding. The key role for the procedure employs the discoloration caused by inelastic deformation by means of image processing. To the author best of knowledge, the method does not exist in the well-known testing standards (e.g., ASTM)
- A Python script was developed and implemented in Abaqus to generate actual micro-voids in finite element models based on their physical sizes/location employing computed tomography (CT) scans. The resulting models enabled an insight into the microstructure of plain epoxy.

- Enabling the framework of XFEM at microscale showed that the largest void is most probably the one leading to micro-cavitation and hence, macroscopic cracks and failure, which is consistent with the current experimental investigation as well as the literature findings.
- The proposed strain energy density (SED) damage model proven to be more accurate than stress/strain built in damage initiation mechanisms in Abaqus. Also, the predicted failure surfaces were realistic signifying that brittleness dominated the failure behavior.
- Also, accounting for precise yield stress using the image processing enabled accurate material model definition in finite element analyses which in turn assisted in obtaining precise numerical results.

Ductile behavior (steels):

- Two-dimensional unit cell models with enough holes representing total volumetric porosity showed predictive capabilities in both linear and non-linear behaviors.
- While irregular holes shape/distribution triggered local plasticity and stress concentrations, the overall mechanical behavior predictions were unaltered.
- A chief contribution of the current work is the extended Ramberg-Osgood (ERO) relationship accounting for metal porosity which was enabled utilizing micromechanical modeling and regression analyses.
- Automating the modeling procedure had a significant effect on minimizing computational effort and alleviating the user-dependency.

Future Work

- Build and test different composite laminates to investigate their complex failure mechanisms
- Advance on what have been already accomplished regarding the developed and implemented damage models by extending the applicability to composite materials by defining competing damage criteria.
- Extending the general algorithm presented in Chapter 8 to three-dimensional domains and incorporate different damage mechanisms within the script.

BIBLIOGRAPHY

- Abaqus Documentation*. (2014). Providence, Rhode Island: Dassault Systèmes.
- Abaqus V6.14– Documentation, Dassault Systèmes Simulia Corporation*. (2013). Providence, Rhode Island.
- AbdelAleem, B. H., & Hassan, A. A. A. (2017). Influence of rubber content on enhancing the structural behaviour of beam–column joints. *Magazine of Concrete Research*, 1–13. <https://doi.org/10.1680/jmacr.17.00323>
- Abdelaziz, Y., & Hamouine, A. (2008). A survey of the extended finite element. *Computers and Structures*, 86(11–12), 1141–1151. <https://doi.org/10.1016/j.compstruc.2007.11.001>
- Aboulkhair, N. T., Everitt, N. M., Ashcroft, I., & Tuck, C. (2014). Reducing porosity in AlSi10Mg parts processed by selective laser melting. *Additive Manufacturing*, 1, 77–86. <https://doi.org/10.1016/j.addma.2014.08.001>
- Aho, T., Nerg, J., & Pyrhönen, J. (2007). Experimental and finite element analysis of solid rotor end effects. *IEEE International Symposium on Industrial Electronics*, 1242–1247. <https://doi.org/10.1109/ISIE.2007.4374776>
- Allison, P. G., Grewal, H., Hammi, Y., Brown, H. R., Whittington, W. R., & Horstemeyer, M. F. (2013). Plasticity and Fracture Modeling/Experimental Study of a Porous Metal Under Various Strain Rates, Temperatures, and Stress States. *Journal of Engineering Materials and Technology*, 135(4), 041008. <https://doi.org/10.1115/1.4025292>
- Aroush, D. R.-B., Maire, E., Gauthier, C., Youssef, S., Cloetens, P., & Wagner, H. D. (2005). A study of fracture of unidirectional composites using in situ high-resolution synchrotron X-ray microtomography. *Composites Science and Technology*, 66(10), 1348–1353. <https://doi.org/10.1016/j.compscitech.2005.09.010>
- Arumugam, V., Saravanakumar, K., & Santulli, C. (2018). Damage characterization of stiffened glass-epoxy laminates under tensile loading with acoustic emission monitoring. *Composites Part B: Engineering*, 147(April), 22–32. <https://doi.org/10.1016/j.compositesb.2018.04.031>
- Asim, U. B., Siddiq, M. A., & Kartal, M. (2018). Representative Volume Element (RVE) based Crystal Plasticity study of Void Growth on Phase Boundary in Titanium alloys. *28th International Workshop on Computational Mechanics of Materials (IWCMM28)*, 161(December 2018), 346–350. <https://doi.org/10.1016/j.commatsci.2019.02.005>
- Asp, L. E., Berglund, L. A., & Talreja, R. (1996). A criterion for crack initiation in glassy polymers subjected to a composite-like stress state. *Composites Science and Technology*, 56(11), 1291–1301. [https://doi.org/10.1016/S0266-3538\(96\)00090-5](https://doi.org/10.1016/S0266-3538(96)00090-5)
- Asp, Leif E., Berglund, L. A., & Gudmundson, P. (1995). Effects of a composite-like stress state on the fracture of epoxies. *Composites Science and Technology*, 53(1), 27–37. [https://doi.org/10.1016/0266-3538\(94\)00075-1](https://doi.org/10.1016/0266-3538(94)00075-1)
- ASTM-D790-17. (2017). Standard Test Methods for Flexural Properties of Unreinforced and Reinforced Plastics and Electrical Insulating Materials 1. *ASTM International. Designation: D*, 1–12. <https://doi.org/10.1520/D0790-17.2>
- ASTM C150/C150M-12, “Standard specification for Portland cement.”*, Philadelphia, PA: American Society for Testing and Materials, 2012.

- ASTM C39. (2016). Standard Test Method for Compressive Strength of Cylindrical Concrete Specimens. *American Society for Testing and Materials*, 1–7. <https://doi.org/10.1520/C0039>
- ASTM C496/C496M – 17. (2011). Standard Test Method for Splitting Tensile Strength of Cylindrical Concrete Specimens ASTM C-496. *ASTM International*, 1–5. <https://doi.org/10.1520/C0496>
- ASTM D638-14. (2014). Standard test method for tensile properties of plastics. *ASTM International. Designation: D, 08*, 46–58. <https://doi.org/10.1520/D0638-14.1>
- ASTM Standard C469/C469M. (2014). Standard Test Method for Static Modulus of Elasticity and Poisson's Ratio of Concrete in Compression. *ASTM International*, 1–5. <https://doi.org/10.1520/C0469>
- Attaran, M. (2017). The rise of 3-D printing: The advantages of additive manufacturing over traditional manufacturing. *Business Horizons*, 60(5), 677–688. <https://doi.org/10.1016/j.bushor.2017.05.011>
- Babu, K. P., Mohite, P. M., & Upadhyay, C. S. (2018). Development of an RVE and its stiffness predictions based on mathematical homogenization theory for short fibre composites. *International Journal of Solids and Structures*, 130–131, 80–104. <https://doi.org/10.1016/j.ijsolstr.2017.10.011>
- BABUŠKA, I., & MELENK, J. M. (1997). the Partition of Unity Method. *International Journal for Numerical Methods in Engineering*, 40(4), 727–758. [https://doi.org/10.1002/\(SICI\)1097-0207\(19970228\)40:4<727::AID-NME86>3.0.CO;2-N](https://doi.org/10.1002/(SICI)1097-0207(19970228)40:4<727::AID-NME86>3.0.CO;2-N)
- Bal'shin, M. Y. (1949). Dependence of the mechanical properties of porous materials on their porosity and the limiting properties of porous sintered materials. *Dokl. Akad. Nauk SSSR*, 67(5), 831–834.
- Baruchel, J., Buffiere, J. Y., Cloetens, P., Di Michiel, M., Ferrie, E., Ludwig, W., ... Salvo, L. (2006). Advances in synchrotron radiation microtomography. *Scripta Materialia*, 55(1 SPEC. ISS.), 41–46. <https://doi.org/10.1016/j.scriptamat.2006.02.012>
- Baumann, K. J., Kennedy, W. H., & Herbert, D. L. (1984). Computed Tomography X-Ray Scanning NDE of Graphite/Epoxy Coupons. *Journal of Composite Materials*, 18(6), 536–544. <https://doi.org/10.1177/002199838401800603>
- Belytschko, T., & Black, T. (1999). Elastic crack growth in finite elements with minimal remeshing. *International Journal for Numerical Methods in Engineering*, 45(5), 601–620. [https://doi.org/10.1002/\(SICI\)1097-0207\(19990620\)45:5<601::AID-NME598>3.0.CO;2-S](https://doi.org/10.1002/(SICI)1097-0207(19990620)45:5<601::AID-NME598>3.0.CO;2-S)
- Belytschko, Ted, Gracie, R., & Ventura, G. (2009a). A review of extended/generalized finite element methods for material modeling. *Modelling and Simulation in Materials Science and Engineering*, 17(4). <https://doi.org/10.1088/0965-0393/17/4/043001>
- Belytschko, Ted, Gracie, R., & Ventura, G. (2009b). A Review of Extended / Generalized Finite Element Methods for Material Modelling. *Modelling and Simulation in Materials Science and Engineering*, 17.4, 0430(4). <https://doi.org/10.1088/0965-0393/17/4/043001>
- Bert, C. W. (1985). Prediction of elastic moduli of solids with oriented porosity. *Journal of Materials Science*, 20(6), 2220–2224. <https://doi.org/10.1007/BF01112307>
- Besson, J. (2010). Continuum models of ductile fracture: A review. In *International Journal of Damage Mechanics* (Vol. 19). <https://doi.org/10.1177/1056789509103482>

- Bieniaś, J., Dębski, H., Surowska, B., & Sadowski, T. (2012). Analysis of microstructure damage in carbon/epoxy composites using FEM. *Computational Materials Science*, *64*, 168–172. <https://doi.org/10.1016/j.commatsci.2012.03.033>
- Biswas, R., & Poh, L. H. (2017). A micromorphic computational homogenization framework for heterogeneous materials. *Journal of the Mechanics and Physics of Solids*, *102*. <https://doi.org/10.1016/j.jmps.2017.02.012>
- Bobinski, J., & Tejchman, J. (2012). Application of Extended Finite Element Method to Cracked Concrete Elements – Numerical Aspects. *Archives of Civil Engineering*, *LVIII*(4), 409–431. <https://doi.org/10.2478/v.10169-012-0022-z>
- Bressers, O. F. J. T. (2002). *Craze initiation in glassy polymer systems*. Technische Universiteit Eindhoven.
- Bryhni Dæhli, L. E., Faleskog, J., Børvik, T., & Hopperstad, O. S. (2017). Unit cell simulations and porous plasticity modelling for strongly anisotropic FCC metals. *European Journal of Mechanics, A/Solids*, *65*, 360–383. <https://doi.org/10.1016/j.euromechsol.2017.05.004>
- C., B. J. (n.d.). Yield condition and propagation of Lüders' lines in tension–torsion experiments on poly(vinyl chloride). *Journal of Polymer Science Part A-2: Polymer Physics*, *1970*(6), 893–901.
- C78/C78M-16: Standard Test Method for Flexural Strength of Concrete (Using Simple Beam with Third-Point Loading)*. , (2010).
- Cain, J. W. (2017). Mathematics of Fitting Scientific Data. *Molecular Life Sciences*, 1–7. https://doi.org/10.1007/978-1-4614-6436-5_560-1
- Camanho, P. P., Arteiro, A., Melro, A. R., Catalanotti, G., & Vogler, M. (2015). Three-dimensional invariant-based failure criteria for fibre-reinforced composites. *International Journal of Solids and Structures*, *55*, 92–107. <https://doi.org/http://dx.doi.org/10.1016/j.ijsolstr.2014.03.038>
- Cao, Y. J., Shen, W. Q., Shao, J. F., & Burlion, N. (2018). European Journal of Mechanics / A Solids Influences of micro-pores and meso-pores on elastic and plastic properties of porous materials. *European Journal of Mechanics / A Solids*, *72*(March), 407–423. <https://doi.org/10.1016/j.euromechsol.2018.06.003>
- Chawla, N., & Deng, X. (2003). Effect of Density on the Microstructure and Mechanical Behavior of Powder Metallurgy Fe-Mo-Ni Steels. ... in *Powder Metallurgy ...*, *6*(March 2014), 7–257. Retrieved from <http://www.yunamedia.com/www.hoegtest.com/TechPapersv2/125.pdf>
- Chawla, N., & Deng, X. (2005). Microstructure and mechanical behavior of porous sintered steels. *Materials Science and Engineering A*, *390*(1–2), 98–112. <https://doi.org/10.1016/j.msea.2004.08.046>
- Chawla, N., Williams, J. J., & Saha, R. (2003). *Mechanical behavior and microstructure characterization of sinter-forged SiC particle reinforced aluminum matrix composites*. *2*(2002), 215–227. [https://doi.org/10.1016/S1471-5317\(03\)00005-1](https://doi.org/10.1016/S1471-5317(03)00005-1)
- Cheng, J., & Ghosh, S. (2015). A crystal plasticity FE model for deformation with twin nucleation in magnesium alloys. *International Journal of Plasticity*, *67*, 148–170. <https://doi.org/10.1016/j.ijplas.2014.10.005>

- Chevalier, J., Morelle, X. P., Camanho, P. P., Lani, F., & Pardoën, T. (2018). On a unique fracture micromechanism for highly cross-linked epoxy resins. *Journal of the Mechanics and Physics of Solids*, 122, 502–519. <https://doi.org/10.1016/J.JMPS.2018.09.028>
- Choren, J. A., Heinrich, S. M., & Silver-Thorn, M. B. (2013). Young's modulus and volume porosity relationships for additive manufacturing applications. *Journal of Materials Science*, 48(15), 5103–5112. <https://doi.org/10.1007/s10853-013-7237-5>
- Christensen, R. M. (2001). a Survey of and Evaluation Methodology for Fiber Composite Material Failure Theories. *Seven*, 25–40.
- Collini, L., & Nicoletto, G. (2005). Determination of the relationship between microstructure and constitutive behaviour of nodular cast iron with a unit cell model. *The Journal of Strain Analysis for Engineering Design*, 40(2), 107–116. Retrieved from <https://doi.org/10.1243/030932405X7692>
- D5045-99(2007). (2013). Standard Test Methods for Plane-Strain Fracture Toughness and Strain Energy Release Rate of Plastic Materials. *ASTM Book of Standards*, 99(Reapproved 2007), 1–9. <https://doi.org/10.1520/D5045-14.priate>
- Dæhli, L. E. ., Faleskog, J., Børvik, T., & Hopperstada, O. S. (2016). Unit cell simulations and porous plasticity modelling for recrystallization textures in aluminium alloys. *Procedia Structural Integrity*, 2, 2535–2542. <https://doi.org/10.1016/j.prostr.2016.06.317>
- Danas, K., & Aravas, N. (2012). Numerical modeling of elasto-plastic porous materials with void shape effects at finite deformations. *Composites Part B: Engineering*, 43(6), 2544–2559. <https://doi.org/10.1016/j.compositesb.2011.12.011>
- Daniel, I. M. (2015). Constitutive behavior and failure criteria for composites under static and dynamic loading. *Meccanica*, 50(2), 429–442. <https://doi.org/10.1007/s11012-013-9829-1>
- Daniel, I. M., Daniel, S. M., & Fenner, J. S. (2018). A new yield and failure theory for composite materials under static and dynamic loading. *International Journal of Solids and Structures*, 148–149, 79–93. <https://doi.org/10.1016/j.ijsolstr.2017.08.036>
- Daniel, I. M., Luo, J. J., Schubel, P. M., & Werner, B. T. (2009). Interfiber/interlaminar failure of composites under multi-axial states of stress. *Composites Science and Technology*, 69(6), 764–771. <https://doi.org/10.1016/j.compscitech.2008.04.016>
- Dávila, C. G., Camanho, P. P., & Rose, C. A. (2005). Failure criteria for FRP laminates. *Journal of Composite Materials*, 39(4), 323–345. <https://doi.org/10.1177/0021998305046452>
- Debboub, S., Boumaiza, Y., & Boudour, A. (2012). Elasticity modulus evaluation for a porous material by acoustic methods. *IOP Conference Series: Materials Science and Engineering*, 28(1). <https://doi.org/10.1088/1757-899X/28/1/012009>
- Deng, X., Piotrowski, G., Chawla, N., & Narasimhan, K. S. (2008). *Fatigue crack growth behavior of hybrid and prealloyed sintered steels Part I. Microstructure characterization*. 491, 19–27. <https://doi.org/10.1016/j.msea.2008.05.009>
- Dewey, J. M. (1947). The elastic constants of materials loaded with non-rigid fillers. *Journal of Applied Physics*, 18(6), 578–581. <https://doi.org/10.1063/1.1697691>
- Di Landro, L., Montalto, A., Bettini, P., Guerra, S., Montagnoli, F., & Rigamonti, M. (2017). Detection of voids in carbon/epoxy laminates and their influence on mechanical properties. *Polymers and Polymer Composites*.

- Dolbow, J., Moës, N., & Belytschko, T. (2001). An extended finite element method for modeling crack growth with frictional contact. *Computer Methods in Applied Mechanics and Engineering*, 190(51–52), 6825–6846. [https://doi.org/10.1016/S0045-7825\(01\)00260-2](https://doi.org/10.1016/S0045-7825(01)00260-2)
- Dong, C. (2016). Effects of Process-Induced Voids on the Properties of Fibre Reinforced Composites. *Journal of Materials Science and Technology*, 32(7), 597–604. <https://doi.org/10.1016/j.jmst.2016.04.011>
- Duarte, A. P. C., Díaz Sáez, A., & Silvestre, N. (2017). Comparative study between XFEM and Hashin damage criterion applied to failure of composites. *Thin-Walled Structures*, 115(October 2016), 277–288. <https://doi.org/10.1016/j.tws.2017.02.020>
- Elnekhaily, S. A., & Talreja, R. (2018). Damage initiation in unidirectional fiber composites with different degrees of nonuniform fiber distribution. *Composites Science and Technology*, 155. <https://doi.org/10.1016/j.compscitech.2017.11.017>
- Esna Ashari, S., & Mohammadi, S. (2012). Fracture analysis of FRP-reinforced beams by orthotropic XFEM. *Journal of Composite Materials*, 46(11), 1367–1389. <https://doi.org/10.1177/0021998311418702>
- Eudier, M. (192AD). The Mechanical Properties of Sintered Low-Alloy Steels. *Otolaryngology–Head and Neck Surgery*, 9(1), 278–290. <https://doi.org/10.1177/019459988609500112>
- Fard, M. Y. (2011). *Nonlinear inelastic mechanical behavior of epoxy resin polymeric materials*. ARIZONA STATE UNIVERSITY.
- Fiedler, B., Hojo, M., Ochiai, S., Schulte, K., & Ando, M. (2001). Failure behavior of an epoxy matrix under different kinds of static loading. *Composites Science and Technology*, 61(11), 1615–1624. [https://doi.org/10.1016/S0266-3538\(01\)00057-4](https://doi.org/10.1016/S0266-3538(01)00057-4)
- Frazier, W. E. (2014). Metal additive manufacturing: A review. *Journal of Materials Engineering and Performance*, 23(6), 1917–1928. <https://doi.org/10.1007/s11665-014-0958-z>
- Fries, T.-P., & Belytschko, T. (2010). The extended/generalized finite element method: An overview of the method and its applications. *International Journal for Numerical Methods in Engineering*, 84(April), 253–304. <https://doi.org/10.1002/nme>
- FRYXELL, R. E., & CHANDLER, B. A. (1964). Creep, Strength, Expansion, and Elastic Moduli of Sintered BeO As a Function of Grain Size, Porosity, and Grain Orientation. *Journal of the American Ceramic Society*, 47(6), 283–291. <https://doi.org/10.1111/j.1151-2916.1964.tb14417.x>
- GAO, L., WANG, C., LIU, Z., & ZHUANG, Z. (2017). Theoretical aspects of selecting repeated unit cell model in micromechanical analysis using displacement-based finite element method. *Chinese Journal of Aeronautics*, 30(4), 1417–1426. <https://doi.org/10.1016/j.cja.2017.05.010>
- Gao, W., Zhang, Y., Ramanujan, D., Ramani, K., Chen, Y., Williams, C. B., ... Zavattieri, P. D. (2015). The status, challenges, and future of additive manufacturing in engineering. *CAD Computer Aided Design*, 69, 65–89. <https://doi.org/10.1016/j.cad.2015.04.001>
- Gaudig, W., Mellert, R., Weber, U., & Schmauder, S. (2003). Self-consistent one-particle 3D unit cell model for simulation of the effect of graphite aspect ratio on Young's modulus of cast-iron. *Computational Materials Science*, 28(3-4 SPEC. ISS.), 654–662. <https://doi.org/10.1016/j.commatsci.2003.08.021>

- Ghayoor, H., Hoa, S. V., & Marsden, C. C. (2018). A micromechanical study of stress concentrations in composites. *Composites Part B: Engineering*, *132*.
<https://doi.org/10.1016/j.compositesb.2017.09.009>
- Gibson, I., Rosen, D., & Stucker, B. (2013). Standard Terminology for Additive Manufacturing Technologies. *Rapid Manufacturing Association*, 10–12. <https://doi.org/10.1520/F2792-12A.2>
- Giddings, P. F., Bowen, C. R., Salo, A. I. T., Kim, H. A., & Ive, A. (2010). Bistable composite laminates: Effects of laminate composition on cured shape and response to thermal load. *Composite Structures*, *92*(9), 2220–2225. <https://doi.org/10.1016/j.compstruct.2009.08.043>
- Gitman, I. M., Askes, H., & Sluys, L. J. (2007). Representative volume: Existence and size determination. *Engineering Fracture Mechanics*, *74*(16), 2518–2534.
<https://doi.org/10.1016/j.engfracmech.2006.12.021>
- GOODIER, & N., J. (1933). Concentration of Stress around Spherical and Cylindrical Inclusions and Flaws. *T. A. S. M. E.*, *55*, 39. Retrieved from <http://ci.nii.ac.jp/naid/20000117887/en/>
- Grogan, D. M., Leen, S. B., & O. Brádaigh, O. C. M. (2014). An XFEM-based methodology for fatigue delamination and permeability of composites. *Composite Structures*, *107*(1).
<https://doi.org/10.1016/j.compstruct.2013.07.050>
- Guidault, P. A., Allix, O., Champaney, L., & Cornuault, C. (2008). A multiscale extended finite element method for crack propagation. *Computer Methods in Applied Mechanics and Engineering*, *197*(5), 381–399. <https://doi.org/10.1016/j.cma.2007.07.023>
- Guo, Z., Wang, L., Chen, Y., Zheng, L., Yang, Z., & Dong, L. (2017). A universal model for predicting the effective shear modulus of two-dimensional porous materials. *Mechanics of Materials*, *110*, 59–67. <https://doi.org/10.1016/j.mechmat.2017.04.006>
- Gupta, P., Pereira, J. P., Kim, D.-J., Duarte, C. A., & Eason, T. (2012). Analysis of three-dimensional fracture mechanics problems: A non-intrusive approach using a generalized finite element method. *Engineering Fracture Mechanics*, *90*, 41–64.
<https://doi.org/10.1016/j.engfracmech.2012.04.014>
- Gupta, V. (2014). *Improved conditioning and accuracy of a two-scale generalized finite element method for fracture mechanics*. University of Illinois at Urbana-Champaign.
- Gupta, V., & Duarte, C. A. (2016). On the enrichment zone size for optimal convergence rate of the Generalized/Extended Finite Element Method. *Computers and Mathematics with Applications*, *72*(3), 481–493. <https://doi.org/10.1016/j.camwa.2016.04.043>
- Gurson, A. L. (1977). Continuum Theory of Ductile Rupture by Void Nucleation and Growth: Part I—Yield Criteria and Flow Rules for Porous Ductile Media. *Journal of Engineering Materials and Technology*, *99*(1), 2. <https://doi.org/10.1115/1.3443401>
- Gusev, A. A. (1997). Representative volume element size for elastic composites: A numerical study. *Journal of the Mechanics and Physics of Solids*, *45*(9), 1449–1459.
[https://doi.org/10.1016/S0022-5096\(97\)00016-1](https://doi.org/10.1016/S0022-5096(97)00016-1)
- Hagstrand, P. O., Bonjour, F., & Månson, J. A. E. (2005). The influence of void content on the structural flexural performance of unidirectional glass fibre reinforced polypropylene composites. *Composites Part A: Applied Science and Manufacturing*, *36*(5), 705–714.
<https://doi.org/10.1016/j.compositesa.2004.03.007>

- Han, F., Tang, B., Kou, H., Li, J., & Feng, Y. (2015). Experiments and crystal plasticity finite element simulations of nanoindentation on Ti-6Al-4V alloy. *Materials Science and Engineering A*, 625, 28–35. <https://doi.org/10.1016/j.msea.2014.11.090>
- Hardin, R. A., & Beckermann, C. (2013). Effect of porosity on deformation, damage, and fracture of cast steel. *Metallurgical and Materials Transactions A: Physical Metallurgy and Materials Science*, 44(12), 5316–5332. <https://doi.org/10.1007/s11661-013-1669-z>
- Hardin, R. a, & Beckermann, C. (2011). Measurement and Prediction of Mechanical Behavior of Cast Steel Plates with Centerline Porosity. *Proceedings of the 65th SFSA Technical and Operating Conference*, (5.4). Chicago, IL: Steel Founders' Society of America.
- Hardin, Richard A., & Beckermann, C. (2007). Effect of porosity on the stiffness of cast steel. *Metallurgical and Materials Transactions A: Physical Metallurgy and Materials Science*, 38 A(12), 2992–3006. <https://doi.org/10.1007/s11661-007-9390-4>
- Hashin, Z., & Rotem, A. (1973). A Fatigue Failure Criterion for Fiber Reinforced Materials. *Journal of Composite Materials*, 7(4), 448–464. <https://doi.org/10.1177/002199837300700404>
- HASSELMAN, D. P. H. (1962). On the Porosity Dependence of the Elastic Moduli of Polycrystalline Refractory Materials. *Journal of the American Ceramic Society*, 45(9), 452–453. <https://doi.org/10.1111/j.1151-2916.1962.tb11191.x>
- HASSELMAN, D. P. H. (1963). Relation Between Effects of Porosity on Strength and on Young's Modulus of Elasticity of Polycrystalline Materials. *Journal of the American Ceramic Society*, 46(11), 564–565. <https://doi.org/10.1111/j.1151-2916.1963.tb14615.x>
- HASSELMAN, D. P. H., & FULRATH, R. M. (1964). Effect of Small Fraction of Spherical Porosity on Elastic Moduli of Glass. *Journal of the American Ceramic Society*, 47(1), 52–53. <https://doi.org/10.1111/j.1151-2916.1964.tb14644.x>
- Hencky, H. (1924). Zur Theorie plastischer Deformationen und der hierdurch im Material hervorgerufenen Nachspannungen. *ZAMM-Journal of Applied Mathematics and Mechanics/Zeitschrift Für Angewandte Mathematik Und Mechanik*, 4(4), 323–334.
- Herzog, D., Seyda, V., Wycisk, E., & Emmelmann, C. (2016). Additive manufacturing of metals. *Acta Materialia*, 117, 371–392. <https://doi.org/10.1016/j.actamat.2016.07.019>
- Hill, R. (1963). Elastic properties of reinforced solids: Some theoretical principles. *Journal of the Mechanics and Physics of Solids*, 11(5), 357–372. [https://doi.org/10.1016/0022-5096\(63\)90036-X](https://doi.org/10.1016/0022-5096(63)90036-X)
- Hill, R. (1998). *The mathematical theory of plasticity* (11th ed.). Oxford university press.
- Hill, R. (2006). The elastic field of an inclusion in an anisotropic medium. *Proceedings of the Royal Society of London. Series A. Mathematical and Physical Sciences*, 300(1461), 270–289. <https://doi.org/10.1098/rspa.1967.0170>
- Hill, Rodney. (1963). Elastic properties of reinforced solids: some theoretical principles. *Journal of the Mechanics and Physics of Solids*, 11(5), 357–372.
- Hinton.M.J, Kaddour.A.S, & Soden.P.D. (2002). A comparison of the predictive capabilities of current failure theories for composite laminates, judged against experimental evidence. In *Composites Science and Technology* (Vol. 62). [https://doi.org/10.1016/S0266-3538\(02\)00125-2](https://doi.org/10.1016/S0266-3538(02)00125-2)

- Hollister, S. J., & Kikuchi, N. (1992). A comparison of homogenization and standard mechanics analyses for periodic porous composites. *Computational Mechanics*, *10*(2), 73–95. <https://doi.org/10.1007/BF00369853>
- Hosseini-Toudeshky, H., & Jamalini, M. (2015). Simulation of micromechanical damage to obtain mechanical properties of bimodal Al using XFEM. *Mechanics of Materials*, *89*, 229–240. <https://doi.org/10.1016/j.mechmat.2015.06.015>
- Huang, H., & Talreja, R. (2005). Effects of void geometry on elastic properties of unidirectional fiber reinforced composites. *Composites Science and Technology*, *65*(13), 1964–1981. <https://doi.org/10.1016/j.compscitech.2005.02.019>
- Isaac, M. D., & Ori, I. (2013). Engineering Mechanics of composite materials. *Oxford University Press*, 2, 1–403. <https://doi.org/5fad72a8bc5942d089cc71406c6287da>
- Jagota, A., Hui, C. Y., & Dawson, P. R. (1987). The determination of fracture toughness for a porous elastic-plastic solid. *International Journal of Fracture*, *33*(2), 111–124. <https://doi.org/10.1007/BF00033743>
- Jeong, H. Y., & Pan, J. (1995). A macroscopic constitutive law for porous solids with pressure-sensitive matrices and its implications to plastic flow localization. *International Journal of Solids and Structures*, *32*(24), 3669–3691. [https://doi.org/10.1016/0020-7683\(95\)00009-Y](https://doi.org/10.1016/0020-7683(95)00009-Y)
- Jones, R. M. (1999). Mechanics of composite materials. *Mechanics of Composite Materials*, p. 519. <https://doi.org/10.1007/BF00611782>
- Jones, R. M. (2009). *Deformation theory of plasticity*. Bull Ridge Corporation.
- Jordan, J. L., Foley, J. R., & Siviour, C. R. (2008). Mechanical properties of Epon 826/DEA epoxy. *Mechanics of Time-Dependent Materials*, *12*(3), 249–272. <https://doi.org/10.1007/s11043-008-9061-x>
- Kalantari, M., Dong, C., & Davies, I. J. (2017). Effect of matrix voids, fibre misalignment and thickness variation on multi-objective robust optimization of carbon/glass fibre-reinforced hybrid composites under flexural loading. *Composites Part B: Engineering*, *123*, 136–147. <https://doi.org/10.1016/j.compositesb.2017.05.022>
- Kim, N. H., & Kim, H. S. (2005). Micro-void toughening of thermosets and its mechanism. *Journal of Applied Polymer Science*, *98*(3), 1290–1295. <https://doi.org/10.1002/app.22262>
- Kinloch, A. J., & Williams, J. G. (1980). Crack blunting mechanisms in polymers. *Journal of Materials Science*, *15*(4), 987–996. <https://doi.org/10.1007/BF00552112>
- Knauss, W. G. (2012). On the importance of the dilatational component of the stress state in the uniaxial yield-like behavior of rate-dependent polymers: C. Bauwens-Crowet revisited. *Mechanics of Time-Dependent Materials*, *16*(2), 223–240. <https://doi.org/10.1007/s11043-011-9149-6>
- KNUDSEN, F. P. (1959). Dependence of Mechanical Strength of Brittle Polycrystalline Specimens on Porosity and Grain Size. *Journal of the American Ceramic Society*, *42*(8), 376–387. <https://doi.org/10.1111/j.1151-2916.1959.tb13596.x>
- Koerber, H., Kuhn, P., Ploekl, M., Otero, F., Gerbaud, P. W., Rolfes, R., & Camanho, P. P. (2018). Experimental characterization and constitutive modeling of the non-linear stress–strain behavior of unidirectional carbon–epoxy under high strain rate loading. *Advanced Modeling and Simulation in Engineering Sciences*. <https://doi.org/10.1186/s40323-018->

- Kruth, J. P., Mercelis, P., Van Vaerenbergh, J., Froyen, L., & Rombouts, M. (2005). Binding mechanisms in selective laser sintering and selective laser melting. *Rapid Prototyping Journal*, 11(1), 26–36. <https://doi.org/10.1108/13552540510573365>
- Lachaud, F., Espinosa, C., Michel, L., Rahme, P., & Piquet, R. (2015). Modelling Strategies for Simulating Delamination and Matrix Cracking in Composite Laminates. *Applied Composite Materials*, 22(4), 377–403. <https://doi.org/10.1007/s10443-014-9413-4>
- Lambert, J., Chambers, A. R., Sinclair, I., & Spearing, S. M. (2012). 3D damage characterisation and the role of voids in the fatigue of wind turbine blade materials. *Composites Science and Technology*, 72(2), 337–343. <https://doi.org/10.1016/j.compscitech.2011.11.023>
- Leblond, J. (2014). An improved description of spherical void growth in plastic porous materials with finite porosities. 3(2013), 1232–1237. <https://doi.org/10.1016/j.mspro.2014.06.200>
- Leclerc, W., Karamian-Surville, P., & Vivet, A. (2015). An efficient and automated 3D FE approach to evaluate effective elastic properties of overlapping random fibre composites. *Computational Materials Science*, 99, 1–15. <https://doi.org/10.1016/j.commatsci.2014.10.047>
- Lee, J., & Lopez, M. M. (2014). An Experimental Study on Fracture Energy of Plain Concrete. *International Journal of Concrete Structures and Materials*, 8(2), 129–139. <https://doi.org/10.1007/s40069-014-0068-1>
- Leszczynski, J., & Shukla, M. (2010). *Practical Aspects of Computational Chemistry*. Springer.
- Li, H., Li, J., & Yuan, H. (2018). A review of the extended finite element method on macrocrack and microcrack growth simulations. *Theoretical and Applied Fracture Mechanics*, 97(August), 236–249. <https://doi.org/10.1016/j.tafmec.2018.08.008>
- Li, Y., Stier, B., Bednarczyk, B., Simon, J. W., & Reese, S. (2016). The effect of fiber misalignment on the homogenized properties of unidirectional fiber reinforced composites. *Mechanics of Materials*, 92, 261–274. <https://doi.org/10.1016/j.mechmat.2015.10.002>
- Liang, X., Li, H., Yu, W., Jiang, X., & Zhang, Z. (2012). A numerical approximation to the elastic properties of hollow particle filled composites. *ICIC Express Letters*, 6(6), 1549–1554. [https://doi.org/10.1016/S0022-5096\(02\)00021-2](https://doi.org/10.1016/S0022-5096(02)00021-2)
- Liebig, W. V., Leopold, C., & Schulte, K. (2013). Photoelastic study of stresses in the vicinity of a unique void in a fibre-reinforced model composite under compression. *Composites Science and Technology*, 84, 72–77. <https://doi.org/10.1016/j.compscitech.2013.04.011>
- Liebig, Wilfried V., Viets, C., Schulte, K., & Fiedler, B. (2015). Influence of voids on the compressive failure behaviour of fibereinforced composites. *Composites Science and Technology*, 117, 225–233. <https://doi.org/10.1016/j.compscitech.2015.06.020>
- Liu, P. F., & Zheng, J. Y. (2010). Recent developments on damage modeling and finite element analysis for composite laminates: A review. *Materials and Design*, 31(8), 3825–3834. <https://doi.org/10.1016/j.matdes.2010.03.031>
- Liu, P., Fu, C., Li, T., & Shi, C. (1999). Relationship between tensile strength and porosity for high porosity metals. *Science in China, Series E: Technological Sciences*, 42(1), 100–107. <https://doi.org/10.1007/BF02917065>
- LS-DYNA. (2013). *LS-DYNA user's manual*. CA, USA: Livermore Software Technology

- Corporation.
- Ma, H., Liu, X., & Hu, G. (2006). Overall elastoplastic property for micropolar composites with randomly oriented ellipsoidal inclusions. *Computational Materials Science*, *37*(4), 582–592. <https://doi.org/10.1016/j.commatsci.2005.12.016>
- MACKENZIE, J. K. (1949). The elastic constants of a material containing spherical coated holes. *Arch. Mech.*, *47*, 223–246.
- Matouš, K., Geers, M. G. D., Kouznetsova, V. G., & Gillman, A. (2017). A review of predictive nonlinear theories for multiscale modeling of heterogeneous materials. *Journal of Computational Physics*, *330*, 192–220. <https://doi.org/10.1016/j.jcp.2016.10.070>
- Mbiakop, A., Constantinescu, A., & Danas, K. (2015). An analytical model for porous single crystals with ellipsoidal voids. *Journal of the Mechanics and Physics of Solids*, *84*, 436–467. <https://doi.org/10.1016/j.jmps.2015.07.011>
- MC90 CEB. Comité Euro-International du Béton, CEB-FIP Model Code 1990. *Bulletin D'Information*. 1993(215).
- Melenk, J. M., & Babuška, I. (1996). The partition of unity finite element method: Basic theory and applications. *Computer Methods in Applied Mechanics and Engineering*, *139*(1–4), 289–314. [https://doi.org/10.1016/S0045-7825\(96\)01087-0](https://doi.org/10.1016/S0045-7825(96)01087-0)
- Mercelis, P., & Kruth, J. P. (2006). Residual stresses in selective laser sintering and selective laser melting. *Rapid Prototyping Journal*, *12*(5), 254–265. <https://doi.org/10.1108/13552540610707013>
- Mignone, P. J., Echlin, M. P., Pollock, T. M., Finlayson, T. R., Riley, D. P., Sesso, M. L., & Franks, G. V. (2017). Modelling the elastic properties of bi-continuous composite microstructures captured with TriBeam serial-sectioning. *Computational Materials Science*, *131*, 187–195. <https://doi.org/10.1016/j.commatsci.2017.01.026>
- Miled, K., Sab, K., & Le Roy, R. (2011). Effective elastic properties of porous materials: Homogenization schemes vs experimental data. *Mechanics Research Communications*, *38*(2), 131–135. <https://doi.org/10.1016/j.mechrescom.2011.01.009>
- Mirkhalaf, S. M., Andrade Pires, F. M., & Simoes, R. (2016). Determination of the size of the Representative Volume Element (RVE) for the simulation of heterogeneous polymers at finite strains. *Finite Elements in Analysis and Design*, *119*, 30–44. <https://doi.org/10.1016/j.finel.2016.05.004>
- Moës, N., & Belytschko, T. (2002). Extended finite element method for cohesive crack growth. *Engineering Fracture Mechanics*, *69*(7), 813–833. [https://doi.org/10.1016/S0013-7944\(01\)00128-X](https://doi.org/10.1016/S0013-7944(01)00128-X)
- Moës, N., Dolbow, J., & Belytschko, T. (1999). A finite element method for crack growth without remeshing. *International Journal for Numerical Methods in Engineering*, *46*(1), 131–150. [https://doi.org/10.1002/\(SICI\)1097-0207\(19990910\)46:1<131::AID-NME726>3.0.CO;2-J](https://doi.org/10.1002/(SICI)1097-0207(19990910)46:1<131::AID-NME726>3.0.CO;2-J)
- Mori, T., & Tanaka, K. (1973). Average stress in matrix and average elastic energy of materials with misfitting inclusions. *Acta Metallurgica*, *21*(5), 571–574. [https://doi.org/10.1016/0001-6160\(73\)90064-3](https://doi.org/10.1016/0001-6160(73)90064-3)
- Morin, L., Leblond, J. B., & Kondo, D. (2015). A Gurson-type criterion for plastically anisotropic solids containing arbitrary ellipsoidal voids. *International Journal of Solids and Structures*,

- 77, 86–101. <https://doi.org/10.1016/j.ijsolstr.2015.05.021>
- Morin, L., Michel, J. C., & Leblond, J. B. (2017). A Gurson-type layer model for ductile porous solids with isotropic and kinematic hardening. *International Journal of Solids and Structures*, 118–119, 167–178. <https://doi.org/10.1016/j.ijsolstr.2017.03.028>
- Nemat-Nasser, S., & Taya, M. (1981). On effective moduli of an elastic body containing periodically distributed voids. *Quarterly of Applied Mathematics*, 39(1), 43–59. <https://doi.org/10.1090/qam/99626>
- Nguyen, V. P., Lloberas-Valls, O., Stroeven, M., & Sluys, L. J. (2011). Homogenization-based multiscale crack modelling: From micro-diffusive damage to macro-cracks. *Computer Methods in Applied Mechanics and Engineering*, 200(9–12), 1220–1236. <https://doi.org/10.1016/j.cma.2010.10.013>
- Nikishkov, Y., Airoidi, L., & Makeev, A. (2013). Measurement of voids in composites by X-ray Computed Tomography. *Composites Science and Technology*, 89, 89–97. <https://doi.org/10.1016/j.compscitech.2013.09.019>
- Nimmo, J. R. (2004). Porosity and pore size distribution. *Encyclopedia of Soils in the Environment*, 295–303. <https://doi.org/10.1016/B978-0-12-409548-9.05265-9>
- Oh, Y., Nam, H., Kim, Y., & Miura, N. (2018). International Journal of Pressure Vessels and Piping Application of the GTN model to ductile crack growth simulation in through-wall cracked pipes. *International Journal of Pressure Vessels and Piping*, 159(November 2017), 35–44. <https://doi.org/10.1016/j.ijpvp.2017.11.006>
- Oliver, J., Caicedo, M., Huespe, A. E., Hernández, J. A., & Roubin, E. (2017). Reduced order modeling strategies for computational multiscale fracture. *Computer Methods in Applied Mechanics and Engineering*, 313, 560–595. <https://doi.org/10.1016/j.cma.2016.09.039>
- Oliver, J., Caicedo, M., Roubin, E., Huespe, A. E., & Hernández, J. A. (2015). Continuum approach to computational multiscale modeling of propagating fracture. *Computer Methods in Applied Mechanics and Engineering*, 294, 384–427. <https://doi.org/10.1016/j.cma.2015.05.012>
- Omairey, S. L., Dunning, P. D., & Sriramula, S. (2018). Development of an ABAQUS plugin tool for periodic RVE homogenisation. *Engineering with Computers*, 0(0), 1–11. <https://doi.org/10.1007/s00366-018-0616-4>
- Otsu, N. (1979). A Threshold Selection Method from Gray-Level Histograms. *IEEE Transactions on Systems, Man, and Cybernetics*, C(1), 62–66. <https://doi.org/10.1109/TSMC.1979.4310076>
- P.K. Mallick. (2007). Fiber-Reinforced Composites: Materials, Manufacturing, and Design. In *CRC Press*.
- Pabst, W., & Gregorová, E. (2015). Critical Assessment 18: Elastic and thermal properties of porous materials -rigorous bounds and cross-property relations. *Materials Science and Technology (United Kingdom)*, 31(15), 1801–1808. <https://doi.org/10.1080/02670836.2015.1114697>
- Panakkal, J. P., Willems, H., & Arnold, W. (1990). Nondestructive evaluation of elastic parameters of sintered iron powder compacts. *Journal of Materials Science*, 25(2), 1397–1402. <https://doi.org/10.1007/BF00585456>

- Papadopoulos, G. A. (1987). The stationary value of the third stress invariant as a local fracture parameter (Det.-criterion). *Engineering Fracture Mechanics*, 27(6), 643–652. [https://doi.org/10.1016/0013-7944\(87\)90156-1](https://doi.org/10.1016/0013-7944(87)90156-1)
- Park, S. Y., Choi, W. J., & Choi, H. S. (2010). The effects of void contents on the long-term hygrothermal behaviors of glass/epoxy and GLARE laminates. *Composite Structures*, 92(1), 18–24. <https://doi.org/10.1016/j.compstruct.2009.06.006>
- Pawar, P. M., & Ganguli, R. (2006). Modeling progressive damage accumulation in thin walled composite beams for rotor blade applications. *Composites Science and Technology*, 66(13), 2337–2349. <https://doi.org/10.1016/j.compscitech.2005.11.033>
- Pelissou, C., Baccou, J., Monerie, Y., & Perales, F. (2009). Determination of the size of the representative volume element for random quasi-brittle composites. *International Journal of Solids and Structures*, 46(14–15), 2842–2855. <https://doi.org/10.1016/j.ijsolstr.2009.03.015>
- Perumal, L., Tso, C. P., & Leng, L. T. (2016). Analysis of thin plates with holes by using exact geometrical representation within XFEM. *Journal of Advanced Research*, 7(3), 445–452. <https://doi.org/10.1016/j.jare.2016.03.004>
- Petrov, N. A., Gorbatiikh, L., & Lomov, S. V. (2018). A parametric study assessing performance of eXtended Finite Element Method in application to the cracking process in cross-ply composite laminates. *Composite Structures*, 187(July 2017), 489–497. <https://doi.org/10.1016/j.compstruct.2017.12.014>
- Phani, K. K. (1986). Elastic-constant-porosity relations for polycrystalline thoria. *Journal of Materials Science Letters*, 5(7), 747–750. <https://doi.org/10.1007/BF01730236>
- Polasik, S. J., Williams, J. J., & Chawla, N. (2002). *Fatigue Crack Initiation and Propagation of Binder-Treated Powder Metallurgy Steels*. 33(January), 73–81.
- Pollayi, H., & Yu, W. (2014). Modeling matrix cracking in composite rotor blades within VABS framework. *Composite Structures*, 110(1), 62–76. <https://doi.org/10.1016/j.compstruct.2013.11.012>
- Pommier, S., Gravouil, A., & Combescure, A. (2013). Extended Finite Element Method X-FEM. In *Extended Finite Element Method for Crack Propagation*.
- Pontefisso, A., Zappalorto, M., & Quaresimin, M. (2015). An efficient RVE formulation for the analysis of the elastic properties of spherical nanoparticle reinforced polymers. *Computational Materials Science*, 96(PA), 319–326. <https://doi.org/10.1016/j.commatsci.2014.09.030>
- Pulungan, D., Lubineau, G., Yudhanto, A., Yaldiz, R., & Schijve, W. (2017). Identifying design parameters controlling damage behaviors of continuous fiber-reinforced thermoplastic composites using micromechanics as a virtual testing tool. *International Journal of Solids and Structures*, 117. <https://doi.org/10.1016/j.ijsolstr.2017.03.026>
- Puydt, Q., Flouriot, S., Ringeval, S., De Geuser, F., Estevez, R., Parry, G., & Deschamps, A. (2014). Relationship Between Microstructure, Strength, and Fracture in an Al-Zn-Mg Electron Beam Weld: Part II: Mechanical Characterization and Modeling. *Metallurgical and Materials Transactions A*, 45(13), 6141–6152. <https://doi.org/10.1007/s11661-014-2567-8>
- Radhakrishnan, H. (2011). *ANSYS Mechanical Tips & Tricks*.
- Raghava, R., Caddell, R. M., & Yeh, G. S. Y. (1973). The macroscopic yield behaviour of

- polymers. *Journal of Materials Science*, 8(2), 225–232. <https://doi.org/10.1007/BF00550671>
- Ramberg, W., & Osgood, W. R. (1943). Description of stress-strain curves by three parameters. In *National Advisory Committee for Aeronautics*. <https://doi.org/10.1016/j.matdes.2009.07.011>
- Rashid, M. M., & Nemat-Nasser, S. (1992). A constitutive algorithm for rate-dependent crystal plasticity. *Computer Methods in Applied Mechanics and Engineering*, 94(2), 201–228. [https://doi.org/10.1016/0045-7825\(92\)90147-C](https://doi.org/10.1016/0045-7825(92)90147-C)
- Ravi, S. K., Seefeldt, M., Van Bael, A., Gawad, J., & Roose, D. (2019). Multi-scale material modelling to predict the material anisotropy of multi-phase steels. *Computational Materials Science*, 160(September 2018), 382–396. <https://doi.org/10.1016/j.commatsci.2019.01.028>
- Reddy, J. N. (2014). *An Introduction to Nonlinear Finite Element Analysis: with applications to heat transfer, fluid mechanics, and solid mechanics*. Oxford: OUP.
- Roberts, a P., & Garboczi, E. J. (2000). Elastic properties of model porous ceramics. *Journal of the American Ceramic Society*, 83(12), 3041–3048. <https://doi.org/10.1111/j.1151-2916.2000.tb01680.x>
- Roters, F., Eisenlohr, P., Hantcherli, L., Tjahjanto, D. D., Bieler, T. R., & Raabe, D. (2010). Overview of constitutive laws, kinematics, homogenization and multiscale methods in crystal plasticity finite-element modeling: Theory, experiments, applications. *Acta Materialia*, 58(4), 1152–1211. <https://doi.org/10.1016/j.actamat.2009.10.058>
- Rousselier, G. (2001). Dissipation in porous metal plasticity and ductile fracture. *Journal of the Mechanics and Physics of Solids*, 49(8), 1727–1746. [https://doi.org/10.1016/S0022-5096\(01\)00013-8](https://doi.org/10.1016/S0022-5096(01)00013-8)
- Saby, M., Bernacki, M., Roux, E., & Bouchard, P. O. (2013). Three-dimensional analysis of real void closure at the meso-scale during hot metal forming processes. *Computational Materials Science*, 77, 194–201. <https://doi.org/10.1016/j.commatsci.2013.05.002>
- Saimoto, S., & Thomas, D. R. M. (1986). A novel method to measure the elastic modulus of polymers as a function of tensile deformation. *Journal of Materials Science*, 21(10), 3686–3690. <https://doi.org/10.1007/BF02403022>
- Salahouelhadj, A., & Haddadi, H. (2010). Estimation of the size of the RVE for isotropic copper polycrystals by using elastic-plastic finite element homogenisation. *Computational Materials Science*, 48(3), 447–455. <https://doi.org/10.1016/j.commatsci.2009.12.014>
- Schell, J. S. U., Renggli, M., van Lenthe, G. H., Müller, R., & Ermanni, P. (2006). Micro-computed tomography determination of glass fibre reinforced polymer meso-structure. *Composites Science and Technology*, 66(13), 2016–2022. <https://doi.org/10.1016/j.compscitech.2006.01.003>
- Schiavone, A., Abeygunawardana-Arachchige, G., & Silberschmidt, V. V. (2016). Crack initiation and propagation in ductile specimens with notches: experimental and numerical study. *Acta Mechanica*, 227(1), 203–215. <https://doi.org/10.1007/s00707-015-1425-0>
- Schmitz, A., & Horst, P. (2014). A finite element unit-cell method for homogenised mechanical properties of heterogeneous plates. *Composites Part A: Applied Science and Manufacturing*, 61, 23–32. <https://doi.org/10.1016/j.compositesa.2014.01.014>
- Schneider, K., Klusemann, B., & Bargmann, S. (2016). Automatic three-dimensional geometry and mesh generation of periodic representative volume elements for matrix-inclusion

- composites. *Advances in Engineering Software*, 99, 177–188.
<https://doi.org/10.1016/j.advengsoft.2016.06.001>
- Sercombe, T. B., Xu, X., Challis, V. J., Green, R., Yue, S., Zhang, Z., & Lee, P. D. (2015). Failure modes in high strength and stiffness to weight scaffolds produced by Selective Laser Melting. *Materials and Design*, 67(November), 501–508.
<https://doi.org/10.1016/j.matdes.2014.10.063>
- Shames, I. H. (1997). *Elastic and inelastic stress analysis*. CRC Press.
- Shan, Z., & Gokhale, A. M. (2002). Representative volume element for non-uniform micro-structure. *Computational Materials Science*, 24(3), 361–379. [https://doi.org/10.1016/S0927-0256\(01\)00257-9](https://doi.org/10.1016/S0927-0256(01)00257-9)
- Sharma, N. K., Mishra, R. K., & Sharma, S. (2016). 3D micromechanical analysis of thermo-mechanical behavior of Al₂O₃/Al metal matrix composites. *Computational Materials Science*, 115, 192–201. <https://doi.org/10.1016/j.commatsci.2015.12.051>
- Sharma, R., Deshpande, V. V., Bhagat, A. R., Mahajan, P., & Mittal, R. K. (2013). X-ray tomographical observations of cracks and voids in 3D carbon/carbon composites. *Carbon*, 60, 335–345. <https://doi.org/10.1016/j.carbon.2013.04.046>
- Shigang, A., Daining, F., Rujie, H., & Yongmao, P. (2015). Effect of manufacturing defects on mechanical properties and failure features of 3D orthogonal woven C/C composites. *Composites Part B: Engineering*, 71, 113–121.
<https://doi.org/10.1016/j.compositesb.2014.11.003>
- Shigang, A., Rujie, H., & Yongmao, P. (2015). A Numerical Study on the Thermal Conductivity of 3D Woven C/C Composites at High Temperature. *Applied Composite Materials*, 22(6), 823–835. <https://doi.org/10.1007/s10443-015-9438-3>
- Shigang, A., Xiaolei, Z., Yiqi, M., Yongmao, P., & Daining, F. (2014). Finite Element Modeling of 3D Orthogonal Woven C/C Composite Based on Micro-Computed Tomography Experiment. *Applied Composite Materials*, 21(4), 603–614. <https://doi.org/10.1007/s10443-013-9353-4>
- Siavouche, N.-N., & Hori, M. (1993). *Micromechanics: overall properties of heterogeneous materials* ((Vol. 37); J. D. Achenbach, B. Budiansky, H. A. Lauwerier, P. G. Saffman, L. Van Wijngaarden, & J. R. Willis, Eds.). Elsevier B.V.
- Sih, G. C. (1991). A three-dimensional strain energy density factor theory of crack propagation. *Mechanics of Fracture Initiation and Propagation*, 23–56.
- Sladek, J., Sladek, V., Krahulec, S., & Song, C. (2016). Micromechanics determination of effective properties of voided magneto-electroelastic materials. *Computational Materials Science*, 116, 103–112. <https://doi.org/10.1016/j.commatsci.2015.05.015>
- Song, B., Zhao, X., Li, S., Han, C., Wei, Q., Wen, S., ... Shi, Y. (2015). Differences in microstructure and properties between selective laser melting and traditional manufacturing for fabrication of metal parts: A review. *Frontiers of Mechanical Engineering*, 10(2), 111–125. <https://doi.org/10.1007/s11465-015-0341-2>
- Song, Danlong, Li, Y., Zhang, K., Cheng, H., Liu, P., & Hu, J. (2016). Micromechanical analysis for microscopic damage initiation in fiber/epoxy composite during interference-fit pin installation. *Materials and Design*, 89, 36–49. <https://doi.org/10.1016/j.matdes.2015.09.118>

- Song, Dawei, & Ponte Castañeda, P. (2017). A finite-strain homogenization model for viscoplastic porous single crystals: I – Theory. *Journal of the Mechanics and Physics of Solids*, 107(3), 560–579. <https://doi.org/10.1016/j.jmps.2017.06.008>
- Song, J. H., Wang, H., & Belytschko, T. (2008). A comparative study on finite element methods for dynamic fracture. *Computational Mechanics*, 42(2), 239–250. <https://doi.org/10.1007/s00466-007-0210-x>
- Soro, N., Brassart, L., Chen, Y., Veidt, M., Attar, H., & Dargusch, M. S. (2018). Finite element analysis of porous commercially pure titanium for biomedical implant application. *Materials Science and Engineering A*, 725(April), 43–50. <https://doi.org/10.1016/j.msea.2018.04.009>
- Spaggiari, A., & O’Dowd, N. (2012a). The influence of void morphology and loading conditions on deformation and failure of porous polymers: A combined finite-element and analysis of variance study. *Computational Materials Science*, 64, 41–46. <https://doi.org/10.1016/j.commatsci.2011.12.022>
- Spaggiari, A., & O’Dowd, N. (2012b). The influence of void morphology and loading conditions on deformation and failure of porous polymers: A combined finite-element and analysis of variance study. *Computational Materials Science*, 64, 41–46. <https://doi.org/10.1016/j.commatsci.2011.12.022>
- SPRIGGS, R. M. (1961). Expression for Effect of Porosity on Elastic Modulus of Polycrystalline. *Journal of The American Ceramic Society-Discussions and Notes*, 28(1), 1960–1961.
- Stephens, R. I., Horn, J. J., Poland, D. D., & Sager, E. A. (1998a). *FATIGUE AND FRACTURE TOUGHNESS OF HIGH STRENGTH FL4405 Materials / Specimens*. 72–101.
- Stephens, R. I., Horn, J. J., Poland, D. D., & Sager, E. A. (1998b). Influence of Density and Porosity Size and Shape on Fatigue and Fracture Toughness of High Strength FL4405 P/M Steel. *Effects of Product Quality and Design Criteria on Structural Integrity, STP1337-EB*, 72–101. Retrieved from <https://doi.org/10.1520/STP12343S>
- Strouboulis, T., Copps, K., & Babuška, I. (2011). The generalized finite element method. *Computer Methods in Applied Mechanics and Engineering*, 190(32–33), 4081–4193.
- Su, S. L., Rao, Q. H., & He, Y. H. (2013). Theoretical prediction of effective elastic constants for new intermetallic compound porous material. *Transactions of Nonferrous Metals Society of China (English Edition)*, 23(4), 1090–1097. [https://doi.org/10.1016/S1003-6326\(13\)62570-4](https://doi.org/10.1016/S1003-6326(13)62570-4)
- Su, Z. C., Tay, T. E., Ridha, M., & Chen, B. Y. (2015). Progressive damage modeling of open-hole composite laminates under compression. *Composite Structures*, 122, 507–517. <https://doi.org/10.1016/j.compstruct.2014.12.022>
- Sukumar, N., Dolbow, J. E., & Moës, N. (2015). Extended finite element method in computational fracture mechanics: a retrospective examination. *International Journal of Fracture*, 196(1–2), 189–206. <https://doi.org/10.1007/s10704-015-0064-8>
- Sumi, Y. (2014). *Mathematical and Computational Analyses of Cracking Formation* (Vol. 2). <https://doi.org/10.1007/978-4-431-54935-2>
- Sumitomo, T., Cáceres, C. H., & Veidt, M. (2002). The elastic modulus of cast Mg-Al-Zn alloys. *Journal of Light Metals*, 2(1), 49–56. [https://doi.org/10.1016/S1471-5317\(02\)00013-5](https://doi.org/10.1016/S1471-5317(02)00013-5)
- Szost, B. A., Terzi, S., Martina, F., Boisselier, D., Prytuliak, A., Pirling, T., ... Jarvis, D. J. (2016). A comparative study of additive manufacturing techniques: Residual stress and

- microstructural analysis of CLAD and WAAM printed Ti-6Al-4V components. *Materials and Design*, 89, 559–567. <https://doi.org/10.1016/j.matdes.2015.09.115>
- Talebi, H., Silani, M., Bordas, S. P. A., Kerfriden, P., & Rabczuk, T. (2014). A computational library for multiscale modeling of material failure. *Computational Mechanics*, 53(5), 1047–1071. <https://doi.org/10.1007/s00466-013-0948-2>
- Talreja, R. (2014). Assessment of the fundamentals of failure theories for composite materials. *Composites Science and Technology*, 105, 190–201. <https://doi.org/10.1016/j.compscitech.2014.10.014>
- Tejchmann, J., & Bobinski, J. (2015). *Continuous and Discontinuous Modelling of Fracture in Concrete Using FEM* (Vol. 1). <https://doi.org/10.1007/978-3-642-28463-2>
- Timoshenko, S. P., & J. N. Goodier. (2010). *Theory of elasticity* (3rd ed.). Singapore: McGraw-Hill Ltd.
- Toro, S., Sánchez, P. J., Blanco, P. J., De Souza Neto, E. A., Huespe, A. E., & Feijóo, R. A. (2016). Multiscale formulation for material failure accounting for cohesive cracks at the macro and micro scales. *International Journal of Plasticity*, 76, 75–110. <https://doi.org/10.1016/j.ijplas.2015.07.001>
- Trias, D., Costa, J., Turon, A., & Hurtado, J. E. (2006). Determination of the critical size of a statistical representative volume element (SRVE) for carbon reinforced polymers. *Acta Materialia*, 54(13), 3471–3484. <https://doi.org/10.1016/j.actamat.2006.03.042>
- Trillat, M., & Pastor, J. (2005). Limit analysis and Gurson's model. *European Journal of Mechanics, A/Solids*, 24(5), 800–819. <https://doi.org/10.1016/j.euromechsol.2005.06.003>
- Trofimov, A., Abaimov, S., Akhatov, I., & Sevostianov, I. (2018). On the bounds of applicability of two-step homogenization technique for porous materials. *International Journal of Engineering Science*, 123, 117–126. <https://doi.org/10.1016/j.ijengsci.2017.11.017>
- Tvergaard, V., & Needleman, A. (1984). Analysis of the cup-cone fracture in a round tensile bar. *Acta Metallurgica*, 32(1), 157–169. [https://doi.org/10.1016/0001-6160\(84\)90213-X](https://doi.org/10.1016/0001-6160(84)90213-X)
- Ukadgaonker, V. G., & Awasare, P. J. (1995). A new criterion for fracture initiation. *Engineering Fracture Mechanics*, 51(2), 265–274. [https://doi.org/10.1016/0013-7944\(94\)00265-J](https://doi.org/10.1016/0013-7944(94)00265-J)
- Unger, J. F., & Eckardt, S. (2011). Multiscale Modeling of Concrete. *Archives of Computational Methods in Engineering*, 18(3), 341–393. <https://doi.org/10.1007/s11831-011-9063-8>
- Uygunoglu, T. K. U., Gunes, I. K. U., & Brostov, W. of N. T. (2015). physical and Mechanical properties of polymer comppsite with high content. *Materials Research*, 18(6), 1188–1196. <https://doi.org/10.1590/1516-1439.009815>
- Vadillo, G., Reboul, J., & Fern, J. (2016). *European Journal of Mechanics A / Solids A modi fi ed Gurson model to account for the in fl uence of the Lode parameter at high triaxialities*. 56, 31–44. <https://doi.org/10.1016/j.euromechsol.2015.09.010>
- Van Der Meer, F. P., Sluys, L. J., Hallett, S. R., & Wisnom, M. R. (2012). Computational modeling of complex failure mechanisms in laminates. *Journal of Composite Materials*, 46(5), 603–623. <https://doi.org/10.1177/0021998311410473>
- Van Der Meer, Frans P. (2016). Micromechanical validation of a mesomodel for plasticity in composites. *European Journal of Mechanics, A/Solids*, 60. <https://doi.org/10.1016/j.euromechsol.2016.06.008>

- van Dongen, B., van Oostrum, A., & Zarouchas, D. (2018). A blended continuum damage and fracture mechanics method for progressive damage analysis of composite structures using XFEM. *Composite Structures*, *184*(September 2017), 512–522.
<https://doi.org/10.1016/j.compstruct.2017.10.007>
- Verges, M. A., Schilling, P. J., Herrington, P. D., Tatiparthi, A. K., & Karedla, B. R. (2005). X-ray computed microtomography of internal damage in fiber reinforced polymer matrix composites. *Composites Science and Technology*, *65*(14), 2071–2078.
<https://doi.org/10.1016/j.compscitech.2005.05.014>
- Vilaro, T., Colin, C., & Bartout, J. D. (2011). As-fabricated and heat-treated microstructures of the Ti-6Al-4V alloy processed by selective laser melting. *Metallurgical and Materials Transactions A: Physical Metallurgy and Materials Science*, *42*(10), 3190–3199.
<https://doi.org/10.1007/s11661-011-0731-y>
- von Mises, R. (1913). Mechanik der festen Körper im plastisch deformablen Zustand. *Göttin. Nachr. Math. Phys.*, *1*, 582–592.
- Wang, F., Williams, S., Colegrove, P., & Antonysamy, A. A. (2013). Microstructure and mechanical properties of wire and arc additive manufactured Ti-6Al-4V. *Metallurgical and Materials Transactions A: Physical Metallurgy and Materials Science*, *44*(2), 968–977.
<https://doi.org/10.1007/s11661-012-1444-6>
- Wang, Zhen, Yu, T., Bui, T. Q., Trinh, N. A., Luong, N. T. H., Duc, N. D., & Doan, D. H. (2016). Numerical modeling of 3-D inclusions and voids by a novel adaptive XFEM. *Advances in Engineering Software*, *102*, 105–122. <https://doi.org/10.1016/j.advengsoft.2016.09.007>
- Wang, Zhenqing, Liu, F., Liang, W., & Zhou, L. (2013). Study on tensile properties of nanoreinforced epoxy polymer: Macroscopic experiments and nanoscale FEM simulation prediction. *Advances in Materials Science and Engineering*, *2013*.
<https://doi.org/10.1155/2013/392450>
- Weinberg, K., Mota, A., & Ortiz, M. (2006). A variational constitutive model for porous metal plasticity. *Computational Mechanics*, *37*(2), 142–152. <https://doi.org/10.1007/s00466-005-0685-2>
- Winkler, B., Hofstetter, G., & Niederwanger, G. (2001). Experimental verification of a constitutive model for concrete cracking. *Proceedings of the Institution of Mechanical Engineers, Part L: Journal of Materials: Design and Applications*, *2015*(2), 75–86.
<https://doi.org/https://doi.org/10.1177/146442070121500202>
- Wright, P., Fu, X., Sinclair, I., & Spearing, S. M. (2008). Ultra high resolution computed tomography of damage in notched carbon fiber-epoxy composites. *Journal of Composite Materials*, *42*(19), 1993–2002. <https://doi.org/10.1177/0021998308092211>
- Wu, E. M., & Tsai, S. W. (1971). A General Theory of Strength for Anisotropic Materials. *Journal of Composite Materials*, *5*(1), 58–80. <https://doi.org/10.1177/002199837100500106>
- Wu, L., Zhang, L. X., & Guo, Y. K. (2013). A Review of the Extended Finite Element for Fracture Analysis of Structures. *Applied Mechanics and Materials*, *444–445*, 96–102.
<https://doi.org/10.4028/www.scientific.net/AMM.444-445.96>
- Xu, W., Sun, X., Li, D., Ryu, S., & Khaleel, M. A. (2013). Mechanism-based representative volume elements (RVEs) for predicting property degradations in multiphase materials.

- Computational Materials Science*, 68, 152–159.
<https://doi.org/10.1016/j.commatsci.2012.10.026>
- Yamini, S., & Young, R. J. (1980). The mechanical properties of epoxy resins - Part 2 Effect of plastic deformation upon crack propagation. *Journal of Materials Science*, 15(7), 1823–1831. <https://doi.org/10.1007/BF00550603>
- Yang, Y., Liu, X., Wang, Y. Q., Gao, H., Li, R., & Bao, Y. (2017). A progressive damage model for predicting damage evolution of laminated composites subjected to three-point bending. *Composites Science and Technology*, 151, 85–93.
<https://doi.org/10.1016/j.compscitech.2017.08.009>
- Yazid, A., Abdelkader, N., & Abdelmadjid, H. (2009). A state-of-the-art review of the X-FEM for computational fracture mechanics. *Applied Mathematical Modelling*, 33(12), 4269–4282.
<https://doi.org/10.1016/j.apm.2009.02.010>
- Yokozeki, T., Iwahori, Y., & Ishiwata, S. (2007). Matrix cracking behaviors in carbon fiber/epoxy laminates filled with cup-stacked carbon nanotubes (CSCNTs). *Composites Part A: Applied Science and Manufacturing*, 38(3), 917–924.
<https://doi.org/10.1016/j.compositesa.2006.07.005>
- Yu, H., Hou, Z., Guo, X., Chen, Y., Li, J., Luo, L., ... Yang, T. (2018). Finite element analysis on flexural strength of Al₂O₃-ZrO₂ composite ceramics with different proportions. *Materials Science and Engineering A*, 738(May), 213–218. <https://doi.org/10.1016/j.msea.2018.05.075>
- Zaharin, H., Abdul Rani, A., Azam, F., Ginta, T., Sallih, N., Ahmad, A., ... Zulkifli, T. Z. A. (2018). Effect of Unit Cell Type and Pore Size on Porosity and Mechanical Behavior of Additively Manufactured Ti6Al4V Scaffolds. *Materials*, 11(12), 2402.
<https://doi.org/10.3390/ma11122402>
- Zhang, C., Gong, B., Deng, C., & Wang, D. (2017). Computational prediction of mechanical properties of a C-Mn weld metal based on the microstructures and micromechanical properties. *Materials Science and Engineering A*, 685(November 2016), 310–316.
<https://doi.org/10.1016/j.msea.2017.01.023>
- Zhang, J., Koo, B., Subramanian, N., Liu, Y., & Chattopadhyay, A. (2016). An optimized cross-linked network model to simulate the linear elastic material response of a smart polymer. *Journal of Intelligent Material Systems and Structures*, 27(11), 1461–1475.
<https://doi.org/10.1177/1045389X15595292>
- Zheng, B., Zhou, Y., Smugeresky, J. E., Schoenung, J. M., & Lavernia, E. J. (2008). Thermal behavior and microstructural evolution during laser deposition with laser-engineered net shaping: Part I. Numerical calculations. *Metallurgical and Materials Transactions A: Physical Metallurgy and Materials Science*, 39(9), 2228–2236.
<https://doi.org/10.1007/s11661-008-9557-7>
- Zhu, H., Wu, B., Li, D., Zhang, D., & Chen, Y. (2011). Influence of Voids on the Tensile Performance of Carbon/epoxy Fabric Laminates. *Journal of Materials Science and Technology*, 27(1), 69–73. [https://doi.org/10.1016/S1005-0302\(11\)60028-5](https://doi.org/10.1016/S1005-0302(11)60028-5)